ABSTRACT

Title of dissertation:	Lattice QCD Simulations of Baryon Spectra and Development of Improved Interpolating Field Operators
	Ikuro Sato, Doctor of Philosophy, 2005
Dissertation directed by:	Professor Stephen J. Wallace Department of Physics

Large sets of baryon interpolating field operators are developed for use in lattice QCD studies of baryons with zero momentum. Because of the discretization of space, the continuum rotational group is broken down to a finite point group of cube. Operators are classified according to the irreducible representations of the double octahedral group. At first, three-quark quasi-local operators are constructed for each isospin and strangeness with suitable symmetry of Dirac indices. Nonlocal baryon operators are formulated in a second step as direct products of the quasi-local spinor structures together with lattice displacements. Appropriate Clebsch-Gordan coefficients of the octahedral group are used to form linear combinations of such direct products. The construction maintains maximal overlap with the continuum $SU(2)$ group in order to provide a physically interpretable basis. Nonlocal operators provide direct couplings to states that have nonzero orbital angular momentum.

Monte Carlo simulations of nucleon and delta baryon spectra are carried out with anisotropic lattices of anisotropy 3.0 with $\beta = 6.1$. Gauge configurations are generated by the Wilson gauge action in quenched approximation with space-time volumes $(1.6\,\mathrm{fm})^3 \times 2.1\,\mathrm{fm}$ and $(2.4\,\mathrm{fm})^3 \times 2.1\,\mathrm{fm}$. The Wilson fermion action is used with pion mass $\simeq 500\,\mathrm{MeV}$. The variational method is applied to matrices of correlation functions constructed using improved operators in order to extract mass eigenstates including excited states. Stability of the obtained masses is confirmed by varying the dimensions of the matrices. The pattern of masses for the low-lying states that we compute is consistent with the pattern that is observed in nature. Ordering of masses is consistent for positive-parity excited states, but mass splittings are considerably larger than the physical values.

Baryon masses for spin $S \geq 5/2$ states are obtained in these simulations. Hyperfine mass splittings are studied for both parities. No significant finite volume effect is seen at the quark mass we used.

Lattice QCD Simulations of Baryon Spectra and Development of Improved Interpolating Field Operators

by

Ikuro Sato

Dissertation submitted to the Faculty of the Graduate School of the
University of Maryland, College Park in partial fulfillment
of the requirements for the degree of
Doctor of Philosophy
2005

Advisory Committee:

Professor Stephen J. Wallace, Chair/Advisor
Professor Xiangdong Ji
Professor Thomas Cohen
Professor James J. Kelly
Professor Alice Mignerey

ACKNOWLEDGMENTS

LIST OF TABLES

Chapter 1

Introduction

One of the main goals that physicists have been working toward for over one hundred years is to find the fundamental constituents of matter and to discover the law that governs their interactions. In the early 20th century, in which modern atomic theory was established, the smallest size that could be detected was of order of 10^{-10} m. In this era atoms were considered as the smallest constituents of matter that are indivisible, as is literally meant by "atom" in Greek. It has been true in history that as time goes on, new technology emerges that enables human to observe physical phenomena at smaller scales. As a result, a "fundamental particle" in one era was no longer a fundamental particle in a later era.

Rutherford's experimental observation of the angular distribution produced by α particles scattered through thin gold foil revealed that an atom is not a fundamental particle but it consists of a heavy point-like nucleus and electrons. In early 1930's, Chadwick found the existence of the non-charged neutron, and immediately after, Heisenberg came up with the idea that a nucleus consists of positively-charged protons and neutrons. Today, protons and neutrons are categorized as members of a family, called baryons, and we know that a baryon consists of three quarks. Together with leptons, the quarks are considered as fundamental particles now. Today's accelerator technology is approaching the ability to explore the size of order of 10^{-20} m. Physicists believe that experimental data at this scale will determine the validity of the existing theory of particle physics and possibly give us a new key that opens the door to new physics.

1.1 Review of particle physics

Baryons are found in scattering experiments using particle accelerators. From the 1950's to 1980's, a large number of different types of baryons was observed. Similarly, many different types of mesons, integer-spin particles including pions first predicted by Yukawa and observed in a cosmic ray experiment, were discovered experimentally. Baryons and mesons are generically called hadrons. More than one hundred hadrons including the excited states and resonances were discovered in that period of time.

Discovery of such a large number of hadrons gave a hint that they are not the fundamental particles but composites of some smaller elements. This inspired Gell-Mann and others to develop quark model [1–4], in which all baryons are considered as composites of three quarks and all mesons are considered as composites of a quark and an antiquark. Quarks carry an electric charge of either $2|e|/3$ or $-|e|/3$ in his theory, but the fractional values of electric charges looked unbelievable to Gell-Mann, so he thought his model was just a mathematical model and quarks were not real. (On the other hand, Zweig, the other founder of quark model, thought quarks should exist.) Today,

Table 1.1: Fundamental particles and their properties.

	quark		lepton	
1st generation	u	d	e	ν_e
2nd generation	c	s	μ	ν_μ
3rd generation	t	b	τ	ν_τ
electric charge	2/3	$-1/3$	-1	0
color charge	r, g, b		neutral	
spin	1/2	1/2	1/2	1/2
baryon number	1/3	1/3	0	0
lepton number	0	0	1	1
forces	strong, weak, e&m		weak, e&m	weak

these fractional values of electric charge are accepted by physicists, and quarks are considered as the fundamental particles, together with leptons. Properties of these particles are listed in Table 1.1 [5, 6]. There are six kinds of quarks, or six *flavors.* There are also six leptons. Quarks and leptons are categorized into three *generations*, where all properties and interactions are the same for the three generations as appear in Table 1.1, except for their masses.

In this section, we briefly review particle physics, introducing the quark model [7], the strong interaction, and the unification of forces in nature.

1.1.1 Quark model

A meson consists of a quark and an antiquark, and a baryon consists of three quarks. Note that an antiquark has opposite electric charge to the quark so that the overall electric charge of a meson or baryon can only be 1, 0, or -1 (see Table 1.1 for quarks' electric charges). Mesons have integer spins and baryons have half-integer spins. Baryons have baryon number of one while mesons have zero.

With only two quarks, up and down quarks, there would be only $2 \times 2 = 4$ mesons. Three out of four belong to totally symmetric combinations that transform amongst themselves under rotations in flavor space. These three mesons are known as π^+, π_0, and π^- forming an isospin triplet. The other set is a singlet that is invariant under such transformation. The fact that the masses of three pions are very close implies that equal masses of up and down quarks is a good approximation. For this reason, the up quark is given an isospin of $I = I_3 = 1/2$ and the down quark is given an isospin of $I = 1/2, I_3 = -1/2$.

With three quarks, up, down and strange quarks, there would be $3 \times 3 = 9$ mesons. They can be classified into a totally-symmetric octet, and a singlet. In terms of irreducible representations of the SU(3) group, they can be written as,

$$\mathbf{3} \otimes \mathbf{3}^* = \mathbf{8} \oplus \mathbf{1}. \tag{1.1}$$

The quark triplet (u, d, s) belongs to $\mathbf{3}$ and the antiquark triplet $(\overline{u}, \overline{d}, \overline{s})$ belongs to $\mathbf{3}^* \neq \mathbf{3}$. By labeling mesons in terms of quantum numbers I_3 and so-called strangeness (S), the octet and
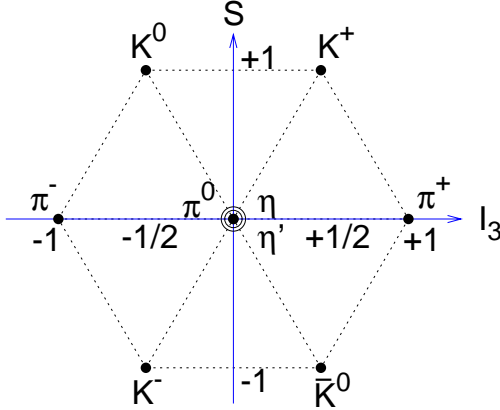
Figure 1.1: Pseudoscalar mesons: octet and singlet (η').

singlet mesons are arranged as shown in Fig. 1.1. Strangeness of a strange quark is defined to be -1 and that of an anti-strange quark is $+1$. All other quarks have no strangeness. Nonzero I_3 is given only to u and d quarks or $\overline{u}$ and $\overline{d}$ antiquarks. All nine mesons shown in Fig 1.1 are pseudoscalar mesons. They are scalar because of the spin-singlet. Since an antiquark has negative intrinsic parity with respect to a quark, for a given orbital angular momentum L the overall parity is given by $P = -(-1)^L$. So, $L = 0$ corresponds to negative parity, which is why they are named "pseudoscalar". Vector mesons that are spin-triplet are also classified into an SU(3) octet and singlet, like the case of pseudoscalar mesons.

Baryon multiplets can be generated by a product of three **3**'s. Group theoretically, such a product is decomposed as

$$\mathbf{3} \otimes \mathbf{3} \otimes \mathbf{3} = \mathbf{10} \oplus \mathbf{8} \oplus \mathbf{8} \oplus \mathbf{1}. \tag{1.2}$$

Irreducible representations shown on the right-hand-side of the equation are: **10** totally symmetric decuplet, **8** mixed-symmetric octet, the other **8** mixed-antisymmetric octet, and **1** totally symmetric singlet. Because of these different symmetries, they have to couple to different spins. With an antisymmetric color structure, which we introduce shortly, the baryon decuplet must have totally symmetric spin indices, i.e., $S = 3/2$ assuming $L = 0$ in order to satisfy Fermi statistics. The

baryon octet must have mixed-symmetric spin indices, i.e., $S = 1/2$ assuming $L = 0$, in which case the two sets of octet become the same. The baryon decuplet and octet can be arranged in terms of the quantum numbers strangeness and the third component of isospin as shown in Fig. 1.2.
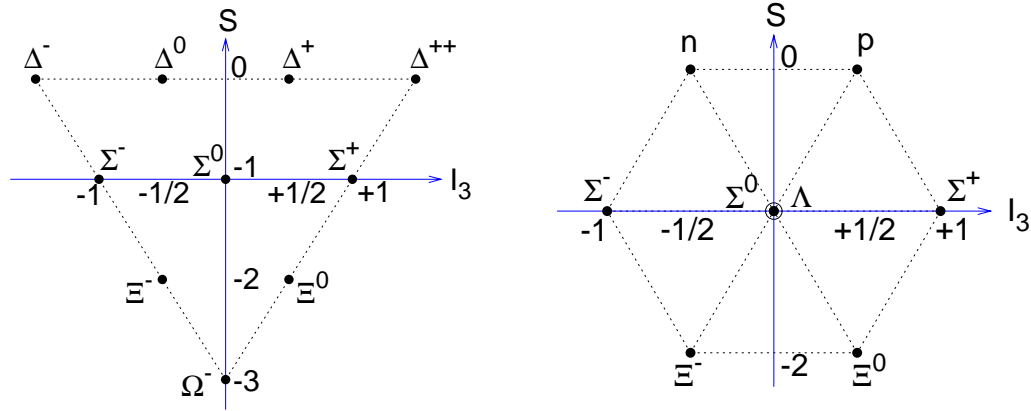
strangeness	decuplet baryon masses		octet baryon masses	
0	M_Δ	$\sim 1232\,\mathrm{MeV}$	M_n	$\sim 939\,\mathrm{MeV}$
-1	M_Σ	$\sim 1384\,\mathrm{MeV}$	M_Σ	$\sim 1193\,\mathrm{MeV}$
			M_Λ	$\sim 1115\,\mathrm{MeV}$
-2	M_Ξ	$\sim 1533\,\mathrm{MeV}$	M_Ξ	$\sim 1318\,\mathrm{MeV}$
-3	M_{Ω^-}	$1672\,\mathrm{MeV}$		

Figure 1.2: SU(3) decuplet baryon (left) and octet baryon (right). Decuplet and octet masses are given below [5].

1.1.2 Color charges

The delta baryon has isospin 3/2, therefore it is flavor symmetric. The ground state has zero orbital angular momentum, so it is S-wave. The spin of the lowest-lying state is known to be 3/2. A simultaneous exchange of flavors, spatial coordinates, and spins is thus symmetric, which contradicts the Pauli-exclusion principle. This led to an idea of introducing a new quantum number, first proposed by Greenberg [8]. This new quantum number carried by quarks and antiquarks is

now known as *color*. The color labels must appear as a totally-antisymmetric combination in hadrons in order to satisfy the Fermi statistics of the quarks. Later it turned out that this new quantum number is the charge of the strong interaction in QCD. The number of colors is $N_c = 3$, which was verified indirectly in experiments such as the decay rate of pion:

$$\Gamma(\pi^0 \to 2\gamma) \propto N_c^2. \tag{1.3}$$

The π^0 decay involves a quark loop and the decay rate is calculable in the quark model. Experimental results confirmed the relation in Eq. (1.3). Another such example is the Drell-Yan process, in which two protons collide to create heavy lepton pairs. Calculation of the cross section based on the quark model yields inverse proportionality to N_c. Experimental evidence showed that $N_c = 3$.

Three components of color charge are given intuitive names: red, green, and blue. The antiquark has anti-color, these are, anti-red, anti-green, and anti-blue. All hadrons are color-neutral. Mesons have color and anti-color, such as red and anti-red to yield overall color-neutral. Baryons always have an antisymmetric combination of red and green and blue, yielding again color-neutral (or white). Because all hadrons are color-singlet, they appear to have no color charge viewed from a large distance. This means that between hadrons separated by more than a scale of a nucleus, the strong interaction is absent, while in a short-range separation hadrons can interact among themselves by the strong force. Because of this, the strong force is called a short-range force. This is much like the van der Waals force between neutral molecules. Nuclear forces are due to this hadronic interaction occurring at hadronic scale separation.

1.1.3 Forces in nature

Another short-range force in nature is the weak force, which is responsible for the nuclear beta decay. The weak force and the long-range electromagnetic force are unified by the work of Glashow, Weinberg and Salam. This theory of electroweak unification is developed in the framework of gauge theory, where all forces are explained by exchanges of gauge bosons. The gauge boson for the electromagnetic interaction is the photon. The gauge bosons for the weak interaction are W bosons also known as weak bosons. Weak bosons were experimentally observed at the predicted

h

Table 1.2: The four fundamental forces in the nature.

	strong	electromagnetic	weak	gravity
interacting particle	quarks, hadrons	electrically charged	quarks, leptons	all particles
gauge boson	gluons	photon	weak bosons W	(graviton)
force range	$\sim 10^{-15}\text{m} \sim 1/M_\pi$	∞	$\sim 10^{-17}\text{m} \sim 1/M_W$	∞
relative strength	1	$\sim 1/137$	$\sim 10^{-5}$	$\sim 10^{-39}$

masses at CERN in 1983. At the unification energy scale, weak bosons are massless and there is no distinction between weak bosons and the photon. Weak bosons acquire masses by the Higgs mechanism, where spontaneous symmetry breaking of the vacuum at low Higgs potential creates Higgs particles whose interactions give masses to weak bosons. The energy density of the current universe is much smaller than the unification scale, so the universe is full of Higgs particles, although Higgs particles are not experimentally confirmed yet.

The gauge bosons for the strong interaction are called "gluons". Gluons are color-carriers and they act on all colored particles. So, gluons can self-interact, which is one of the essential features of the strong interaction. Because there are three colors, all gluon fields are described by generators of the SU(3) group. The theory that describes the dynamics of quarks and gluons is called Quantum Chromodynamics (QCD).

The electroweak force and the strong force are theoretically unified in the framework of local gauge theory. This unified theory is called the Standard Model (SM). The action of this model has symmetry of the form, $SU(2)_{\text{weak}} \times U(1)_{\text{em}} \times SU(3)_{\text{strong}}$. The Standard Model is a very successful theory of elementary particles up to today. However, the Standard Model is not the ultimate theory of physics, because it does not unify the gravitational force. It is much more difficult to construct a local gauge theory of gravity. However, the typical magnitude of the gravitational force is much, much smaller than that of the other three forces so gravity plays almost no role in subatomic

physics. The four fundamental forces are briefly summarized in Table 1.2 [6].

1.2 Quantum Chromodynamics

Quantum Chromodynamics is accepted as the theory of the strong interaction. The building blocks to this theory are quarks and gluons. The gauge group of the strong interaction is SU(3), which has eight generators. Each generator corresponds to one type of gluon field, so there are eight types of gluon in the theory. Let us denote quark fields as q^f with flavor f and gluon fields as A_μ^a with $a = 1, \cdots, 8$. In the color space, quark fields are three-component "color-vector", and gluon fields are 3×3 "color-matrix".

We outline the basics of QCD in Subsections 1.2.1 and 1.2.2 [9–11]. The Euclidean field theory is introduced in Subsection 1.2.3 [12, 13]. The basics of lattice QCD are then given in Subsections 1.2.4 1.2.5, and 1.2.6 [13–18].

1.2.1 QCD lagrangian

The QCD lagrangian density is of the form,

$$\mathcal{L}_{\text{QCD}}(x) = \mathcal{L}_G(x) + \mathcal{L}_F(x), \tag{1.4}$$

where $\mathcal{L}_G$ consists of purely gluon fields and determines the dynamics of gluons. It has the form,

$$\mathcal{L}_G(x) = -\frac{1}{4}\text{Tr}\left[G^{\mu\nu}(x)G_{\mu\nu}(x)\right], \tag{1.5}$$

where the gluon field tensor is given by

$$G_{\mu\nu}(x) = \partial_\mu A_\nu(x) - \partial_\nu A_\mu(x) + ig\left[A_\mu(x), A_\nu(x)\right], \tag{1.6}$$

$$A_\mu(x) = \sum_{a=1}^{N_c^2-1} A_\mu^a(x)\frac{\lambda^a}{2}, \tag{1.7}$$

where g is the coupling constant, and λ^a are the Gell-Mann matrices satisfying the following commutation relation

$$\left[\frac{\lambda^a}{2}, \frac{\lambda^b}{2}\right] = if_{abc}\frac{\lambda^c}{2}, \tag{1.8}$$

where f_{abc} are structure constants of SU(N_c). The fermion sector of the lagrangian is

$$\mathcal{L}_F(x) = \sum_f \overline{q}^f(x) \left(i\gamma^\mu D_\mu - m\right) q^f(x). \tag{1.9}$$

Here, the gauge-covariant first-derivative defined as

$$D_\mu = \partial_\mu + igA_\mu \tag{1.10}$$

in order to maintain gauge-invariance of the theory under the following local gauge transformation:

$$q^f \quad \rightarrow \quad V(x)q^f, \tag{1.11}$$

$$A_\mu(x) \quad \rightarrow \quad V(x)A_\mu(x)V^\dagger(x) + \frac{i}{g}V(x)\partial_\mu V^\dagger(x), \tag{1.12}$$

$$= \quad V(x)\left(A_\mu + \frac{i}{g}\partial_\mu\right)V^\dagger(x), \tag{1.13}$$

where $V(x) = \exp(i\alpha^a(x)\lambda^a/2)$ with arbitrary, differentiable, real functions $\alpha^a(x)$. Under an infinitesimal transformation

$$
\begin{aligned}
D_\mu q^f(x) \quad \rightarrow \quad & \left(\partial_\mu + igA_\mu^a\frac{\lambda^a}{2} + i\partial_\mu\alpha^a(x)\frac{\lambda^a}{2} - g\left[\alpha^a\frac{\lambda^a}{2}, A_\mu^b\frac{\lambda^b}{2}\right]\right)\left(1 + i\alpha^c(x)\frac{\lambda^c}{2}\right)q^f(x) \\
\simeq \quad & \left(1 + i\alpha^a(x)\frac{\lambda^a}{2}\right)D_\mu q^f(x) \\
= \quad & V(x)D_\mu q^f(x) \tag{1.14}
\end{aligned}
$$

up to terms of order $(\alpha^a)^2$. In other words, the covariant derivative and the commutator of covariant derivatives transform as

$$D_\mu \quad \rightarrow \quad V(x)D_\mu V^\dagger(x), \tag{1.15}$$

$$[D_\mu, D_\nu] \quad \rightarrow \quad V(x)\left[D_\mu, D_\nu\right]V^\dagger(x). \tag{1.16}$$

The commutator, in fact, gives the gluon field tensor

$$[D_\mu, D_\nu] = igG_{\mu\nu}, \tag{1.17}$$

then it immediately follows

$$G_{\mu\nu}(x) \rightarrow V(x)G_{\mu\nu}(x)V^\dagger(x). \tag{1.18}$$

1.2.2 Asymptotic freedom

The QCD coupling constant $\alpha_s \equiv g^2/4\pi$ is a function of momentum transfer Q. Because of this, α_s is called the "running coupling constant". The QCD coupling constant at leading order is given by

$$\alpha_s(Q^2) = \frac{\alpha_s(\Lambda)}{1 + \alpha_s(\Lambda)\frac{33-2n_f}{12\pi}\ln\left(\frac{Q^2}{\Lambda^2}\right)}, \tag{1.19}$$

where Λ is a cutoff energy of the theory, which lies in the range of $100-500\,\mathrm{MeV}$, and n_f is the number of quark flavors. As is clear from the equation, $\alpha_s(Q^2)$ decreases as Q^2 increases when $n_f = 6$. Eventually with $Q^2 \to \infty$, α_s becomes zero. This means that quarks behave as free particles, and the gluon's self-interactions also vanish. This high energy behavior of quarks and gluons is referred to as "asymptotic freedom". This is a characteristic of the strong coupling whose importance was first emphasized by Gross, Wilczek, and Politzer[1] [19, 20]. Since the coupling constant is small at high energy, perturbation theory can be applied just like QED. For instance at $Q^2 = (30\,\mathrm{GeV})^2$ scale, α_s is of order of 0.1, so a perturbative expansion makes sense. However when the momentum transfer is of the order of the hadronic energy scale (about $1\,\mathrm{GeV}$), the coupling constant becomes $\alpha_s \sim 1$, and traditional perturbation theory fails. This failure of the main analytical approach makes the study of hadronic physics difficult. However, the work of Wilson showed that there is a theoretical method to calculate the strong interaction from first principles. Wilson's method involves calculating physical quantities by Monte Carlo computer simulations using hypercubic lattices.

1.2.3 Euclidean path integral approach and Monte Carlo simulation

In field theory, physical quantities can be obtained by taking the vacuum expectation value of a physical operator $\mathcal{O}$, which involves integrating over all possible values of fields. In Minkowski space-time each configuration of fields is weighted by e^{iS_M}, which is an oscillatory factor that is not suitable for numerical computations. A mathematical trick employed for numerical simulations of QCD is to rotate the time axis in the complex plane to a purely imaginary time axis $x_0 \to -ix_4$,

---

[1] They were awarded Nobel Prize in 2004.

where x_4 is called the Euclidean time and is real. This yields a positive time evolution operator e^{-Hx_4} where H is the Euclidean hamiltonian. Then the functional integral becomes

$$\langle \mathcal{O} \rangle = \frac{1}{Z} \int D\bar{q} Dq DU \mathcal{O}[\bar{q}, q, A] \, e^{-S_E[\bar{q}, q, A]}, \tag{1.20}$$

where S_E is the Euclidean action and the denominator is a partition function

$$Z = \int D\bar{q} Dq DU e^{-S_E[\bar{q}, q, A]}. \tag{1.21}$$

With real and positive S_E, the integral weight e^{-S_E} can be interpreted as the probability weight just as the Boltzmann factor in classical statistical mechanics. All Feynman propagators calculated using the Euclidean field theory are identical to those calculated using Minkowski field theory, analytically continued to imaginary time. Another benefit of the use of Euclidean space-time is that since the Euclidean metric is of the form $\delta_{\mu\nu}$, the spatial coordinates and time can be treated in the same manner and there is no distinction between covariant and contravariant quantities.

The connections of coordinates and derivatives for Minkowski and Euclidean space-time are given by

$$x^4 = x_4 = ix_M^0 = ix_0^M, \quad x^j = x_j = x_M^j = -x_j^M,$$

$$\partial^4 = \partial_4 = -i\partial_M^0 = -i\partial_0^M, \quad \partial^j = \partial_j = -\partial_M^j = \partial_j^M, \tag{1.22}$$

where a superscript or subscript M denotes Minkowski space-time and the other quantities are defined as Euclidean space-time. In Euclidean space-time the time axis is denoted by label 4, while the spatial axes are denoted by label $j = 1, 2, 3$, the same as Minkowski axis. The vector potential $A_\mu(x)$ in Euclidean time is defined to be

$$A^4 = A_4 = -iA_M^0 = -iA_0^M, \quad A^j = A_j = -A_M^j = A_j^M \tag{1.23}$$

It follows that the Euclidean field tensor takes the form

$$G^{4i} = G_{4i} = iG_M^{0i} = -iG_{0i}^M, \quad G^{ij} = G_{ij} = G_M^{ij} = G_{ij}^M. \tag{1.24}$$

The gauge sector of the action S_E^G in Euclidean space-time is written as

$$iS_M^G = i \int dx_M^0 \int d^3\mathbf{x}_M \left(-\frac{1}{4} G_{\mu\nu}^M G_M^{\mu\nu} \right)$$

$$
\begin{aligned}
&= \quad i \int (-i dx_4) \int d^3\mathbf{x} \left(-\frac{1}{4} \right) \left[(iG_{4k})(-iG_{4k}) + (-iG_{4k})(iG_{4k}) + G_{ij}G_{ij} \right] \\
&= \quad -\int d^4x \frac{1}{4} G_{\mu\nu}G_{\mu\nu} \equiv -S_E^G. \quad\quad (1.25)
\end{aligned}
$$

To construct a fermion action in Euclidean space-time, one has to define the Euclidean Dirac γ matrices. They are given by

$$
\gamma^4 = \gamma_4 = \gamma_M^0 = \gamma_0^M, \quad \gamma^j = \gamma_j = -i\gamma_M^j = i\gamma_j^M, \quad \gamma_5 = \gamma_4\gamma_1\gamma_2\gamma_3 = \gamma_5^M. \quad\quad (1.26)
$$

The Euclidean Dirac γ matrices satisfy

$$
\{\gamma_\mu, \gamma_\nu\} = 2\delta_{\mu\nu}, \quad \gamma_\mu^\dagger = \gamma_\mu. \quad\quad (1.27)
$$

The fermion sector of the action, S_E^F, in Euclidean space-time is written as

$$
\begin{aligned}
iS_M^F &= \quad i \int dx_M^0 \int d^3\mathbf{x}_M \overline{\psi}_M \left(i\gamma_M^0 D_0^M + i\gamma_M^j D_j^M - m \right) \psi_M \\
&= \quad i \int (-idx_4) \int d^3\mathbf{x} \overline{\psi} \left(i\gamma_4(iD_4) + i(i\gamma_j)D_j - m \right) \psi \\
&= \quad -\int d^4x \overline{\psi} \left(\gamma_\mu D_\mu + m \right) \psi = -\int d^4x \overline{\psi} K \psi \equiv -S_E^F. \quad\quad (1.28)
\end{aligned}
$$

Note that the covariant derivative in Euclidean space-time is given by

$$
D_\mu^M = (\partial_0^M + igA_0^M, \ \partial_j^M + igA_j^M) = ((i\partial_4) + ig(iA_4), \ \partial_j + igA_j) \equiv (iD_4, \ D_j). \quad\quad (1.29)
$$

From Eqs. (1.25) and (1.28), it follows that

$$
iS_M = -S_E \quad\quad (1.30)
$$

as desired.

The fields U_μ appearing as an integration variable of Eq. (1.20) are defined as the path-ordered Schwinger line integral

$$
U_\mu(x_0, x_1) = Pe^{ig \int_{x_0}^{x_1} A_\mu(x)dx}. \quad\quad (1.31)
$$

Then under a gauge transformation, the line integral transforms as

$$
U_\mu(x_0, x_1) \rightarrow V(x_0)U_\mu(x_0, x_1)V^\dagger(x_1). \quad\quad (1.32)
$$

Quark and antiquark fields are Grassmann-valued fields. Integrations of Eq. (1.20) over fermion fields can be analytically taken and give a factor $\det(K[U])$, where K is the fermion matrix, which will be discussed in Subsection 1.2.4. The path integral in Eq. (1.20) becomes

$$\langle \mathcal{O} \rangle = \frac{1}{Z} \int DU \mathcal{O}^{\text{W.C.}}[U] \det(K[U]) \, e^{-S_E^G[U]}, \tag{1.33}$$

where $\mathcal{O}^{\text{W.C.}}[U]$ is the observable, for which the Wick contractions of quark-antiquark fields are taken, and S_E^G is the Euclidean action of gluon fields. In numerical calculations, it is impossible to take an integral over all possible gluon fields. Instead, one simply takes a finite number of statistically uncorrelated ensembles, so-called gauge (field) configurations. Gauge configurations $U^{(i)}$, $i = 1, \cdots, N$ are distributed with a probability density given by the product of the factor $e^{-S_E^G}$ and fermion matrix determinant $\det(K[U])$. The functional integral in Eq. (1.33) is now replaced by a finite sum

$$\langle \mathcal{O} \rangle = \frac{1}{N} \sum_{i=1}^{N} \mathcal{O}^{\text{W.C.}}[U^{(i)}] \tag{1.34}$$

with a large number of N. Many computer algorithms are developed to generate such gauge configurations. Readers are referred to standard lattice QCD textbooks for details [13, 14].

1.2.4 Lattice gauge theory

All fields and the action are defined on a discretized space-time in lattice QCD. Space-time discretization of the naive Euclidean action in Eq. (1.28) is, in fact, ill-defined because of the existence of unphysical fermion states. We explain briefly this problem, known as the fermion doubling problem, and introduce Wilson's trick to circumvent this problem below.

A fermion propagator using the naive action in Eq. (1.28) is given by taking the inverse of the fermion kernel, K, as

$$K_{\alpha\beta}^{-1}(x, y). \tag{1.35}$$

and it satisfies the following linear equation,

$$\sum_{\lambda, l} K_{\alpha, \lambda}(x, l) K_{\lambda, \beta}^{-1}(l, y) = \delta_{\alpha\beta} \delta_{xy}. \tag{1.36}$$

Let us ignore the gluon interaction for the time being. The lattice derivative of the fermion field can be defined as the following form

$$\partial_\mu q(x) = \frac{1}{2a} \left[q(x + a\hat{\mu}) - q(x - a\hat{\mu}) \right]. \tag{1.37}$$

In momentum space, this gives $\frac{1}{a}\sin(p_\mu a)$, instead of p_μ. The propagator in Eq. (1.35) is easily calculated using the fermion kernel defined in Eq. (1.28) as the following form

$$K_{\alpha\beta}^{-1} = \lim_{a \to 0} \int_{-\pi/a}^{\pi/a} \frac{d^4 p}{(2\pi)^4} \frac{\left[-i\gamma_\mu \frac{1}{a}\sin(p_\mu a) + M \right]_{\alpha\beta}}{(\frac{1}{a}\sin(p_\mu a))^2 + M^2} e^{ip(x-y)}. \tag{1.38}$$

In the limit $M \to 0$, zero energy modes correspond to: $p_\mu = (0,0,0,0), (0,0,0,\pi/a), (0,0,\pi/a,0), \cdots$. Because of the sine function of momentum in Eq. (1.38), the corners of Brillouin zone in each momentum axis have the same energy as zero momentum in the computation of the propagator. There are $2^4 = 16$ such zero-energy states, but only the state, $p_\mu = (0,0,0,0)$, corresponds to the physical zero-energy mode and the other 15 are artifacts due to the space-time discretization. These unphysical states are called fermion doublers.

Wilson proposed a new formalism of the lattice fermion action that eliminates the fermion doubling problem, known as the Wilson fermion [21]. The Wilson fermion action is of the form

$$S_F^{(W)} = S_F - a\frac{r}{2} \sum_{x,\mu} \bar{q}(x)\nabla_\mu^2 q(x), \tag{1.39}$$

where S_F is the fermion action introduced in Eq. (1.28) with lattice derivative, r is called the Wilson parameter and ∇_μ^2 is the lattice laplacian operator defined as,

$$\nabla_\mu^2 \equiv \frac{1}{a^2} \left[q(x + a\hat{\mu}) + q(x - a\hat{\mu}) - 2q(x) \right]. \tag{1.40}$$

Then the kernel of the Wilson fermion action is given by

$$\begin{aligned} S_F^{(W)} &= \sum_{x,y} \bar{q}_\alpha(x) K_{\alpha\beta}^{(W)}(x,y) q_\beta(y), \\ K_{\alpha\beta}^{(W)}(x,y) &= \frac{1}{a}(Ma + 4r)\delta_{xy}\delta_{\alpha\beta} - \frac{1}{2a}\sum_\mu \left[(r - \gamma_\mu)_{\alpha\beta}\delta_{y,x+a\hat{\mu}} + (r + \gamma_\mu)_{\alpha\beta}\delta_{y,x-a\hat{\mu}} \right]. \end{aligned} \tag{1.41}$$

Note that in the continuum limit $a \to 0$, the Wilson term in Eq. (1.39) vanishes, thus $K_{\alpha\beta}^{(W)}(x,y) = K_{\alpha\beta}(x,y)$. The propagator of the Wilson fermion is given by the same form as in Eq. (1.38) with

the following replacement:

$$M \rightarrow M + \frac{2r}{a} \sum_{\mu} \sin^2 \left(\frac{p_\mu a}{2} \right).$$ (1.42)

In the limit $M \rightarrow 0$, the second term in Eq. (1.42) still gives a nonzero value for $p_\mu \neq 0$. The fermion doublers are now eliminated because the energy is shifted by this additional term, which give nonzero values in the vicinity of Brillouin zone. The Wilson fermion has only one zero-energy solution.

The lattice gluon fields are defined on every line segment of the lattice, taking the first order approximation of Eq. (1.31) in the integral as

$$U_\mu(x) = e^{iagA_\mu(x)},$$ (1.43)

where a is the lattice spacing. In principle, the lattice spacing can be different along each spatial and temporal direction, but it is customary to use a fixed lattice spacing a_s for each spatial direction. The temporal lattice spacing a_t can be different from a_s, and recent works often employ anisotropic lattices where $a_t < a_s$ in order to probe higher frequency modes. Our simulations of excited baryons also use anisotropic lattices, but we keep a_t the same as a_s in this chapter for simplicity.

With the gauge interaction, the Wilson fermion action becomes of the form,

$$\begin{aligned} S_F^{(W)}[U] &= \frac{1}{a} \sum_x \overline{q}(x)(Ma + 4r)q(x) \\ &- \frac{1}{2a} \sum_{x,\mu} \left[\overline{q}(x)(r - \gamma_\mu)U_\mu(x)q(x + a\hat{\mu}) + \overline{q}(x)(r + \gamma_\mu)U_\mu^\dagger(x - a\hat{\mu})q(x - a\hat{\mu}) \right]. \end{aligned}$$ (1.44)

This action is invariant under the following local gauge transformations,

$$\begin{aligned} q(x) &\rightarrow V(x)q(x), \\ \overline{q}(x) &\rightarrow \overline{q}(x)V^\dagger(x), \\ U_\mu(x) &\rightarrow V(x)U_\mu(x)V^\dagger(x + a\hat{\mu}), \\ U_\mu^\dagger(x) &\rightarrow V(x + a\hat{\mu})U_\mu^\dagger(x)V^\dagger(x). \end{aligned}$$ (1.45)

The line integral U_μ works as a parallel-transporter of color between neighboring space-time points. Therefore quark fields defined at different points in space-time must be linked by SU(3) parallel-

transporters in order to maintain local gauge invariance. The lattice covariant derivative is defined as

$$D_\mu q(x) = \frac{1}{2a} \left[U_\mu(x) q(x + a\hat{\mu}) - U_\mu^\dagger(x - a\hat{\mu}) q(x - a\hat{\mu}) \right]. \tag{1.46}$$

Expansion of U_μ to first order in a gives the covariant derivative mentioned earlier in Eq. (1.29).

Since the gauge link U_μ transforms according to Eq. (1.45), the following path-ordered product of gauge links is invariant under a local gauge transformation,

$$U_{\mu\nu}(x) = U_\mu(x) U_\nu(x + a\hat{\mu}) U_\mu^\dagger(x + a\hat{\nu}) U_\nu^\dagger(x). \tag{1.47}$$

This path-ordered product $U_{\mu\nu}(x)$ is referred to as a plaquette. Schematically, the plaquette is represented by a "loop" in the $\mu - \nu$ plane.

In U(1) abelian gauge theory, it is easy to show that the plaquette has the following form,

$$U_{\mu\nu}^{(U(1))}(x) = e^{iea^2 F_{\mu\nu}(x)}, \tag{1.48}$$

where e is the coupling constant of the U(1) gauge theory and $F_{\mu\nu}$ is the field strength tensor:

$$
\begin{aligned}
F_{\mu\nu}(x) &= \frac{1}{a} \left[A_\mu(x + a\hat{\nu}) - A_\mu(x) - A_\nu(x + a\hat{\mu}) + A_\nu(x) \right] \\
&\rightarrow \partial_\mu A_\nu(x) - \partial_\nu A_\mu(x), \qquad a \rightarrow 0.
\end{aligned} \tag{1.49}
$$

The U(1) gauge action can be written straightforwardly in terms of the plaquette as

$$\frac{1}{4} \sum_{\mu,\nu,x} a^4 F_{\mu\nu}(x) F_{\mu\nu}(x) = \frac{1}{e^2} \sum_{\mu<\nu,x} \left[1 - \frac{1}{2}(U_{\mu\nu}(x) + U_{\mu\nu}^\dagger(x)) \right] \tag{1.50}$$

for small a.

Below we show that in the non-abelian case the field tensor can be written as a form that is analogous to the abelian case. The plaquette in $SU(N_c)$ abelian gauge theory, with N_c being the number of color charges, can be written as,

$$U_{\mu\nu}(x) = e^{iga^2 G_{\mu\nu}(x)}. \tag{1.51}$$

Since the $SU(N_c)$ generators do not commute for $N_c > 1$, we must use the Baker-Campbell-Hausdorff formula for the expansion

$$e^A e^B = e^{A+B+\frac{1}{2}[A,B]+\cdots}. \tag{1.52}$$

Then from Eqs. (1.43), (1.47), and (1.51),

$$
\begin{aligned}
U_{\mu\nu}(x) &= e^{iga^2 G_{\mu\nu}(x)} \\
&= e^{iga^2 \partial_\mu A_\nu(x) + iga^2 \partial_\nu A_\mu(x) - \frac{1}{2}a^2 g^2 [A_\mu, A_\nu] - \frac{1}{2}a^2 g^2 [A_\mu(x+a\hat{\nu}), A_\nu(x+a\hat{\mu})] + \cdots}.
\end{aligned} \tag{1.53}
$$

From this equation, the following identity is confirmed.

$$
G_{\mu\nu}(x) = \partial_\mu A_\nu(x) - \partial_\nu A_\mu(x) + ig[A_\mu(x), A_\nu(x)]. \tag{1.54}
$$

The lattice gauge action of the $SU(N_c)$ non-abelian gauge theory has the following form,

$$
S_G^{(W)}[U] = \beta \sum_{\mu<\nu,x} \left[1 - \frac{1}{2N_c} \text{Tr}(U_{\mu\nu}(x) + U_{\mu\nu}^\dagger(x)) \right], \tag{1.55}
$$

where β is given by

$$
\beta = \frac{2N_c}{g^2}. \tag{1.56}
$$

The lattice gauge action given in Eq. (1.55) is referred as the Wilson gauge action or the plaquette action.

1.2.5 Conversion into physical scale

Having defined the elementary field operators and Euclidean lattice actions, one is ready to use the theory and apply the Monte Carlo algorithm. The physical observables are obtained in lattice units. To obtain physical units one needs to convert lattice units into physical units. One method for the conversion of units uses the masses of the pion and rho-mesons. One can perform Monte Carlo simulations at the same coupling constant to obtain different pion masses aM_π and rho-meson masses aM_ρ in units of lattice spacing a, by changing the bare quark mass am. From current algebra the following relations hold

$$
\begin{aligned}
M_\pi^2 &= \lambda_\pi m, \\
M_\rho &= \lambda_\rho m + \beta_\rho.
\end{aligned} \tag{1.57}
$$

Having several different values of meson masses and bare quark masses, one can fit the parameters $\lambda_\pi, \lambda_\rho$, and β_ρ. Then inserting the physical values of $M_\pi = 140\,\text{MeV}$ and $M_\rho = 770\,\text{MeV}$ into

Eq. (1.57), one can obtain the lattice spacing a and bare quark mass m in physical units, assuming that the lattice spacing is a function only of the coupling constant.

1.2.6 Quenched approximation

Generation of gauge field configurations involves taking the determinant of the fermion matrix. Since the fermion matrix is defined nonlocally, taking a determinant of such a matrix in each Monte Carlo update step is computationally very demanding. In fact, calculations of the determinants occupy most of the computational time of an entire simulation. To cut down the computational burden most of the simulations done to date, including the simulation presented in this thesis, employ the *quenched approximation*, where the fermion determinant is set to 1 for every gauge configuration,

$$\det K[U] = 1. \tag{1.58}$$

The fermion matrix with constant determinant means that dynamical quarks do not interact with neighboring gluons. In other words, the quenched approximation is equivalent to having infinitely heavy dynamical quarks. Quenched QCD is not the right theory of the strong interaction because quark loop effects are completely ignored. However, some observables have small quark loop effects, such as heavy baryon spectra. The quenched approximation is also interesting in a sense that comparison with dynamical QCD simulation can tell us how much the effect of quark loops are.

For hadron spectra, it has been reported that the discrepancy of hadron spectra calculated using quenched QCD simulations and the physical values is about 10%. For the most recent such results, readers are recommended to see lattice conference proceedings [23]. Here, we show representative results of quenched QCD simulation of hadron spectra done by CP-PACS Collaboration in Figure 1.3 [22]. It is obvious from the figure that the lattice QCD simulations reproduce the physical hadron spectra of ground states quite well even in the absence of the dynamical quarks.
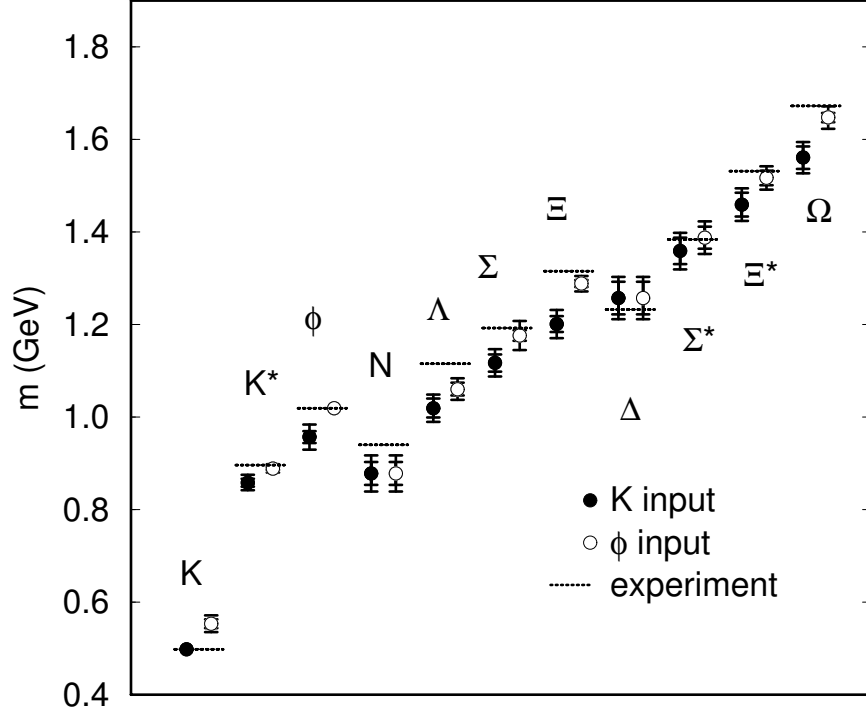
Figure 1.3: Quenched QCD simulations of hadron spectra reported by CP-PACS Collaboration [22]. Masses are obtained by chiral extrapolations. The physical scale is determined by using the physical masses of π, ρ, and either K or ϕ mesons. The Wilson fermion action and the plaquette gauge action are used.

1.3 Hadronic resonances on lattice

Masses and widths of excited-state hadrons are not directory calculable in lattice simulations with realistic pion masses even with full QCD and large volumes because unstable hadrons decay to hadronic scattering states such as $\pi - N$ states. Energy eigenstates of all the particles on finite lattices occur at discrete levels due to momentum quantization in units of $2\pi/L$, where L is the box size. The relative momentum between scattering particles is varied by changing L, but the energy of a resonance state is fixed. Finite volumes of the lattice can be used as a probe to detect hadronic resonances by varying the energy of scattering states so as to find "avoided level crossings", where there is a large mixing of single-particle resonance states with multi-particle decay states. The phase shift rises through $\pi/2$ as the energy of the scattering states increases through the resonance

energy. The scattering phase shift in finite volumes was formulated in Ref. [24–26]. Avoided level crossings for $O(4)$ non-linear σ model were demonstrated in Ref. [27], and those of coupled scalar fields were demonstrated in Ref. [28]. Computations of resonance parameters require a huge amount of computational resources because a number of gauge configurations need to be generated for each lattice volume.

In this thesis, only three-quark operators are developed and the scattering states are not included. We ultimately intend to include scattering states and to apply the method of finite volumes in order to compute masses of hadronic resonances. This requires building suitable operators for multi-hadron scattering states.

1.4 Overview of thesis

In spite of the success of quenched lattice QCD simulations for ground-state hadron spectra, very little is known for excited hadrons. Various phenomenological models have been developed, such as the bag model, the nonrelativistic quark model, effective field theory, QCD sum rules, *etc.*, to explain the excited states of hadrons. However, nonperturbative studies of excited hadrons are necessary to examine the validity of QCD as the theory of strong interaction.

This thesis contains exploratory lattice QCD simulations for baryon spectroscopy, consisting of two main parts: (1) construction of a large set of baryon field operators suitable for lattice QCD, and (2) the results of quenched QCD simulations of excited baryons using these improved operators at a relatively low pion mass $\sim 500\,\mathrm{MeV}$. Baryon masses and optimal baryon field operators are determined reliably by diagonalizing baryon correlation matrices constructed from a sufficiently large set of operators, which is motivated by the variational principle. Operator construction takes advantage of the cubic symmetry of the lattice to have better overlap with physical states of interest, especially baryons with higher spins. Nonlocality of operators is implemented in order to impose orbital structures to the operators. Lattice operators are developed in detail in Chapter 2. The computational techniques for Monte Carlo simulations are introduced in Chapter 3. The action used in these simulations is explained, and parameters of the simulations are given also. Chapter 4

shows the lattice QCD results for N^* and Δ baryons in different irreducible representations of the cubic group, and mass ratios are compared with empirical data. Hyperfine mass splittings are studied. The analysis of excited baryons is based on $16^3 \times 64$ lattices. Very recently, we completed the analysis using $24^3 \times 64$ lattices with the same pion mass. The volume dependence of baryon masses is examined using these two lattices and the results are reported at the end of Chapter 4. A summary of the thesis is given in Chapter 5.

Chapter 2

The Invariant Groups on Cubic Lattice and Baryon Source Construction

2.1 Motivation and overview

Theoretical determination of the spectrum of baryon resonances from QCD has been an important goal. Lattice QCD calculations have succeeded in part to meet the goal by providing convincing results for the lowest mass for each baryon. Recently, studies of negative-parity baryons have been reported by several groups [29–36]. Nemoto *et al.* and Melnitchouk *et al.* considered the $\Lambda(1405)$ baryon, which is the lightest of all negative-parity baryons in spite of its nonzero strangeness. They used a three-quark source operator motivated by the spin-flavor SU(6) quark model and concluded that $\Lambda(1405)$ is not evident from their data. However, there is a possibility that the operators used couple weakly to $\Lambda(1405)$ while other three-quark operators that were not used would provide better coupling to $\Lambda(1405)$.

Most lattice simulations so far are restricted to $j^P = 1/2^\pm, 3/2^\pm$ states. Much less is known about excited states. The first preliminary lattice calculation of $5/2^\pm$ excited nucleon masses was reported by the Lattice Hadron Physics Collaboration [37, 38] using one of the operators that we develop in this thesis. Similar operators are designed and reported in Ref. [39, 40], where large sets of operators are constructed in an automated procedure using the group theoretical projection method.

The variational method was successfully used to determine the spectrum of glueball masses by Morningstar and Peardon [41]. They used a large number of interpolating field operators for glueballs to form matrices of lattice correlation functions. The spectrum of effective masses

was obtained by diagonalizing the matrices of correlation functions to isolate mass eigenstates in each symmetry channel [42, 43]. In effect, one allows the dynamics to determine the optimal linear combination of operators that couple to each mass state. A similar program for baryon spectroscopy has been undertaken by the Lattice Hadron Physics Collaboration. The first step is to construct a large number of suitable baryon interpolating operators that correspond to states of zero momentum, definite parity and definite total angular momentum $j = \frac{1}{2}, \frac{3}{2}, \frac{5}{2}, \cdots$.

Use of a cubic lattice breaks the continuum rotational symmetry down to a finite group called the octahedral group, O. States of good angular momentum correspond to states that occur in certain patterns distributed over the irreducible representations (*irreps*) of O. Although mass calculations are insensitive to the angular momentum projection j_z, other applications may require baryons with a definite angular momentum projection. We develop operators that are classified into irreps of O using a basis that keeps the correspondence to the continuum j, j_z states as close as possible.

It is desirable to use nonlocal baryon operators as well as the usual local operators. Nonlocal operators can provide a variety of radial and angular distributions of quarks within a baryon so as to couple more efficiently to excited states. Nonlocal operators also are needed in order to realize the total angular momentum greater than $\frac{3}{2}$ and to have large sets of operators.

In this chapter, we first review the basics of the octahedral group [44–49] for integer and half-integer spins in Section 2.2. Quasi-local baryon operators are developed in Section 2.3 for each baryon flavor: N, Δ, Λ, Σ and Ω. Nonlocal operators are developed in Section 2.4 in a fashion that illustrates many additional possibilities for operator construction. The nonlocal operators involve a spatial distribution that transforms according to an irrep of the octahedral group in a direct product with a combination of Dirac indices that also transforms according to an irrep of the group. The Clebsch-Gordan series for the octahedral group is used to form linear combinations of such direct products that transform irreducibly. Some concluding remarks are presented in Section 2.5.

2.2 Octahedral Group and Lattice Operators

In lattice QCD, hadron field operators are composed of quark fields on a spatially isotropic lattice. The lattice is symmetric with respect to a restricted set of rotations that form the octahedral group, O, which is a subgroup of the continuum rotational group SO(3). The octahedral group consists of 24 group elements, each corresponding to a discrete rotation that leaves invariant a cube, or an octahedron embedded within the cube. When the objects that are rotated involve half-integer values of the angular momentum, the group elements double to extend the range of rotational angles from 2π to 4π, forming the double octahedral group O^D.

Spatial inversion commutes with all rotations and forms a two-element point group together with the identity. Thus inclusion of the spatial inversion into the finite rotational group simply doubles the number of group elements. When spatial inversion is included, the groups are denoted by O_h and O_h^D for integer spins and half-integer spins, respectively.

Given a quantum field operator for a hadron on a cubic lattice, one may generate other operators by applying the inversion and each rotation of the octahedral group to the given operator. This produces a set of operators that transform amongst themselves with respect to the octahedral group. The set provides a representation of the octahedral group, i.e., when a group element, G_a, is applied to operator $\mathcal{O}_i$ in the set, the result is a linear combination of other operators in the set, $\sum_j T_{ij}(G_a)\mathcal{O}_j$, where $T_{ij}(G_a)$ is a representation matrix of the group element G_a. Such representation matrices are in general reducible. In order to identify operators that correspond to specific hadrons with specific spins, it is necessary to find irreducible representations of the octahedral group.

Elements of a non-abelian group occur in conjugacy classes where all elements in a class are conjugate[1] to one another, and no element belongs to more than one class. A finite group has a finite number of irreducible representations; the number of irreps is equal to the number of conjugacy classes. Let the irreps be denoted by Λ_1, Λ_2, and so on. An irreducible representation

---

[1] A group element G_a is said to be conjugate to another element G_b, if there exists an element G_m such that $G_a = G_m G_b G_m^{-1}$.

for irrep Λ_i and group element G_a is written as $T^{(\Lambda_i)}(G_a)$. A general representation matrix $T(G_a)$ is reducible to a block-diagonal form in which each block is an irreducible representation as follows,

$$
T(G_a) = \begin{pmatrix} T^{(\Lambda_1)}(G_a) & & & 0 \\ & T^{(\Lambda_2)}(G_a) & & \\ & & \ldots & \\ 0 & & & T^{(\Lambda_n)}(G_a) \end{pmatrix}. \tag{2.1}
$$

This block-diagonal form holds for all G_a and is achieved by using a particular choice of operators, the irrep basis operators. Typical irrep basis operators of the octahedral group are called "cubic harmonics" or "lattice harmonics" [50, 51].

2.2.1 Integer angular momentum : O

We first review the proper point group O (rotations without spatial inversion) of a cubic lattice. Its 24 group elements fall into five conjugacy classes: I—identity; $3C_2$—rotations by π about three coordinate axes; $8C_3$—rotations by $\pm 2\pi/3$ about four body-diagonal axes[2] ; $6C_4$—rotations by $\pm \pi/2$ about three coordinate axes; $6C_2'$—rotations by π about six face-diagonal axes[3] of the cube. We employ the conventions of ref. [44]. The point group O has five irreps, which are usually called A_1, A_2, E, T_1 and T_2. They have dimensions 1, 1, 2, 3, and 3, respectively.

The character χ_p of a class p is defined to be

$$
\chi_p = \sum_{j=1}^{d} T_{jj}(G_a), \quad G_a \in p \tag{2.2}
$$

where p denotes a conjugacy class and d is the dimension of the representation. All group elements in a conjugacy class have the same character. Similarly, the irreducible character $\chi_p^{(\Lambda)}$ is defined as

$$
\chi_p^{(\Lambda)} = \sum_{j=1}^{d_\Lambda} T_{jj}^{(\Lambda)}(G_a), \quad G_a \in p, \tag{2.3}
$$

where d_Λ is the dimension of irrep Λ. Table 2.1 gives the irreducible characters of group O. In the table N_p represents the number of group elements in class p, and θ is the set of rotation angles for the class.

---

[2] A body-diagonal axis goes from one corner of the cube to the opposite corner of the cube.

[3] A face-diagonal axis is parallel to a diagonal line passing on a surface of cube.

Table 2.1: Irreducible character table of O

	I	$3C_2$	$8C_3$	$6C_4$	$6C_2'$
A_1	1	1	1	1	1
A_2	1	1	1	-1	-1
E	2	2	-1	0	0
T_1	3	-1	0	1	-1
T_2	3	-1	0	-1	1
N_p	1	3	8	6	6
θ	0	π	$\pm 2\pi/3$	$\pm\pi/2$	π

The connection of irreps of $\mathcal{O}$ to irreps of the continuum rotational group SU(2) may be found from a subduction of SU(2) to O. Let $\chi_p^{(J)}$ denote the character of the irrep of SU(2) with angular momentum j. It is computed from SU(2) matrices for spin j by taking appropriate limits to evaluate the expression,

$$\chi_p^{(j)} = \frac{\sin[\left(j + \frac{1}{2}\right)\theta]}{\sin(\frac{1}{2}\theta)}, \tag{2.4}$$

where θ is to be found from Table 2.1. Then the number of occurrences of cubic irrep Λ in the j irrep of SU(2) is given by

$$n_\Lambda^j = \frac{1}{g_O} \sum_p N_p \chi_p^{(\Lambda)*} \chi_p^{(J)} \tag{2.5}$$

where g_O is the number of group elements. The subduction for integer values of j is given in Table 2.2, adapted from Ref. [46]. The subduction table for $n = 0$ shows the patterns that correspond to continuum states with the lowest j values. For example, a $j = 0$ state must show up in the A_1 irrep, but in no other irreps of O. A $j = 1$ state must show up in the T_1 irrep but in no other irreps. A $j = 2$ state must show up in the E and T_2 irreps.

Irreducible representations depend upon the choice of basis operators. For integer spins, we choose the standard "lattice harmonics" as the basis operators for irreps of the octahedral group. They have a straightforward connection to irreps of the rotation group SO(3) in the continuum

Table 2.2: The subduction of SU(2) to O for integer j

j	O	
$12n+0$	A_1	$\oplus\, n(A_1 \oplus A_2 \oplus 2E \oplus 3T_1 \oplus 3T_2)$
$12n+1$	T_1	$\oplus\, n(A_1 \oplus A_2 \oplus 2E \oplus 3T_1 \oplus 3T_2)$
$12n+2$	$E \oplus T_2$	$\oplus\, n(A_1 \oplus A_2 \oplus 2E \oplus 3T_1 \oplus 3T_2)$
$12n+3$	$A_2 \oplus T_1 \oplus T_2$	$\oplus\, n(A_1 \oplus A_2 \oplus 2E \oplus 3T_1 \oplus 3T_2)$
$12n+4$	$A_1 \oplus E \oplus T_1 \oplus T_2$	$\oplus\, n(A_1 \oplus A_2 \oplus 2E \oplus 3T_1 \oplus 3T_2)$
$12n+5$	$E \oplus 2T_1 \oplus T_2$	$\oplus\, n(A_1 \oplus A_2 \oplus 2E \oplus 3T_1 \oplus 3T_2)$
$12n+6$	$A_1 \oplus A_2 \oplus E \oplus T_1 \oplus 2T_2$	$\oplus\, n(A_1 \oplus A_2 \oplus 2E \oplus 3T_1 \oplus 3T_2)$
$12n+7$	$A_2 \oplus E \oplus 2T_1 \oplus 2T_2$	$\oplus\, n(A_1 \oplus A_2 \oplus 2E \oplus 3T_1 \oplus 3T_2)$
$12n+8$	$A_1 \oplus 2E \oplus 2T_1 \oplus 2T_2$	$\oplus\, n(A_1 \oplus A_2 \oplus 2E \oplus 3T_1 \oplus 3T_2)$
$12n+9$	$A_1 \oplus A_2 \oplus E \oplus 3T_1 \oplus 2T_2$	$\oplus\, n(A_1 \oplus A_2 \oplus 2E \oplus 3T_1 \oplus 3T_2)$
$12n+10$	$A_1 \oplus A_2 \oplus 2E \oplus 2T_1 \oplus 3T_2$	$\oplus\, n(A_1 \oplus A_2 \oplus 2E \oplus 3T_1 \oplus 3T_2)$
$12n+11$	$A_2 \oplus 2E \oplus 3T_1 \oplus 3T_2$	$\oplus\, n(A_1 \oplus A_2 \oplus 2E \oplus 3T_1 \oplus 3T_2)$

limit. Table 2.3 shows the spherical harmonics $Y_{l,m}$ for the lowest values of angular momentum that provide irreps for the octahedral group. For example, the $Y_{1,m}$ for $m = 1, 0, -1$ transform under the rotations of Table 2.1 as the three-dimensional T_1 irrep. We choose our basis operators to be the ones in Table 2.3 in order to keep the connection to irreps of SO(3) as close as possible. The same basis convention for T_1 appears in Ref. [52], and same basis convention for E appears in Ref. [53].

Table 2.3: Bases of irreducible representations of O in terms of spherical harmonics, $Y_{l,m}$ for the lowest values of l.

Λ	d_Λ	row 1	row 2	row 3
A_1	1	$Y_{0,0}$	–	–
A_2	1	$Y_{3,2} - Y_{3,-2}$	–	–
E	2	$Y_{2,0}$	$Y_{2,2} + Y_{2,-2}$	–
T_1	3	$Y_{1,1}$	$Y_{1,0}$	$Y_{1,-1}$
T_2	3	$Y_{2,1}$	$Y_{2,0}$	$Y_{2,-1}$

2.2.2 Half-integer angular momenta: O^D

There are 48 elements in the double octahedral group O^D and they fall into eight classes: I—identity; J—rotation by 2π; $6C_4$—rotations by $\pm\pi$ about three coordinate axes; $8C_3$—rotations by $\pm 4\pi/3$ about body-diagonal lines; $8C_6$—rotations by $\pm 2\pi/3$ about body-diagonals axes; $6C_8$—rotations $\pm 3\pi/2$ about three coordinate axes; $6C_8'$—rotations by $\pm\pi/2$ about three coordinate axes; $12C_4'$—rotations by $\pm\pi$ about six face-diagonal axes. The eight irreps of O^D are: A_1, A_2, E, T_1, T_2, G_1, G_2, and H. As before A_1, A_2, E, T_1 and T_2 correspond to integer spins. The additional

Table 2.4: Irreducible character table of O^D. Only the spinorial irrep are presented.

	I	J	$6C_4$	$8C_3$	$8C_6$	$6C_8$	$6C_8'$	$12C_4'$
G_1	2	-2	0	-1	1	$-\sqrt{2}$	$\sqrt{2}$	0
G_2	2	-2	0	-1	1	$\sqrt{2}$	$-\sqrt{2}$	0
H	4	-4	0	1	-1	0	0	0
N_p	1	1	6	8	8	6	6	12
θ	0	2π	$\pm\pi$	$\pm 4\pi/3$	$\pm 2\pi/3$	$\pm 3\pi/2$	$\pm\pi/2$	$\pm\pi$

irreps G_1, G_2, and H correspond to half-integer spins and they have dimensions 2, 2, and 4,

respectively. Fermionic operators on a cubic lattice should be written in terms of irrep basis operators of G_1, G_2, and H. The irreducible characters $\chi_p^{(\Lambda)}$ for half-integer spins are listed in Table 2.4. Subduction of SU(2) onto O^D for half-integer values of j is summarized in Table 2.5. The subduction table for $n = 0$ shows the patterns that correspond to continuum states with the

Table 2.5: The subduction of SU(2) to O^D

j	O^D	
$12n + 1/2$	G_1	$\oplus\, 2n(G_1 \oplus 2H \oplus G_2)$
$12n + 3/2$	H	$\oplus\, 2n(G_1 \oplus 2H \oplus G_2)$
$12n + 5/2$	$H \oplus G_2$	$\oplus\, 2n(G_1 \oplus 2H \oplus G_2)$
$12n + 7/2$	$G_1 \oplus H \oplus G_2$	$\oplus\, 2n(G_1 \oplus 2H \oplus G_2)$
$12n + 9/2$	$G_1 \oplus 2H$	$\oplus\, 2n(G_1 \oplus 2H \oplus G_2)$
$12n + 11/2$	$G_1 \oplus 2H \oplus G_2$	$\oplus\, 2n(G_1 \oplus 2H \oplus G_2)$
$12n + 13/2$	$G_1 \oplus 2H \oplus 2G_2$	$\oplus\, 2n(G_1 \oplus 2H \oplus G_2)$
$12n + 15/2$	$G_1 \oplus 3H \oplus G_2$	$\oplus\, 2n(G_1 \oplus 2H \oplus G_2)$
$12n + 17/2$	$2G_1 \oplus 3H \oplus G_2$	$\oplus\, 2n(G_1 \oplus 2H \oplus G_2)$
$12n + 19/2$	$2G_1 \oplus 3H \oplus 2G_2$	$\oplus\, 2n(G_1 \oplus 2H \oplus G_2)$
$12n + 21/2$	$G_1 \oplus 4H \oplus 2G_2$	$\oplus\, 2n(G_1 \oplus 2H \oplus G_2)$
$12n + 23/2$	$2(G_1 \oplus 2H \oplus G_2)$	$\oplus\, 2n(G_1 \oplus 2H \oplus G_2)$

lowest j values. For example, a $j = 1/2$ state should show up in irrep G_1 but not in other irreps. A spin $3/2$ state should show up in irrep H but not other irreps. A spin $5/2$ state should show up in irreps H and G_2 but not in G_1. A $j = 7/2$ state should show up in irreps G_1, H and G_2.

A suitable set of irrep bases for half-integer angular momenta is given by the $|j, j_z\rangle$ states that are listed in Table 2.6. Explicit forms of the G_1 and H bases for three quarks are given in Appendix C. Note that G_2 basis operators cannot be built using three Dirac spinors unless nonzero orbital angular momentum is added.

Table 2.6: Bases of irreducible representations of O^D.

Λ	d_Λ	row 1	row 2	row 3	row 4
G_1	2	$\left\|\frac{1}{2},\frac{1}{2}\right\rangle$	$\left\|\frac{1}{2},-\frac{1}{2}\right\rangle$	–	–
H	4	$\left\|\frac{3}{2},\frac{3}{2}\right\rangle$	$\left\|\frac{3}{2},\frac{1}{2}\right\rangle$	$\left\|\frac{3}{2},-\frac{1}{2}\right\rangle$	$\left\|\frac{3}{2},-\frac{3}{2}\right\rangle$
G_2	2	$\sqrt{\frac{1}{6}}\left\|\frac{5}{2},\frac{5}{2}\right\rangle - \sqrt{\frac{5}{6}}\left\|\frac{5}{2},-\frac{3}{2}\right\rangle$	$-\sqrt{\frac{5}{6}}\left\|\frac{5}{2},\frac{3}{2}\right\rangle + \sqrt{\frac{1}{6}}\left\|\frac{5}{2},-\frac{5}{2}\right\rangle$	–	–

2.2.3 Improper point groups and parity

The improper point groups O_h and O_h^D consist of rotations that leave the cube invariant taken together with the spatial inversion. The parity transformation of a Dirac field involves multiplication by the γ_4 Dirac matrix as follows,

$$\mathcal{P}q(\mathbf{x},t)\mathcal{P}^{-1} = \gamma_4 q(-\mathbf{x},t), \tag{2.6}$$

where $\mathcal{P}$ is the parity operator. For operator construction, we employ throughout this work the Dirac-Pauli representation for Dirac γ matrices, where $\gamma_4 = \mathrm{diag}(1,1,-1,-1)$. However, our results may be used with any representation of the Dirac γ matrices by applying the appropriate unitary transformation as discussed in Appendix B.

Each Dirac matrix can be written as a direct product of the form $\mathrm{SU}(2)_\rho \otimes \mathrm{SU}(2)_s$ where $\mathrm{SU}(2)_\rho$ is generated by the 2×2 Pauli matrices for ρ-spin [54, 55] and $\mathrm{SU}(2)_s$ by the 2×2 Pauli matrices for spin. See Appendix B for details of the construction. Expressed in terms of the $\mathrm{SU}(2)_\rho \otimes \mathrm{SU}(2)_s$ matrices, $\gamma_4 = \rho_3 \otimes \sigma_4$ where $\rho_3 = \mathrm{diag}(1,-1)$ and $\sigma_4 = \mathrm{diag}(1,1)$. A fermion field satisfies

$$(\rho_3 \otimes \sigma_4)q_\mu(\mathbf{x},t) = \rho q_\mu(\mathbf{x},t), \tag{2.7}$$

where $\rho = +1$ for $\mu = 1$ or 2 and $\rho = -1$ for $\mu = 3$ or 4. Similarly, using $\rho_4 = \mathrm{diag}(1,1)$ and $\sigma_3 = \mathrm{diag}(1,-1)$, the fermion field satisfies

$$(\rho_4 \otimes \sigma_3)q_\mu(\mathbf{x},t) = s q_\mu(\mathbf{x},t), \tag{2.8}$$

where $s = +1$ for $\mu = 1$ or 3 and $s = -1$ for $\mu = 2$ or 4. There is an equivalence between the Dirac index μ in the Dirac-Pauli representation and the ρ, s values defined by Eqs. (2.7) and (2.8) as shown in Table 2.7. Thus the notation $q_s^{\rho}(\mathbf{x}, t)$ for a field is equivalent to the usual $q_{\mu}(\mathbf{x}, t)$ notation.

Table 2.7: Translation of Dirac index μ to ρ- and s-spin indices. Index μ is expressed in Dirac-Pauli representation.

Dirac index μ	ρ	s
1	$+$	$+$
2	$+$	$-$
3	$-$	$+$
4	$-$	$-$

We refer to the ρ value given by Eq. (2.7) as ρ-parity because of its role in the parity transformation of Eq. (2.6). For the parity transformation of a product of three quark fields,

$$\mathcal{P} q_{s_1}^{\rho_1}(\mathbf{x}, t) q_{s_2}^{\rho_2}(\mathbf{x}, t) q_{s_3}^{\rho_3}(\mathbf{x}, t) \mathcal{P}^{-1} = \rho_1 \rho_2 \rho_3 \, q_{s_1}^{\rho_1}(-\mathbf{x}, t) q_{s_2}^{\rho_2}(-\mathbf{x}, t) q_{s_3}^{\rho_3}(-\mathbf{x}, t), \quad (2.9)$$

where we have evaluated the requisite γ_4 matrices as the product of the ρ-parities. A baryon operator consists of three quark fields, where each quark field typically is a smeared field. The smearing distribution of each quark field is designed to be even or odd with respect to a spatial inversion about the center of the lattice, which gives an additional parity factor s_p that we refer to as spatial parity. Operators constructed in this way have a definite parity that is equal to the product of the ρ-parities and the spatial parities,

$$\text{parity of a baryon operator} = \rho_1 \rho_2 \rho_3 \, s_{p1} s_{p2} s_{p3}, \quad (2.10)$$

where ρ_i and s_{pi} are the ρ-parity and the spatial parity of i-th quark, respectively. We refer to $\rho_1 \rho_2 \rho_3$ as the ρ-parity of the baryon operator and to $s_{p1} s_{p2} s_{p3}$ as the spatial parity of the baryon operator.

Rotation of a quark field with a given Dirac index gives a linear combination of fields with different s labels but the same ρ-parity,

$$U(R)\overline{q}_s^{\rho}(\mathbf{x},t)U^{\dagger}(R) = \sum_{s'}\overline{q}_{s'}^{\rho}(R^{-1}\mathbf{x},t)T_{s's}(R), \tag{2.11}$$

where $T_{s's}(R)$ is a matrix representation of rotation R. This insight into the transformations of Dirac indices with respect to rotations is the first reason that we find the ρ, s labels useful.

Note that a "barred" field transforms in the same manner as a quantum "ket" transforms when the unitary quantum operator $U(R)$ is applied, i.e.,

$$U(R)\left|s\right\rangle = \sum_{s'}\left|s'\right\rangle\left\langle s'\right|U(R)\left|s\right\rangle = \sum_{s'}\left|s'\right\rangle T_{s's}(R). \tag{2.12}$$

However, "unbarred" fields also are required. Although they are independent fields in the Euclidean theory, their transformations are the same as quantum "bras"

$$U(R)q_s^{\rho}(\mathbf{x},t)U^{\dagger}(R) = \sum_{s'}q_{s'}^{\rho}(R^{-1}\mathbf{x},t)T_{ss'}^{\dagger}(R). \tag{2.13}$$

In this work we state results generally in terms of "barred" fields in order to have a transparent connection between transformations of fields and those of the quantum states that they create. "Unbarred" operators generally involve the same constructions except that any coefficients involved in the construction must be hermitian conjugated.

Operators that are even with respect to parity are labeled with a subscript g (for *gerade*) and operators that are odd are labeled with a subscript u (for *ungerade*). There are 10 irreducible representations in O_h: $A_{1g}, A_{2g}, E_g, T_{1g}, T_{2g}, A_{1u}, A_{2u}, E_u, T_{1u}, T_{2u}$. For half-integer spin, there are 16 irreducible representations of O_h^D, ten of which are the same as those of O_h. The additional six irreps are: $G_{1g}, G_{2g}, H_g, G_{1u}, G_{2u}, H_u$. We will use these notations throughout this work.

Because of the parity transformation of Eq. (2.9) and because linear combinations of three-quark operators may be arranged to have either even or odd spatial parity, there are two independent ways to make operators of a given parity. Gerade operators can be made either with even spatial parity together with positive ρ-parity or with odd spatial parity together with negative ρ-parity. These sets are not connected by rotations because neither the spatial parity nor the

ρ-parity can be changed by a rotation. Similarly, there are two disjoint sets of ungerade operators: odd spatial parity together with positive ρ-parity or even spatial parity together with negative ρ-parity. However, gerade operators with either spatial parity are related by ρ-spin raising or lowering operations to ungerade operators with the same spatial parity. This is the second reason that the ρ, s labeling is useful. Although the ρ, s labeling is used sparingly in the main portions of this thesis, it is central to the method used in Appendix C to construct combinations of Dirac indices that transform irreducibly.

Each baryon operator carries a row label, λ, whose meaning depends upon the bases used for irreps. The row label distinguishes between the d_Λ members of irrep Λ. If a representation contains more than one occurrence of irrep Λ, we say that there are multiple embeddings of that irrep. We use a label k to distinguish between the different embeddings. Therefore, a generic baryon operator is denoted as $\overline{B}_\lambda^{\Lambda,k}(\mathbf{x}, t)$, or in "unbarred" form as $B_\lambda^{\Lambda,k}(\mathbf{x}, t)$, where the operator belongs to the k-th embedding of irrep Λ and row λ of the octahedral group. Types of baryons are indicated by the use of appropriate symbols, such as $\overline{N}_\lambda^{\Lambda,k}(\mathbf{x}, t)$ (for isospin 1/2 operators), $\overline{\Delta}_\lambda^{\Lambda,k}(\mathbf{x}, t)$ (for isospin 3/2 operators), $\overline{\Sigma}_\lambda^{\Lambda,k}(\mathbf{x}, t)$ (for strangeness -1 operators), and so on.

Two-point correlation functions whose source and sink operators belong to different irreps, or to different rows of one irrep vanish if the lattice has the rotational and parity invariance. The proof of these orthogonality relations of lattice operators is simple using the orthogonality property of irreducible representations provided in Appendix A and invariance of the vacuum under the group operations. The proof is as follows,

$$
\begin{aligned}
\sum_x & \langle 0| T B_{\lambda'}^{\Lambda',k'}(\mathbf{x}, t) \overline{B}_\lambda^{\Lambda,k}(0) |0\rangle \\
&= \frac{1}{g_{O_h^D}} \sum_{G_a \in O_h^D} \sum_x \langle 0| T U^\dagger(G_a) U(G_a) B_{\lambda'}^{\Lambda',k'}(\mathbf{x}, t) U^\dagger(G_a) U(G_a) \overline{B}_\lambda^{\Lambda,k}(0) U^\dagger(G_a) U(G_a) |0\rangle \\
&= \frac{1}{g_{D_h^D}} \sum_{G_a \in O_h^D} \sum_{\alpha'\alpha} T_{\lambda'\alpha'}^{\dagger(\Lambda')}(G_a) T_{\alpha\lambda}^{(\Lambda)}(G_a) \sum_x \langle 0| T B_{\alpha'}^{\Lambda',k'}(\mathbf{x}, t) \overline{B}_\alpha^{\Lambda,k}(0) |0\rangle \\
&= \delta_{\Lambda'\Lambda} \delta_{\lambda'\lambda} \sum_x \langle 0| T B_\lambda^{\Lambda,k'}(\mathbf{x}, t) \overline{B}_\lambda^{\Lambda,k}(0) |0\rangle \\
&= \delta_{\Lambda'\Lambda} \delta_{\lambda'\lambda} C_{k'k}^{(\Lambda)}(t), \quad\quad\quad\quad\quad\quad\quad\quad\quad\quad\quad\quad (2.14)
\end{aligned}
$$

where the sum over group elements is done using Eq. (A.4). Different embeddings belonging to

the same irrep and row provide sets of operators suitable for constructing a matrix of correlation functions $C_{k'k}^{(\Lambda)}(t)$ and applying the variational method. The orthogonality holds exactly for correlation functions based upon constant gauge fields. It holds for correlation functions based upon averages over a sufficiently large number of gauge field configurations. Operators with different types of baryons are orthogonal to one another.

2.3 Quasi-local Baryonic Operators

The first step in the construction of field operators suitable for baryons is to specify primitive three-quark operators. Consider a generic operator formed from three-quark fields as follows,

$$\epsilon_{abc}\, \overline{q}_{\mu_1}^{af_1}(\mathbf{x}, t)\overline{q}_{\mu_2}^{bf_2}(\mathbf{x}, t)\overline{q}_{\mu_3}^{cf_3}(\mathbf{x}, t), \tag{2.15}$$

where a, b and c are color indices, f_1, f_2 and f_3 are flavor indices and μ_1, μ_2 and μ_3 are Dirac indices with values 1 to 4. Each Dirac index μ_i could be replaced by the corresponding ρ_i, s_i labels according to Table 2.7. The operator is antisymmetrized in color by the ϵ_{abc} factor when the (implicit) sums over a, b and c are performed.

Operators must be antisymmetric with respect to simultaneous exchange of all colors, flavors and Dirac indices of the quarks but this requirement is satisfied by the color antisymmetry. Given that the quark fields have a common location $\mathbf{x}$, their spatial distribution is symmetric. Thus the combination of flavor and Dirac indices must be symmetric. An operator that is symmetric in flavor labels $(\overline{\Delta}, \overline{\Omega})$ must be symmetric also in Dirac indices, and an operator that is mixed-antisymmetric in flavor labels $(\overline{N})$ must be mixed antisymmetric in Dirac indices, assuming that masses of the up and down quarks are equal. An operator that is mixed-antisymmetric in flavor labels and that has nonzero strangeness $(\overline{\Lambda})$ can have mixed-antisymmetric or totally antisymmetric Dirac indices, and an operator that is mixed-symmetric in flavor labels and that has nonzero strangeness $(\overline{\Sigma})$ can have mixed-symmetric or totally symmetric Dirac indices. All possible symmetries of the Dirac indices are encountered in the consideration of the different baryons. In this section, we take up the different baryons one at a time and develop tables of operators classified according to irreps of O_h^D.

34

Although quark fields anticommute with one another, they may be treated as boson fields in a color-singlet combination of three quarks as in Eq. (2.15), provided that we adopt a standard order for the color indices, namely the order a, b, c from left to right. When two quark fields are commuted, the sign reversal from their anticommutation property is canceled by a sign reversal from permuting and relabeling the ϵ-tensor indices back to the standard order.

Each quark field can be a smeared field that has a spatially extended distribution. Standard gauge-covariant methods such as Jacobi smearing [56] or so-called Wuppertal smearing [57] can be used to enhance the coupling to the low-lying states. One of the methods is Gaussian smearing [58] defined as

$$q_\mu(\mathbf{x}, t) \rightarrow \sum_{x'} \hat{G}^{(N)}(\mathbf{x}, \mathbf{x}') q_\mu(\mathbf{x}', t), \tag{2.16}$$

where $\hat{G}^{(N)}$ is defined by a recursion relation

$$\begin{aligned} \hat{G}^{(N)}(\mathbf{x}, \mathbf{x}') &= \sum_y \left(\delta_{x,y} + \frac{\sigma^2 \nabla^2_{x,y}}{4N} \right) \hat{G}^{(N-1)}(\mathbf{y}, \mathbf{x}'), \\ \hat{G}^{(0)}(\mathbf{x}, \mathbf{x}') &= \delta_{x,x'}, \end{aligned} \tag{2.17}$$

and

$$\nabla^2_{x,x'} = \sum_{i=1}^{3} \left[U_i(x) \delta_{x+\hat{i}, x'} + U_i^\dagger(x - \hat{i}) \delta_{x-\hat{i}, x'} - 2\delta_{x,x'} \right], \tag{2.18}$$

is a three-dimensional gauge-covariant Laplacian operator. Constants σ and N control the smearing, which as $N \rightarrow \infty$ tends to a gaussian distribution, i.e., $q_\mu(\mathbf{x}, t) \rightarrow e^{\sigma^2 \nabla^2/4} q_\mu(\mathbf{x}, t)$ in the continuum limit. Gauge links appearing in the hopping terms in Eq. (2.18) can be replaced by *smeared* gauge links using any of the standard link-smearing methods [59–61].

Baryon operators composed of three smeared fields, with each quark field using the same smearing parameters, are referred as *quasi-local* baryon operators in this paper. They have the same transformations under the double octahedral group as point (unsmeared), local operators assuming gauge fields preserve cubic symmetry after a configuration average. Baryon operators discussed throughout this section are to be understood as quasi-local operators. Baryon operators composed of smeared quark fields using different smearing parameters for two or more quark fields differ from the quasi-local operators owing to the different spatial symmetries that are possible.

We discuss this "multi-smearing" in Section 2.4.

2.3.1 Quasi-local Nucleon Operators

Consider operators made from quasi-local quark fields for isospin quantum numbers $I = 1/2, I_z = 1/2$. These operators correspond to the N^* family of baryons and they may be chosen to be

$$\overline{N}^{(\text{MA})}_{\mu_1\mu_2\mu_3} = \epsilon_{abc}\frac{1}{\sqrt{2}}\left(\bar{u}^a_{\mu_1}\bar{d}^b_{\mu_2} - \bar{d}^a_{\mu_1}\bar{u}^b_{\mu_2}\right)\bar{u}^c_{\mu_3}, \tag{2.19}$$

where u is an up quark and d is a down quark. All (smeared) quark fields are defined at space-time point $(\mathbf{x}, t)$. Equation (2.19) provides a proton operator and a neutron operator can be obtained using the isospin lowering operation. The operator defined in Eq. (2.19) corresponds to the mixed-

Figure 2.1: Young tableaux for three-quark $SU(2)_I$ irreducible representations. The first tableau is antisymmetric in labels of particles 1 and 2 (denoted MA for mixed-antisymmetric), while the second tableau is symmetric in the labels of particles 1 and 2 (denoted MS for mixed-symmetric). The third tableau is fully symmetric (denoted S).

MA   MS   S
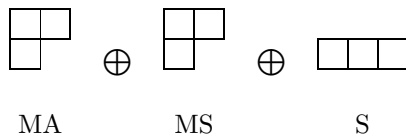
antisymmetric Young tableau for isospin in Fig. 2.1. Each $N^{(\text{MA})}_{\mu_1\mu_2\mu_3}(\mathbf{x}, t)$ operator of Eq. (2.19) is manifestly antisymmetric with respect to the flavor interchange $u \leftrightarrow d$ applied to the first two quark fields. This leads to the following restrictions on Dirac indices,

$$\overline{N}^{(\text{MA})}_{\mu_1\mu_2\mu_3} + \overline{N}^{(\text{MA})}_{\mu_2\mu_1\mu_3} = 0, \tag{2.20}$$
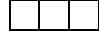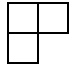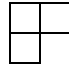
$$\overline{N}^{(\text{MA})}_{\mu_1\mu_2\mu_3} + \overline{N}^{(\text{MA})}_{\mu_2\mu_3\mu_1} + \overline{N}^{(\text{MA})}_{\mu_3\mu_1\mu_2} = 0. \tag{2.21}$$

Some general considerations are stated most simply using the Dirac indices. For example, there are $4^3 = 64$ combinations of Dirac indices for operators formed from three quark fields. They may be classified by the four Young tableaux of Fig. 2.2, where each box is understood to take the

values $\mu = 1, 2, 3$ or 4. Standard rules for counting the dimensions of the tableaux show that the

Figure 2.2: Young tableaux for three Dirac indices.

totally symmetric tableau includes 20 operators, the mixed-symmetric and mixed-antisymmetric tableaux each have 20 operators and the totally antisymmetric tableau has 4 operators, thus accounting for all 64 possibilities. Groupings of Dirac indices according to the symmetries of Fig. 2.2 are useful. Given that color labels are antisymmetric, a quasi-local baryonic operator must be symmetric with respect to simultaneous exchange of flavor labels and Dirac indices. This rule associates each baryon operator with one of the symmetries of Dirac indices found in the tableaux of Fig. 2.2. All the combinations of Dirac indices that correspond to each Young tableau are given explicitly in Appendix C. Three Dirac spinors whose spin indices are written in accord with one Young tableau in Fig. 2.2 form a closed set under the group rotation and parity transformations. These group representations have been reduced to $G_{1g/u}$ and $H_{g/u}$ irreps of Dirac indices by working with the ρ, s labeling as discussed in Appendix C.

Nucleon operators with MA isospin symmetry in Eq. (2.19) have restrictions on Dirac indices as stated in Eqs. (2.20) and (2.21). These restrictions allow only the MA symmetry of Dirac indices, corresponding to the third tableau of Fig. 2.2. For any other choice of the symmetry of Dirac indices the $\overline{N}^{(\mathrm{MA})}$ operator vanishes. Table 2.8 gives explicit forms for the 20 quasi-local nucleon operators classified into irreps G_{1g}, H_g, G_{1u}, and H_u. Dirac indices in the table come from Table C.3 in Appendix C, but they have been simplified using the relation in Eq. (2.20). Because all the coefficients are real, "unbarred" operators are obtained by replacing $\overline{N}$ by N in the same linear combinations . The left column of the table shows 10 gerade nucleon operators and the right one shows 10 ungerade operators. For a given parity there are three sets of G_1 operators

37

Table 2.8: Quasi-local Nucleon operators. All operators have MA Dirac indices.

$\overline{\Psi}^{\Lambda,k}_{S,S_z}$	$\overline{N}_{\mu_1\mu_2\mu_3}$	$\overline{\Psi}^{\Lambda,k}_{S,S_z}$	$\overline{N}_{\mu_1\mu_2\mu_3}$
$\overline{\Psi}^{G_{1g},1}_{\frac{1}{2},\frac{1}{2}}$	$\overline{N}_{121}$	$\overline{\Psi}^{G_{1u},1}_{\frac{1}{2},\frac{1}{2}}$	$\frac{1}{\sqrt{3}}(\overline{N}_{123}+\overline{N}_{141}+\overline{N}_{321})$
$\overline{\Psi}^{G_{1g},1}_{\frac{1}{2},-\frac{1}{2}}$	$\overline{N}_{122}$	$\overline{\Psi}^{G_{1u},1}_{\frac{1}{2},-\frac{1}{2}}$	$\frac{1}{\sqrt{3}}(\overline{N}_{124}+\overline{N}_{142}+\overline{N}_{322})$
$\overline{\Psi}^{G_{1g},2}_{\frac{1}{2},\frac{1}{2}}$	$\frac{1}{\sqrt{3}}(\overline{N}_{143}+\overline{N}_{323}+\overline{N}_{341})$	$\overline{\Psi}^{G_{1u},2}_{\frac{1}{2},\frac{1}{2}}$	$\overline{N}_{343}$
$\overline{\Psi}^{G_{1g},2}_{\frac{1}{2},-\frac{1}{2}}$	$\frac{1}{\sqrt{3}}(\overline{N}_{144}+\overline{N}_{324}+\overline{N}_{342})$	$\overline{\Psi}^{G_{1u},2}_{\frac{1}{2},-\frac{1}{2}}$	$\overline{N}_{344}$
$\overline{\Psi}^{G_{1g},3}_{\frac{1}{2},\frac{1}{2}}$	$\frac{1}{\sqrt{3}}(\overline{N}_{134}+\overline{N}_{323}-\overline{N}_{341})$	$\overline{\Psi}^{G_{1u},3}_{\frac{1}{2},\frac{1}{2}}$	$\frac{1}{\sqrt{3}}(-\overline{N}_{141}-\overline{N}_{312}+\overline{N}_{123})$
$\overline{\Psi}^{G_{1g},3}_{\frac{1}{2},-\frac{1}{2}}$	$\frac{1}{\sqrt{3}}(\overline{N}_{144}+\overline{N}_{423}-\overline{N}_{342})$	$\overline{\Psi}^{G_{1u},3}_{\frac{1}{2},-\frac{1}{2}}$	$\frac{1}{\sqrt{3}}(-\overline{N}_{322}-\overline{N}_{241}+\overline{N}_{124})$
$\overline{\Psi}^{H_g}_{\frac{3}{2},\frac{3}{2}}$	$\overline{N}_{133}$	$\overline{\Psi}^{H_u}_{\frac{3}{2},\frac{3}{2}}$	$\overline{N}_{131}$
$\overline{\Psi}^{H_g}_{\frac{3}{2},\frac{1}{2}}$	$\frac{1}{\sqrt{3}}(\overline{N}_{134}+\overline{N}_{143}+\overline{N}_{233})$	$\overline{\Psi}^{H_u}_{\frac{3}{2},\frac{1}{2}}$	$\frac{1}{\sqrt{3}}(\overline{N}_{132}+\overline{N}_{141}+\overline{N}_{231})$
$\overline{\Psi}^{H_g}_{\frac{3}{2},-\frac{1}{2}}$	$\frac{1}{\sqrt{3}}(\overline{N}_{144}+\overline{N}_{234}+\overline{N}_{243})$	$\overline{\Psi}^{H_u}_{\frac{3}{2},-\frac{1}{2}}$	$\frac{1}{\sqrt{3}}(\overline{N}_{142}+\overline{N}_{232}+\overline{N}_{241})$
$\overline{\Psi}^{H_g}_{\frac{3}{2},-\frac{3}{2}}$	$\overline{N}_{244}$	$\overline{\Psi}^{H_u}_{\frac{3}{2},-\frac{3}{2}}$	$\overline{N}_{242}$

(three embeddings of G_1) and one set of H operators. Each G_1 irrep contains two operators that transform amongst themselves under rotations of the group and each H irrep contains four operators that transform amongst themselves. Operators in each irrep are given spin projection labels, S_z, which are also equivalent to "row" labels but more physically meaningful. In a given embedding the operator with the largest S_z is designated "row 1", the next largest S_z is designated "row 2", and so on. The notation $\overline{\Psi}^{\Lambda,k}_{S,S_z}$ represents a general quasi-local baryonic operator with spin S and spin projection S_z, transforming according to the k-th embedding of irrep Λ of the group O^D_h.

Spin-raising and spin-lowering operators for a Dirac spinor are

$$s^{\pm} = \frac{1}{2}\begin{pmatrix} \sigma_1 \pm i\sigma_2 & 0 \\ 0 & \sigma_1 \pm i\sigma_2 \end{pmatrix}, \tag{2.22}$$

in the Dirac-Pauli representation. For a three-quark state, the spin raising or lowering operator is a sum of three terms, for example, $S^- = \sum_{j=1}^3 s^{\pm}_j$, where $s^{\pm}_j$ acts on the j-th quark. The

same operations carry over to the "barred" field operators of Table 2.8. Different rows in the same embedding of an irrep are related to one another by spin raising and lowering operations. For example, the transformation of the first G_1 embedding of Table 2.8 proceeds schematically as follows,

$$S^-\overline{\Psi}^{G_{1g},1}_{1/2,1/2} = S^-\overline{N}_{121} = S^-\overline{N}^{+++}_{+-+} = \overline{N}^{+++}_{+--} = \overline{N}_{122} = \overline{\Psi}^{G_{1g},1}_{1/2,-1/2}, \tag{2.23}$$

where the notation $\overline{N}^{\rho_1\rho_2\rho_3}_{s_1s_2s_3}$ is used in the intermediate steps. Note that a spin-lowering operation on the second quark in Eq. (2.23) vanishes because it has spin down and spin-lowering of the first quark also vanishes because $s_1^-\overline{N}^{+++}_{+-+} = \overline{N}^{+++}_{--+} = 0$ by Eq. (2.20). Spin raising and lowering operations can be applied repeatedly and the following relation holds,

$$0 \underset{S^+}{\longleftarrow} \overline{\Psi}^{G_{1g/u},k}_{1/2,1/2} \quad \underset{S^+}{\overset{S^-}{\rightleftarrows}} \quad \overline{\Psi}^{G_{1g/u},k}_{1/2,-1/2} \overset{S^-}{\longrightarrow} 0,$$

$$0 \underset{S^+}{\longleftarrow} \overline{\Psi}^{H_{g/u},k}_{3/2,3/2} \underset{S^+}{\overset{S^-}{\rightleftarrows}} \overline{\Psi}^{H_{g/u},k}_{3/2,1/2} \quad \underset{S^+}{\overset{S^-}{\rightleftarrows}} \quad \overline{\Psi}^{H_{g/u},k}_{3/2,-1/2} \underset{S^+}{\overset{S^-}{\rightleftarrows}} \overline{\Psi}^{H_{g/u},k}_{3/2,-3/2} \overset{S^-}{\longrightarrow} 0. \tag{2.24}$$

A gerade operator in a row of Table 2.8 and the ungerade one in the same row are related to each other by ρ-spin raising and lowering operations. For Dirac spinors, the operators are $\rho^\pm = \sum_{j=1}^3 \rho_j^\pm$, $\rho_j^\pm = (1/2)(\rho_j^1 \pm i\rho_j^2)$, where j specifies the first, second, or the third quark. An example is

$$\begin{aligned}
\rho^-\overline{\Psi}^{G_{1g},1}_{1/2,1/2} &= \rho^-\overline{N}_{121} = \rho^-\overline{N}^{+++}_{+-+}, \\
&\rightarrow \frac{1}{\sqrt{3}}\left(\overline{N}^{++-}_{+-+} + \overline{N}^{+-+}_{+-+} + \overline{N}^{-++}_{+-+}\right) \\
&= \frac{1}{\sqrt{3}}\left(\overline{N}_{123} + \overline{N}_{141} + \overline{N}_{321}\right) \\
&= \overline{\Psi}^{G_{1u},1}_{1/2,1/2}, \tag{2.25}
\end{aligned}$$

where an appropriate normalization is included in the resultant operator. Note that ρ-spin raising and lowering operations change the ρ-parity of one quark and thus change the product $\rho_1\rho_2\rho_3$ which is the ρ-parity of the operator. However, they preserve the s labels and leave the transformation properties under rotations unchanged.

Mixed-symmetric isospin operators with $I = 1/2, I_z = 1/2$ may also be defined by

$$\overline{N}^{+(\text{MS})}_{\mu_1\mu_2\mu_3} = \epsilon_{abc}\frac{1}{\sqrt{6}}(2\bar{u}^a_{\mu_1}\bar{u}^b_{\mu_2}\bar{d}^c_{\mu_3} - \bar{u}^a_{\mu_1}\bar{d}^b_{\mu_2}\bar{u}^c_{\mu_3} - \bar{d}^a_{\mu_1}\bar{u}^b_{\mu_2}\bar{u}^c_{\mu_3}). \tag{2.26}$$

However, for quasi-local operators they can be rewritten in terms of the MA isospin operators defined in Eq. (2.19) as follows,

$$\overline{N}^{(MS)}_{\mu_1\mu_2\mu_3} = \overline{N}^{(MA)}_{\mu_3\mu_2\mu_1} + \overline{N}^{(MA)}_{\mu_1\mu_3\mu_2}, \tag{2.27}$$

showing that the quasi-local, MS isospin operators are not linearly independent of quasi-local MA operators. It is sufficient to consider only the MA operators of Eq. (2.19) in order to construct a complete, linearly independent set of isospin 1/2, quasi-local operators.

Relations of the operators presented in Table 2.8 to operators that are commonly used in the literature for a nucleon are given in Appendix D.

2.3.2 Quasi-local Δ and Ω Operators

The isospin of a Δ baryon is 3/2 and there are four different operators corresponding to isospin projections $I_z = 3/2, 1/2, -1/2$, and $-3/2$:

$$
\begin{aligned}
\overline{\Delta}^{++}_{\mu_1\mu_2\mu_3} &= \epsilon_{abc}\, \bar{u}^a_{\mu_1} \bar{u}^b_{\mu_2} \bar{u}^c_{\mu_3}, \\
\overline{\Delta}^{+}_{\mu_1\mu_2\mu_3} &= \frac{\epsilon_{abc}}{\sqrt{3}} \left(\bar{u}^a_{\mu_1} \bar{u}^b_{\mu_2} \bar{d}^c_{\mu_3} + \bar{u}^a_{\mu_1} \bar{d}^b_{\mu_2} \bar{u}^c_{\mu_3} + \bar{d}^a_{\mu_1} \bar{u}^b_{\mu_2} \bar{u}^c_{\mu_3} \right), \\
\overline{\Delta}^{0}_{\mu_1\mu_2\mu_3} &= \frac{\epsilon_{abc}}{\sqrt{3}} \left(\bar{u}^a_{\mu_1} \bar{d}^b_{\mu_2} \bar{d}^c_{\mu_3} + \bar{d}^a_{\mu_1} \bar{u}^b_{\mu_2} \bar{d}^c_{\mu_3} + \bar{d}^a_{\mu_1} \bar{d}^b_{\mu_2} \bar{u}^c_{\mu_3} \right), \\
\overline{\Delta}^{-}_{\mu_1\mu_2\mu_3} &= \epsilon_{abc}\, \bar{d}^a_{\mu_1} \bar{d}^b_{\mu_2} \bar{d}^c_{\mu_3},
\end{aligned}
$$

$$\tag{2.28}$$

where all fields are defined at space-time point $(\mathbf{x}, t)$. Because of the totally symmetric flavors and totally antisymmetric colors, the Δ baryon operators must have totally symmetric combinations of Dirac indices, otherwise the operator vanishes. According to Table C.2 in Appendix C there are 20 combinations of totally symmetric Dirac indices. As noted earlier, the quark fields may be commuted with one another with no change of sign so Dirac indices can be rearranged to a standard order in which they do not decrease from left to right. This produces 20 irreducible operators that are given in Table 2.9. For each parity, two embeddings of the H irrep occur, while there is one embedding of the G_1 irrep. Table 2.9 holds for any I_z value. Spin-raising and lowering operations as in Eq. (2.24) and ρ-spin raising and lowering operations as in Eq. (2.25) can be applied to relate

Table 2.9: Quasi-local Δ operators. All operators have S Dirac indices.

$\overline{\Psi}_{S,S_z}^{\Lambda,k}$	$\overline{\Delta}_{\mu_1\mu_2\mu_3}$	$\overline{\Psi}_{S,S_z}^{\Lambda,k}$	$\overline{\Delta}_{\mu_1\mu_2\mu_3}$
$\overline{\Psi}_{\frac{1}{2},\frac{1}{2}}^{G_{1g},1}$	$\overline{\Delta}_{134} - \overline{\Delta}_{233}$	$\overline{\Psi}_{\frac{1}{2},\frac{1}{2}}^{G_{1u},1}$	$\overline{\Delta}_{114} - \overline{\Delta}_{123}$
$\overline{\Psi}_{\frac{1}{2},-\frac{1}{2}}^{G_{1g},1}$	$\overline{\Delta}_{144} - \overline{\Delta}_{234}$	$\overline{\Psi}_{\frac{1}{2},-\frac{1}{2}}^{G_{1u},1}$	$\overline{\Delta}_{124} - \overline{\Delta}_{223}$
$\overline{\Psi}_{\frac{3}{2},\frac{3}{2}}^{H_g,1}$	$\overline{\Delta}_{111}$	$\overline{\Psi}_{\frac{3}{2},\frac{3}{2}}^{H_u,1}$	$\sqrt{3}\,\overline{\Delta}_{113}$
$\overline{\Psi}_{\frac{3}{2},\frac{1}{2}}^{H_g,1}$	$\sqrt{3}\,\overline{\Delta}_{112}$	$\overline{\Psi}_{\frac{3}{2},\frac{1}{2}}^{H_u,1}$	$\overline{\Delta}_{114} + 2\overline{\Delta}_{123}$
$\overline{\Psi}_{\frac{3}{2},-\frac{1}{2}}^{H_g,1}$	$\sqrt{3}\,\overline{\Delta}_{122}$	$\overline{\Psi}_{\frac{3}{2},-\frac{1}{2}}^{H_u,1}$	$2\overline{\Delta}_{124} + \overline{\Delta}_{223}$
$\overline{\Psi}_{\frac{3}{2},-\frac{3}{2}}^{H_g,1}$	$\overline{\Delta}_{222}$	$\overline{\Psi}_{\frac{3}{2},-\frac{3}{2}}^{H_u,1}$	$\sqrt{3}\,\overline{\Delta}_{224}$
$\overline{\Psi}_{\frac{3}{2},\frac{3}{2}}^{H_g,2}$	$\sqrt{3}\,\overline{\Delta}_{133}$	$\overline{\Psi}_{\frac{3}{2},\frac{3}{2}}^{H_u,2}$	$\overline{\Delta}_{333}$
$\overline{\Psi}_{\frac{3}{2},\frac{1}{2}}^{H_g,2}$	$2\overline{\Delta}_{134} + \overline{\Delta}_{233}$	$\overline{\Psi}_{\frac{3}{2},\frac{1}{2}}^{H_u,2}$	$\sqrt{3}\,\overline{\Delta}_{334}$
$\overline{\Psi}_{\frac{3}{2},-\frac{1}{2}}^{H_g,2}$	$\overline{\Delta}_{144} + 2\overline{\Delta}_{234}$	$\overline{\Psi}_{\frac{3}{2},-\frac{1}{2}}^{H_u,2}$	$\sqrt{3}\,\overline{\Delta}_{344}$
$\overline{\Psi}_{\frac{3}{2},-\frac{3}{2}}^{H_g,2}$	$\sqrt{3}\,\overline{\Delta}_{244}$	$\overline{\Psi}_{\frac{3}{2},-\frac{3}{2}}^{H_u,2}$	$\overline{\Delta}_{444}$

operators in different rows or operators in different columns of Table 2.9.

Ω baryons are composed of three strange quarks with isospin zero,

$$\overline{\Omega}_{\mu_1\mu_2\mu_3}^{-}(\mathbf{x},t) = \epsilon_{abc}\,\bar{s}_{\mu_1}^{a}(\mathbf{x},t)\bar{s}_{\mu_2}^{b}(\mathbf{x},t)\bar{s}_{\mu_3}^{c}(\mathbf{x},t). \tag{2.29}$$

The quark flavors are clearly totally symmetric so only the totally symmetric Dirac indices are allowed. Therefore, Table 2.9 can be used for an Ω baryon. In summary the $\overline{\Delta}$ symbol in Table 2.9 may be replaced with any of $\{\overline{\Delta}^{++},\overline{\Delta}^{+},\overline{\Delta}^{0},\overline{\Delta}^{-},\overline{\Omega}^{-}\}$.

2.3.3 Quasi-local Λ Baryon Operators

The Λ baryons have isospin zero and strangeness -1. Appropriate quasi-local Λ-baryon operators have the form,

$$\overline{\Lambda}_{\mu_1\mu_2\mu_3}^{0} = \epsilon_{abc}\frac{1}{\sqrt{2}}\left(\bar{u}_{\mu_1}^{a}\bar{d}_{\mu_2}^{b} - \bar{d}_{\mu_1}^{a}\bar{u}_{\mu_2}^{b}\right)\bar{s}_{\mu_3}^{c}, \tag{2.30}$$

where space-time arguments $(\mathbf{x},t)$ are omitted from each quark field. The Λ baryon operator has a pair of up and down quarks in the isospin zero state, which is the same as the mixed-antisymmetric

nucleon operator. Because the operator in Eq. (2.30) satisfies the relation

$$\overline{\Lambda}^0_{\mu_1\mu_2\mu_3} + \overline{\Lambda}^0_{\mu_2\mu_1\mu_3} = 0, \tag{2.31}$$

it is antisymmetric with respect to exchange of μ_1 and μ_2 indices. Allowed symmetries of Dirac indices for the quasi-local Λ baryon operator are mixed-antisymmetric and totally antisymmetric. The difference from the local nucleon operator is that the Λ baryon operator is allowed to have totally antisymmetric Dirac indices, because the strange quark removes the restriction of Eq. (2.21). Table 2.10 gives all quasi-local Λ baryon operators. Twelve positive-parity operators are given

Table 2.10: Quasi-local Λ baryon operators.

$\overline{\Psi}^{\Lambda,k}_{S,S_z}$	$\overline{\Lambda}_{\mu_1\mu_2\mu_3}$	$\overline{\Psi}^{\Lambda,k}_{S,S_z}$	$\overline{\Lambda}_{\mu_1\mu_2\mu_3}$
$\overline{\Psi}^{G_{1g},1}_{\frac{1}{2},\frac{1}{2}}$	$\overline{\Lambda}_{121}$	$\overline{\Psi}^{G_{1u},1}_{\frac{1}{2},\frac{1}{2}}$	$\overline{\Lambda}_{123} + \overline{\Lambda}_{141} + \overline{\Lambda}_{321}$
$\overline{\Psi}^{G_{1g},1}_{\frac{1}{2},-\frac{1}{2}}$	$\overline{\Lambda}_{122}$	$\overline{\Psi}^{G_{1u},1}_{\frac{1}{2},-\frac{1}{2}}$	$\overline{\Lambda}_{124} + \overline{\Lambda}_{142} + \overline{\Lambda}_{322}$
$\overline{\Psi}^{G_{1g},2}_{\frac{1}{2},\frac{1}{2}}$	$\overline{\Lambda}_{143} + \overline{\Lambda}_{323} + \overline{\Lambda}_{341}$	$\overline{\Psi}^{G_{1u},1}_{\frac{1}{2},\frac{1}{2}}$	$\overline{\Lambda}_{343}$
$\overline{\Psi}^{G_{1g},2}_{\frac{1}{2},-\frac{1}{2}}$	$\overline{\Lambda}_{144} + \overline{\Lambda}_{324} + \overline{\Lambda}_{342}$	$\overline{\Psi}^{G_{1u},1}_{\frac{1}{2},-\frac{1}{2}}$	$\overline{\Lambda}_{344}$
$\overline{\Psi}^{G_{1g},3}_{\frac{1}{2},\frac{1}{2}}$	$\overline{\Lambda}_{134} + \overline{\Lambda}_{323} - \overline{\Lambda}_{341}$	$\overline{\Psi}^{G_{1u},1}_{\frac{1}{2},\frac{1}{2}}$	$-\overline{\Lambda}_{141} - \overline{\Lambda}_{312} + \overline{\Lambda}_{123}$
$\overline{\Psi}^{G_{1g},3}_{\frac{1}{2},-\frac{1}{2}}$	$\overline{\Lambda}_{144} + \overline{\Lambda}_{423} - \overline{\Lambda}_{342}$	$\overline{\Psi}^{G_{1u},1}_{\frac{1}{2},-\frac{1}{2}}$	$-\overline{\Lambda}_{322} - \overline{\Lambda}_{241} + \overline{\Lambda}_{124}$
$\overline{\Psi}^{G_{1g},4}_{\frac{1}{2},\frac{1}{2}}$	$\sqrt{\frac{2}{3}}(\overline{\Lambda}_{134}+\overline{\Lambda}_{341}+\overline{\Lambda}_{413})$	$\overline{\Psi}^{G_{1u},4}_{\frac{1}{2},\frac{1}{2}}$	$-\sqrt{\frac{2}{3}}(\overline{\Lambda}_{123}+\overline{\Lambda}_{231}+\overline{\Lambda}_{312})$
$\overline{\Psi}^{G_{1g},4}_{\frac{1}{2},-\frac{1}{2}}$	$\sqrt{\frac{2}{3}}(\overline{\Lambda}_{234}+\overline{\Lambda}_{342}+\overline{\Lambda}_{423})$	$\overline{\Psi}^{G_{1u},4}_{\frac{1}{2},-\frac{1}{2}}$	$-\sqrt{\frac{2}{3}}(\overline{\Lambda}_{124}+\overline{\Lambda}_{241}+\overline{\Lambda}_{412})$
$\overline{\Psi}^{H_g}_{\frac{3}{2},\frac{3}{2}}$	$\overline{\Lambda}_{133}$	$\overline{\Psi}^{H_u}_{\frac{3}{2},\frac{3}{2}}$	$\overline{\Lambda}_{131}$
$\overline{\Psi}^{H_g}_{\frac{3}{2},\frac{1}{2}}$	$\overline{\Lambda}_{134} + \overline{\Lambda}_{143} + \overline{\Lambda}_{233}$	$\overline{\Psi}^{H_u}_{\frac{3}{2},\frac{1}{2}}$	$\overline{\Lambda}_{132} + \overline{\Lambda}_{141} + \overline{\Lambda}_{231}$
$\overline{\Psi}^{H_g}_{\frac{3}{2},-\frac{1}{2}}$	$\overline{\Lambda}_{144} + \overline{\Lambda}_{234} + \overline{\Lambda}_{243}$	$\overline{\Psi}^{H_u}_{\frac{3}{2},-\frac{1}{2}}$	$\overline{\Lambda}_{142} + \overline{\Lambda}_{232} + \overline{\Lambda}_{241}$
$\overline{\Psi}^{H_g}_{\frac{3}{2},-\frac{3}{2}}$	$\overline{\Lambda}_{244}$	$\overline{\Psi}^{H_u}_{\frac{3}{2},-\frac{3}{2}}$	$\overline{\Lambda}_{242}$

in the left half of the table and twelve negative-parity operators are given in the right half. The symmetry of Dirac indices is listed in the middle column for each parity. Only four combinations of Dirac indices are totally antisymmetric under exchange, and they all belong to G_1 irreps. Because the mixed-antisymmetric combinations of Dirac indices provide three embeddings of the G_1 irrep,

the local Λ baryon operators have a total of four embeddings of the G_1 irrep in each parity and one embedding of the H irrep.

Irreducible basis operators for Λ_c and Λ_b baryons are exactly the same except that the third quark is replaced by a charm or bottom quark.

2.3.4 Quasi-local Σ and Ξ Operators

A Σ baryon has two light quarks forming an isospin triplet combination and a strange quark. Suitable Σ operators are defined such that the first two Dirac indices refer to the light quarks,

$$
\begin{aligned}
\overline{\Sigma}^+_{\mu_1\mu_2\mu_3} &= \epsilon_{abc}\, \bar{u}^a_{\mu_1}\, \bar{u}^b_{\mu_2}\, \bar{s}^c_{\mu_3}, \\
\overline{\Sigma}^0_{\mu_1\mu_2\mu_3} &= \epsilon_{abc}\frac{1}{\sqrt{2}}\left(\bar{u}^a_{\mu_1}\bar{d}^b_{\mu_2} + \bar{d}^a_{\mu_1}\bar{u}^b_{\mu_2}\right)\bar{s}^c_{\mu_3}, \\
\overline{\Sigma}^-_{\mu_1\mu_2\mu_3} &= \epsilon_{abc}\, \bar{d}^a_{\mu_1}\bar{d}^b_{\mu_2}\bar{s}^c_{\mu_3}.
\end{aligned}
\tag{2.32}
$$

Such operators satisfy the relation,

$$
\overline{\Sigma}_{\mu_1\mu_2\mu_3} - \overline{\Sigma}_{\mu_2\mu_1\mu_3} = 0,
\tag{2.33}
$$

showing that the Dirac indices must be totally symmetric or mixed-symmetric.

A Ξ baryon has two strange quarks and one light quark forming an isospin doublet,

$$
\begin{aligned}
\overline{\Xi}^0 &= \epsilon_{abc}\, \bar{s}^a_{\mu_1}\, \bar{s}^b_{\mu_2}\, \bar{u}^c_{\mu_3}, \\
\overline{\Xi}^- &= \epsilon_{abc}\, \bar{s}^a_{\mu_1}\, \bar{s}^b_{\mu_2}\, \bar{d}^c_{\mu_3}.
\end{aligned}
\tag{2.34}
$$

Again the operators are symmetric under the exchange of μ_1 and μ_2. Thus, the allowed combinations of Dirac indices are the same as for the quasi-local Σ baryon operators. Table 2.11 presents all operators with symmetric and mixed-symmetric Dirac indices. Note that there are 20 operators for totally symmetric Dirac indices (as in the quasi-local Δ operators) and 20 operators for mixed-symmetric Dirac indices, giving a total of 40 operators for Σ or Ξ baryons. Four G_1 embeddings and three H embeddings occur in each parity. In Table 2.11 the symbol $\overline{\Sigma}$ may be replaced by any of $\{\overline{\Sigma}^+, \overline{\Sigma}^0, \overline{\Sigma}^-, \overline{\Xi}^0, \overline{\Xi}^-\}$.

Table 2.11: Quasi-local Σ operators.

$\overline{\Psi}_{S,S_z}^{\Lambda,k}$	$\overline{\Sigma}_{\mu_1\mu_2\mu_3}$ notation	$\overline{\Psi}_{S,S_z}^{\Lambda,k}$	$\overline{\Sigma}_{\mu_1\mu_2\mu_3}$ notation
$\overline{\Psi}_{\frac{1}{2},\frac{1}{2}}^{G_{1g},1}$	$\frac{\sqrt{2}}{3}[-\overline{\Sigma}_{332} - 2\overline{\Sigma}_{233} + \overline{\Sigma}_{341} + \overline{\Sigma}_{413} + \overline{\Sigma}_{134}]$	$\overline{\Psi}_{\frac{1}{2},\frac{1}{2}}^{G_{1u},1}$	$\frac{\sqrt{2}}{3}[\overline{\Sigma}_{114} + 2\overline{\Sigma}_{141} - \overline{\Sigma}_{123} - \overline{\Sigma}_{312} - \overline{\Sigma}_{231}]$
$\overline{\Psi}_{\frac{1}{2},-\frac{1}{2}}^{G_{1g},1}$	$\frac{\sqrt{2}}{3}[2\overline{\Sigma}_{144} + \overline{\Sigma}_{441} - \overline{\Sigma}_{234} - \overline{\Sigma}_{342} - \overline{\Sigma}_{423}]$	$\overline{\Psi}_{\frac{1}{2},-\frac{1}{2}}^{G_{1u},1}$	$\frac{\sqrt{2}}{3}[-\overline{\Sigma}_{223} - 2\overline{\Sigma}_{232} + \overline{\Sigma}_{124} + \overline{\Sigma}_{241} + \overline{\Sigma}_{412}]$
$\overline{\Psi}_{\frac{1}{2},\frac{1}{2}}^{G_{1g},2}$	$\sqrt{\frac{2}{3}}[\overline{\Sigma}_{112} - \overline{\Sigma}_{121}]$	$\overline{\Psi}_{\frac{1}{2},\frac{1}{2}}^{G_{1u},2}$	$\frac{\sqrt{2}}{3}[\overline{\Sigma}_{114} + 2\overline{\Sigma}_{312} - \overline{\Sigma}_{123} - \overline{\Sigma}_{141} - \overline{\Sigma}_{231}]$
$\overline{\Psi}_{\frac{1}{2},-\frac{1}{2}}^{G_{1g},2}$	$\sqrt{\frac{2}{3}}[-\overline{\Sigma}_{221} + \overline{\Sigma}_{122}]$	$\overline{\Psi}_{\frac{1}{2},-\frac{1}{2}}^{G_{1u},2}$	$\frac{\sqrt{2}}{3}[-\overline{\Sigma}_{223} - 2\overline{\Sigma}_{241} + \overline{\Sigma}_{124} + \overline{\Sigma}_{232} + \overline{\Sigma}_{412}]$
$\overline{\Psi}_{\frac{1}{2},\frac{1}{2}}^{G_{1g},3}$	$\frac{\sqrt{2}}{3}[\overline{\Sigma}_{332} + 2\overline{\Sigma}_{134} - \overline{\Sigma}_{341} - \overline{\Sigma}_{233} - \overline{\Sigma}_{413}]$	$\overline{\Psi}_{\frac{1}{2},\frac{1}{2}}^{G_{1u},3}$	$\sqrt{\frac{2}{3}}[\overline{\Sigma}_{334} - \overline{\Sigma}_{343}]$
$\overline{\Psi}_{\frac{1}{2},-\frac{1}{2}}^{G_{1g},3}$	$\frac{\sqrt{2}}{3}[-\overline{\Sigma}_{441} - 2\overline{\Sigma}_{423} + \overline{\Sigma}_{342} + \overline{\Sigma}_{144} + \overline{\Sigma}_{234}]$	$\overline{\Psi}_{\frac{1}{2},-\frac{1}{2}}^{G_{1u},3}$	$\sqrt{\frac{2}{3}}[-\overline{\Sigma}_{443} + \overline{\Sigma}_{344}]$
$\overline{\Psi}_{\frac{1}{2},\frac{1}{2}}^{G_{1g},4}$	$\frac{\sqrt{2}}{3}[-\overline{\Sigma}_{332} - 2\overline{\Sigma}_{413} + \overline{\Sigma}_{233} + \overline{\Sigma}_{134} + \overline{\Sigma}_{341}]$	$\overline{\Psi}_{\frac{1}{2},\frac{1}{2}}^{G_{1u},4}$	$\frac{\sqrt{2}}{3}[\overline{\Sigma}_{114} + 2\overline{\Sigma}_{231} - \overline{\Sigma}_{141} - \overline{\Sigma}_{312} - \overline{\Sigma}_{123}]$
$\overline{\Psi}_{\frac{1}{2},-\frac{1}{2}}^{G_{1g},4}$	$\frac{\sqrt{2}}{3}[\overline{\Sigma}_{441} + 2\overline{\Sigma}_{234} - \overline{\Sigma}_{144} - \overline{\Sigma}_{423} - \overline{\Sigma}_{342}]$	$\overline{\Psi}_{\frac{1}{2},-\frac{1}{2}}^{G_{1u},4}$	$\frac{\sqrt{2}}{3}[-\overline{\Sigma}_{223} - 2\overline{\Sigma}_{412} + \overline{\Sigma}_{232} + \overline{\Sigma}_{241} + \overline{\Sigma}_{124}]$
$\overline{\Psi}_{\frac{3}{2},\frac{3}{2}}^{H_g,1}$	$\overline{\Sigma}_{111}$	$\overline{\Psi}_{\frac{3}{2},\frac{3}{2}}^{H_u,1}$	$\frac{1}{\sqrt{3}}[\overline{\Sigma}_{113} + 2\overline{\Sigma}_{131}]$
$\overline{\Psi}_{\frac{3}{2},\frac{1}{2}}^{H_g,1}$	$\frac{1}{\sqrt{3}}[\overline{\Sigma}_{112} + 2\overline{\Sigma}_{121}]$	$\overline{\Psi}_{\frac{3}{2},\frac{1}{2}}^{H_u,1}$	$\frac{1}{3}[2\overline{\Sigma}_{141} + \overline{\Sigma}_{114} + 2\overline{\Sigma}_{312} + 2\overline{\Sigma}_{123} + 2\overline{\Sigma}_{231}]$
$\overline{\Psi}_{\frac{3}{2},-\frac{1}{2}}^{H_g,1}$	$\frac{1}{\sqrt{3}}[2\overline{\Sigma}_{122} + \overline{\Sigma}_{221}]$	$\overline{\Psi}_{\frac{3}{2},-\frac{1}{2}}^{H_u,1}$	$\frac{1}{3}[2\overline{\Sigma}_{232} + \overline{\Sigma}_{223} + 2\overline{\Sigma}_{412} + 2\overline{\Sigma}_{124} + 2\overline{\Sigma}_{241}]$
$\overline{\Psi}_{\frac{3}{2},-\frac{3}{2}}^{H_g,1}$	$\overline{\Sigma}_{222}$	$\overline{\Psi}_{\frac{3}{2},-\frac{3}{2}}^{H_u,1}$	$\frac{1}{\sqrt{3}}[\overline{\Sigma}_{224} + 2\overline{\Sigma}_{242}]$
$\overline{\Psi}_{\frac{3}{2},\frac{3}{2}}^{H_g,2}$	$\frac{1}{\sqrt{3}}[2\overline{\Sigma}_{133} + \overline{\Sigma}_{331}]$	$\overline{\Psi}_{\frac{3}{2},\frac{3}{2}}^{H_u,2}$	$\overline{\Sigma}_{333}$
$\overline{\Psi}_{\frac{3}{2},\frac{1}{2}}^{H_g,2}$	$\frac{1}{3}[2\overline{\Sigma}_{233} + \overline{\Sigma}_{332} + 2\overline{\Sigma}_{134} + 2\overline{\Sigma}_{341} + 2\overline{\Sigma}_{413}]$	$\overline{\Psi}_{\frac{3}{2},\frac{1}{2}}^{H_u,2}$	$\frac{1}{\sqrt{3}}[\overline{\Sigma}_{334} + 2\overline{\Sigma}_{343}]$
$\overline{\Psi}_{\frac{3}{2},-\frac{1}{2}}^{H_g,2}$	$\frac{1}{3}[2\overline{\Sigma}_{144} + \overline{\Sigma}_{441} + 2\overline{\Sigma}_{234} + 2\overline{\Sigma}_{342} + 2\overline{\Sigma}_{423}]$	$\overline{\Psi}_{\frac{3}{2},-\frac{1}{2}}^{H_u,2}$	$\frac{1}{\sqrt{3}}[2\overline{\Sigma}_{344} + \overline{\Sigma}_{443}]$
$\overline{\Psi}_{\frac{3}{2},-\frac{3}{2}}^{H_g,2}$	$(1/\sqrt{3})[2\overline{\Sigma}_{244} + \overline{\Sigma}_{442}]$	$\overline{\Psi}_{\frac{3}{2},-\frac{3}{2}}^{H_u,2}$	$\overline{\Sigma}_{444}$
$\overline{\Psi}_{\frac{3}{2},\frac{3}{2}}^{H_g,3}$	$\sqrt{\frac{2}{3}}[-\overline{\Sigma}_{331} + \overline{\Sigma}_{133}]$	$\overline{\Psi}_{\frac{3}{2},\frac{3}{2}}^{H_u,3}$	$\sqrt{\frac{2}{3}}[\overline{\Sigma}_{113} - \overline{\Sigma}_{131}]$
$\overline{\Psi}_{\frac{3}{2},\frac{1}{2}}^{H_g,3}$	$\frac{\sqrt{2}}{3}[-\overline{\Sigma}_{332} - 2\overline{\Sigma}_{341} + \overline{\Sigma}_{134} + \overline{\Sigma}_{233} + \overline{\Sigma}_{413}]$	$\overline{\Psi}_{\frac{3}{2},\frac{1}{2}}^{H_u,3}$	$\frac{\sqrt{2}}{3}[\overline{\Sigma}_{114} + 2\overline{\Sigma}_{123} - \overline{\Sigma}_{312} - \overline{\Sigma}_{141} - \overline{\Sigma}_{231}]$
$\overline{\Psi}_{\frac{3}{2},-\frac{1}{2}}^{H_g,3}$	$\frac{\sqrt{2}}{3}[-2\overline{\Sigma}_{342} - \overline{\Sigma}_{441} + \overline{\Sigma}_{234} + \overline{\Sigma}_{144} + \overline{\Sigma}_{423}]$	$\overline{\Psi}_{\frac{3}{2},-\frac{1}{2}}^{H_u,3}$	$\frac{\sqrt{2}}{3}[2\overline{\Sigma}_{124} + \overline{\Sigma}_{223} - \overline{\Sigma}_{412} - \overline{\Sigma}_{232} - \overline{\Sigma}_{241}]$
$\overline{\Psi}_{\frac{3}{2},-\frac{3}{2}}^{H_g,3}$	$\sqrt{\frac{2}{3}}[-\overline{\Sigma}_{442} + \overline{\Sigma}_{244}]$	$\overline{\Psi}_{\frac{3}{2},-\frac{3}{2}}^{H_u,3}$	$\sqrt{\frac{2}{3}}[\overline{\Sigma}_{224} - \overline{\Sigma}_{242}]$

2.4 Nonlocal Baryonic Operators

In this section we discuss how to construct baryon operators that create states whose wavefunctions have angular or radial excitation. Orbital angular momentum or radial excitation is expected to be of particular interest for operators that couple to excited baryons.

In Section 2.3, all possible symmetries of the Dirac indices of three quarks were encountered. When nonlocal operators are constructed, we can build upon the quasi-local operators already found by adding a nontrivial spatial structure. This basically amounts to allowing different smearings of the quark fields.

Nonlocal operators are constructed by displacing at least one quark from the others. The set of displacements is first arranged to belong to the basis of irreps of the octahedral group. Then there arises the issue of combining the irreps of spatial distributions of displacements with irreps of the Dirac indices that have been developed for quasi-local operators. With respect to the octahedral group, the spatial and spin irreps transform as direct products. Using Clebsch-Gordan coefficients, we form linear combinations of the direct products so as to obtain nonlocal operators that transform as overall irreps of the group.

2.4.1 Displaced quark fields and irreps of O

Relative displacement of quarks requires insertion of a path-dependent gauge link in order to maintain gauge invariance. The simplest such displaced three-quark operator would be of the form,

$$\overline{b}^{(i)f_1 f_2 f_3}_{\mu_1 \mu_2 \mu_3}(\mathbf{x}) = \epsilon_{abc}\, \overline{q}^{af_1}_{\mu_1}(\mathbf{x}) \overline{q}^{bf_2}_{\mu_2}(\mathbf{x}) \overline{q}^{c'f_3}_{\mu_3}(\mathbf{x}+\hat{\imath}) U^{\dagger c'c}_i(\mathbf{x}), \tag{2.35}$$

where the time argument is omitted from quark fields, and $\hat{\imath}$ is one of the six spatial directions $\{\pm\hat{\mathbf{x}}, \pm\hat{\mathbf{y}}, \pm\hat{\mathbf{z}}\}$. The third quark is displaced in a gauge invariant manner by one site from the other two in Eq. (2.35). For a smeared quark field, the displacement is applied so as to displace each term in the sum of fields in Eq. (2.16).

Spatial displacements of Eq. (2.35) with $\hat{\imath} \in \{\pm\hat{\mathbf{x}}, \pm\hat{\mathbf{y}}, \pm\hat{\mathbf{z}}\}$ transform amongst themselves under the rotations of the octahedral group O assuming that gauge links are cubically invariant

(approximately true for averages over large sets of gauge-field configurations). The six-dimensional representation of O that is formed by the six displacements can be reduced to the irreps A_1, T_1 and E. In order to combine displacements into operators that transform as the preferred A_1, E, T_1 irreps of Table 2.3, the first step is to define the following even and odd combinations of forward and backward displacements:

$$
\begin{aligned}
\hat{S}_i \bar{b}^{f_1 f_2 f_3}_{\mu_1 \mu_2 \mu_3} &= \bar{b}^{(i) f_1 f_2 f_3}_{\mu_1 \mu_2 \mu_3} + \bar{b}^{(-i) f_1 f_2 f_3}_{\mu_1 \mu_2 \mu_3}, \\
\hat{D}_i \bar{b}^{f_1 f_2 f_3}_{\mu_1 \mu_2 \mu_3} &= \bar{b}^{(i) f_1 f_2 f_3}_{\mu_1 \mu_2 \mu_3} - \bar{b}^{(-i) f_1 f_2 f_3}_{\mu_1 \mu_2 \mu_3},
\end{aligned}
\tag{2.36}
$$

with $i = x, y, z$. The difference of forward and backward displacements, $\hat{D}_i$, has negative spatial-parity and involves a lattice first-derivative, while the sum of forward and backward displacements, $\hat{S}_i$, has positive spatial-parity. Note that the lattice first-derivative is an anti-hermitian operator. The second step is to form irrep operators using the $\hat{S}_i$ and $\hat{D}_i$ combinations as follows:

$$
\hat{A}_1 \bar{b}^{f_1 f_2 f_3}_{\mu_1 \mu_2 \mu_3}(\mathbf{x}) \equiv \frac{1}{\sqrt{6}} \sum_{i=1,2,3} \hat{S}_i \bar{b}^{f_1 f_2 f_3}_{\mu_1 \mu_2 \mu_3}(\mathbf{x}),
\tag{2.37}
$$

$$
\hat{E}^1 \bar{b}^{f_1 f_2 f_3}_{\mu_1 \mu_2 \mu_3}(\mathbf{x}) \equiv \frac{1}{2\sqrt{3}} \left(2\hat{S}_3 \bar{b}^{f_1 f_2 f_3}_{\mu_1 \mu_2 \mu_3}(\mathbf{x}) - \hat{S}_1 \bar{b}^{f_1 f_2 f_3}_{\mu_1 \mu_2 \mu_3}(\mathbf{x}) - \hat{S}_2 \bar{b}^{f_1 f_2 f_3}_{\mu_1 \mu_2 \mu_3}(\mathbf{x}) \right),
\tag{2.38}
$$

$$
\hat{E}^2 \bar{b}^{f_1 f_2 f_3}_{\mu_1 \mu_2 \mu_3}(\mathbf{x}) \equiv \frac{1}{2} \left(\hat{S}_1 \bar{b}^{f_1 f_2 f_3}_{\mu_1 \mu_2 \mu_3}(\mathbf{x}) - \hat{S}_2 \bar{b}^{f_1 f_2 f_3}_{\mu_1 \mu_2 \mu_3}(\mathbf{x}) \right),
\tag{2.39}
$$

$$
\begin{aligned}
\hat{T}_1^1 \bar{b}^{f_1 f_2 f_3}_{\mu_1 \mu_2 \mu_3}(\mathbf{x}) &\equiv \frac{i}{2} \left(\hat{D}_x \bar{b}^{f_1 f_2 f_3}_{\mu_1 \mu_2 \mu_3}(\mathbf{x}) + i\hat{D}_y \bar{b}^{f_1 f_2 f_3}_{\mu_1 \mu_2 \mu_3}(\mathbf{x}) \right) \\
&\equiv \hat{D}^+ \bar{b}^{f_1 f_2 f_3}_{\mu_1 \mu_2 \mu_3}(\mathbf{x}),
\end{aligned}
\tag{2.40}
$$

$$
\begin{aligned}
\hat{T}_1^2 \bar{b}^{f_1 f_2 f_3}_{\mu_1 \mu_2 \mu_3}(\mathbf{x}) &\equiv -\frac{i}{\sqrt{2}} \hat{D}_z \bar{b}^{f_1 f_2 f_3}_{\mu_1 \mu_2 \mu_3}(\mathbf{x}) \\
&\equiv \hat{D}^0 \bar{b}^{f_1 f_2 f_3}_{\mu_1 \mu_2 \mu_3}(\mathbf{x}),
\end{aligned}
\tag{2.41}
$$

$$
\begin{aligned}
\hat{T}_1^3 \bar{b}^{f_1 f_2 f_3}_{\mu_1 \mu_2 \mu_3}(\mathbf{x}) &\equiv -\frac{i}{2} \left(\hat{D}_x \bar{b}^{f_1 f_2 f_3}_{\mu_1 \mu_2 \mu_3}(\mathbf{x}) - i\hat{D}_y \bar{b}^{f_1 f_2 f_3}_{\mu_1 \mu_2 \mu_3}(\mathbf{x}) \right) \\
&\equiv \hat{D}^- \bar{b}^{f_1 f_2 f_3}_{\mu_1 \mu_2 \mu_3}(\mathbf{x}),
\end{aligned}
\tag{2.42}
$$

These definitions produce spatial distributions $\hat{A}_1, \hat{E}^\lambda, \hat{T}_1^\lambda$ corresponding to the lattice harmonics of Table 2.3. Superscripts on $\hat{E}$ and $\hat{T}_1$ operators refer to the rows of the irreps. For the $\hat{T}_1^{1,2,3}$ combinations of displacements, we will generally denote operators by using the spherical notation $\hat{D}^{+,0,-}$ as defined by Eqs. (2.40-2.42).

We refer to these simplest nonlocal operators, involving linear combinations of operators

with the third quark field displaced by one lattice site, as *one-link* operators. Let us denote the general form of a one-link operator as

$$\mathcal{D}_\lambda^\Lambda \overline{b}_{\mu_1\mu_2\mu_3}^{f_1 f_2 f_3}(\mathbf{x}) \equiv \epsilon_{abc}\,\overline{q}_{\mu_1}^{a f_1}(\mathbf{x})\overline{q}_{\mu_2}^{b f_2}(\mathbf{x})\left[\mathcal{D}_\lambda^\Lambda \overline{q}_{\mu_3}^{f_3}(\mathbf{x})\right]^c, \tag{2.43}$$

where Λ specifies the type of spatial irrep (A_1, T_1 or E) and λ specifies the row of the irrep. In order to combine the spatial irreps of the displacement operators with the irreps of Dirac indices, we need the direct product rules.

2.4.2 Direct products and Clebsch-Gordan coefficients

Nonlocal operators involve direct products of two different irreps of the octahedral group, one irrep associated with the combinations of displacement operators and the other associated with the Dirac indices. Linear combinations of such direct products can be formed so that they transform irreducibly amongst themselves by using Clebsch-Gordan coefficients for the octahedral group. These have been published by Altmann and Herzig [46].

Clebsch-Gordan coefficients depend upon the basis of irrep operators but different choices of the bases are related to one another by unitary transformations. Because our basis operators differ from those published by Altmann and Herzig, we have performed the required unitary transformations and obtained suitable Clebsch-Gordan coefficients for all possible direct products of irreps of the double octahedral group. The coefficients are provided in Appendix E. The relative phases of operators from different rows within an irrep should be fixed in lattice calculations in order to allow averaging over rows when that is appropriate, as it is in mass calculations. However, different ways of forming a given irrep as direct products need not have the same *overall* phases. We have used this freedom to eliminate phases within each table of Clebsch-Gordan coefficients such that all of our coefficients are real.

A one-link operator that transforms as overall irrep Λ and row λ of O^D is written as a linear combination of displacement operators acting on irreps of Dirac indices as

$$\overline{\mathcal{O}}_\lambda^\Lambda = \sum_{\lambda_1,\lambda_2} C\begin{pmatrix} \Lambda & \Lambda_1 & \Lambda_2 \\ \lambda & \lambda_1 & \lambda_2 \end{pmatrix} \mathcal{D}_{\lambda_1}^{\Lambda_1} \overline{\Psi}_{\lambda_2}^{\Lambda_2,k}. \tag{2.44}$$

where $C \begin{pmatrix} \Lambda & \Lambda_1 & \Lambda_2 \\ \lambda & \lambda_1 & \lambda_2 \end{pmatrix}$ is the Clebsch-Gordan coefficients of the coupling of irrep Λ_1 row λ_1 and irrep Λ_2 row λ_2 to yield overall irrep Λ row λ. In the above equation the quasi-local baryon operator is written as $\overline{\Psi}_\lambda^{\Lambda,k}$ instead of $\overline{\Psi}_{S,S_z}^{\Lambda,k}$ and the relation of λ and S, S_z is obvious from Table 2.6. For one-link operators, we need direct products of the spatial irreps $\Lambda_1 = A_1, E$ and T_1 with the spin irreps $\Lambda_2 = G_1$ and H of quasi-local baryon operators. The following rules of group multiplication show which overall irreps Λ are obtained from such direct products of spatial and spinorial irreps,

$$A_1 \otimes G_1 = G_1,$$

$$A_1 \otimes H = H,$$

$$E \otimes G_1 = H,$$

$$E \otimes H = G_1 \oplus G_2 \oplus H,$$

$$T_1 \otimes G_1 = G_1 \oplus H,$$

$$T_1 \otimes H = G_1 \oplus G_2 \oplus H \oplus H. \tag{2.45}$$

2.4.3 One-link operators

Baryon operators with one-link displacements can be categorized into two sets, one with antisymmetric and the other with symmetric Dirac indices of the first two quarks. The antisymmetric category includes the nucleon with MA isospin and the Λ baryon operators. The symmetric category includes the nucleon with MS isospin, and the Δ, Ω, Σ and Ξ baryon operators. These symmetries determine the spinorial structures of the one-link operators.

One-link operators for the nucleon with MA isospin and for the Λ baryon are taken to be of the form,

$$\mathcal{D}_\lambda^{(3)\Lambda} \overline{N}_{\mu_1\mu_2\mu_3}^{(\mathrm{MA})} = \frac{\epsilon_{abc}}{\sqrt{2}} \left[\overline{u}_{\mu_1}^a \overline{d}_{\mu_2}^b - \overline{d}_{\mu_1}^a \overline{u}_{\mu_2}^b \right] \left(\mathcal{D}_\lambda^\Lambda \overline{u}_{\mu_3} \right)^c, \tag{2.46}$$

$$\mathcal{D}_\lambda^{(3)\Lambda} \overline{\Lambda}_{\mu_1\mu_2\mu_3} = \frac{\epsilon_{abc}}{\sqrt{2}} \left[\overline{u}_{\mu_1}^a \overline{d}_{\mu_2}^b - \overline{d}_{\mu_1}^a \overline{u}_{\mu_2}^b \right] \left(\mathcal{D}_\lambda^\Lambda \overline{s}_{\mu_3} \right)^c, \tag{2.47}$$

where the superscript 3 of $\mathcal{D}_\lambda^{(3)\Lambda}$ denotes that the displacement operator $\mathcal{D}_\lambda^\Lambda \in \{\hat{A}_1, \hat{E}^\lambda, \hat{T}_1^\lambda\}$ acts on the third quark, and $N^{(\mathrm{MA})}$ denotes the isospin symmetry. This choice of one-link operators

preserves the antisymmetry under $\mu_1 \leftrightarrow \mu_2$, and therefore requires Dirac indices to be MA (20 combinations) or A (4 combinations). Taking into account the six possible $\mathcal{D}_\lambda^\Lambda$ combinations of displacements, the total number of operators of the form of Eq. (2.46) or Eq. (2.47) is $(20+4)\times 6 = 144$.

One-link operators for the nucleon with MS isospin, or for the Δ, Ω, Σ and Ξ baryons have the following forms:

$$\mathcal{D}_\lambda^{\Lambda(3)}\overline{N}_{\mu_1\mu_2\mu_3}^{(\mathrm{MS})} = \frac{\epsilon_{abc}}{\sqrt{6}}\left[2\overline{u}_{\mu_1}^a\,\overline{u}_{\mu_2}^b\left(\mathcal{D}_\lambda^\Lambda\overline{d}_{\mu_3}\right)^c\right.$$
$$\left.-\left(\overline{u}_{\mu_1}^a\,\overline{d}_{\mu_2}^b+\overline{d}_{\mu_1}^a\,\overline{u}_{\mu_2}^b\right)\left(\mathcal{D}_\lambda^\Lambda\overline{u}_{\mu_3}\right)^c\right], \tag{2.48}$$

$$\mathcal{D}_\lambda^{\Lambda(3)}\overline{\Delta}_{\mu_1\mu_2\mu_3}^{++} = \epsilon_{abc}\,\overline{u}_{\mu_1}^a\,\overline{u}_{\mu_2}^b\left(\mathcal{D}_\lambda^\Lambda\overline{u}_{\mu_3}\right)^c, \tag{2.49}$$

$$\mathcal{D}_\lambda^{\Lambda(3)}\overline{\Omega}_{\mu_1\mu_2\mu_3}^{-} = \epsilon_{abc}\,\overline{s}_{\mu_1}^a\,\overline{s}_{\mu_2}^b\left(\mathcal{D}_\lambda^\Lambda\overline{s}_{\mu_3}\right)^c, \tag{2.50}$$

$$\mathcal{D}_\lambda^{\Lambda(3)}\overline{\Sigma}_{\mu_1\mu_2\mu_3}^{+} = \epsilon_{abc}\,\overline{u}_{\mu_1}^a\,\overline{u}_{\mu_2}^b\left(\mathcal{D}_\lambda^\Lambda\overline{s}_{\mu_3}\right)^c, \tag{2.51}$$

$$\mathcal{D}_\lambda^{\Lambda(3)}\overline{\Xi}_{\mu_1\mu_2\mu_3}^{0} = \epsilon_{abc}\,\overline{s}_{\mu_1}^a\,\overline{s}_{\mu_2}^b\left(\mathcal{D}_\lambda^\Lambda\overline{u}_{\mu_3}\right)^c. \tag{2.52}$$

These operators are symmetric under $\mu_1 \leftrightarrow \mu_2$, so the allowed combinations of Dirac indices are totally symmetric (20 combinations) or mixed-symmetric (20 combinations). There are $(20+20)\times 6 = 240$ such operators for each baryon.

The A_1 one-link operators

The reduction is the simplest for the $\hat{A}_1$ combination of one-link operators because it is just a scalar "smearing". We show it as a first example. The MA isospin nucleon operator of Eq. (2.46) and the Λ baryon operator of Eq. (2.47) have the same restriction on Dirac indices as in Eq. (2.31). Because the A_1 combination of displacements is cubically symmetric, these operators have the same transformations under group rotations as the quasi-local Λ baryon operators in Eq. (2.30), except that the strange quark is replaced by $(\hat{A}_1\overline{u}_{\mu_3})^c$ and $(\hat{A}_1\overline{s}_{\mu_3})^c$, respectively. Dirac indices for $\hat{A}_1^{(3)}\overline{N}^{(\mathrm{MA})}$ and $\hat{A}_1^{(3)}\overline{\Lambda}$ are obtained from Table 2.10, the quasi-local Λ baryon operator table.

For each operator in Eqs. (2.48)-(2.52), the displacement makes the third quark distinct but the operators are symmetric under $\mu_1 \leftrightarrow \mu_2$ as in Eq. (2.33). This means that these operators

transform in the same manner as the quasi-local Σ baryon operators and Table 2.11 can be used for any of the operators in Eqs. (2.48)-(2.52).

We note in passing that the kernel of Gaussian smearing given in Eq. (2.16) can be rewritten in terms of the $\hat{A}_1$ operator by

$$\hat{G}^{(N)}(\mathbf{x}, \mathbf{x}') = \sum_y \alpha \left(\delta_{x,y} + \beta \hat{A}_{1x,y} \right) \hat{G}^{(N-1)}(\mathbf{y}, \mathbf{x}'), \tag{2.53}$$

where $\alpha = 1 - \frac{3\sigma^2}{2N}$ and $\beta = \frac{\sigma^2/4N}{1-3\sigma^2/2N}$. Thus, Gaussian smearing, or any other scalar smearing constructed from powers of $\hat{A}_1$ such that the third quark is distinct from the first two, can be substituted for the $\hat{A}_1$ combination of displacements of the third quark. All such operators have the same transformations and thus the same irreps of Dirac indices.

The T_1, E one-link operators

In order to construct operators that have the T_1 or E combinations of one-link displacements, we apply the Clebsch-Gordan formula of Eq. (2.44) using the coefficients for the double octahedral group from Appendix E. The resulting one-link operators are given in Table 2.12 and Table 2.13. These tables give *all* possible T_1 and E one-link baryon operators. In Table 2.12 we employ the notation of $\hat{D}^{+,-,0}$, instead of $\hat{T}_1^{1,2,3}$. The displacements are understood to act on the third quark. These tables are general in the sense that they apply to any baryon, e.g., $\overline{N}, \overline{\Delta}, \overline{\Lambda}, \overline{\Sigma},$ or $\overline{\Xi}$.

The notation $\overline{\Psi}_\lambda^{\Lambda,k}$ describes a *quasi-local* operator whose spin belongs to the k-th embedding of irrep Λ and row λ. These operators are taken directly from the tables for quasi-local baryon operators discussed in Section 2.3 in a similar fashion as for the A_1 one-link operators. One-link nucleon operators with MA isospin and one-link Λ baryon operators employ the spinorial structures $\overline{\Psi}_\lambda^{\Lambda,k}$ used for quasi-local Λ baryon operators given in Table 2.10, together with Table 2.12 for T_1 and Table 2.13 for E. One-link nucleon operators with MS isospin or one-link Δ, Ω Σ and Ξ operators employ the same spinorial structures $\overline{\Psi}_\lambda^{\Lambda,k}$ that are given for the quasi-local Σ baryon operators in Table 2.11.

The T_1 one-link operators in Table 2.12 are strictly "barred" fields. The corresponding "unbarred" T_1 operators use hermitian conjugated lattice first-derivatives. The factor i that has

Table 2.12: The T_1 one-link baryon operators. Note that $\hat{D}^+ \equiv \hat{T}_1^1$, $\hat{D}^0 \equiv \hat{T}_1^2$, and $\hat{D}^- \equiv \hat{T}_1^3$.

irrep	row	$C\begin{pmatrix} \Lambda & T_1 & \Lambda_2 \\ \lambda & \lambda_1 & \lambda_2 \end{pmatrix} \hat{D}^{(3)\lambda_1}\overline{\Psi}^{\Lambda_2,k}_{\lambda_2}$	$\sim |J,J_z\rangle$
$H_{g/u}$	1	$\hat{D}^+\overline{\Psi}^{G_{1u/g},k}_{\frac{1}{2},\frac{1}{2}}$	$\left|\frac{3}{2},+\frac{3}{2}\right\rangle$
	2	$\frac{1}{\sqrt{3}}\hat{D}^+\overline{\Psi}^{G_{1u/g},k}_{\frac{1}{2},-\frac{1}{2}} + \sqrt{\frac{2}{3}}\hat{D}^0\overline{\Psi}^{G_{1u/g},k}_{\frac{1}{2},\frac{1}{2}}$	$\left|\frac{3}{2},+\frac{1}{2}\right\rangle$
	3	$\sqrt{\frac{2}{3}}\hat{D}^0\overline{\Psi}^{G_{1u/g},k}_{\frac{1}{2},-\frac{1}{2}} + \frac{1}{\sqrt{3}}\hat{D}^-\overline{\Psi}^{G_{1u/g},k}_{\frac{1}{2},\frac{1}{2}}$	$\left|\frac{3}{2},-\frac{1}{2}\right\rangle$
	4	$\hat{D}^-\overline{\Psi}^{G_{1u/g},k}_{\frac{1}{2},-\frac{1}{2}}$	$\left|\frac{3}{2},-\frac{3}{2}\right\rangle$
$H_{g/u}$	1	$\sqrt{\frac{3}{5}}\hat{D}^0\overline{\Psi}^{H_{u/g},k}_{\frac{3}{2},\frac{3}{2}} - \sqrt{\frac{2}{5}}\hat{D}^+\overline{\Psi}^{H_{u/g},k}_{\frac{3}{2},\frac{1}{2}}$	$\left|\frac{3}{2},+\frac{3}{2}\right\rangle$
	2	$\sqrt{\frac{2}{5}}\hat{D}^-\overline{\Psi}^{H_{u/g},k}_{\frac{3}{2},\frac{3}{2}} + \frac{1}{\sqrt{15}}\hat{D}^0\overline{\Psi}^{H_{u/g},k}_{\frac{3}{2},\frac{1}{2}} - \sqrt{\frac{8}{15}}\hat{D}^+\overline{\Psi}^{H_{u/g},k}_{\frac{3}{2},-\frac{1}{2}}$	$\left|\frac{3}{2},+\frac{1}{2}\right\rangle$
	3	$\sqrt{\frac{8}{15}}\hat{D}^-\overline{\Psi}^{H_{u/g},k}_{\frac{3}{2},\frac{1}{2}} - \frac{1}{\sqrt{15}}\hat{D}^0\overline{\Psi}^{H_{u/g},k}_{\frac{3}{2},-\frac{1}{2}} - \sqrt{\frac{2}{5}}\hat{D}^+\overline{\Psi}^{H_{u/g},k}_{\frac{3}{2},-\frac{3}{2}}$	$\left|\frac{3}{2},-\frac{1}{2}\right\rangle$
	4	$\sqrt{\frac{2}{5}}\hat{D}^-\overline{\Psi}^{H_{u/g},k}_{\frac{3}{2},-\frac{1}{2}} - \sqrt{\frac{3}{5}}\hat{D}^0\overline{\Psi}^{H_{u/g},k}_{\frac{3}{2},-\frac{3}{2}}$	$\left|\frac{3}{2},-\frac{3}{2}\right\rangle$
$H_{g/u}$	1	$\frac{1}{\sqrt{10}}\hat{D}^+\overline{\Psi}^{H_{u/g},k}_{\frac{3}{2},\frac{1}{2}} + \sqrt{\frac{5}{6}}\hat{D}^-\overline{\Psi}^{H_{u/g},k}_{\frac{3}{2},-\frac{3}{2}} + \frac{1}{\sqrt{15}}\hat{D}^0\overline{\Psi}^{H_{u/g},k}_{\frac{3}{2},\frac{3}{2}}$	$\frac{1}{\sqrt{6}}\left|\frac{5}{2},+\frac{3}{2}\right\rangle + \sqrt{\frac{5}{6}}\left|\frac{5}{2},-\frac{5}{2}\right\rangle$
	2	$-\frac{1}{\sqrt{10}}\hat{D}^-\overline{\Psi}^{H_{u/g},k}_{\frac{3}{2},\frac{3}{2}} - \sqrt{\frac{3}{5}}\hat{D}^0\overline{\Psi}^{H_{u/g},k}_{\frac{3}{2},\frac{1}{2}} - \sqrt{\frac{3}{10}}\hat{D}^+\overline{\Psi}^{H_{u/g},k}_{\frac{3}{2},-\frac{1}{2}}$	$\left|\frac{5}{2},+\frac{1}{2}\right\rangle$
	3	$\sqrt{\frac{3}{10}}\hat{D}^-\overline{\Psi}^{H_{u/g},k}_{\frac{3}{2},\frac{1}{2}} + \sqrt{\frac{3}{5}}\hat{D}^0\overline{\Psi}^{H_{u/g},k}_{\frac{3}{2},-\frac{1}{2}} + \frac{1}{\sqrt{10}}\hat{D}^+\overline{\Psi}^{H_{u/g},k}_{\frac{3}{2},-\frac{3}{2}}$	$\left|\frac{5}{2},-\frac{1}{2}\right\rangle$
	4	$-\sqrt{\frac{5}{6}}\hat{D}^+\overline{\Psi}^{H_{u/g},k}_{\frac{3}{2},\frac{3}{2}} - \frac{1}{\sqrt{10}}\hat{D}^-\overline{\Psi}^{H_{u/g},k}_{\frac{3}{2},-\frac{1}{2}} - \frac{1}{\sqrt{15}}\hat{D}^0\overline{\Psi}^{H_{u/g},k}_{\frac{3}{2},-\frac{3}{2}}$	$\sqrt{\frac{5}{6}}\left|\frac{5}{2},+\frac{5}{2}\right\rangle + \frac{1}{\sqrt{6}}\left|\frac{5}{2},-\frac{3}{2}\right\rangle$
$G_{1g/u}$	1	$\sqrt{\frac{2}{3}}\hat{D}^+\overline{\Psi}^{G_{1u/g},k}_{\frac{1}{2},-\frac{1}{2}} - \frac{1}{\sqrt{3}}\hat{D}^0\overline{\Psi}^{G_{1u/g},k}_{\frac{1}{2},\frac{1}{2}}$	$\left|\frac{1}{2},+\frac{1}{2}\right\rangle$
	2	$\frac{1}{\sqrt{3}}\hat{D}^0\overline{\Psi}^{G_{1u/g},k}_{\frac{1}{2},-\frac{1}{2}} - \sqrt{\frac{2}{3}}\hat{D}^-\overline{\Psi}^{G_{1u/g},k}_{\frac{1}{2},\frac{1}{2}}$	$\left|\frac{1}{2},-\frac{1}{2}\right\rangle$
$G_{1g/u}$	1	$\frac{1}{\sqrt{2}}\hat{D}^-\overline{\Psi}^{H_{u/g},k}_{\frac{3}{2},\frac{3}{2}} - \frac{1}{\sqrt{3}}\hat{D}^0\overline{\Psi}^{H_{u/g},k}_{\frac{3}{2},\frac{1}{2}} + \frac{1}{\sqrt{6}}\hat{D}^+\overline{\Psi}^{H_{u/g},k}_{\frac{3}{2},-\frac{1}{2}}$	$\left|\frac{1}{2},+\frac{1}{2}\right\rangle$
	2	$\frac{1}{\sqrt{6}}\hat{D}^-\overline{\Psi}^{H_{u/g},k}_{\frac{3}{2},\frac{1}{2}} - \frac{1}{\sqrt{3}}\hat{D}^0\overline{\Psi}^{H_{u/g},k}_{\frac{3}{2},-\frac{1}{2}} + \frac{1}{\sqrt{2}}\hat{D}^+\overline{\Psi}^{H_{u/g},k}_{\frac{3}{2},-\frac{3}{2}}$	$\left|\frac{1}{2},-\frac{1}{2}\right\rangle$
$G_{2g/u}$	1	$-\frac{1}{\sqrt{2}}\hat{D}^-\overline{\Psi}^{H_{u/g},k}_{\frac{3}{2},-\frac{1}{2}} - \frac{1}{\sqrt{3}}\hat{D}^0\overline{\Psi}^{H_{u/g},k}_{\frac{3}{2},-\frac{3}{2}} + \frac{1}{\sqrt{6}}\hat{D}^+\overline{\Psi}^{H_{u/g},k}_{\frac{3}{2},\frac{3}{2}}$	$\frac{1}{\sqrt{6}}\left|\frac{5}{2},+\frac{5}{2}\right\rangle - \sqrt{\frac{5}{6}}\left|\frac{5}{2},-\frac{3}{2}\right\rangle$
	2	$\frac{1}{\sqrt{6}}\hat{D}^-\overline{\Psi}^{H_{u/g},k}_{\frac{3}{2},-\frac{3}{2}} - \frac{1}{\sqrt{3}}\hat{D}^0\overline{\Psi}^{H_{u/g},k}_{\frac{3}{2},\frac{3}{2}} - \frac{1}{\sqrt{2}}\hat{D}^+\overline{\Psi}^{H_{u/g},k}_{\frac{3}{2},\frac{1}{2}}$	$-\sqrt{\frac{5}{6}}\left|\frac{5}{2},+\frac{3}{2}\right\rangle + \frac{1}{\sqrt{6}}\left|\frac{5}{2},-\frac{5}{2}\right\rangle$

Table 2.13: The E one-link baryon operators. All operators have mixed J_z.

irrep	row	$C\begin{pmatrix}\Lambda & E & \Lambda_2 \\ \lambda & \lambda_1 & \lambda_2\end{pmatrix}\hat{E}^{(3)\lambda_1}\overline{\Psi}_{\lambda_2}^{\Lambda_2,k}$
$H_{g/u}$	1	$-\hat{E}2\,\overline{\Psi}_{\frac{1}{2},-\frac{1}{2}}^{G_{1g/u},k}$
	2	$\hat{E}1\,\overline{\Psi}_{\frac{1}{2},\frac{1}{2}}^{G_{1g/u},k}$
	3	$-\hat{E}1\,\overline{\Psi}_{\frac{1}{2},-\frac{1}{2}}^{G_{1g/u},k}$
	4	$\hat{E}2\,\overline{\Psi}_{\frac{1}{2},\frac{1}{2}}^{G_{1g/u},k}$
$H_{g/u}$	1	$-\hat{E}1\,\overline{\Psi}_{\frac{3}{2},\frac{3}{2}}^{H_{g/u},k} - \hat{E}2\,\overline{\Psi}_{\frac{3}{2},-\frac{1}{2}}^{H_{g/u},k}$
	2	$\hat{E}1\,\overline{\Psi}_{\frac{3}{2},\frac{1}{2}}^{H_{g/u},k} - \hat{E}2\,\overline{\Psi}_{\frac{3}{2},-\frac{3}{2}}^{H_{g/u},k}$
	3	$\hat{E}1\,\overline{\Psi}_{\frac{3}{2},-\frac{1}{2}}^{H_{g/u},k} - \hat{E}2\,\overline{\Psi}_{\frac{3}{2},\frac{3}{2}}^{H_{g/u},k}$
	4	$-\hat{E}1\,\overline{\Psi}_{\frac{3}{2},-\frac{3}{2}}^{H_{g/u},k} - \hat{E}2\,\overline{\Psi}_{\frac{3}{2},\frac{1}{2}}^{H_{g/u},k}$
$G_{1g/u}$	1	$\hat{E}1\,\overline{\Psi}_{\frac{3}{2},\frac{1}{2}}^{H_{g/u},k} + \hat{E}2\,\overline{\Psi}_{\frac{3}{2},-\frac{3}{2}}^{H_{g/u},k}$
	2	$-\hat{E}1\,\overline{\Psi}_{\frac{3}{2},-\frac{1}{2}}^{H_{g/u},k} - \hat{E}2\,\overline{\Psi}_{\frac{3}{2},\frac{3}{2}}^{H_{g/u},k}$
$G_{2g/u}$	1	$\hat{E}1\,\overline{\Psi}_{\frac{3}{2},-\frac{3}{2}}^{H_{g/u},k} - \hat{E}2\,\overline{\Psi}_{\frac{3}{2},\frac{1}{2}}^{H_{g/u},k}$
	2	$-\hat{E}1\,\overline{\Psi}_{\frac{3}{2},\frac{3}{2}}^{H_{g/u},k} + \hat{E}2\,\overline{\Psi}_{\frac{3}{2},-\frac{1}{2}}^{H_{g/u},k}$

been included in the T_1 one-link operators provides the same hermiticity property as spherical harmonics, i.e., $Y_{l,m}^{\dagger} = (-1)^m Y_{l,-m}$. Note that because the spatial parity of the T_1 displacement is negative, the overall ρ-parity is opposite to the overall parity for T_1 one-link operators.

The last column of Table 2.12 shows the total angular momentum and its projection onto the z-axis. The first set of H operators involves the same Clebsch-Gordan coefficients as would apply to the formation of continuum states: $l = 1) \otimes (s = 1/2) \rightarrow (j = 3/2)$. This is a result of using the combinations of displacements that correspond to the bases of Table 2.3. The second set of H operators has the continuum Clebsch-Gordan coefficients for $(l = 1) \otimes (s = 3/2) \rightarrow (j = 3/2)$. The third set of H operators corresponds to $(l = 1) \otimes (s = 3/2) \rightarrow (j = 5/2)$, but j_z values are mixed in row 1 and row 4. Similarly, the first set of G_1 operators in Table 2.12 is $(l = 1) \otimes (s = 1/2) \rightarrow (j = 1/2)$, and the second one is $(l = 1) \otimes (s = 3/2) \rightarrow (j = 1/2)$, both having the continuum Clebsch-Gordan coefficients. The G_2 operators correspond to $(l = 1) \otimes (s = 3/2) \rightarrow (j = 5/2)$,

but j_z values are mixed.

Direct products involving the $\hat{E}$ spatial irrep of displacements and spinorial irreps are given in Table 2.13. No operators involve *continuum* Clebsch-Gordan coefficients in Table 2.13 because the E irrep has mixed j_z, i.e., $\hat{E}^2 \sim Y_{2,2} + Y_{2-2}$. The $\hat{E}$ combinations of displacements provide two members of the rank-two spherical harmonics. The remaining three members belong to the T_2 irrep and they cannot be constructed unless there are least two displacements in perpendicular directions, as will be discussed in the next section.

For baryon fields with projection to zero total momentum, the following linear dependence holds,

$$\sum_x \overline{q}_\alpha(\mathbf{x})\overline{q}_\beta(\mathbf{x})\hat{D}^i\overline{q}_\gamma(\mathbf{x}) = -\sum_x \overline{q}_\alpha(\mathbf{x})\left(\hat{D}^i\overline{q}_\beta(\mathbf{x})\right)\overline{q}_\gamma(\mathbf{x}) - \sum_x \left(\hat{D}^i\overline{q}_\alpha(\mathbf{x})\right)\overline{q}_\beta(\mathbf{x})\overline{q}_\gamma(\mathbf{x}) + O(a^2). \quad (2.54)$$

This relation derives from the fact that after projection to zero total momentum, a total derivative of a baryon field vanishes and a total derivative is equivalent to order a^2 to a sum of lattice derivatives applied to each quark field. Some of the T_1 one-link nucleon operators are not linearly independent because of this. A nucleon operator with MS isospin having MS Dirac indices is equivalent (within a total derivative) to a nucleon operator with MA isospin having MA Dirac indices, for the T_1 one-link construction. It is easy to show that $\hat{D}_i^{(3)}\overline{N}_{\alpha\beta\gamma}^{(MS)} + \frac{1}{2}(\beta \leftrightarrow \gamma) + \frac{1}{2}(\alpha \leftrightarrow \gamma)$ can be written as a linear combination of $\hat{D}_i^{(3)}\overline{N}_{\alpha\beta\gamma}^{(MA)}$'s by applying Eq. (2.54). This identity reduces the number of T_1 one-link nucleon operators by $20 \times 3 = 60$, where the number 20 comes from the number of MS Dirac indices (or MA Dirac indices). The number of distinct one-link nucleon operators (both MA and MS isospin) after projection to zero total momentum is 64 for A_1, 132 for T_1, and 128 for E. The total number is 324.

Operators that are totally symmetric with respect to flavor exchanges, such as the Δ baryon, have a similar restriction. Such operators vanish when a first-derivative acts on one quark in a totally symmetric combination of Dirac indices. There are sixty Δ baryon operators with the T_1 one-link displacements that vanish after projection to zero total momentum.

The correspondence between the type of baryon and the symmetry of Dirac indices for the two categories of one-link baryon operators is summarized in Table 2.14. The numbers of possible

Table 2.14: Allowed combinations of Dirac indices for different one-link (A_1, T_1, E) baryons. The displacement is always taken on the third quark for simplicity. The third quark of the Λ and Σ baryons is chosen to be strange quark, and the third quark of the Ξ baryon is the light quark. The numbers of operators for A_1, T_1, or E combinations of displacements are listed in the fifth column and the numbers of operators for each overall irrep of O^D are shown in the last three columns, counting both parities, all embeddings and all rows. Linear dependencies resulting from a projection to zero total momentum are not taken into account in this table.

one-link baryon	spin sym.	Table	disp.	#	G_1	G_2	H
$N^{(\mathrm{MA})}, \Lambda$	MA, A	2.10	A_1	24	16	0	8
		2.12, 2.10	T_1	72	20	4	48
		2.13, 2.10	E	48	4	4	40
$N^{(\mathrm{MS})}, \Delta, \Omega, \Sigma, \Xi$	MS, S	2.11	A_1	40	16	0	24
		2.12,2.11	T_1	120	28	12	80
		2.12,2.11	E	80	12	12	56

operators are shown for constructions using A_1, T_1, or E spatial irreps to obtain G_1, G_2, or H overall irreps.

2.4.4 Two-link operators

One-link operators make it possible to realize $\hat{A}_1$, $\hat{T}_1$ and $\hat{E}$ types of spatial smearing, but not the $\hat{T}_2$ or $\hat{A}_2$ types. The latter two types appear in the two-link operator constructions. We define a *two-link operator* as follows,

$$\mathcal{D}_{\lambda_2}^{(3)\Lambda_2}\mathcal{D}_{\lambda_1}^{(3)\Lambda_1}\overline{b}_{\mu_1\mu_2\mu_3}^{f_1 f_2 f_3}(\mathbf{x}) \equiv \epsilon_{abc}\overline{q}_{\mu_1}^{a f_1}(\mathbf{x})\overline{q}_{\mu_2}^{b f_2}(\mathbf{x})\left[\mathcal{D}_{\lambda_2}^{\Lambda_2}\mathcal{D}_{\lambda_1}^{\Lambda_1}\overline{q}_{\mu_3}^{f_3}(\mathbf{x})\right]^c, \qquad (2.55)$$

where the third quark is displaced covariantly by two displacement operators $\mathcal{D}_{\lambda_1}^{\Lambda_1}, \mathcal{D}_{\lambda_2}^{\Lambda_2} \in \{A_1, E^\lambda, T_1^\lambda\}$. The first displacement acts on the third quark and defines a modified quark field, $\tilde{q}_{\mu_3,\lambda_1}^{c' f_3, \Lambda_1}(\mathbf{x}) \equiv$

$\left[\mathcal{D}_{\lambda_1}^{\Lambda_1}\overline{q}_{\mu_3}^{f_3}(\mathbf{x})\right]^{c'}$ at the same position $\mathbf{x}$. Then the second displacement further displaces the field and so defines a second modified field at the same position, $\tilde{\tilde{q}}_{\mu_3,\lambda_1,\lambda_2}^{cf_3,\Lambda_1,\Lambda_2}(\mathbf{x}) \equiv \left[\mathcal{D}_{\lambda_2}^{\Lambda_2}\tilde{q}_{\mu_3,\lambda_1}^{f_3,\Lambda_1}(\mathbf{x})\right]^{c}$.

Figure 2.3: Schematic view of two-link baryon.

Figure 2.3 shows schematic illustrations of three distinct displacement configurations for a two-link baryon operator. The first figure shows the "bent-link" operator, where a line denotes the gauge link and the arrow specifies the point at which the displaced quark's color index forms a color singlet with the other quarks. The second figure shows the possibility that the third quark is translated back to its original position by the second displacement, which is equivalent to a quasi-local operator because $U_i(x)U_i^\dagger(x) = 1$. The third figure shows the possibility of two displacements along the same direction, which gives a straight path differing from a one-link displacement only by its length. Inclusion of the bent-links can enrich the angular distribution and recover parts of the continuum spherical harmonics that cannot be obtained from one-link displacements.

First, we classify the spatial degrees of freedom into a single irrep of O by forming linear combinations of the elemental operators of Eq. (2.55). The overall spatial irrep Λ and row λ are determined by the direct product of the two spatial displacements $\mathcal{D}_{\lambda_1}^{\Lambda_1}$ and $\mathcal{D}_{\lambda_2}^{\Lambda_2}$ with appropriate Clebsch-Gordan coefficients,

$$\sum_{\lambda_1,\lambda_2} C\begin{pmatrix} \Lambda & \Lambda_1 & \Lambda_2 \\ \lambda & \lambda_1 & \lambda_2 \end{pmatrix} \mathcal{D}_{\lambda_2}^{\Lambda_2}\mathcal{D}_{\lambda_1}^{\Lambda_1}. \tag{2.56}$$

A particular example is instructive. Suppose one chooses $\mathcal{D}_{\lambda_1}^{\Lambda_1}$ to belong to the T_1 irrep, and $\mathcal{D}_{\lambda_2}^{\Lambda_2}$ to belong to the E irrep and desires the overall spatial irrep to be T_1. Then Eq.(2.56) is used with Clebsch-Gordan coefficients from the $E \otimes T_1$ table in Appendix E, which gives

$$\hat{T}_1^1 \sim \frac{1}{2}\hat{E}^1 \times \hat{T}_1^1 + \frac{\sqrt{3}}{2}\hat{E}^2 \times \hat{T}_1^3,$$
$$\hat{T}_1^2 \sim -\hat{E}^1 \times \hat{T}_1^2,$$

$$\hat{T}_1^3 \quad \sim \quad \frac{1}{2}\hat{E}^1 \times \hat{T}_1^3 + \frac{\sqrt{3}}{2}\hat{E}^2 \times \hat{T}_1^1.$$

In this way the two-link operator is determined so that its spatial part transforms according to a particular irrep (in this case T_1). Once the overall spatial irrep is obtained, Clebsch-Gordan coefficients for the direct products of the overall spatial irrep and a selected spinorial irrep are used to form an operator that overall transforms irreducibly according to $G_1, H,$ or G_2. Because the spatial irrep in the example above is T_1, which has been considered already in the construction of one-link operators, Table 2.12 provides the result. The only change is to use the T_1 distribution of two-link displacements in place of the T_1 distribution of one-link displacements. The use of Clebsch-Gordan coefficients of the cubic group has reduced the problem of finding irreps of two-link baryon operators to the already solved problem of finding one-link baryon operators.

However, new possibilities exist with the two-link displacements. One can form the A_2 and T_2 spatial irreps that did not appear in the one-link construction. The Clebsch-Gordan coefficients for the direct products of $A_2 \otimes \{G_1, G_2, H\}$ or $T_2 \otimes \{G_1, G_2, H\}$ may be found in Appendix E. Two-link A_2 and T_2 lattice harmonics correspond to the spherical harmonics in the continuum:

$$\hat{T}_2^1 \quad \sim \quad Y_{2,1},$$

$$\hat{T}_2^2 \quad \sim \quad Y_{2,2} - Y_{2,-2},$$

$$\hat{T}_2^3 \quad \sim \quad Y_{2,-1}, \tag{2.57}$$

for lowest l. These together with the E irrep provide all spherical harmonics of rank-two. Two-link A_2 lattice harmonics have a form

$$\hat{A}_2 \sim Y_{3,2} - Y_{3,-2} \tag{2.58}$$

in terms of continuum spherical harmonics for the lowest value of l, which is a part of the rank-three tensor. For the completeness, the T_2 and A_2 one-link baryon operators are provided in Tables 2.15 and 2.16.

Proceeding in this fashion, one may construct *multi-link* baryon operators

$$\mathcal{D}_{\lambda_n}^{(3)\Lambda_n} \cdots \mathcal{D}_{\lambda_2}^{(3)\Lambda_2} \mathcal{D}_{\lambda_1}^{(3)\Lambda_1} \overline{b}_{\mu_1\mu_2\mu_3}^{f_1 f_2 f_3}(\mathbf{x}) \equiv \epsilon_{abc} \overline{q}_{\mu_1}^{a f_1}(\mathbf{x}) \overline{q}_{\mu_2}^{b f_2}(\mathbf{x}) \left[\mathcal{D}_{\lambda_n}^{\Lambda_n} \cdots \mathcal{D}_{\lambda_2}^{\Lambda_2} \mathcal{D}_{\lambda_1}^{\Lambda_1} \overline{q}_{\mu_3}^{f_3}(\mathbf{x}) \right]^c, \tag{2.59}$$

56

Table 2.15: The T_2 one-link baryon operators. Note that $\hat{T}_2^+ \equiv \hat{T}_2^1$, $\hat{T}_2^0 \equiv \hat{T}_2^2$, and $\hat{T}_2^- \equiv \hat{T}_2^3$.

irrep	row	$C\begin{pmatrix} \Lambda & T_2 & \Lambda_2 \\ \lambda & \lambda_1 & \lambda_2 \end{pmatrix} \hat{T}_2^{(3)\lambda_1}\overline{\Psi}_{\lambda_2}^{\Lambda_2,k}$
$H_{g/u}$	1	$\frac{1}{\sqrt{3}}\hat{T}_2^+\overline{\Psi}_{\frac{1}{2},\frac{1}{2}}^{G_{1g/u},k} + \sqrt{\frac{2}{3}}\hat{T}_2^0\overline{\Psi}_{\frac{1}{2},-\frac{1}{2}}^{G_{1g/u},k}$
	2	$-\hat{T}_2^+\overline{\Psi}_{\frac{1}{2},-\frac{1}{2}}^{G_{1g/u},k}$
	3	$\hat{T}_2^-\overline{\Psi}_{\frac{1}{2},\frac{1}{2}}^{G_{1g/u},k}$
	4	$\sqrt{\frac{2}{3}}\hat{T}_2^0\overline{\Psi}_{\frac{1}{2},\frac{1}{2}}^{G_{1g/u},k} - \frac{1}{\sqrt{3}}\hat{T}_2^-\overline{\Psi}_{\frac{1}{2},-\frac{1}{2}}^{G_{1g/u},k}$
$H_{g/u}$	1	$\sqrt{\frac{8}{15}}\hat{T}_2^+\overline{\Psi}_{\frac{3}{2},\frac{1}{2}}^{H_{g/u},k} - \frac{1}{\sqrt{15}}\hat{T}_2^0\overline{\Psi}_{\frac{3}{2},-\frac{1}{2}}^{H_{g/u},k} + \sqrt{\frac{2}{5}}\hat{T}_2^-\overline{\Psi}_{\frac{3}{2},-\frac{3}{2}}^{H_{g/u},k}$
	2	$-\sqrt{\frac{2}{5}}\hat{T}_2^+\overline{\Psi}_{\frac{3}{2},-\frac{1}{2}}^{H_{g/u},k} + \sqrt{\frac{3}{5}}\hat{T}_2^0\overline{\Psi}_{\frac{3}{2},-\frac{3}{2}}^{H_{g/u},k}$
	3	$-\sqrt{\frac{3}{5}}\hat{T}_2^0\overline{\Psi}_{\frac{3}{2},\frac{3}{2}}^{H_{g/u},k} - \sqrt{\frac{2}{5}}\hat{T}_2^-\overline{\Psi}_{\frac{3}{2},\frac{1}{2}}^{H_{g/u},k}$
	4	$\sqrt{\frac{2}{5}}\hat{T}_2^+\overline{\Psi}_{\frac{3}{2},\frac{3}{2}}^{H_{g/u},k} + \frac{1}{\sqrt{15}}\hat{T}_2^0\overline{\Psi}_{\frac{3}{2},\frac{1}{2}}^{H_{g/u},k} + \sqrt{\frac{8}{15}}\hat{T}_2^-\overline{\Psi}_{\frac{3}{2},-\frac{1}{2}}^{H_{g/u},k}$
$H_{g/u}$	1	$\sqrt{\frac{3}{10}}\hat{T}_2^+\overline{\Psi}_{\frac{3}{2},\frac{1}{2}}^{H_{g/u},k} + \sqrt{\frac{3}{5}}\hat{T}_2^0\overline{\Psi}_{\frac{3}{2},-\frac{1}{2}}^{H_{g/u},k} - \frac{1}{\sqrt{10}}\hat{T}_2^-\overline{\Psi}_{\frac{3}{2},-\frac{3}{2}}^{H_{g/u},k}$
	2	$\frac{1}{\sqrt{10}}\hat{T}_2^+\overline{\Psi}_{\frac{3}{2},-\frac{1}{2}}^{H_{g/u},k} + \frac{1}{\sqrt{15}}\hat{T}_2^0\overline{\Psi}_{\frac{3}{2},-\frac{3}{2}}^{H_{g/u},k} - \sqrt{\frac{5}{6}}\hat{T}_2^-\overline{\Psi}_{\frac{3}{2},\frac{3}{2}}^{H_{g/u},k}$
	3	$-\sqrt{\frac{5}{6}}\hat{T}_2^+\overline{\Psi}_{\frac{3}{2},-\frac{3}{2}}^{H_{g/u},k} - \frac{1}{\sqrt{15}}\hat{T}_2^0\overline{\Psi}_{\frac{3}{2},\frac{3}{2}}^{H_{g/u},k} + \frac{1}{\sqrt{10}}\hat{T}_2^-\overline{\Psi}_{\frac{3}{2},\frac{1}{2}}^{H_{g/u},k}$
	4	$-\frac{1}{\sqrt{10}}\hat{T}_2^+\overline{\Psi}_{\frac{3}{2},\frac{3}{2}}^{H_{g/u},k} - \sqrt{\frac{3}{5}}\hat{T}_2^0\overline{\Psi}_{\frac{3}{2},\frac{1}{2}}^{H_{g/u},k} + \sqrt{\frac{3}{10}}\hat{T}_2^-\overline{\Psi}_{\frac{3}{2},-\frac{1}{2}}^{H_{g/u},k}$
$G_{1g/u}$	1	$\frac{1}{\sqrt{2}}\hat{T}_2^+\overline{\Psi}_{\frac{3}{2},-\frac{1}{2}}^{H_{g/u},k} + \frac{1}{\sqrt{3}}\hat{T}_2^0\overline{\Psi}_{\frac{3}{2},-\frac{3}{2}}^{H_{g/u},k} + \frac{1}{\sqrt{6}}\hat{T}_2^-\overline{\Psi}_{\frac{3}{2},\frac{3}{2}}^{H_{g/u},k}$
	2	$-\frac{1}{\sqrt{6}}\hat{T}_2^+\overline{\Psi}_{\frac{3}{2},-\frac{3}{2}}^{H_{g/u},k} + \frac{1}{\sqrt{3}}\hat{T}_2^0\overline{\Psi}_{\frac{3}{2},\frac{3}{2}}^{H_{g/u},k} - \frac{1}{\sqrt{2}}\hat{T}_2^-\overline{\Psi}_{\frac{3}{2},\frac{1}{2}}^{H_{g/u},k}$
$G_{2g/u}$	1	$-\frac{1}{\sqrt{3}}\hat{T}_2^0\overline{\Psi}_{\frac{1}{2},\frac{1}{2}}^{G_{1g/u},k} - \sqrt{\frac{2}{3}}\hat{T}_2^-\overline{\Psi}_{\frac{1}{2},-\frac{1}{2}}^{G_{1g/u},k}$
	2	$-\sqrt{\frac{2}{3}}\hat{T}_2^+\overline{\Psi}_{\frac{1}{2},\frac{1}{2}}^{G_{1g/u},k} + \frac{1}{\sqrt{3}}\hat{T}_2^0\overline{\Psi}_{\frac{1}{2},-\frac{1}{2}}^{G_{1g/u},k}$
$G_{2g/u}$	1	$\frac{1}{\sqrt{2}}\hat{T}_2^+\overline{\Psi}_{\frac{3}{2},\frac{3}{2}}^{H_{g/u},k} - \frac{1}{\sqrt{3}}\hat{T}_2^0\overline{\Psi}_{\frac{3}{2},\frac{1}{2}}^{H_{g/u},k} - \frac{1}{\sqrt{6}}\hat{T}_2^-\overline{\Psi}_{\frac{3}{2},-\frac{1}{2}}^{H_{g/u},k}$
	2	$\frac{1}{\sqrt{6}}\hat{T}_2^+\overline{\Psi}_{\frac{3}{2},\frac{1}{2}}^{H_{g/u},k} - \frac{1}{\sqrt{3}}\hat{T}_2^0\overline{\Psi}_{\frac{3}{2},-\frac{1}{2}}^{H_{g/u},k} - \frac{1}{\sqrt{2}}\hat{T}_2^-\overline{\Psi}_{\frac{3}{2},-\frac{3}{2}}^{H_{g/u},k}$

Table 2.16: The A_2 one-link baryon operators.

irrep	row	$C\begin{pmatrix} \Lambda & A_2 & \Lambda_2 \\ \lambda & 1 & \lambda_2 \end{pmatrix} \hat{A}^{(3)}\overline{\Psi}_{\lambda_2}^{\Lambda_2,k}$
$H_{g/u}$	1	$\hat{A}_2\overline{\Psi}_{\frac{3}{2},-\frac{1}{2}}^{H_{u/g},k}$
	2	$-\hat{A}_2\overline{\Psi}_{\frac{3}{2},-\frac{3}{2}}^{H_{u/g},k}$
	3	$-\hat{A}_2\overline{\Psi}_{\frac{3}{2},\frac{3}{2}}^{H_{u/g},k}$
	4	$\hat{A}_2\overline{\Psi}_{\frac{3}{2},\frac{1}{2}}^{H_{u/g},k}$
$G_{2g/u}$	1	$\hat{A}_2\overline{\Psi}_{\frac{1}{2},\frac{1}{2}}^{G_{1u/g},k}$
	2	$\hat{A}_2\overline{\Psi}_{\frac{1}{2},-\frac{1}{2}}^{G_{1u/g},k}$

that involve n-site displacements in space allowing a quark to be displaced over a finer angular distribution so as to yield higher rank spherical harmonics. The reduction procedure is essentially the same as for the two-link case, except that multiple direct products of spatial irreps are used.

2.4.5 One-link displacements applied to two different quarks

Consider an operator with one-link displacements applied to two different quarks in the following way,

$$\mathcal{D}_{\lambda_2}^{(1\pm2)\Lambda_2}\mathcal{D}_{\lambda_1}^{(3)\Lambda_1}\overline{b}_{\mu_1\mu_2\mu_3}^{f_1f_2f_3} \equiv \frac{\epsilon_{abc}}{\sqrt{2}}\left[\left(\mathcal{D}_{\lambda_2}^{\Lambda_2}\overline{q}_{\mu_1}^{f_1}\right)^a \overline{q}_{\mu_2}^{bf_2} \pm \overline{q}_{\mu_1}^{af_1}\left(\mathcal{D}_{\lambda_2}^{\Lambda_2}\overline{q}_{\mu_2}^{f_2}\right)^b\right]\left(\mathcal{D}_{\lambda_1}^{\Lambda_1}\overline{q}_{\mu_3}^{f_3}\right)^c, \qquad (2.60)$$

where $\mathcal{D}_{\lambda}^{(1\pm2)\Lambda}$ indicates that the first two quark fields are symmetric or antisymmetric with respect to exchange of their spatial dependencies,

$$\mathcal{D}_{\lambda}^{(1\pm2)\Lambda} = \frac{1}{\sqrt{2}}\left(\mathcal{D}_{\lambda}^{(1)\Lambda} \pm \mathcal{D}_{\lambda}^{(2)\Lambda}\right). \qquad (2.61)$$

We refer to $\mathcal{D}_{\lambda}^{(1+2)\Lambda}$ as *space-symmetric* and to $\mathcal{D}_{\lambda}^{(1-2)\Lambda}$ as *space-antisymmetric* combinations of displacements. The symmetry of the spatial displacements must be taken into account in the overall antisymmetry of operators in order to identify the symmetry of Dirac indices that produces nonvanishing operators.

For the case of MA isospin nucleon operators with one-link displacements applied to two

quarks, we obtain

$$
\begin{aligned}
\mathcal{D}_{\lambda_2}^{(1\pm2)\Lambda_2}\mathcal{D}_{\lambda_1}^{(3)\Lambda_1}\overline{N}_{\mu_1\mu_2\mu_3}^{(MA)} &= \epsilon_{abc}\frac{1}{2}\left(\mathcal{D}_{\lambda_2}^{\Lambda_2}\overline{u}_{\mu_1}^a\overline{d}_{\mu_2}^b - \mathcal{D}_{\lambda_2}^{\Lambda_2}\overline{d}_{\mu_1}^a\overline{u}_{\mu_2}^b\right)\left(\mathcal{D}_{\lambda_1}^{\Lambda_1}\overline{u}_{\mu_3}\right)^c \\
&\pm \epsilon_{abc}\frac{1}{2}\left(\overline{u}_{\mu_1}^a\mathcal{D}_{\lambda_2}^{\Lambda_2}\overline{d}_{\mu_2}^b - \overline{d}_{\mu_1}^a\mathcal{D}_{\lambda_2}^{\Lambda_2}\overline{u}_{\mu_2}^b\right)\left(\mathcal{D}_{\lambda_1}^{\Lambda_1}\overline{u}_{\mu_3}\right)^c, \quad (2.62)
\end{aligned}
$$

and the following relation between spatial symmetry of displacements and the symmetry of Dirac indices holds

$$
\begin{aligned}
\mathcal{D}_{\lambda_2}^{(1+2)\Lambda_2}\mathcal{D}_{\lambda_1}^{(3)\Lambda_1}\overline{N}_{\mu_1\mu_2\mu_3}^{(MA)} &\rightarrow \quad \text{A, MA Dirac indices} \\
\mathcal{D}_{\lambda_2}^{(1-2)\Lambda_2}\mathcal{D}_{\lambda_1}^{(3)\Lambda_1}\overline{N}_{\mu_1\mu_2\mu_3}^{(MA)} &\rightarrow \quad \text{S, MS Dirac indices.} \quad (2.63)
\end{aligned}
$$

Because of symmetry, the operators of Eq. (2.62) with MA Dirac indices and those with MS Dirac indices are identical.

Group theoretically, rotations of operators with one-link displacements applied to two different quarks are the same as those of two-link operators. Therefore the reduction to irreps is exactly the same as for the two-link case. First use the Clebsch-Gordan coefficients to obtain an irrep for the product of two displacements, and second use the Clebsch-Gordan coefficients for the direct product of spatial and spinorial irreps to obtain operators corresponding to overall irreps. The only additional step is to determine the allowed symmetries of Dirac indices such that the operator is antisymmetric under simultaneous exchange of displacements, flavors, colors, and Dirac indices.

2.5   Summary

The constructions given in this chapter provide a variety of quasi-local and nonlocal three-quark operators for use as zero-momentum baryon interpolating field operators in lattice QCD simulations. All operators are categorized into irreps of the double octahedral group O_h^D, they have definite parities and they are gauge covariant. By use of the Clebsch-Gordan coefficients of the octahedral group, it is straightforward to construct many more operators than have been discussed here.

Complete sets of quasi-local operators are presented in Section 2.3 for each baryon. These quasi-local constructions provide templates for the Dirac indices that should be used to construct

nonlocal operators. Nonlocal operators have been developed in Section 2.4 based on adding combinations of one-link displacements to one or more quarks. By use of the building blocks given in this paper, a variety of additional operators can be constructed by 1) using the Clebsch-Gordan series to form overall irreps of the spatial distribution, and 2) combining the spatial irreps with irreps of Dirac indices to form operators corresponding to overall irreps. Identification of the correct symmetry of Dirac indices is straightforward when space-symmetric or space-antisymmetric combinations of displacements are used.

Reference [38] has demonstrated numerically that our quasi-local and one-link operators are orthogonal in the sense of Eq. (2.14), i.e., a correlation function vanishes if sink and source operators belong to different irreps and rows. For calculations of baryon masses, one should select source operators within a fixed irrep and row from the various tables. Using operators from different embeddings of the irrep and row, matrices of correlation functions may be calculated and mass spectra extracted. Correlation matrices can be made hermitian by including a γ_4 matrix for each quark of the source. Operators from our tables have the form $\overline{B}_\lambda^{\Lambda,k} = c_{\mu_1\mu_2\mu_3}^{(\Lambda,\lambda,k)} \overline{B}_{\mu_1\mu_2\mu_3}$, where $\overline{B}_{\mu_1\mu_2\mu_3}$ is an elemental baryon operator and a summation over repeated indices is understood. A hermitian correlation matrix can be calculated in following way.

$$
\begin{aligned}
C_{kk'}^{\prime(\Lambda)}(t) &= \sum_x \langle 0| T B_\lambda^{\Lambda,k}(\mathbf{x},t) \overline{B}_\lambda^{\Lambda,k'}(0) |0\rangle \Gamma_4 \\
&= \sum_x c_{\mu_1\mu_2\mu_3}^{(\Lambda,\lambda,k)*} c_{\mu_1'\mu_2'\mu_3'}^{(\Lambda,\lambda,k')} \langle 0| T B_{\mu_1\mu_2\mu_3}(\mathbf{x},t) \overline{B}_{\nu_1\nu_2\nu_3}(0) |0\rangle \times \gamma_{4\nu_1\mu_1'} \gamma_{4\nu_2\mu_2'} \gamma_{4\nu_3\mu_3'}. (2.64)
\end{aligned}
$$

Exploratory calculations for baryon spectra along this line have been reported in Ref. [37]. The dimension of the matrix of correlation functions depends on the types of spatial distributions used (one-link, two-link, *etc.*), baryonic isospin, and overall irrep. For nucleon operators with quasi-local and one-link displacements, 23 G_{1g} operators, 28 H_g operators, and 7 G_{2g} operators are available. The numbers of operators in each irrep and row can be extended without limit by using two-link and three-link operators and using different choices of smearing.

Searches for the Roper resonance by lattice simulation using three valence quarks have been pursued by different approaches [62–64]. Smeared sources with and without some power of one-link, A_1 operator discussed in Section 2.4.3 may help to give distinct mass eigenstates using

the variational method based on matrices of correlation functions. To have more extended radial structure, one can use a modified A_1 operator constructed from straight links over two or more lattice sites. The irreps are the same as for A_1 discussed in Section 2.4.3.

Chapter 3

Computational Techniques and Lattice Setup for the Simulations

3.1 Overview

Methods to extract masses from a large set of baryon interpolating operators, such as those constructed in Chapter 2, are detailed in this chapter. Construction of a correlation matrix and the variational method are discussed in Section 3.2. We discuss the definition of the effective mass, the backward propagation of baryon correlation functions, and the generalized eigenvalue problem applied to correlation matrices. The orthogonality relations of the correlation matrix are explicitly proved in the non-interacting theory in Section 3.3. Anisotropic lattice actions that are used in our simulations are discussed in Section 3.4, where also tuning of the anisotropy is described. The linear relation between the pion mass squared and bare quark mass is numerically demonstrated. Quark field smearing and gauge-link smearing are performed in our simulations. Tuning of the smearing parameters is detailed and comparisons with unsmeared operators are demonstrated in Section 3.5. Lastly, all parameters that we used in our simulations are summarized in Section 3.6.

3.2 Correlation matrix and variational method

Lattice QCD calculations of baryon masses are based on the analysis of two-point correlation functions, defined by

$$C_{\vec{\mu}\vec{\nu}}(t, t_i) = \sum_{x-x_0} \langle 0| B_{\vec{\mu}}(\mathbf{x}, t)\overline{B}_{\vec{\nu}}(\mathbf{x_0}, t_i) |0\rangle, \tag{3.1}$$

where $B_{\vec{\mu}}$ is color-singlet baryon interpolating field, with subscript $\vec{\mu}$ denoting the Dirac indices of three constituent quarks, i.e., $\vec{\mu} = (\mu_1, \mu_2, \mu_3)$. The space-time point $(\mathbf{x_0}, t_i)$ of the source operator

is usually fixed to $(0, 0)$. Summation over $\mathbf{x}$ projects intermediate states to zero total momentum. In Hilbert space the correlation function can be expanded by mass eigenstates $|n\rangle$ and their charge conjugate states $|\overline{n}\rangle$

$$
\begin{aligned}
C_{\vec{\mu}\vec{\nu}}(t) \;=\;\; & \theta(t) \sum_n \langle 0| \, B_{\vec{\mu}} \, |n\rangle \, \langle n| \, \overline{B}_{\vec{\nu}} \, |0\rangle \, e^{-M_n t} \\
& -\; \theta(-t) \sum_{\overline{n}} \langle 0| \, \overline{B}_{\vec{\nu}} \, |\overline{n}\rangle \, \langle \overline{n}| \, B_{\vec{\mu}} \, |0\rangle \, e^{M_{\overline{n}} t}
\end{aligned}
\tag{3.2}
$$

where M_n denotes the mass corresponding to state $|n\rangle$ and $M_{\overline{n}}$ denotes that of state $|\overline{n}\rangle$. For periodic temporal boundary conditions, $\theta(-t) \to +\theta(T-t)$, and for anti-periodic boundary conditions, $\theta(-t) \to -\theta(T-t)$, then in the interval $0 \le t < T$,

$$
\begin{aligned}
C_{\vec{\mu}\vec{\nu}}(t) \;=\;\; & \sum_n \langle 0| \, B_{\vec{\mu}} \, |n\rangle \, \langle n| \, \overline{B}_{\vec{\nu}} \, |0\rangle \, e^{-M_n t} \\
& \mp\; \sum_{\overline{n}} \langle 0| \, \overline{B}_{\vec{\nu}} \, |\overline{n}\rangle \, \langle \overline{n}| \, B_{\vec{\mu}} \, |0\rangle \, e^{-M_{\overline{n}}(T-t)}.
\end{aligned}
\tag{3.3}
$$

The second term is the contribution from the anti-baryon propagating backward in time.

The charge conjugation operator $\mathcal{C}$ may be defined such that a quark and an antiquark transform in the following fashion,

$$
\begin{aligned}
\mathcal{C} q_\mu(x) \mathcal{C}^\dagger &= \overline{q}_\nu(x) C^\dagger_{\nu\mu}, \\
\mathcal{C} \overline{q}_\mu(x) \mathcal{C}^\dagger &= -C_{\mu\nu} q_\nu(x),
\end{aligned}
\tag{3.4}
$$

with

$$
C^\dagger C = 1, \quad C^\dagger \gamma_\mu^T C = -\gamma_\mu.
\tag{3.5}
$$

In Dirac-Pauli representation of Dirac γ matrices, $C = \gamma_4 \gamma_2$ is a suitable choice. The charge conjugation operator is written in terms of a product of ρ-spin matrix and s-spin matrix as follows,

$$
C = \gamma_4 \gamma_2 = (\rho_3 \otimes \sigma_4)(\rho_2 \otimes \sigma_2) = (\rho_3 \rho_2) \otimes (\sigma_4 \sigma_2) = (-i\rho_1) \otimes \sigma_2 = \rho_1 \otimes (-i\sigma_2).
\tag{3.6}
$$

Quark and antiquark fields with ρ-spin ρ and s-spin σ transform under the charge conjugation as

$$
\mathcal{C} q_s^\rho \mathcal{C}^\dagger = \overline{q}_{s'}^{\rho'} \left[\begin{pmatrix} 0 & 1 \\ 1 & 0 \end{pmatrix}_{\rho'\rho} \otimes \begin{pmatrix} 0 & 1 \\ -1 & 0 \end{pmatrix}_{\sigma'\sigma} \right] = -\sigma \overline{q}_{-\sigma}^{-\rho},
$$

$$\mathcal{C}\overline{q}_\sigma^\rho\mathcal{C}^\dagger = -\left[\begin{pmatrix} 0 & 1 \\ 1 & 0 \end{pmatrix}_{\rho\rho'} \otimes \begin{pmatrix} 0 & -1 \\ 1 & 0 \end{pmatrix}_{\sigma\sigma'}\right] q_{\sigma'}^{\rho'} = \sigma q_{-\sigma}^{-\rho}. \tag{3.7}$$

Let the baryon's Dirac labels $\vec{\mu}$ be denoted in terms of ρ-spin labels $\vec{\rho} = (\rho_1, \rho_2, \rho_3)$ and s-spin labels $\vec{\sigma} = (\sigma_1, \sigma_2, \sigma_3)$. Then, the field that annihilates an anti-baryon state transforms under charge conjugation as

$$\langle 0| \overline{B}_{\vec{\nu}} |\overline{n}\rangle = \langle 0| \overline{B}_{\vec{\sigma}'}^{\vec{\rho}'} |\overline{n}\rangle = \langle 0| \mathcal{C}^\dagger \mathcal{C} B_{\vec{\sigma}'}^{\vec{\rho}'} \mathcal{C}^\dagger \mathcal{C} |\overline{n}\rangle = \eta' \langle 0| B_{-\vec{\sigma}'}^{-\vec{\rho}'} \mathcal{C} |\overline{n}\rangle, \tag{3.8}$$

where $\eta' = -\sigma_1'\sigma_2'\sigma_3'$. Since $\mathcal{C}|\overline{n}\rangle = \phi|n\rangle$, in which ϕ is a phase factor, one obtains

$$\langle 0| \overline{B}_{\vec{\nu}} |\overline{n}\rangle = \phi\eta' \langle 0| B_{-\vec{\sigma}'}^{-\vec{\rho}'} |n\rangle. \tag{3.9}$$

Similarly,

$$\langle \overline{n}| B_{\vec{\mu}} |0\rangle = \langle \overline{n}| \mathcal{C}^\dagger \mathcal{C} \overline{B}_{-\vec{\sigma}}^{-\vec{\rho}} \mathcal{C}\mathcal{C}^\dagger |0\rangle = \eta \langle \overline{n}| \mathcal{C}^\dagger \overline{B}_{-\vec{\sigma}}^{-\vec{\rho}} |0\rangle = \phi^* \eta \langle n| \overline{B}_{-\vec{\sigma}}^{-\vec{\rho}} |0\rangle. \tag{3.10}$$

where $\eta = \sigma_1\sigma_2\sigma_3$. Finally, the correlation function in Eq. (3.3) is written as

$$\begin{aligned} C_{\vec{\mu}\vec{\nu}}(t) &= \sum_n \langle 0| B_{\vec{\sigma}}^{\vec{\rho}} |n\rangle \langle n| \overline{B}_{\vec{\sigma}'}^{\vec{\rho}'} |0\rangle e^{-M_n t} \\ &\mp \eta\eta' \sum_{\overline{n}} \langle 0| B_{-\vec{\sigma}'}^{-\vec{\rho}} |n\rangle \langle n| \overline{B}_{-\vec{\sigma}}^{-\vec{\rho}} |0\rangle e^{-M_n(T-t)}, \end{aligned} \tag{3.11}$$

where $\eta\eta' = -(\sigma_1\sigma_2\sigma_3)(\sigma_1'\sigma_2'\sigma_3')$. Because of the exponential factor in Eq. (3.11) in the region $t \gtrsim 0$ signals from the first term dominate, while in the region $t \lesssim T$ signals from the second term dominate. If $\overline{B}_{\vec{\sigma}}^{\vec{\rho}}$ creates a parity P state, then $\overline{B}_{-\vec{\sigma}}^{-\vec{\rho}}$ creates a parity $-P$ state. Therefore, the second term propagating backward in time corresponds to states with opposite parity to those contributing to the first term propagating forward in time.

The effective mass for the ground state from the forward propagating piece is defined as,

$$M_{eff} = -\ln\left[\frac{C(t+1, t_i)}{C(t, t_i)}\right]. \tag{3.12}$$

The time t must be sufficiently later than the source point so that exponential factors from excited states $e^{-M_n t}, n = 1, 2, \cdots$ in Eq. (3.3) are much smaller than those from the ground state $e^{-M_0 t}$ so that $M_{eff} \simeq M_0$ is realized. But at the same time, t must be smaller than half of the temporal

64

extent, $T/2$, so that backward propagating signals are weak. In lattice QCD a correlation function is calculated for each gauge-configuration. Physical observables are then obtained as averages over a large number of uncorrelated gauge configurations using the jackknife method to reduce the bias of statistical samples. The details of the jackknife method are provided in Appendix F.

Because of the zero momentum projection, baryon fields are translationaly invariant; thus they obey the point rotational group of the cubic lattice, as discussed in Chapter 3. When the sink and source operators belong to different irreps or rows, the correlation function vanishes within statistical errors as in Eq. (2.14). A sets of operators with the same irrep and row labels can be used to form a matrix of correlation functions, i.e.,

$$C_{ij}^{(\Lambda)}(t) = \sum_x \langle 0| B_i^{\Lambda,\lambda}(\mathbf{x},t)\overline{B}_j^{\Lambda,\lambda}(0,0) |0\rangle, \tag{3.13}$$

where the indices i,j run through all embeddings of available operators for irrep Λ and row λ. In order to extract a mass spectrum the matrix of correlation functions is analyzed by the variational method. Eigenvalues $\alpha^{(n)}(t,t_0)$ are required for the following generalized eigenvalue equation,

$$\sum_j C_{ij}^{(\Lambda)}(t)v_j^{(n)}(t,t_0) = \alpha^{(n)}(t,t_0)\sum_j C_{ij}^{(\Lambda)}(t_0)v_j^{(n)}(t,t_0), \tag{3.14}$$

where n specifies the label for mass eigenstates, such as ground state, first excited state, and so forth. The reference time t_0 is fixed and usually taken close to $t = 0$. Lüscher and Wolff explicitly showed that the eigenvalue $\alpha^{(n)}(t,t_0)$ is given by

$$\alpha^{(n)}(t,t_0) = e^{-M_n(t-t_0)}, \tag{3.15}$$

in their study of the spectrum of a two-particle system on the lattice [43]. Equation (3.15) holds *exactly* under the assumption that a correlation function constructed from r linearly independent fields $\mathcal{O}_i$, $i = 1,\cdots,r$ is written as a linear combination of a finite number of exponential-falloffs, i.e.,

$$C_{ij}(t) = \sum_{k=1}^r Z_i^{k*} Z_j^k e^{-M_k t}, \tag{3.16}$$

which, in fact, is a good approximation to the forward-propagating part of the correlation functions.

The reference time t_0 in Eq. (3.14) is taken near the source time so that eigenvalues are sensitive to the signals of excited states. Another reason is that the signal-to-noise ratio of cor-

relation functions becomes worse as time increases, therefore the inversion of the matrix becomes unstable at large reference time t_0 due to the statistical noise. Finally, the effective masses M_n for n-th excited states are extracted from the generalized eigenvalues given by

$$M_n = -\ln\left[\frac{\alpha^{(n)}(t+1,t_0)}{\alpha^{(n)}(t,t_0)}\right]. \tag{3.17}$$

To obtain the solution to the generalized eigenvalue equation, we perform following numerical procedure.

(1) Redefine the sources with k-th embedding of irrep Λ and row λ,

and modify the correlation matrix:

$$\overline{B}_\lambda^{\Lambda,k} = c_{\mu_1\mu_2\mu_3}^{(\Lambda,\lambda,k)}\overline{B}_{\mu_1\mu_2\mu_3} \longrightarrow$$

$$\overline{B}_\lambda^{\prime\Lambda,k} = c_{\mu_1\mu_2\mu_3}^{(\Lambda,\lambda,k)}\overline{B}_{\mu_1'\mu_2'\mu_3'}(\gamma_4)_{\mu_1'\mu_1}(\gamma_4)_{\mu_2'\mu_2}(\gamma_4)_{\mu_3'\mu_3};$$

$$C_{kk'}^{\prime(\Lambda)}(t) = \sum_x \langle 0|\, B_\lambda^{\Lambda,k}(\mathbf{x},t)\overline{B}_\lambda^{\prime\Lambda,k'}(0,0)\,|0\rangle\,,$$

(2) Symmetrize the matrix: $\quad C_{kk'}^{\prime\prime(\Lambda)}(t) = \frac{1}{2}\left[C_{kk'}^{\prime(\Lambda)}(t) + C_{k'k}^{\prime(\Lambda)*}(t)\right],$

(3) Cholesky-decompose the matrix: $\quad A^T A = C^{\prime\prime(\Lambda)}(t_0),$

(4) Define the transfer matrix: $\quad T(t,t_0) = (A^T)^{-1}C^{\prime\prime(\Lambda)}(t)A^{-1},$

(5) Solve the eigenvalue problem for the transfer matrix:

$$T(t,t_0)_{ij}v_j^{(n)}(t,t_0) = \alpha^{(n)}(t,t_0)v_i^{(n)}(t,t_0).$$

With the new definition in step (1), the correlation matrix $C_{ij}^{\prime\Lambda,\lambda}(t)$ becomes a real and symmetric matrix when constant background gauge fields are used, as will be explained shortly. Given this definition, the transfer matrix $T(t,t_0)_{ij}$ is also real and symmetric as a gauge average, thus its left and right eigenvalues/eigenvectors are the same. Note that the procedure given above is not a unique choice to obtain the solution of the generalized eigenvalue problem given in Eq. (3.14).

This method of extracting masses from baryon correlation functions is called the variational method. Another method is the Maximum Entropy Method (MEM) based on Bayesian statistics. MEM involves fitting the correlation function with many exponentials so as to give spectral densities. This method gives an alternative way to measure signals from excited states [65–67, 69, 70]. The Singular Value Decomposition of correlation matrices is shown to be identical under certain conditions to the diagonalization method discussed here [71].

3.3 Constant gauge-fields and orthogonality relation

In the noninteracting theory [72], a fermion propagator on the Euclidean lattice of size $L^3 \times L_4$ is of the form,

$$S(x - x_0) \quad = \quad \frac{1}{L^3} \frac{1}{L_4} \sum_{\vec{k}} \sum_{k_4} e^{ik \cdot (x - x_0)} S(k), \tag{3.18}$$

$$S(k) \quad = \quad R(k) \left[-i\gamma_4 \sin k_4 + r(1 - \cos k_4) + r \sum_j (1 - \cos k_j) + m - i\gamma_j \sin k_j \right], \tag{3.19}$$

where the factor $R(k)$ is an even function of k as

$$R(k)^{-1} = \sin^2 k_4 + (\gamma_j k_j)^2 + \left[r(1 - \cos k_4) + r \sum_j (1 - \cos k_j) + m \right]^2. \tag{3.20}$$

Discrete momenta on the lattice are given by $k_\mu = \frac{2\pi n_\mu}{L_\mu}$, $n_\mu = 0, 1, ..., (L_\mu - 1)$ with periodic boundary conditions. To simplify the following arguments, we adopt the Dirac-Pauli representation of Dirac γ matrices, where γ_4 matrix is diagonal. Let $D(k)$ denote all terms in the nominator of $S(k)$ that are diagonal matrices,

$$D(k) \equiv -i\gamma_4 \sin k_4 + r(1 - \cos k_4) + r \sum_j (1 - \cos k_j) + m. \tag{3.21}$$

Define a three-quark propagator as,

$$C_{AB}(t) \equiv \sum_{\vec{x}} c^A_{\alpha_1 \alpha_2 \alpha_3} c^{*B}_{\beta_1 \beta_2 \beta_3} S^1_{\alpha_1 \beta_1}(x - x_0) S^2_{\alpha_2 \beta_2}(x - x_0) S^3_{\alpha_3 \beta_3}(x - x_0). \tag{3.22}$$

Indices A and B are the sink and source labels. This is a correlation function of three point fermions in a non-interacting background. Allowing the operator labels to vary, $C_{AB}(t)$ becomes a matrix of correlation functions. It is often useful to label the states using two component ρ-spin and two-component spin, instead of the four-component Dirac index. We defined the ρ-parity as an eigenvalue of γ_4 matrix in Eq. (2.7). Then ρ-parity takes the values $\rho = \pm$ for positive/negative-parity projected states, or simply for upper-two/lower-two components of a Dirac spinor in the Dirac-Pauli representation. Parity-projected spinors transform amongst themselves without changing their parity under rotations. Rotations are the transformations of two-component

spins, which can be labeled by eigenstates of

$$S_z = \begin{pmatrix} \sigma_3 & 0 \\ 0 & \sigma_3 \end{pmatrix} \tag{3.23}$$

in Dirac-Pauli representation. We refer to the eigenvalues as s-spin. Note that overall parity of the operator is given by the product of ρ-parity from each fermion, i.e., $P = \rho_1 \rho_2 \rho_3$ assuming that spatial distribution is even under spatial inversion. The overall spin component along z-axis is given by the sum of three s-spins, i.e., $S_z = \frac{1}{2}(s_1 + s_2 + s_3)$.

It is intriguing to show that correlation function is indeed orthogonal when source and sink have different parities in the non-interacting theory. Let $B^{g/u}_{\mu_1 \mu_2 \mu_3}(x)$ be the positive/negative-parity baryon operator formed from three quarks with (fixed) Dirac indices μ_1, μ_2, and μ_3. The correlation function for positive-parity sink and negative-parity source operators is

$$\sum_{\vec{x}} \langle 0| B^u_{\mu_1 \mu_2 \mu_3}(x) \overline{B}^g_{\nu_1 \nu_2 \nu_3}(0) |0\rangle = \sum_{\vec{x}} \langle 0| \mathcal{P}^{-1} \mathcal{P} B^u_{\mu_1 \mu_2 \mu_3}(x) \mathcal{P}^{-1} \mathcal{P} \overline{B}^g_{\nu_1 \nu_2 \nu_3}(0) \mathcal{P}^{-1} \mathcal{P} |0\rangle, \tag{3.24}$$

where $\mathcal{P}$ is a parity operator. The parity transformation of a baryon field is given by

$$\begin{aligned} \mathcal{P} B_{\mu_1 \mu_2 \mu_3}(\vec{x}, t) \mathcal{P}^{-1} &= (\gamma_4)_{\mu_1 \mu_1'} (\gamma_4)_{\mu_2 \mu_2'} (\gamma_4)_{\mu_3 \mu_3'} B_{\mu_1' \mu_2' \mu_3'}(-\vec{x}, t) \\ &= \rho_1 \rho_2 \rho_3 B_{\mu_1 \mu_2 \mu_3}(-\vec{x}, t). \end{aligned} \tag{3.25}$$

For positive parity, the product of three ρ-spins is $+1$ and for negative parity, it is -1. The fact that the vacuum is invariant under the parity transformation simplifies Eq. (3.24) to

$$\sum_{\vec{x}} \langle 0| (-1) B^u_{\mu_1 \mu_2 \mu_3}(x) \overline{B}^g_{\nu_1 \nu_2 \nu_3}(0) |0\rangle. \tag{3.26}$$

Since the correlation function is equal to minus times itself, the correlation function vanishes.

One can show that operators of different S_z do not mix by working explicitly through the integrations. The correlation function is written in explicit form in terms of non-interacting fermion

propagators using Eqs. (3.19)-(3.22) as

$$
\begin{aligned}
C_{AB}(t) \;=\; & \sum_{\vec{x}} \sum_{\vec{k}^1,\vec{k}^2,\vec{k}^3} \sum_{k_4^1,k_4^2,k_4^3} c^A_{\mu_1\mu_2\mu_3} c^{*B}_{\nu_1\nu_2\nu_3} R(k^1)R(k^2)R(k^3) e^{i(k_4^1+k_4^2+k_4^3)(t-t_0)} e^{i(\vec{k}^1+\vec{k}^2+\vec{k}^3)(\vec{x}-\vec{x}_0)} \\
& \times \left[D_{\mu_1\nu_1}(k^1) + \begin{pmatrix} 0 & & -k_z^1 & -k_-^1 \\ & & -k_+^1 & k_z^1 \\ k_z^1 & k_-^1 & 0 & \\ k_+^1 & -k_z^1 & & \end{pmatrix}_{\mu_1\nu_1} \right] \times \left[k^1 \leftrightarrow k^2\right] \times \left[k^1 \leftrightarrow k^3\right] \ (3.27)
\end{aligned}
$$

where the $-i\gamma_j \sin k_j$ part in each propagator is replaced by $-i\gamma_j k_j$ for simplicity, because that does not affect the argument here. A positive parity operator has a ρ-spin configuration of either $\rho = (+++)$ or $\rho = (+--)$. The first configuration is that three quarks have all upper components, and the second is that one out of three has upper components and the other two have lower components. They will form a non-vanishing correlator if the sink and source have the same S_z. An example is instructive; let sink and source operators have $\vec{\mu} = (1,1,1)$ and $\vec{\nu} = (1,3,3)$ in Dirac-Pauli representation. They should admix because both have the same parity and the same S_z. The correlator involves an integration from Eq (3.27),

$$
\sum_z \sum_{k_3's} (-k_z^2)(-k_z^3) e^{i(k_z^1+k_z^2+k_z^3)z}, \tag{3.28}
$$

which is nonzero and real. If the S_z were different such as $\vec{\mu} = (1,1,1)$ and $\vec{\nu} = (1,3,4)$, the correlator vanishes because it has an integral,

$$
\sum_{x,y,z} \sum_{\vec{k}'s} \left[(-k_z^2)(-k_x^3 + ik_y^3)\right] e^{i(k_x^1+k_x^2+k_x^3)x} e^{i(k_y^1+k_y^2+k_y^3)y} e^{i(k_z^1+k_z^2+k_z^3)z}, \tag{3.29}
$$

which involves an odd function of momenta in the square bracket. Any pair of operators with different S_z vanishes because of this.

One can also easily show that positive parity and negative parity do not mix by taking the integrals explicitly. An example may be $\vec{\mu} = (1,1,1)$ and $\vec{\nu} = (1,1,3)$. They have the same S_z but opposite parities. The correlation function is zero because it involves an integration,

$$
\sum_z \sum_{k_z's} (-k_z^3) e^{i(k_z^1+k_z^2+k_z^3)z}, \tag{3.30}
$$

which is vanishing. Any pair of operators with opposite parities vanishes because the integration of an odd function in momentum is involved.

Because of these orthogonalities, the correlation matrix has a block-diagonal form, where sink and source operators in a block have the same parity and the same S_z. Nonvanishing correlation functions involve integrations of even functions of momenta, which gives a real result; therefore, the correlation matrix can be made real when the coefficients of the operators $c^A_{\alpha_1 \alpha_2 \alpha_3}$ are real, as is the case in our quasi-local construction.

Insertion of γ_4 in each source index will not change the orthogonalities. Define a modified correlator matrix, $C'_{AB}(t)$ as

$$C'_{AB}(t) \equiv \sum_{\vec{x}} c^A_{\mu_1 \mu_2 \mu_3} c^B_{\nu_1 \nu_2 \nu_3} \langle 0 | B^A_{\mu_1 \mu_2 \mu_3}(x) \overline{B}^B_{\nu'_1 \nu'_2 \nu'_3}(0) | 0 \rangle (\gamma_4)_{\nu'_1 \nu_1} (\gamma_4)_{\nu'_2 \nu_2} (\gamma_4)_{\nu'_3 \nu_3}. \tag{3.31}$$

This definition leaves the block with positive-parity sources in the three-quark propagator invariant, but changes the sign of all elements in the block with negative-parity sources. It makes the three-quark propagator in Eq. (3.27) hermitian.

3.4 Anisotropic lattices

One of the technical difficulties in extraction of excited baryon masses from lattice QCD simulations is that the signal-to-noise ratio quickly degrades in time due to their heavy masses, such that the effective masses do not stay on a plateaux for many time-slices. Two ways to overcome this problem are 1) to use more gauge-configurations to increase the statistical ensemble, or 2) use anisotropic lattices. Use of more gauge-configurations certainly makes the noise smaller, but calculation of a large number of configurations is demanding. Anisotropic lattices are designed so that the temporal lattice spacing a_t is smaller than the spatial lattice spacing a_s. By having a finer lattice spacing along time direction, one can pick more time-slices to analyze the behavior at small time separation. Since only the number of temporal lattice sites is increased, the cost is relatively low. However, anisotropic lattices require tuning of coefficients, which we will explain shortly.

Having small temporal lattice spacing is also important for measuring heavy particles so as to have a sensitive probe of high frequency modes. Anisotropic lattices have been applied to

simulations such as glueballs, hybrids, finite temperature transition, *etc.* [41, 73, 82]. Many groups have developed improved anisotropic actions for lattice simulations. The improved anisotropic quark action, so-called D234 action, is studied in Ref. [74], where the Symanzik improvement program of classical action is applied. A tadpole-improved quark action that contains a next nearest neighbor interaction term to the Wilson quark action is proposed and tested in Ref. [75–78]. A fermion action that is suitable for highly anisotropic lattice, i.e., $\xi \gg 1$ is developed in Ref. [79].

The anisotropic (unimproved) Wilson action is

$$S^\xi = S_G^\xi + S_F^\xi, \tag{3.32}$$

where S_G^ξ is the gauge action and S_F^ξ is the fermion action. The anisotropy $\xi = a_s/a_t > 1$ is a renormalized value to be determined nonperturbatively.

3.4.1 Anisotropic Wilson gauge action

The anisotropic Wilson gauge action is [73, 80–82]

$$S_G^\xi = \frac{\beta}{N_c} \left[\frac{1}{\xi_0} \sum_{x, s > s'} \mathrm{ReTr}\left(1 - P_{ss'}(x)\right) + \xi_0 \sum_{x, s} \mathrm{ReTr}\left(1 - P_{st}(x)\right) \right]. \tag{3.33}$$

Note that $\xi_0 = 1$ leads to the original Wilson plaquette action. Usually, the renormalized anisotropy ξ is held fixed, say at an integer value, and the bare anisotropy appearing in the action, ξ_0, is tuned for a given β. In order to determine the renormalized anisotropy, static potentials of a quark-antiquark pair are measured. The static (sideways) potential is calculated by taking the ratio of Wilson loops,

$$
\begin{aligned}
R_{ss}(x, y) &= \frac{W_{ss}(x, y)}{W_{ss}(x+1, y)} \longrightarrow e^{-a_s V_s(y a_s)}, \\
R_{st}(x, t) &= \frac{W_{st}(x, t)}{W_{st}(x+1, t)} \longrightarrow e^{-a_s V_s(t a_t)}, \qquad \text{for large } x.
\end{aligned} \tag{3.34}
$$

The spatial Wilson loop is denoted as $W_{ss}(x, y)$ and the temporal Wilson loop is denoted as $W_{st}(x, t)$. The sizes of the loop are $x \times y$ and $x \times t$, respectively, where x and y are in units of a_s and t is in units of a_t. Then two ratios in Eq. (3.34) become equal, when $t = \xi y$.

3.4.2 Anisotropic Wilson fermion action

For the fermion action, the spatial part and the temporal part have to be treated differently also. The reason for this is to have a correct relativistic dispersion relation between energy and momentum. We introduce a new parameter that distinguishes terms between spatial and temporal directions. The anisotropic Wilson fermion action has a form,

$$S_F^\xi = a_t a_s^3 \sum_x \overline{q}(x) \left[m_0 - \nu_t \left(\gamma_4 \nabla_t - \frac{a_t}{2} \Delta_t \right) + \nu_s \sum_s \left(\gamma_s \nabla_s - \frac{a_s}{2} \Delta_s \right) \right] q(x), \tag{3.35}$$

where

$$\nabla_\mu q(x) = \frac{1}{2a_\mu} \left[U_\mu(x) q(x + \hat{\mu}) - U_\mu^\dagger(x - \hat{\mu}) q(x - \hat{\mu}) \right],$$

$$\Delta_\mu q(x) = \frac{1}{a_\mu^2} \left[U_\mu(x) q(x + \hat{\mu}) + U_\mu^\dagger(x - \hat{\mu}) q(x - \hat{\mu}) - 2q(x) \right]. \tag{3.36}$$

Let us define $\hat{m}_0, \hat{q}(x), \hat{\nabla}_\mu$, and $\hat{\Delta}_\mu$ as dimensionless quantities where $\hat{m}_0 = a_t m_0$, $\hat{q}(x) = a_s^{3/2} q(x)$, $\hat{\nabla}_\mu = a_\mu \nabla_\mu$, and $\hat{\Delta}_\mu = a_\mu^2 \Delta_\mu$. Then, the anisotropic Wilson fermion action becomes

$$S_F^\xi = \sum_x \overline{q}(x) \left[\left(\hat{m}_0 + \nu_t + 3\frac{\nu_s}{\xi_0} \right) - \left(\nu_t W_t + \frac{\nu_s}{\xi_0} \sum_s W_s \right) \right] \hat{q}(x), \tag{3.37}$$

where

$$W_\mu = \frac{1}{2} \left[(1 - \gamma_\mu) U_\mu(x) \delta_{x+\hat{\mu},y} + (1 + \gamma_\mu) U_\mu^\dagger(x - \hat{\mu}) \delta_{x-\hat{\mu},y} \right]. \tag{3.38}$$

Note that when $\nu_t = \nu_s$, the fermion action in Eq. (3.35) becomes the original Wilson fermion action [21]. Either ν_t or ν_s has to be tuned, in addition to the bare quark mass m_0 to give the correct relativistic dispersion relation, i.e.,

$$E^2(\mathbf{p}) = m^2 + c^2 \mathbf{p}^2, \tag{3.39}$$

where $E(\mathbf{p})$ is the energy of a pion with total momentum $\mathbf{p}$ and $m = E(0)$. For a given bare quark mass m_0 we tune the value of ν_s while $\nu_t = 1$ to give the speed of light $c = 1$. Energy E and momentum $\mathbf{p}$ are measured in lattice units. The effective speed of light $c(\mathbf{p})$ is given by

$$c(\mathbf{p}) = \xi \sqrt{\frac{(a_t E(\mathbf{p}))^2 - (a_t m)^2}{(a_s \mathbf{p})^2}}, \tag{3.40}$$

where ξ is again the renormalized anisotropy.
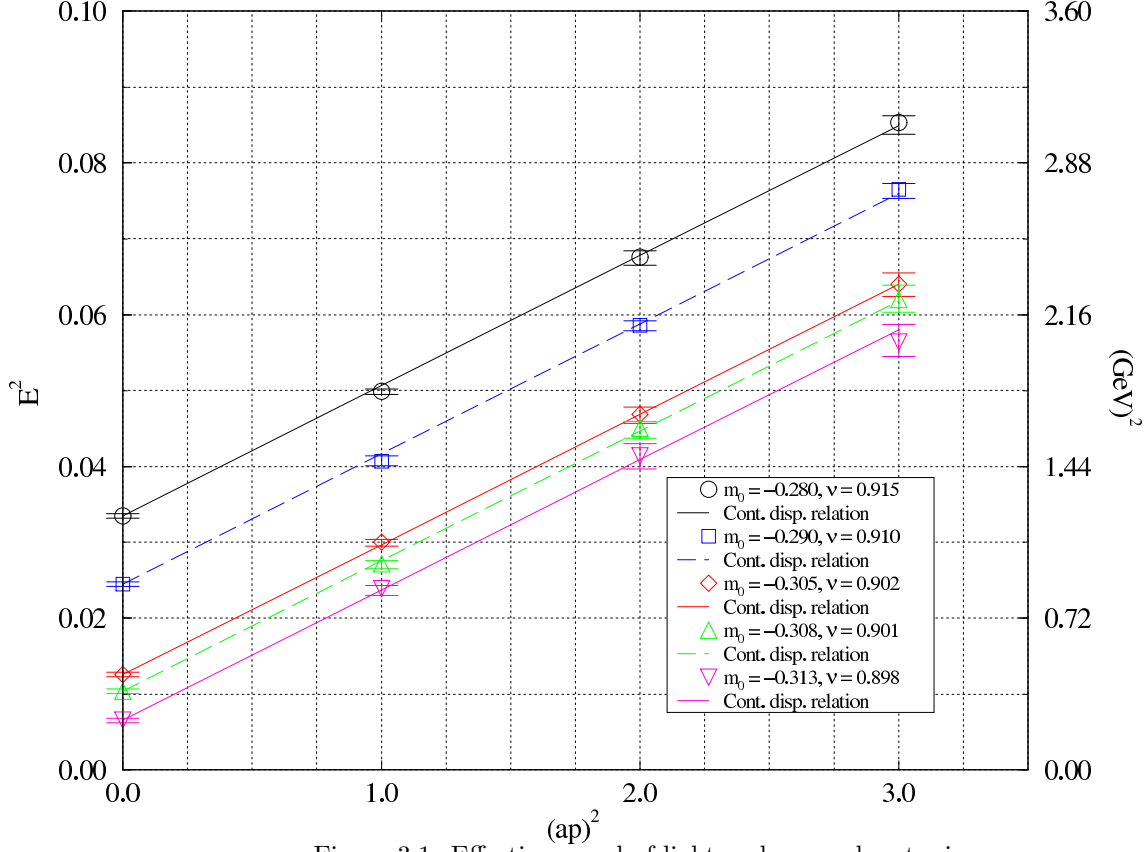
Figure 3.1: Effective speed of light and m_0 and ν_s tuning

We measured pion energy $E(\mathbf{p})$ for the lowest three values of momentum $\mathbf{p}$. Namely, $\mathbf{p} = \frac{2\pi}{L}(1,0,0)$, $\frac{2\pi}{L}(1,1,0)$, and $\frac{2\pi}{L}(1,1,1)$. We tuned ν_s for five different bare quark masses m_0. The dispersion relation for tuned parameter ν_s is plotted in Fig. 3.1. The horizontal axis is momentum squared in lattice units, divided by a factor $\left(\frac{2\pi}{L}\right)^2$ and the vertical axis is the energy squared in lattice units. The straight line passing through the mean value of $E^2(0)$ shows the desired continuum dispersion relation. The target anisotropy (or the renormalized anisotropy) is $\xi = 3$. The lattice space-time volume is $16^3 \times 64$, where, in physical units, the volume is about $(1.6\,\mathrm{fm})^3 \times (2.1\,\mathrm{fm})$.

Lastly, the relation of pion mass and bare quark mass is studied numerically using anisotropic lattices discussed here. Pion mass squared as a function of bare quark mass is plotted for tuned
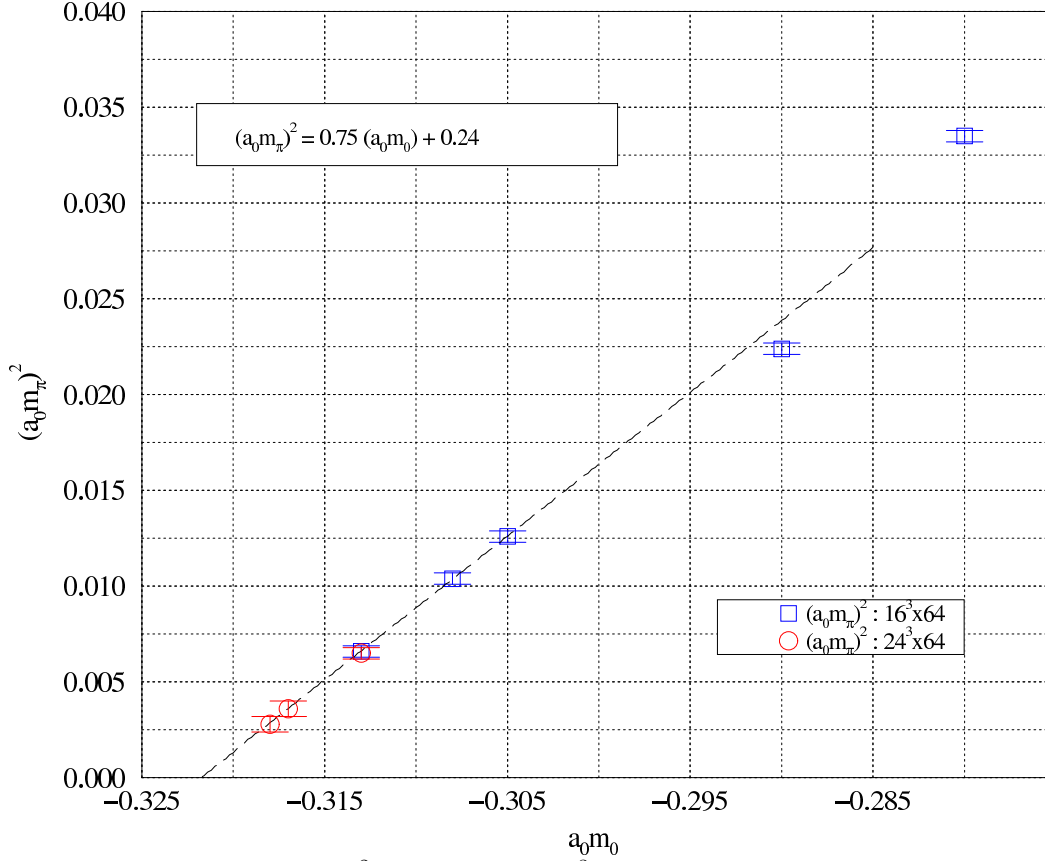
Figure 3.2: Plot for $(a_t m_\pi)^2$ v.s. $a_t m_0$ with $16^3 \times 64$ lattices. The gauge action has parameters $\beta = 6.1$ and $\xi = 3.0$.

values of ν_s in Fig. 3.2. The straight line drawn in the plot is fitted to the data based on an ansatz $m_\pi^2 = c_1 m_0 + c_2$. The fitted values are shown in the figure. A linear relation is observed for lower pion masses.

3.5 Smearing methods

For hadron spectroscopy in lattice QCD, it is a common practice to smear quark fields in order to have better coupling to the low-lying states. Quark smearing is performed in an iterative fashion so the resulting weight of a field operator has roughly a Gaussian distribution. One could think of the
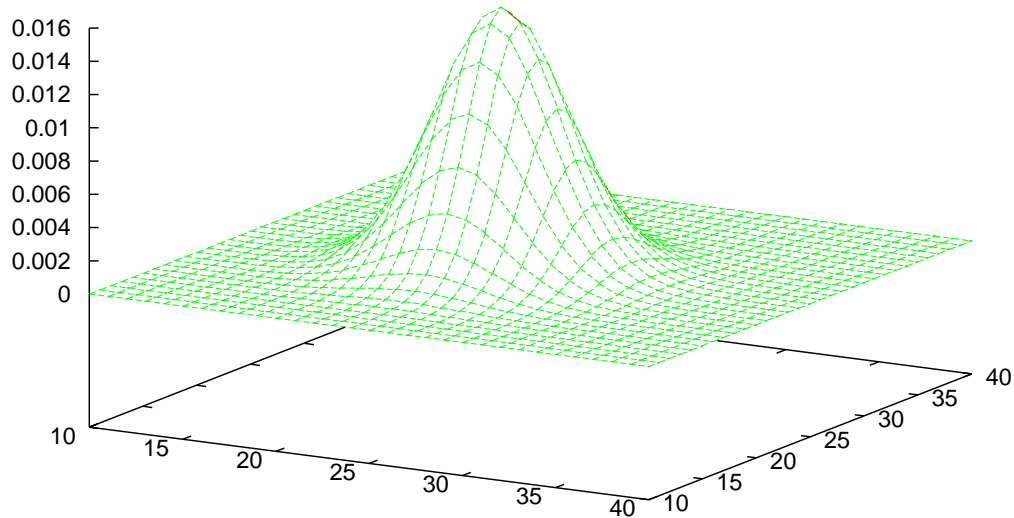
Figure 3.3: Demonstrative plot for smeared source amplitudes in two-dimensional space.

spatial weight distribution of the field as the "spatial wavefunction" of a state, which implies that the shape has to be "smooth" and has to vanish for large distance [57]. Figure 3.3 demonstrates a typical weight distribution of a smeared source field in two-dimensional space. Gaussian smearing is performed recursively on a point field according to Eq. (2.16) with parameters $(N, \sigma) = (50, 4.5)$ in no background fields. In a classical picture a particle with a narrow wavefunction acquires a significant contribution from large momenta, while a particle with a more spatially extended wavefunction has smaller momenta. This picture gives an intuitive explanation why smeared fields couple to low-lying states in a cleaner fashion than point fields. A smeared field with a first-derivative along some axis is given by taking the wavefunction shown in Fig. 3.3 displaced along a backward direction and subtracting it from a forward displaced one. The resulting wavefunction is shown in Fig. 3.4.

Quark field smearing involves gauge-links in the construction, and use of gauge-link smearing or fuzzing is known to reduce the contamination from high frequency modes of the theory. Smeared
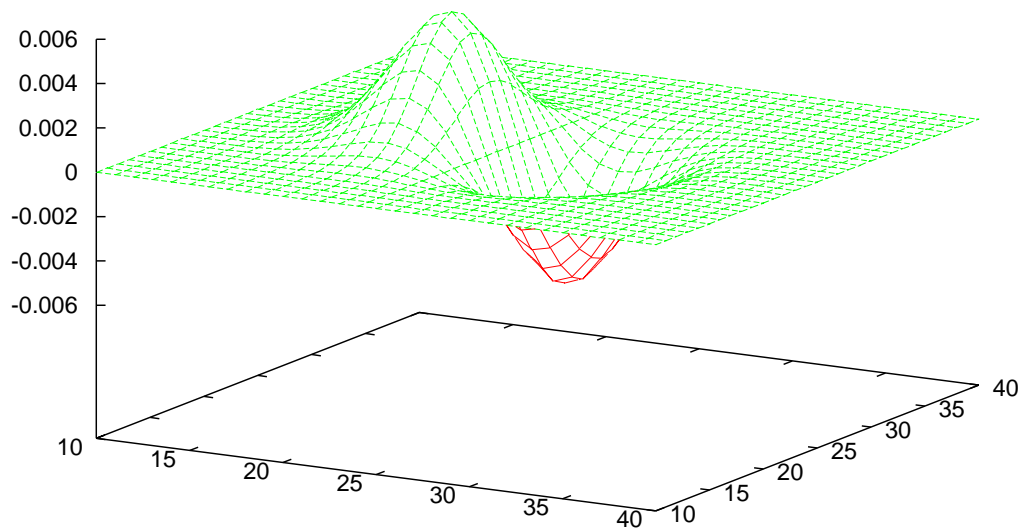
Figure 3.4: Demonstrative plot for a first-derivative, smeared source amplitudes in two-dimensional space.
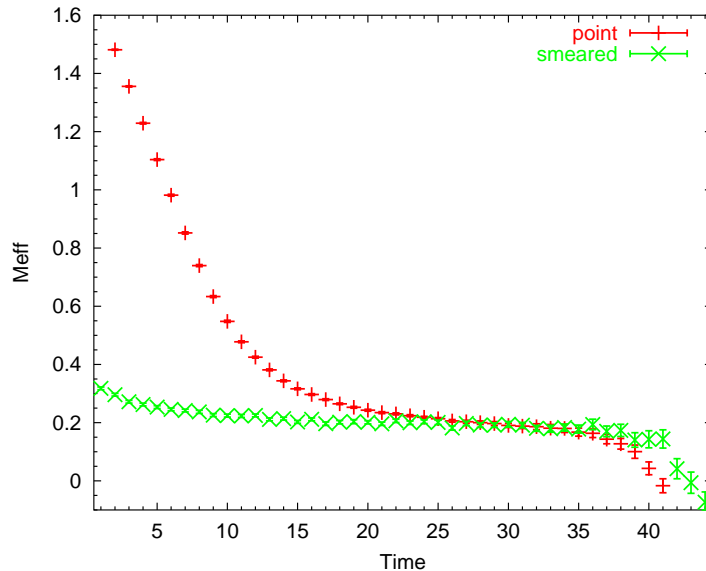
Figure 3.5: Effective masses for point-point correlation and smeared-smeared correlation. The operator is chosen to be the first embedding of G_{1g} row 1 from Table 2.8. Temporal lattice size is 64.

gauge-links are useful especially for glueballs, hybrids, and measuring static potentials [41,59].

The behavior of a quasi-local operator with smeared gauge-links and that of a point operator are quite different in an effective mass plot. Representative effective masses calculated using a nucleon operator from G_{1g} row 1 are shown in Fig. 3.5. One can clearly observe that the correlation function using a point source operator and a point sink operators suffers from coupling to highly excited states, while the correlation function using a quasi-local source with smeared gauge-links and a quasi-local sink with smeared gauge-links strongly couples to the ground state at early times. The effective mass of the point-point correlation function needs many more time-slices to reach a plateau where the ground mass can be extracted [83]. But, in reality, lattice calculations with such a large separation in time are computationally demanding. Use of quasi-local operators is an economical way to obtain the effective masses of low-lying states.

The gauge-link smearing method used for Fig. 3.5 is so-called APE-smearing [59]. The APE-smearing is performed iteratively. In each step every spatial gauge-link on the lattice is replaced

by itself and sum of spatial "staples" with a factor,

$$U_j^{(n+1)}(x) \longrightarrow P_{\mathrm{SU}(3)} \left[U_j^{(n)}(x) + \frac{1}{\alpha} \sum_{k \perp j} U_k^{(n)}(x) U_j^{(n)}(x+\hat{k}) U_k^{\dagger(n)}(x+\hat{j}) \right], \qquad (3.41)$$

where $P_{\mathrm{SU}(3)}$ is a projection operator that projects the 3×3 matrix onto SU(3). Equation (3.41) is schematically represented in Fig. 3.6. Integer n and a constant factor α control the link-smearing.

Figure 3.6: Schematic view of APE-smearing at one iterative step. The parameter r is equal to $1/\alpha$.

This iterative process redefines gauge-links as averages of the old gauge-links and their neighbors in gauge invariant way, and eliminates the unphysical short distance fluctuations of the original gauge fields.

A few other link smearing methods have been proposed such as hypercubic (HYP) fat links [60] and stout links [61]. It has been shown that use of fat links in a staggered fermion action significantly decreases flavor symmetry breaking [60, 84–87]. One of the improved Wilson fermion actions employs fat links in the irrelevant chromo-electromagnetic term. Such an action is called the fat-link irrelevant clover (FLIC) action [88] and it has $O(a)$ improvement. The stout link smearing is unique among various link smearing methods in the sense that its procedure is completely analytic. Unlike other link smearing methods that use a SU(3) projection, stout link smearing preserves all symmetry properties of the link variables. This method is computationally much faster, but it requires a careful parameter tuning; the stout links involve lots of complicated paths even at a single iteration step, thus they are very sensitive to the controling parameters.

3.6 Lattice setup

We used a $16^3 \times 64$ lattice and an ensemble of 239 gauge configurations created using the anisotropic Wilson gauge action in quenched approximation with renormalized anisotropy $\xi = 3.0$ and $\beta = 6.1$. The temporal lattice spacing corresponds to $a_t^{-1} = 6.0$ Gev [37]. The pion mass measured on this lattice is about 500 MeV and rho meson mass is about 840 MeV.

We used anisotropic, unimproved Wilson fermion action. For the given pion mass we tuned the fermion action and the correct dispersion relation is obtained at $\nu_s = 0.898$ while ν_t is fixed at 1. A periodic boundary condition is employed for spatial directions and an anti-periodic boundary condition is employed for the temporal direction.

For smearing we first tuned APE-smearing parameters. We measured effective masses from the quasi-local correlation functions using an ensemble of 40 gauge configurations for different input APE-smearing parameters while quark smearing parameters were kept fixed. After reaching reasonable effective masses, we then fixed the obtained APE-smearing parameters and tuned quark smearing parameters. We observed that the effective mass behavior is most stable with APE-smearing parameters, $(\alpha, n) = (2.5, 3)$, and with quark smearing parameters, $(\sigma, N) = (3.0, 20)$. We used these smearing parameters for our calculations of baryon spectra.

We recently repeated the analysis using a $24^3 \times 64$ quenched lattice with the same lattice spacings and an ensemble of 167 gauge configurations generated by the same action. The pion mass is chosen to be the same. The volume dependence of baryon masses is studied by comparing the results for the $16^3 \times 64$ lattice and for the $24^3 \times 64$ lattice.

Chapter 4

Lattice QCD Simulations of Excited Baryon Masses

4.1 Overview

Results of Monte Carlo simulations for excited baryon masses are provided in this chapter. A numerical test of the orthogonality relations of the correlation matrix is given in Section 4.2. Equality of different rows for a certain embedding of a given irrep is checked in Section 4.3. These checks are important to see that the operator constructions and corresponding programming are correct. All numerical results for N^* spectra are shown in Section 4.4. The six distinct irreps are separately examined in detail. For a given irrep, correlation matrices of different dimensions are analyzed in order to clarify the stability of mass eigenstates. Results based on the linear χ^2 fitting are provided for generalized eigenvalues of the correlation matrices. Results for excited delta baryon spectra are provided in Section 4.5 in a manner similar to the N^* results. Calculated baryon spectra are compared with the physical baryon spectra in Section 4.6, where the hyperfine mass splittings are studied and compared with work done by another group. Very recently, we completed the analysis of baryon spectra using lattices with different volume. We then examined the volume dependence of excited baryon spectra that we computed, and the results are briefly reported in Section 4.7. A brief summary of this chapter is given at Section 4.8.

4.2 Numerical check of orthogonality

We discussed in Chapter 3 that when operators are written in terms of the basis of irreps of the group, correlation functions satisfy an orthogonality relation as in Eq. (2.14). Namely, correlation functions are nonvanishing if and only if the sink and source operators belong to the same irrep and the same row. Operators from different embeddings are expected to admix as long as they
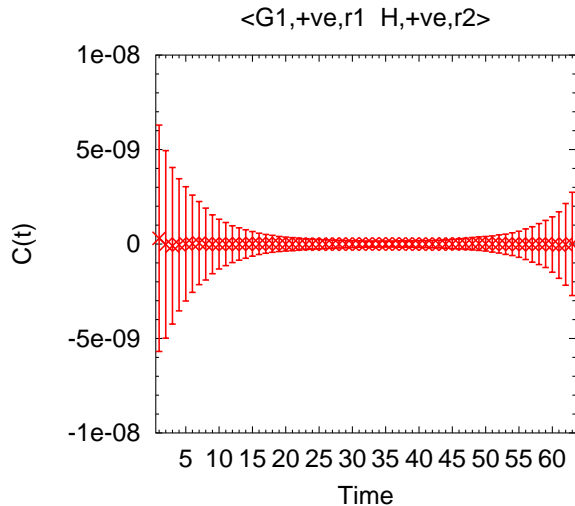
Figure 4.1: Correlation function in time. The sink operator is chosen to be the first embedding of quasi-local G_{1g} row 1 nucleon operator, whereas the source operator is chosen to be the quasi-local H_g row 2 operator. Note that they have the same S_z.

share the same irrep and row, and a set of such operators is used to form a matrix of correlation functions. The matrix of correlation functions is then diagonalized according to Eq. (3.14) in order to separate the mass eigenstates.

We observed the orthogonality relation in the actual numerical simulation. We categorize our analysis of orthogonality into three cases; 1) sink and source belonging to different irreps, but having the same S_z, 2) sink and source belonging to the same irrep, but having different S_z's, and 3) sink and source belonging to the same irrep and having the same S_z, but their parities are different. In this section we use the word *irrep* to express the rotational irreducible representations G_1, H, or G_2, not including the parity. The first case is demonstrated in Fig. 4.1. The plot shows a correlation function using a linear scale as a function of time. Clearly, the correlation function is zero within one error bar. The description of the operators is in the caption. The second case is demonstrated in Fig. 4.2, and sink and source are also clearly orthogonal as they should be. We also confirmed the orthogonality relation for different rows of G_2 and H irreps. The third case is plotted in Fig. 4.3. It has been checked that different parities do not mix no matter what type of

Figure 4.2: Correlation function in time. The sink operator is chosen to be the first embedding of quasi-local G_{1g} row 1 nucleon operator, whereas the source operator is chosen to be also G_{1g} but row 2.
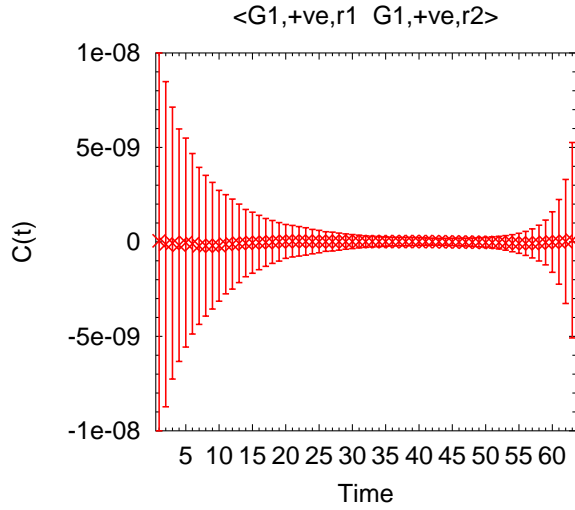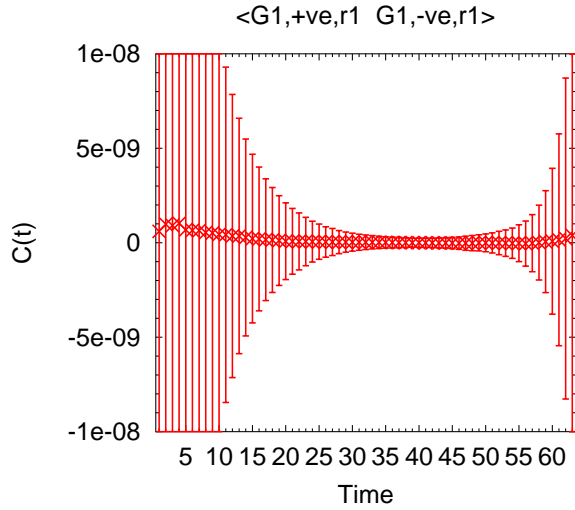

Figure 4.3: Correlation function in time. The sink operator is chosen to be the first embedding of quasi-local G_{1g} row 1 nucleon operator, whereas the source operator is chosen to be the first embedding of quasi-local G_{1u} row 1 nucleon operator.
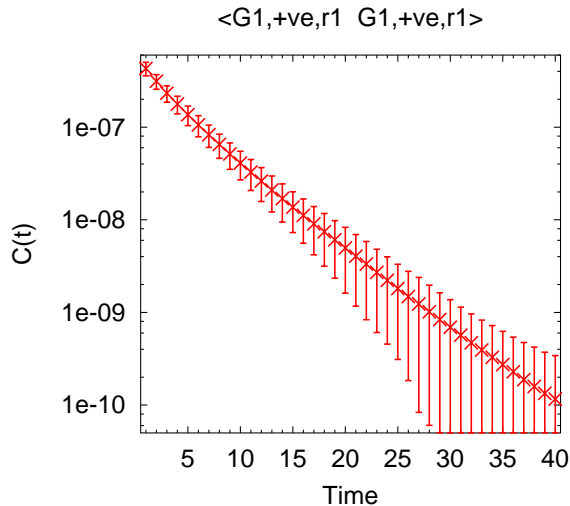
Figure 4.4: Correlation function in time. The sink operator and source operator are the same and chosen to be the first embedding of quasi-local G_{1g} row 1 nucleon operator.

irreps or rows are used. These orthogonality relations have been verified for all available nucleon correlation functions using the quasi-local and one-link operators.

A representative correlation function that should *not* be orthogonal is shown in Fig. 4.4 using a log scale for the purpose of comparison with other figures. The same operator is used for sink and source. The effective mass can be extracted from the slope of this plot.

4.3 Equality of different rows

For a given embedding of a certain irrep, row labels basically distinguish different S_z states. For instance, row 1 and row 2 of G_1 representations correspond to $\left|\frac{1}{2}, \frac{1}{2}\right\rangle$ and $\left|\frac{1}{2}, -\frac{1}{2}\right\rangle$, respectively, for the lowest value of total spin S. However, the values of S_z can be mixed in a single row; for instance, the row 1 and row 2 of G_2 representations correspond to $\sqrt{\frac{1}{6}}\left|\frac{5}{2}, \frac{5}{2}\right\rangle - \sqrt{\frac{5}{6}}\left|\frac{5}{2}, -\frac{3}{2}\right\rangle$ and $-\sqrt{\frac{5}{6}}\left|\frac{5}{2}, \frac{3}{2}\right\rangle + \sqrt{\frac{1}{6}}\left|\frac{5}{2}, -\frac{5}{2}\right\rangle$, respectively, for the lowest value of J. Baryon correlation functions should not depend on S_z, unless an interaction term that can break the cubic symmetry is introduced. For baryon spectroscopy there are no such terms; therefore, correlation functions can be averaged among rows for a given embedding of a certain irrep. This corresponds to the spin average by taking the trace

of free spin indices of sink and source operators in the field theory.

A translationally invariant baryon operator obeys the following transformation under a group rotation,

$$U(G_a)B^{\Lambda\lambda}(t)U^\dagger(G_a) = \sum_{\lambda'} T^{(\Lambda)\dagger}(G_a)_{\lambda\lambda'} B^{\Lambda\lambda'}(t), \tag{4.1}$$

where $T^{(\Lambda)}(G_a)$ is an irreducible representation of group element G_a. Irrep and row into which the baryon operator is categorized are Λ and λ, respectively. A rotation applies to the "barred" fields in the form,

$$U(G_a)\overline{B}^{\Lambda\lambda}(t)U^\dagger(G_a) = \sum_{\lambda'} \overline{B}^{\Lambda\lambda'}(t)T^{(\Lambda)}(G_a)_{\lambda'\lambda}. \tag{4.2}$$

The orthogonality of different rows is realized based on the correlation function after averaging over a large number of gauge configurations.

$$\delta_{\lambda\lambda'}C_{ij}^{\Lambda\lambda}(t) = \sum_{x} \langle 0| B_i^{\Lambda\lambda'}(\mathbf{x},t)\overline{B}_j^{\Lambda\lambda}(0,0) |0\rangle, \tag{4.3}$$

where indices i,j specify embeddings. Correlation functions that we are interested in involve operators from the same row λ. Using the unitarity relation $U^\dagger(G_a)U(G_a) = 1$, the sink and source operators can be rotated in following way.

$$C_{ij}^{\Lambda\lambda} = \sum_{x} \langle 0| U(G_a)B_i^{\Lambda\lambda}(\mathbf{x},t)U^\dagger(G_a)U(G_a)\overline{B}_j^{\Lambda\lambda}(0,0)U^\dagger(G_a) |0\rangle. \tag{4.4}$$

Note that the vacuum is invariant under rotation and the sum over all spatial lattice sites removes any dependence on the rotation of coordinates. Substituting the rotational properties of Eqs. (4.1) and (4.2), and using the orthogonality of Eq. (4.3) leads to

$$C_{ij}^{\Lambda\lambda} = \sum_{\lambda'} T_{\lambda\lambda'}^{(\Lambda)\dagger}(G_a)C_{ij}^{\Lambda\lambda'}(t)T_{\lambda'\lambda}^{(\Lambda)}(G_a). \tag{4.5}$$

These linear relations between correlation functions from every row contain coefficients that depend on the irreducible representation of the group element. Let us denote the coefficient using a little simpler notation by introducing

$$|f_{\lambda'}|^2 \equiv T_{\lambda\lambda'}^{(\Lambda)\dagger}(G_a)T_{\lambda'\lambda}^{(\Lambda)}(G_a). \tag{4.6}$$

No summation over λ is taken in Eq. (4.6). Note that the coefficients obey the rule,

$$\sum_{\lambda'} |f_{\lambda'}|^2 = \sum_{\lambda'} T_{\lambda\lambda'}^{(\Lambda)\dagger}(G_a)T_{\lambda'\lambda}^{(\Lambda)}(G_a) = T_{\lambda\lambda}^{(\Lambda)}(G_a^{-1}G_a) = 1. \tag{4.7}$$

For two-dimensional irreps, such as G_1 or G_2, a correlation function of a certain row, say $\lambda = 1$, can be written as a linear combinations of other rows. From Eqs. (4.5) and (4.6) one obtains

$$C_{ij}^{G_1 1} = |f_1|^2 C_{ij}^{G_1 1}(t) + |f_2|^2 C_{ij}^{G_1 2}(t). \tag{4.8}$$

where $|f_1|^2 + |f_2|^2 = 1$. It immediately follows that,

$$
\begin{aligned}
C_{ij}^{G_1 1} &= |f_1|^2 C_{ij}^{G_1 1}(t) + (1 - |f_1|^2) C_{ij}^{G_1 2}(t), \\
0 &= (1 - |f_1|^2) \left(C_{ij}^{G_1 1} - C_{ij}^{G_1 2} \right).
\end{aligned}
\tag{4.9}
$$

Since the choice of group element G_a is arbitrary, $1 - |f_1|^2$ is not zero in general. Therefore, correlation functions from row 1 and from row 2 must be equal.

$$C_{ij}^{G_1 1} = C_{ij}^{G_1 2}. \tag{4.10}$$

For the four-dimensional irrep H, the proof of the equality of correlation functions from different rows goes in similar fashion as for two-dimensional case. A correlation function of row $\lambda = 1$ from H is written as

$$C_{ij}^{H1}(t) = |f_1|^2 C_{ij}^{H1}(t) + |f_2|^2 C_{ij}^{H2}(t) + |f_3|^2 C_{ij}^{H3}(t) + |f_4|^2 C_{ij}^{H4}(t). \tag{4.11}$$

Since $|f_1|^2 + |f_2|^2 + |f_3|^2 + |f_4|^2 = 1$, it follows,

$$0 = |f_2|^2 \left(C_{ij}^{H2}(t) - C_{ij}^{H1}(t) \right) + |f_3|^2 \left(C_{ij}^{H3}(t) - C_{ij}^{H1}(t) \right) + |f_4|^2 \left(C_{ij}^{H4}(t) - C_{ij}^{H1}(t) \right). \tag{4.12}$$

Applying two additional group rotations, one obtains a system of equations whose solution requires equality of correlation functions from the different rows,

$$C_{ij}^{H1} = C_{ij}^{H2} = C_{ij}^{H3} = C_{ij}^{H4}. \tag{4.13}$$

A numerical proof of the equality of correlation functions from different rows of the same irrep is demonstrated using the quasi-local H irrep. Figure 4.5 shows four correlation functions plotted using a log scale. One can clearly see that correlation functions from different rows, i.e., $C_{ij}^{H1}, C_{ij}^{H2}, C_{ij}^{H3}, C_{ij}^{H4}$, are almost exactly on top of each other, verifying the equality of Eq. (4.13).

The correlation functions from different rows are averaged configuration by configuration for our calculations of excited baryons. This technique improves the statistical data.
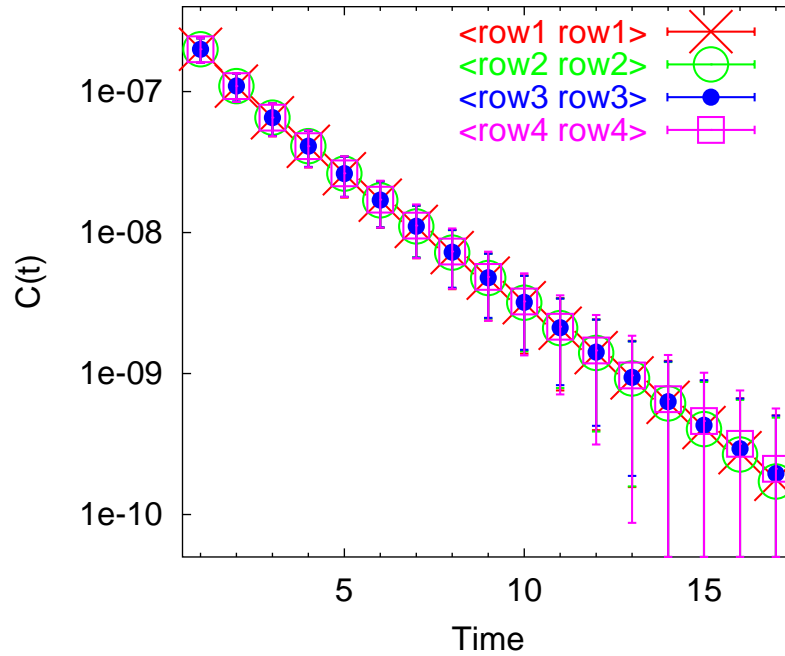
Figure 4.5: Correlation function using a log scale. The sink operator and source operator are the same and chosen to be the first embedding of the quasi-local H_g nucleon operator. A cross is for the row 1 sink and row 1 source operator, a circle is for the row 2 sink and row 2 source operator, a bullet is for the row 3 sink and row 3 source operator, and a square is for the row 4 sink and row 4 source operator.

4.4 N^* spectrum

We computed quark propagators by numerically solving the linear equation of the lattice fermion matrix using the stabilized BiConjugate Gradient algorithm. We used the QDP++ Data-parallel Programming Interface and Chroma Lattice Field Theory Library ("chroma" is color in Greek) developed mainly by R. Edwards with the support of the Lattice QCD SciDAC project[1]. The code is written in object-oriented language, C++, and mathematical or physical operators can be applied on lattice wide objects. The interface provides suitable executables for a single proces-

---

[1]The source codes of QDP++ and chroma are available on line at `http://www.jlab.org/~edwards/qdp/index.html` and `http://www.jlab.org/~edwards/chroma/index.html`

sor workstation or multiprocessor nodes with parallel data communications. Our computations have been carried out using the 256-node gig-E cluster and 128-node Myrinet cluster in the High Performance Computing (HPC) facility at Jefferson National Laboratory.

The gauge configurations that we used have been calculated by D. G. Richards using Jefferson Lab computing resources. The Monte Carlo updating procedure is coded in the SZIN Software System ("szin" is color in Hungarian), which also supports various types of computer architectures. The program is written in object-oriented macro-based C language.

Table 4.1: Nucleon operators with quasi-local and with one-link displacement used in our simulation. The numbers of operators for G_{1g} row 1, G_{2g} row 1, and H_g row 1 are listed. Numbers of ungerade operators are exactly the same. The $\hat{T}_1 \overline{N}^{(MS)}$ operators are not included because they are equivalent to $\hat{T}_1 \overline{N}^{(MA)}$ operators, as explained in Section 2.4.3

Type	Eq.	Table	G_{1g}	H_g	G_{2g}
quasi-local	2.19	2.8	3	1	0
one-link A_1	2.46	2.10	4	1	0
one-link E	2.46	2.13, 2.10	1	5	1
one-link T_1	2.46	2.12, 2.10	5	6	1
one-link A_1	2.48	2.11	4	3	0
one-link E	2.48	2.13, 2.11	3	7	3
one-link T_1	2.48	2.12, 2.11	3	5	2
			23	28	7

We used nucleon operators from all quasi-local and all one-link displacements discussed in Chapter 2. For a given row there are 23 G_{1g} operators, 28 H_g operators, and 7 G_2 operators as shown in Table 4.1. These sets of operators are used to form matrices of correlation functions in order to extract masses for excited N^* states.

4.4.1 The G_1 spectrum

Let us introduce a new notation for operators. The notation should include (1) the irrep with parity, a direct product of (2) isospin symmetry and (3) Dirac indices symmetry, (4) spinorial irrep $\overline{\Psi}^{\Lambda,k}$ with k being an embedding, and the type of one-link displacements, $\hat{A}_1, \hat{E}$, or $\hat{T}_1$ for the nonlocal operators. For example, a quasi-local operator for the nucleon based on the G_{1g}, k-th embedding is described by

$$| \, N^* : (1), (2) \otimes (3), (4) \, \rangle = \Big| \, N^* : \, G_{1g}, \, \mathrm{MA_{iso}} \otimes \mathrm{MA_{Drc}}, \, \overline{\Psi}^{G_{1g},k} \, \Big\rangle. \qquad (4.14)$$

One of the one-link operators for the nucleon is described by

$$| \, N^* : (1), (2) \otimes (3), (4) \, \rangle = \Big| \, N^* : \, G_{1g}, \, \mathrm{MA_{iso}} \otimes \mathrm{MA_{Drc}}, \, \hat{T}_1 \overline{\Psi}^{G_{1u},k} \, \Big\rangle. \qquad (4.15)$$

For a quasi-local nucleon operator a MA-isospin and a MS-isospin are equivalent and we only use MA-isospin as discussed in Section 2.3.1 (Eq. (2.27) shows their equivalence). We still denote this as $\mathrm{MA_{iso}} \otimes \mathrm{MA_{Drc}}$ in order to make operator notations consistent. In this section *ket* notations are adapted for *source operators*, and *bra* notations are used for *sink operators*. All G_1, gerade (positive-parity) operators used in our simulation are shown in Eqs. (4.16)-(4.28). Ungerade (negative-parity) operators are obtained by changing the parity of the local operators, $\overline{\Psi}^{\Lambda,k}$.

$$\Big| \, N^* : \, G_{1g}, \, \mathrm{MA_{iso}} \otimes \mathrm{MA_{Drc}}, \, \overline{\Psi}^{G_{1g},k} \, \Big\rangle, \quad k = 1, 2, 3; \qquad (4.16)$$

$$\Big| \, N^* : \, G_{1g}, \, \mathrm{MA_{iso}} \otimes \mathrm{MA_{Drc}}, \, \hat{T}_1 \overline{\Psi}^{G_{1u},k} \, \Big\rangle, \quad k = 1, 2, 3; \qquad (4.17)$$

$$\Big| \, N^* : \, G_{1g}, \, \mathrm{MA_{iso}} \otimes \mathrm{MA_{Drc}}, \, \hat{T}_1 \overline{\Psi}^{H_u} \, \Big\rangle; \qquad (4.18)$$

$$\Big| \, N^* : \, G_{1g}, \, \mathrm{MA_{iso}} \otimes \mathrm{MA_{Drc}}, \, \hat{E} \overline{\Psi}^{H_g} \, \Big\rangle; \qquad (4.19)$$

$$\Big| \, N^* : \, G_{1g}, \, \mathrm{MA_{iso}} \otimes \mathrm{MA_{Drc}}, \, \hat{A}_1 \overline{\Psi}^{G_{1g},k} \, \Big\rangle, \quad k = 1, 2, 3; \qquad (4.20)$$

$$\Big| \, N^* : \, G_{1g}, \, \mathrm{MA_{iso}} \otimes \mathrm{A_{Drc}}, \, \hat{T}_1 \overline{\Psi}^{G_{1u},k} \, \Big\rangle; \qquad (4.21)$$

$$\Big| \, N^* : \, G_{1g}, \, \mathrm{MA_{iso}} \otimes \mathrm{A_{Drc}}, \, \hat{A}_1 \overline{\Psi}^{G_{1g},k} \, \Big\rangle; \qquad (4.22)$$

$$\Big| \, N^* : \, G_{1g}, \, \mathrm{MS_{iso}} \otimes \mathrm{MS_{Drc}}, \, \hat{E} \overline{\Psi}^{H_g} \, \Big\rangle; \qquad (4.23)$$

$$\Big| \, N^* : \, G_{1g}, \, \mathrm{MS_{iso}} \otimes \mathrm{MS_{Drc}}, \, \hat{A}_1 \overline{\Psi}^{G_{1g},k} \, \Big\rangle, \quad k = 1, 2, 3; \qquad (4.24)$$

$$\left| \ N^* : \ G_{1g}, \ \mathrm{MA}_{\mathrm{iso}} \otimes \mathrm{S}_{\mathrm{Drc}}, \ \hat{T}_1 \overline{\Psi}^{G_{1u}} \ \right\rangle, \tag{4.25}$$

$$\left| \ N^* : \ G_{1g}, \ \mathrm{MA}_{\mathrm{iso}} \otimes \mathrm{S}_{\mathrm{Drc}}, \ \hat{T}_1 \overline{\Psi}^{H_u,k} \ \right\rangle, \quad k = 1, 2; \tag{4.26}$$

$$\left| \ N^* : \ G_{1g}, \ \mathrm{MA}_{\mathrm{iso}} \otimes \mathrm{S}_{\mathrm{Drc}}, \ \hat{E} \overline{\Psi}^{H_g,k} \ \right\rangle, \quad k = 1, 2; \tag{4.27}$$

$$\left| \ N^* : \ G_{1g}, \ \mathrm{MA}_{\mathrm{iso}} \otimes \mathrm{S}_{\mathrm{Drc}}, \ \hat{A}_1 \overline{\Psi}^{G_{1g}} \ \right\rangle. \tag{4.28}$$

First, we observed behaviors of diagonal elements of a correlation matrix, $C_{ii}^{G_1}(t)$, for both parities in order to identify which types of operators give cleaner signals. Effective masses using three quasi-local operators in Eq (4.16) are shown in Fig. 4.6 (a) and (b). The first embedding of the G_{1g} quasi-local operator couples to the ground state most cleanly of all the available nucleon operators. The fact that this operator consists of purely non-relativistic spin components may explain the good overlap to the ground state. The second embedding of G_{1g} couples to an excited state fairly strongly and stays on a plateau for time-slices, say, 13 to 21. The effective mass for the G_{1u} ground state is clearly above the G_{1g} ground state. This is in agreement with the empirical data, i.e., $1/2^-$ is heavier than $1/2^+$.

Representative effective masses based on the T_1 one-link operators are given in Fig. 4.6 (c) and (d). Four operators of the type $\mathrm{MA}_{\mathrm{iso}} \otimes \mathrm{MA}_{\mathrm{Drc}}$ are used in each parity. These effective masses hardly reach plateaux, but continuously drift down toward the ground states. These drifting-down effective masses are due to the fact that the operators couple to more than one mass eigenstate. In general, effective masses for non-local operators are found to be statistically noisier than for quasi-local operators.

Nonlocal E link operators create highly excited states, especially for the G_{1u} channel. Fig. 4.6 (e) and (f) show their effective masses. The E link corresponds to orbital angular momentum $L \geq 2$. whereas the T_1 link corresponds to $L \geq 1$. The E link operators do not couple strongly to their ground states in our data. Gauge fluctuations overwhelm the signals from ground states. It is generally true that highly excited states suffer from gauge fluctuations a lot even at early time-slices. This is because the signals of highly excited states decay so rapidly that the background noise overcomes the faint signals from the ground state.

Examinations of effective masses for diagonal elements of a correlation matrix not only
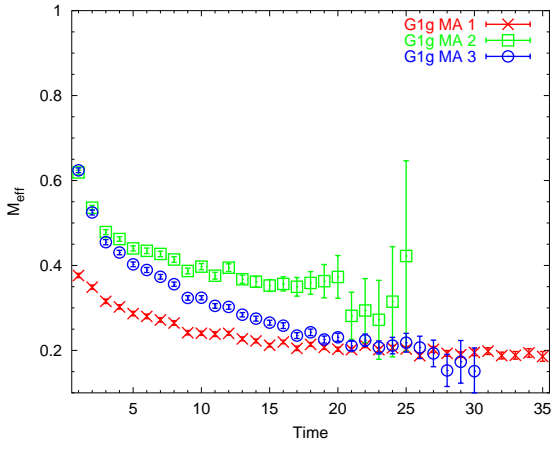
(a) Gerade, quasi-local ops
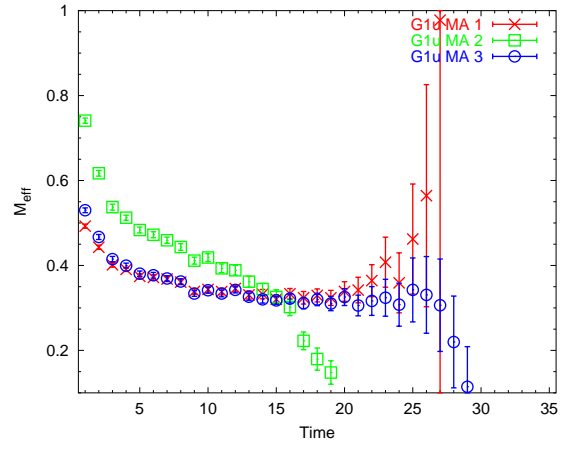
(b) Ungerade, quasi-local ops
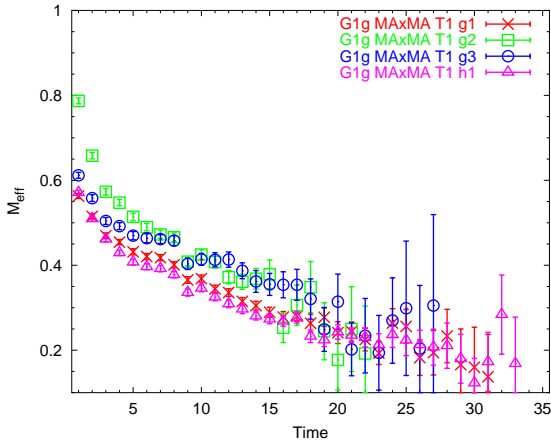
(c) Gerade, $MA_{iso} \otimes MA_{Drc}, T_1$ ops
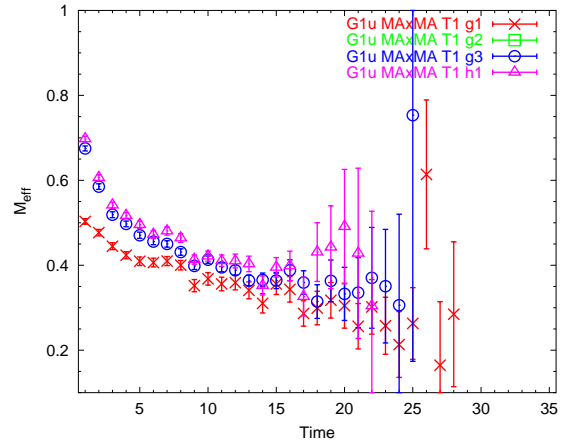
(d) Ungerade, $MA_{iso} \otimes MA_{Drc}, T_1$ ops
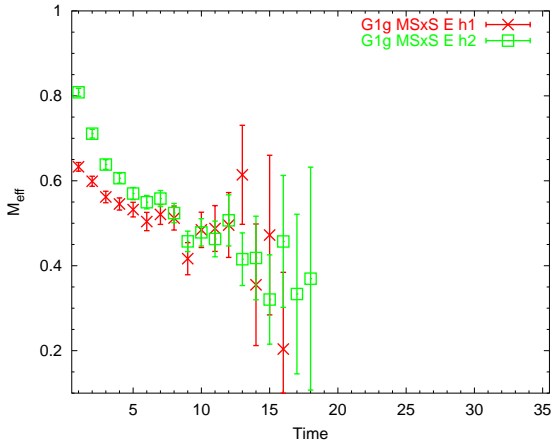
(e) Gerade, $MS_{iso} \otimes S_{Drc}, E$ ops

(f) Ungerade, $MS_{iso} \otimes S_{Drc}, E$ ops

Figure 4.6: Effective masses of the diagonal elements of the G_1 correlation matrix. The vertical axis is in lattice units. Note that $a_t^{-1} \sim 6.0\,\mathrm{GeV}$.

reveal the mass of the lowest-lying state, but also help to identify what type of operators should be used to construct a correlation matrix for diagonalization. There is no guarantee that the generalized eigenvalue problem of Eq. (3.14) is always solvable. The diagonalization fails, if two or more operators share the same s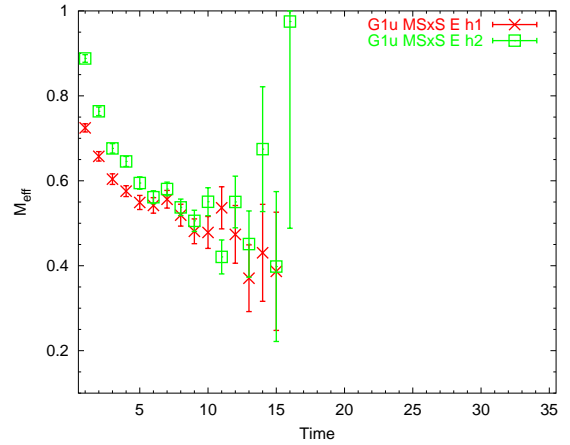pectral density. In this case the basis operators are approximately parallel, thus the matrix has approximately zero determinant. Another unfavorable scenario is when the diagonalization succeeds but the resulting spectrum is too heavily contaminated to extract masses. This happens, when operators that couple to highly excited states are included in the correlation matrix, because these operators introduce noise to the spectrum for the time range where masses would be extracted. The E link operators give typical examples. Therefore inclusion of E link operators into the construction of the correlation matrix has to be done with care. This suggests that the lattice eigenstates do not have much D-wave content.

It turns out that the generalized eigenvalue problem of Eq. (3.14) is not solvable if all available 23 operators of $G_{1g/u}$ are used to construct a matrix of correlation functions. There are some type of operators whose spectra are not distinct from the other, as we will explain at the end of this section.

We first take a close look at the gerade spectrum of the G_1 irrep by the diagonalization method. By carefully selecting operators, we found 10 operators whose correlation matrix is diagonalizable and the spectrum shows clear splittings between a few low-lying states. Figure 4.7 shows the obtained spectrum for G_{1g}. Part (a) of the figure shows the lowest three effective masses and part (b) shows the next three effective masses. The lowest-lying mass of G_{1g} is observed to be about 0.197 in lattice units fitted in the time range $17-25$. The generalized eigenvector $v_j(t, t_0)$ is dominated by the first embedding of the quasi-local operator. The mass of the state expressed by open circles with "m1" label in the figure is about 0.411 in lattice units fitted in the time range $10-14$. This mass is roughly twice as heavy as the ground state, and there are no states in between. Another state shown by open squares is nearly degenerate to the open circles, but slightly heavier by approximately 1%. Two states, shown in Fig. 4.7 (b) with open square symbols and circles, have masses also close to the first two excited states with a little more statistical noise. The state
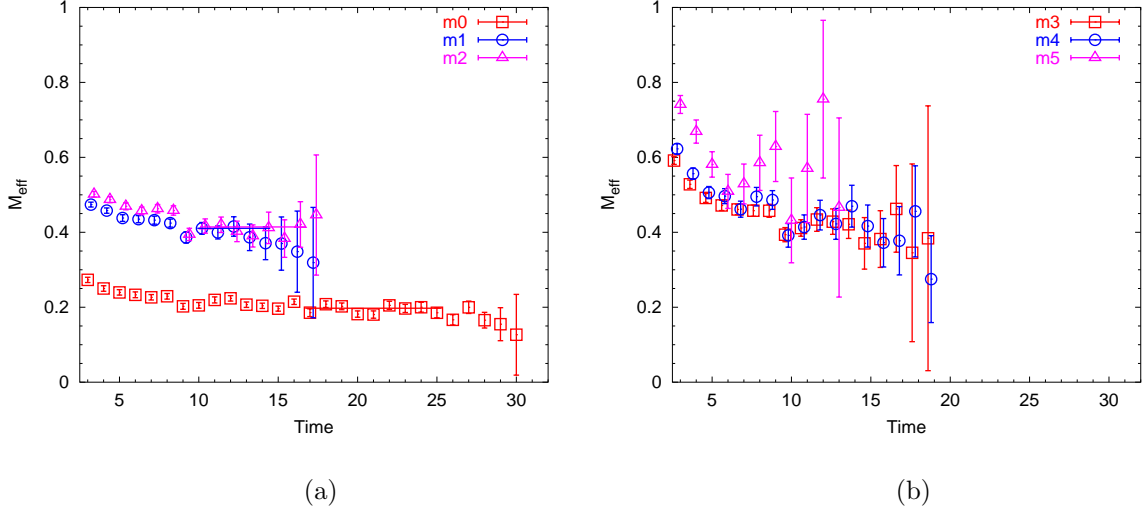
Figure 4.7: The effective masses of G_{1g} obtained by the diagonalization method based on a 10×10 correlation matrix. The lowest three masses are shown in (a) and the next three are shown in (b).

shown with open triangles in Fig. 4.7 and states above (not shown) this state are contaminated too much from highly excited states to obtain masses.

The generalized eigenvectors corresponding to the ground, first-excited, and second-excited states of G_{1g} are plotted in Fig. 4.8. The components are normalized to one, i.e., $\sum_j \left[v_j^{(n)}(t, t_0) \right]^2 = 1$ for each state n. For the ground state the eigenvector stays almost unchanged with respect to time. The first embedding of the quasi-local operator or $\left| N^* : G_{1g}, \mathrm{MA_{iso}} \otimes \mathrm{MA_{Drc}}, \overline{\overline{\Psi}}^{G_{1g},1} \right\rangle$ dominates the ground state clearly. Next most important operators are $\left| N^* : G_{1g}, \mathrm{MA_{iso}} \otimes \mathrm{MA_{Drc}}, \hat{T}_1 \overline{\overline{\Psi}}^{G_{1u},1} \right\rangle$ and $\left| N^* : G_{1g}, \mathrm{MA_{iso}} \otimes \mathrm{S_{Drc}}, \hat{T}_1 \overline{\overline{\Psi}}^{H_u,1} \right\rangle$ operators. The first-excited state of G_{1g} is dominated by the second embedding of quasi-local operator. Some coefficients change signs in the middle of forward propagation, say between $t = 10$ to 20. From the second-excited state onwards, the coefficients become unstable with respect to time and errors get large, and generally states are dominated by two or more operators instead of a single operator.

We examine the stability of the spectrum for G_{1g} by reducing the dimension of the matrix by one and rediagonalizing it. The reduction of the matrix dimension is done by eliminating one
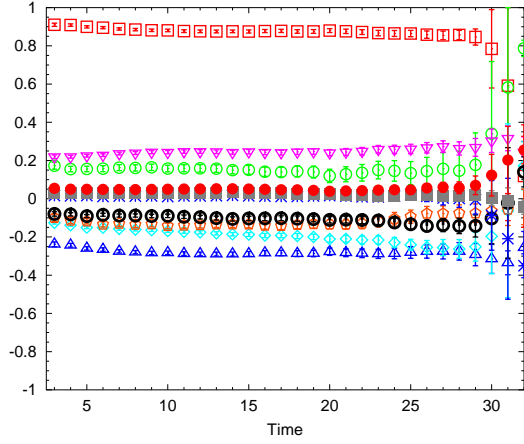
(a) Ground state
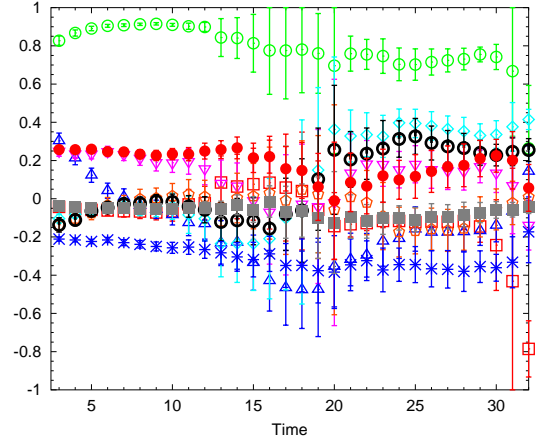
(b) first-excited state
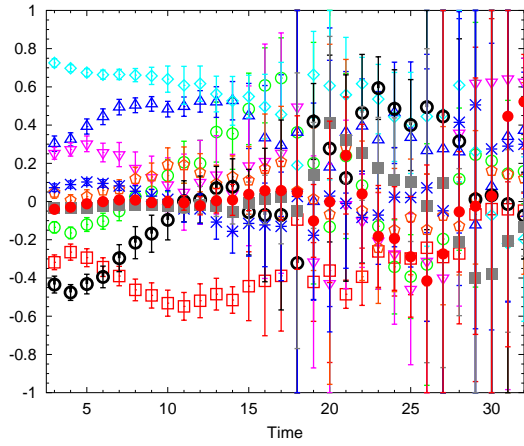
(c) second-excited state
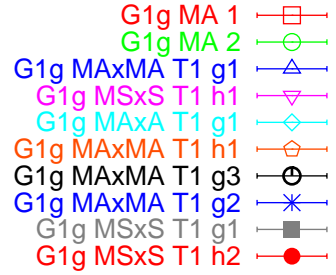
(d) Description

Figure 4.8: The eigenvectors obtained by the diagonalization method based on the G_{1g}, $10 \times$ 10 correlation matrix. The eigenvectors corresponding to the ground state, the first-excited state, and the second-excited state are shown in (a), (b), and (c), respectively. Eigenvectors are normalized to one. The description of the operators is given in (d).
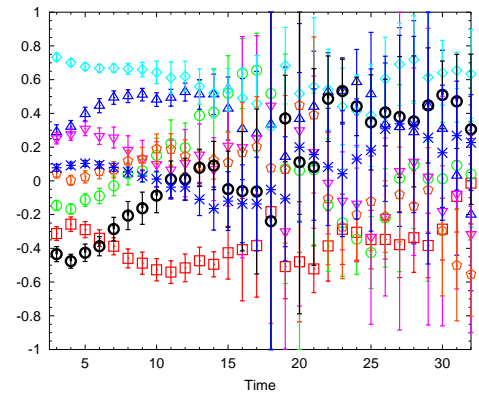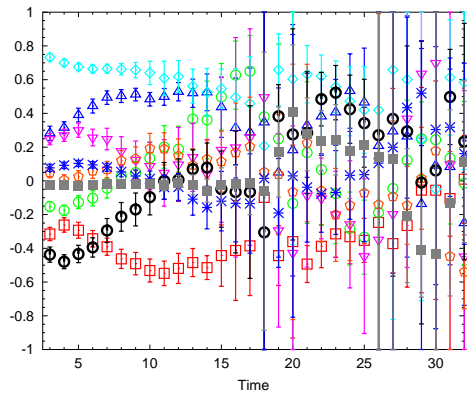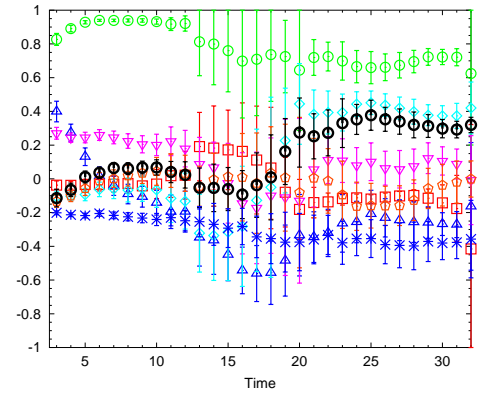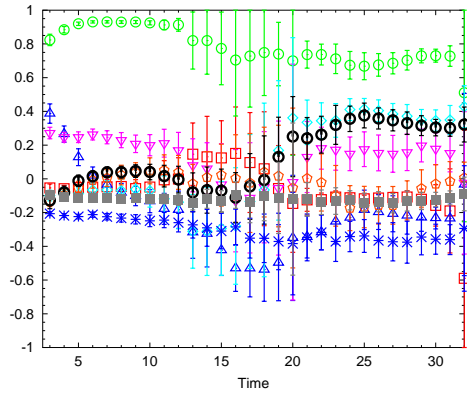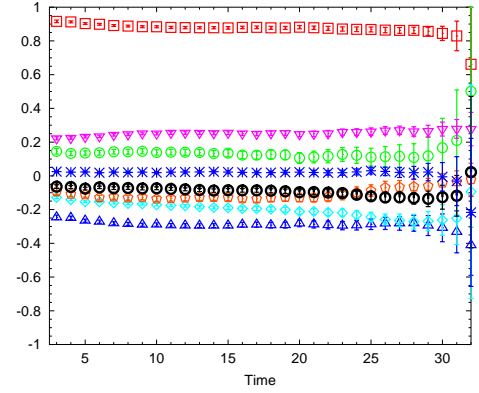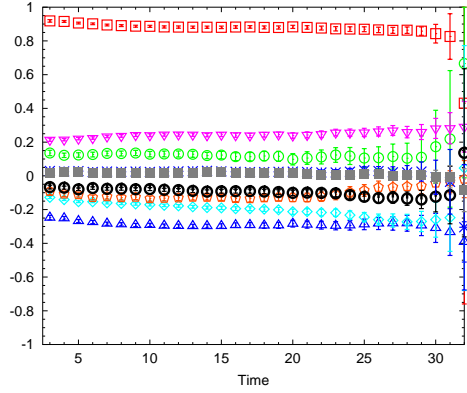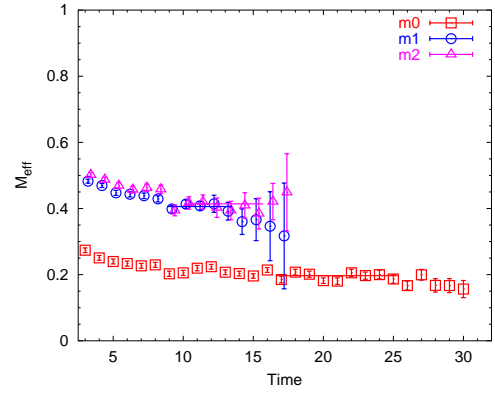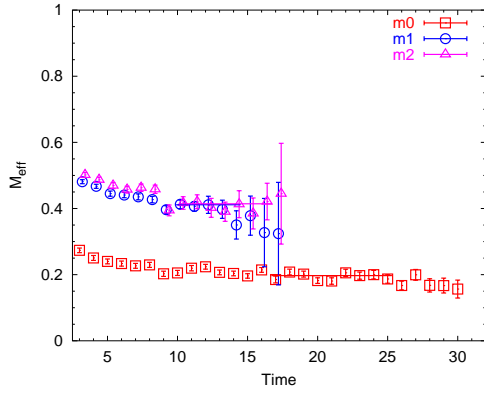
(a) 9×9 (b) 8×8

Figure 4.9: The stability check for the G_{1g} spectrum.

(c) 7×7 (d) 6×6

95

(e) 5×5 (f) 4×4

96
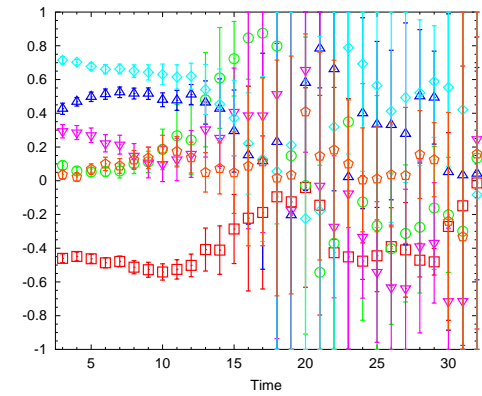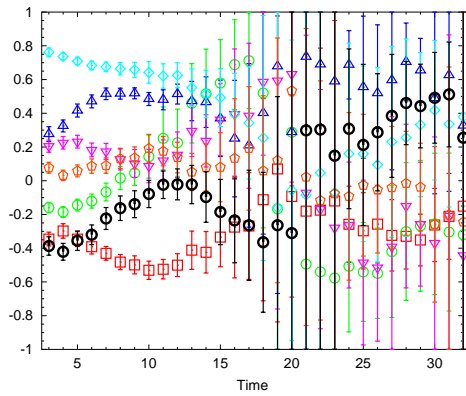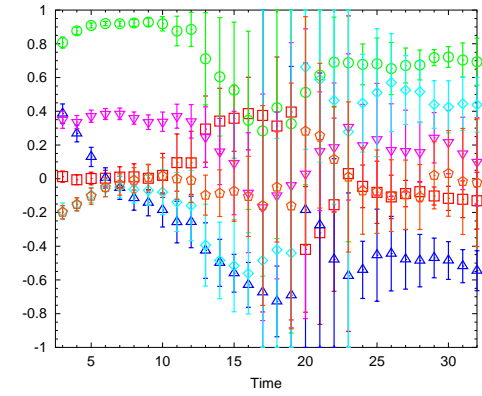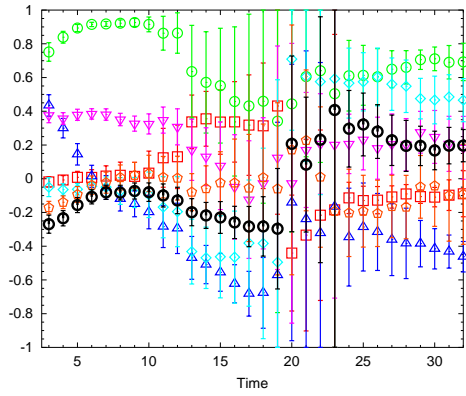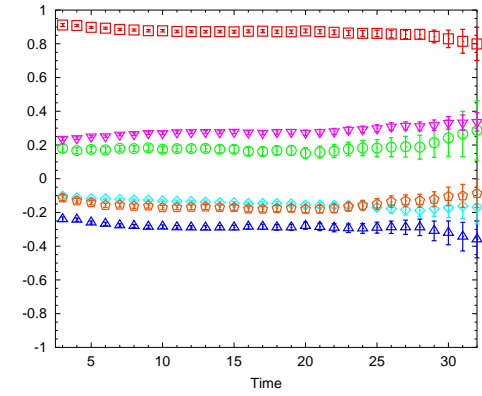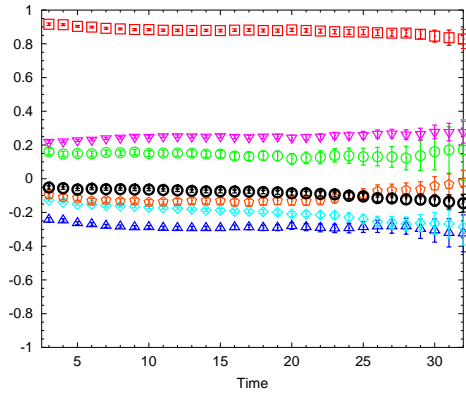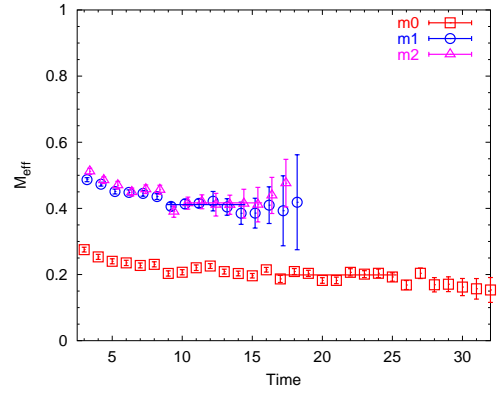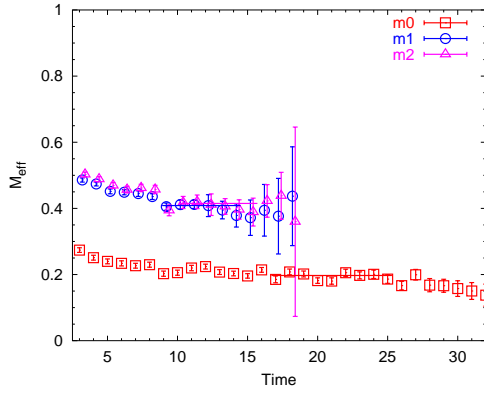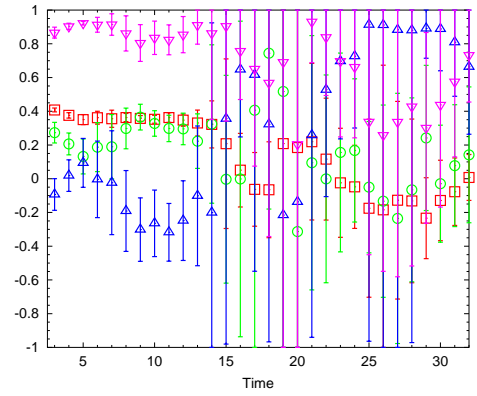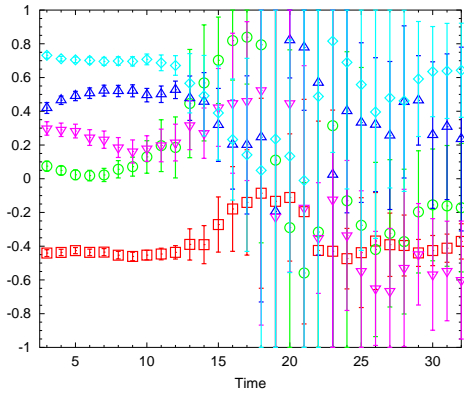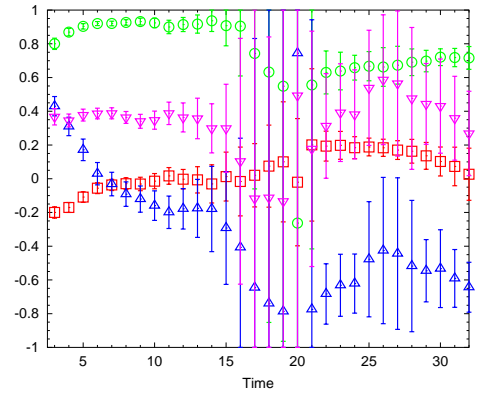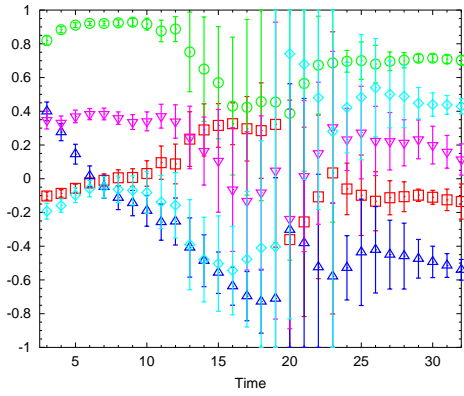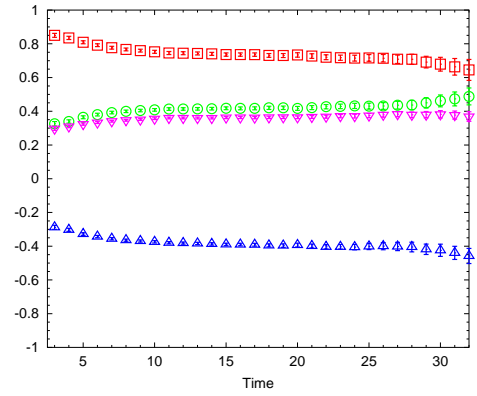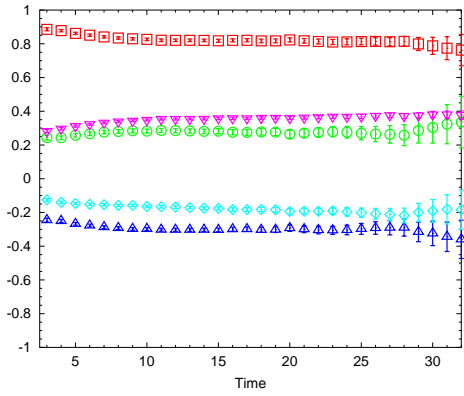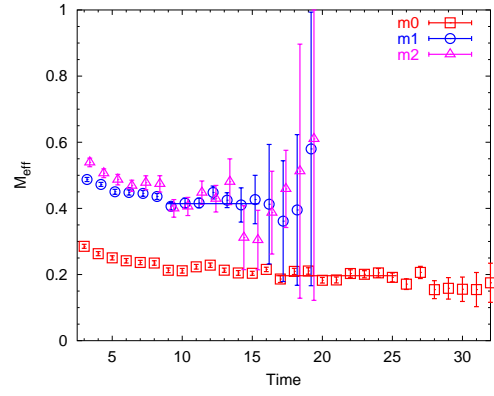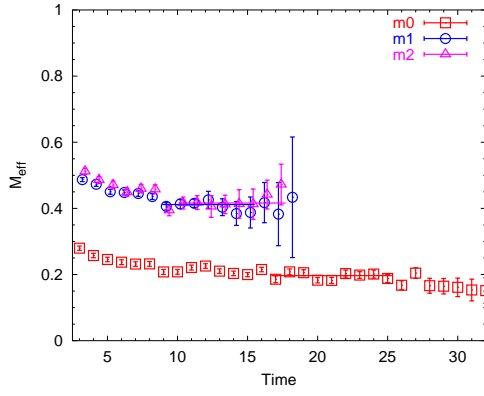
operator that contributes little to the low-lying states we are interested in. We start from the 10×10 matrix, and gradually reduce the dimension to 4×4 matrix. Matrices of dimensions less than four do not give good excited states, so we do not use them in our analysis. Operators are eliminated from the bottom entry of the list in Fig. 4.8 (d). Figure 4.9 shows the results of this stability check. Part (a) in the figure has the results for a 9×9 matrix. In the figure, the lowest three masses are on the top, the eigenvector of the ground state is shown below, that of the first-excited state is shown next and that of the second-excited state is shown at the bottom. A similar description applies for (b)-(f) in Fig. 4.9. The effective masses for the ground state and the first-excited state are fairly stable, independent of the size of matrix is used. The mass of second-excited state is also reasonably stable, except for the 4×4 matrix, where the mass is not well-determined. Eigenvectors are quite consistent for the ground state and the coefficients are almost time-independent. For the first-excited state, the eigenvectors acquire statistical noise, however the mixing ratio of a few dominant operators has a similar pattern for the 10×10 through the 4×4 matrices.

Linear χ^2 fittings to the generalized eigenvalues of the correlation matrices of different dimensions are summarized in Table 4.2. The generalized eigenvalues based on the ansatz given in Eq. (3.15) are fitted to linear functions $f(t)$ given by

$$f(t) = \ln\left[\alpha^{(n)}(t, t_0)\right] = -M_n(t - t_0). \tag{4.29}$$

Then the slope of these functions correspond to the effective mass times minus one. Table 4.2 also gives mean values of the fitted effective masses and standard deviations originating from the diagonalizations of matrices of different dimensions. These fluctuations[2] associated with different matrices are consistently smaller than statistical errors associated with fitting based on jackknife ensembles. This means that each eigenstate is quite stable with respect to the change in the dimension of correlation matrices. The fitted effective masses are plotted in Fig. 4.10 with error bars associated with statistical error by the fit.

[2]The error is based on a small ensemble. The purpose is just to give a rough comparison with the standard deviation originated from gauge fluctuations.

Table 4.2: The effective masses obtained by linear χ^2 fits to the generalized eigenvalues for the N^*, G_{1g} channel.

	M	δM	time	χ^2/N
10×10 g.s.	0.197287	0.00620658	$17-25$	1.733433
10×10 1st e.s.	0.410683	0.012763	$10-14$	0.272811
10×10 2nd e.s.	0.414346	0.0126705	$10-16$	0.229494
9×9 g.s.	0.197224	0.00622591	$17-25$	1.713066
9×9 1st e.s.	0.411411	0.0114095	$10-14$	0.150955
9×9 2nd e.s.	0.414238	0.0126516	$10-16$	0.236173
8×8 g.s.	0.197009	0.0062025	$17-25$	1.719829
8×8 1st e.s.	0.405836	0.00927867	$9-13$	0.587614
8×8 2nd e.s.	0.41408	0.0125537	$10-15$	0.188678
7×7 g.s.	0.197248	0.00617204	$17-25$	1.770641
7×7 1st e.s.	0.40868	0.00869434	$9-14$	0.195865
7×7 2nd e.s.	0.41508	0.012251	$10-15$	0.156590
6×6 g.s.	0.198792	0.00613364	$17-25$	1.763049
6×6 1st e.s.	0.411368	0.00869679	$9-14$	0.243949
6×6 2nd e.s.	0.416596	0.0128265	$10-15$	0.022378
5×5 g.s.	0.196782	0.00596678	$17-25$	1.619532
5×5 1st e.s.	0.411676	0.00947066	$9-15$	0.485028
5×5 2nd e.s.	0.416198	0.0118526	$10-17$	0.170451
4×4 g.s.	0.196348	0.00682413	$17-25$	1.738369
4×4 1st e.s.	0.414313	0.00860465	$9-15$	1.567506
4×4 2nd e.s.	$-$	$-$	$-$	$-$

	g.s.	1st e.s.	2nd e.s.
Average effective mass for different size of matrices	0.197241	0.410567	0.41509
Standard deviation	0.000760483	0.00266374	0.0010766
Largest statistical error (largest δM)	0.00682413	0.012763	0.0128265
Smallest statistical error (smallest δM)	0.00596678	0.00860465	0.0118526
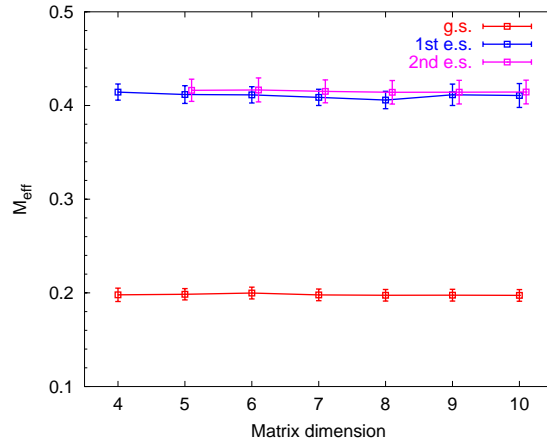
Figure 4.10: Plot of the fitted effective masses for G_{1g}. The lowest three effective masses are shown based on correlation matrices of dimension 4×4 up to 10×10. The error bars are the statistical errors of the fit.
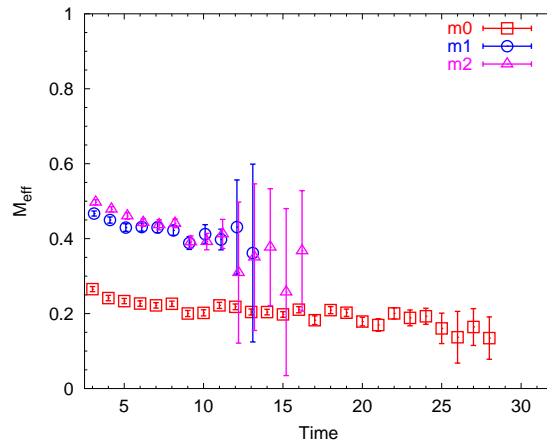
Figure 4.11: The three lightest effective masses for G_{1g} obtained by the diagonalization method based on a 13×13 correlation matrix. The error bars on the effective mass of the ground state cross zero at time-slice 29.

Certain operators must be included so that the matrix diagonalization gives clear mass splittings between low-lying states. These operators are

$$\left| \, N^* : \ G_{1g}, \ \mathrm{MA}_{\mathrm{iso}} \otimes \mathrm{MA}_{\mathrm{Drc}}, \ \overline{\Psi}^{G_{1g},k} \, \right\rangle, \quad k = 1, 2;$$

$$\left| \, N^* : \ G_{1g}, \ \mathrm{MA}_{\mathrm{iso}} \otimes \mathrm{MA}_{\mathrm{Drc}}, \ \hat{T}_1 \overline{\Psi}^{G_{1u},1} \, \right\rangle;$$

$$\left| \, N^* : \ G_{1g}, \ \mathrm{MS}_{\mathrm{iso}} \otimes \mathrm{S}_{\mathrm{Drc}}, \ \hat{T}_1 \overline{\Psi}^{G_{1u},1} \, \right\rangle.$$

Inclusion of other operators does not drastically change the spectrum. However, inclusion of certain operators that are likely to couple with noise may worsen the quality of effective mass plots. For instance, one could diagonalize a 13×13 matrix for G_{1g}, consisting of 10 operators used in Fig. 4.7, the third embedding of quasi-local operator and two E-link operators demonstrated in Fig. 4.6 (e). The result of diagonalizing this 13×13 G_{1g} correlation matrix is shown in Fig. 4.11. The obtained spectrum has a poor quality, compared to what we observed with the 10×10 matrix through 4×4 matrix.

We have applied the diagonalization method to the G_{1u} correlation matrices of various dimensions. All available operators are given in Eqs. (4.16)-(4.28) by using opposite parity of the local spinors. Like the case of G_{1g}, we also found 10 ungerade operators whose correlation matrix is diagonalizable with a spectrum stable enough to extract masses. The stability of the spectrum is examined by reducing the dimension of the matrix by eliminating operators that have less influence on low-lying states. The obtained spectrum based on a 10×10 correlation matrix is shown in Fig. 4.12. The stability tests for the G_{1u} effective masses are shown in Fig. 4.13. The dimension of the matrix is reduced down to 4×4. In the figure the lowest three masses are plotted along with the eigenvectors of the ground state and first-excited state.

The fitted effective masses are quite stable with respect to the diagonalizations of matrices of different dimensions. The fluctuations of the mean values are smaller than statistical errors caused by the fits.
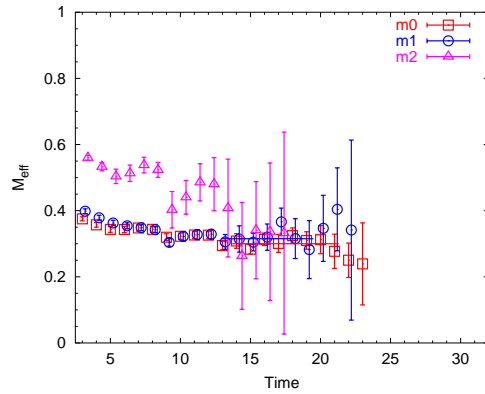
(a) Three lowest effective masses
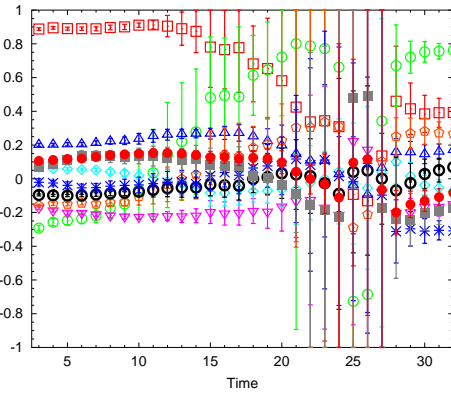
(a) Ground state
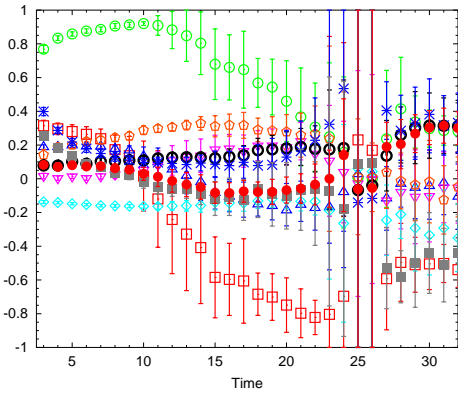
(b) first-excited state
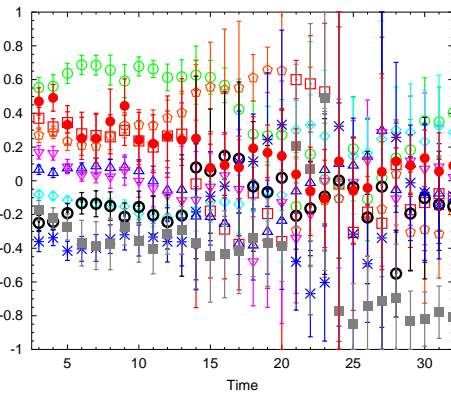
(c) second-excited state
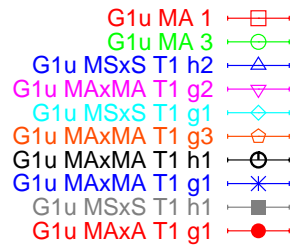
(d) Description

Figure 4.12: The two lowest effective masses of G_{1u} obtained by the diagonalization method based on a 10×10 correlation matrix and corresponding eigenvectors.

101
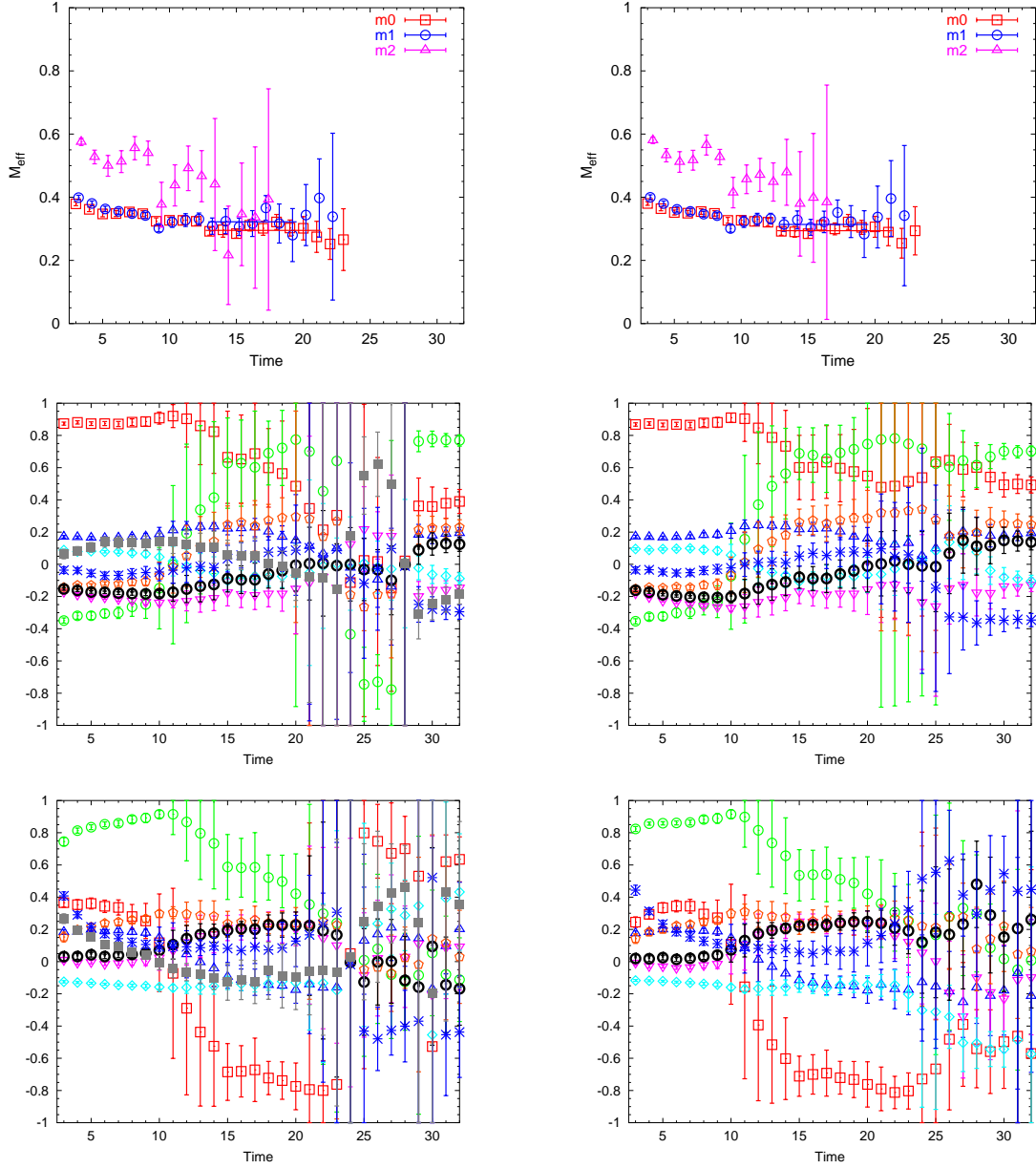
(a) 9×9

(b) 8×8

Figure 4.13: The stability check for the G_{1u} spectrum.

(c) 7×7

(d) 6×6
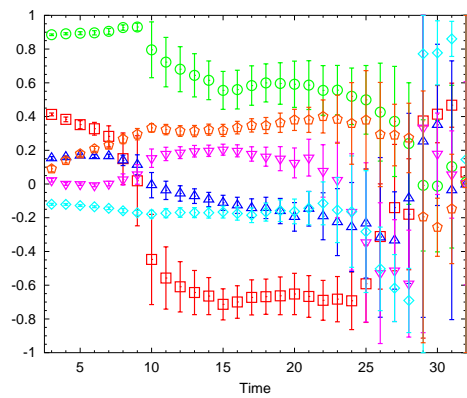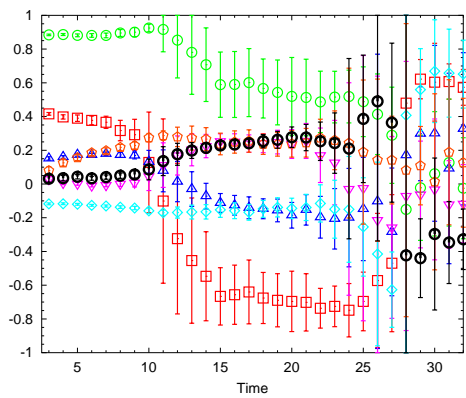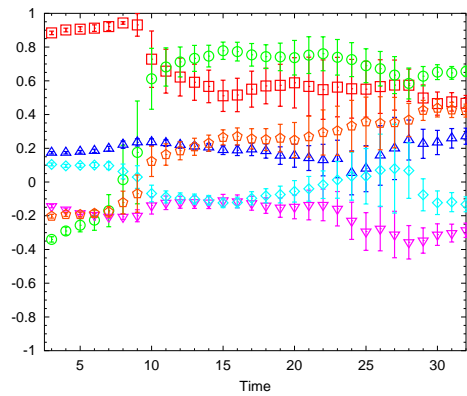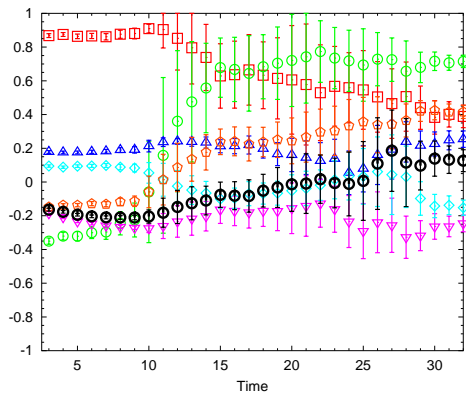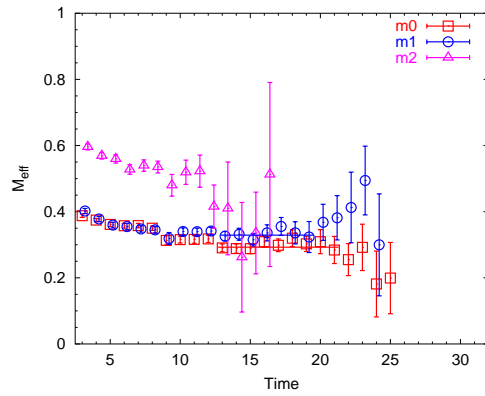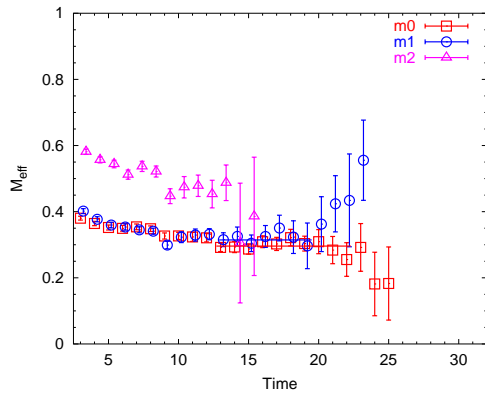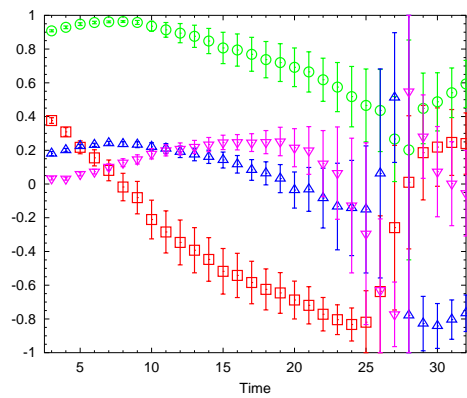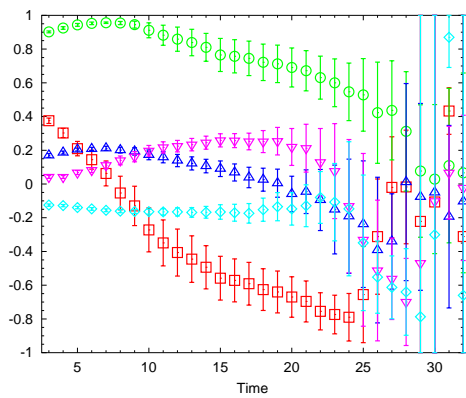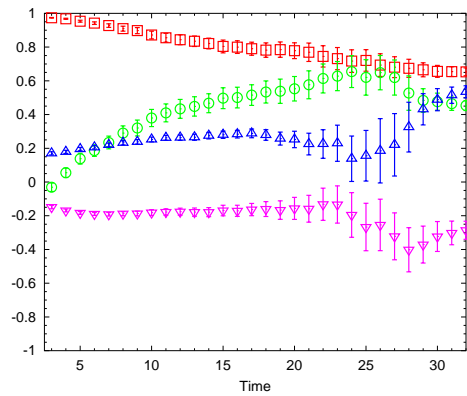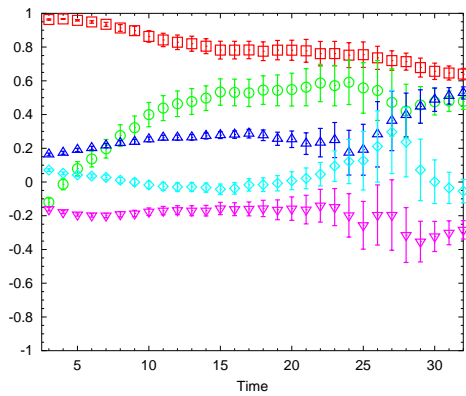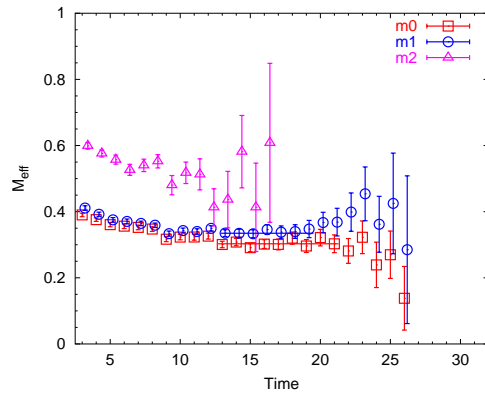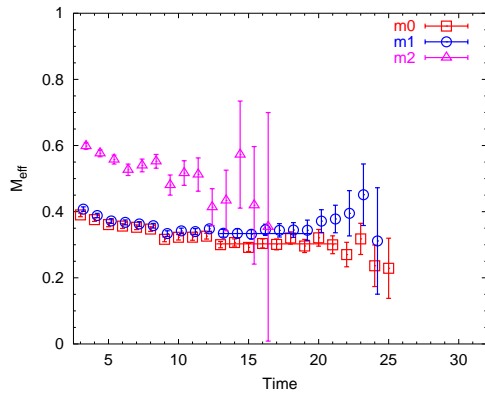
(e) 5×5 (f) 4×4

104

Table 4.3: The effective masses obtained of linear χ^2 fits to the generalized eigenvalues for the N^*, G_{1u} channel.

	M	δM	time	χ^2/N
10×10 g.s.	0.300069	0.0118569	$14-21$	0.790939
10×10 1st e.s.	0.315239	0.0174172	$13-19$	0.661942
9×9 g.s.	0.295021	0.00965541	$13-21$	0.557208
9×9 1st e.s.	0.322247	0.0194698	$13-19$	0.643443
8×8 g.s.	0.294028	0.00959138	$13-21$	0.550465
8×8 1st e.s.	0.313748	0.0191419	$13-19$	0.556882
7×7 g.s.	0.295868	0.00968092	$13-22$	0.465307
7×7 1st e.s.	0.314546	0.0189847	$13-19$	0.532433
6×6 g.s.	0.292638	0.00890889	$13-21$	0.413541
6×6 1st e.s.	0.32897	0.0140602	$13-19$	0.737918
5×5 g.s.	0.302723	0.00752812	$13-21$	0.538606
5×5 1st e.s.	0.333883	0.0113844	$13-19$	0.303935
4×4 g.s.	0.302828	0.00768184	$13-21$	0.577917
4×4 1st e.s.	0.334651	0.00979897	$13-19$	0.309060

|	g.s.	1st e.s.
Average effective mass for different size of matrices	0.297596	0.323326
Standard deviation	0.00421712	0.00919194
Largest statistical error (largest δM)	0.0118569	0.0194698
Smallest statistical error (smallest δM)	0.00752812	0.00979897
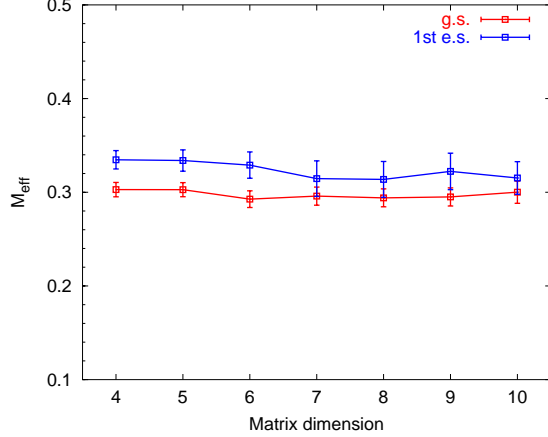
Figure 4.14: Plot of the fitted effective masses for G_{1u}. The lowest two effective masses are shown based on correlation matrices of dimension 4×4 up to 10×10. The error bars are the statistical errors of the fit.

4.4.2 The G_2 spectrum

The irreducible representations for G_2 correspond to spin $5/2$ or higher. Operators for G_2 must be constructed using nonlocally distributed quark fields because quasi-local operators can have at most spin $3/2$. Eqs. (4.30)-(4.34) below show all available G_2 operators using one-link construction,

$$\left| \, N^* : \ G_{2g}, \ \mathrm{MA_{iso}} \otimes \mathrm{MA_{Drc}}, \ \hat{T}_1 \overline{\Psi}^{H_u} \, \right\rangle ; \tag{4.30}$$

$$\left| \, N^* : \ G_{2g}, \ \mathrm{MS_{iso}} \otimes \mathrm{S_{Drc}}, \ \hat{T}_1 \overline{\Psi}^{H_u,k} \, \right\rangle , \quad k = 1, 2; \tag{4.31}$$

$$\left| \, N^* : \ G_{2g}, \ \mathrm{MA_{iso}} \otimes \mathrm{MA_{Drc}}, \ \hat{E} \overline{\Psi}^{H_g} \, \right\rangle ; \tag{4.32}$$

$$\left| \, N^* : \ G_{2g}, \ \mathrm{MS_{iso}} \otimes \mathrm{MS_{Drc}}, \ \hat{E} \overline{\Psi}^{H_g} \, \right\rangle ; \tag{4.33}$$

$$\left| \, N^* : \ G_{2g}, \ \mathrm{MS_{iso}} \otimes \mathrm{S_{Drc}}, \ \hat{E} \overline{\Psi}^{H_g,k} \, \right\rangle , \quad k = 1, 2; \tag{4.34}$$

$$\tag{4.35}$$

The effective mass plots for selected diagonal elements of G_2 correlation matrices are given in Fig. 4.15. Operators in Eqs. (4.32) and (4.33) are far too noisy, so they are excluded from the correlation matrix. Generally speaking, effective masses of G_2 are noisy and the signals do not last very long in time, which makes it difficult to extract masses.
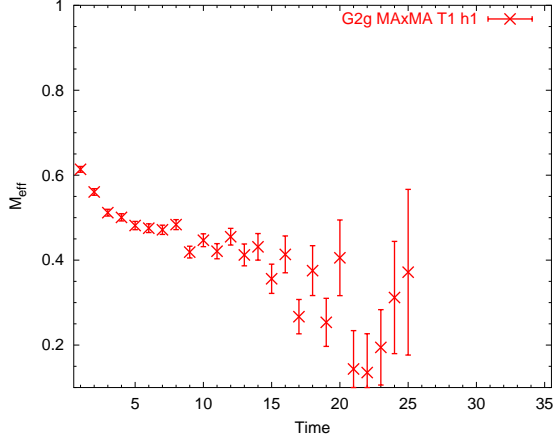
(a) Gerade, $MA_{iso} \otimes MA_{Drc}, T_1$ ops
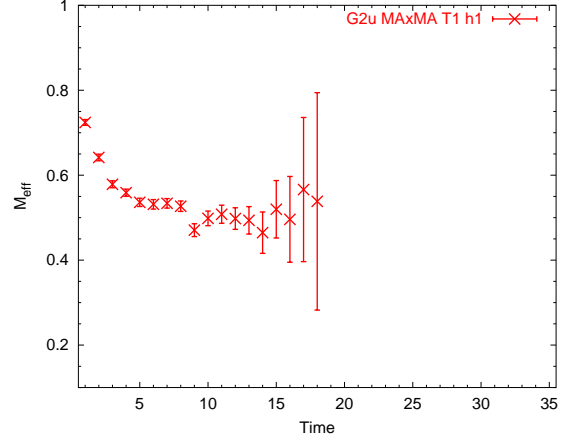
(b) Ungerade, $MA_{iso} \otimes MA_{Drc}, T_1$ ops
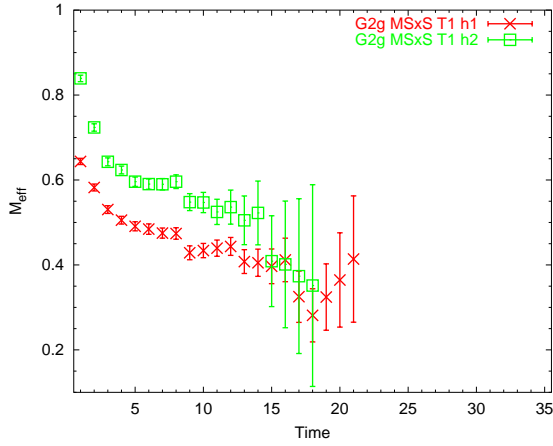
(c) Gerade, $MS_{iso} \otimes S_{Drc}, T_1$ ops
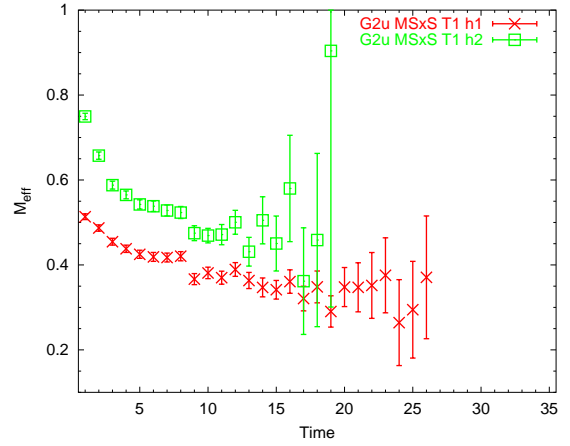
(d) Ungerade, $MS_{iso} \otimes S_{Drc}, T_1$ ops
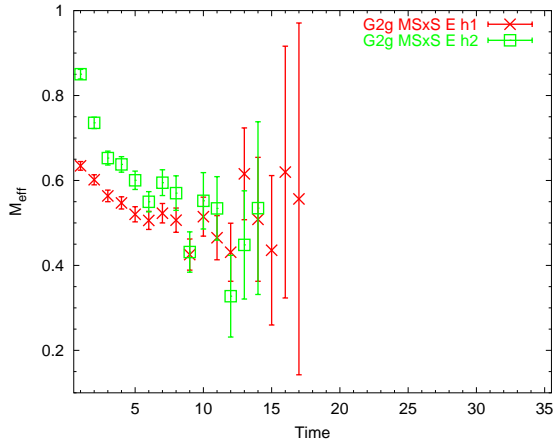
(e) Gerade, $MS_{iso} \otimes S_{Drc}, E$ ops
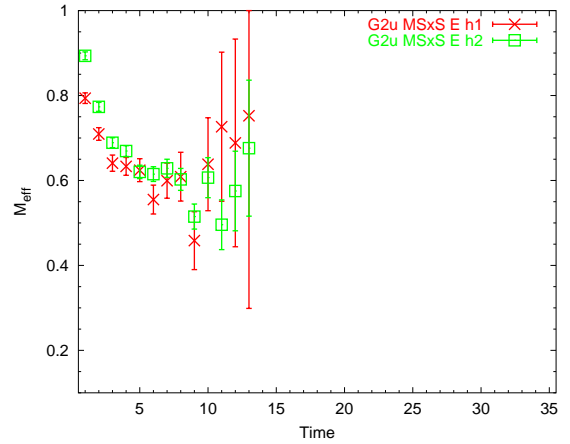
(f) Ungerade, $MS_{iso} \otimes S_{Drc}, E$ ops

Figure 4.15: The effective masses of diagonal elements of the G_2 correlation matrix. The vertical axis is in lattice units. Note that $a_t^{-1} \sim 6.0\,\text{GeV}$.

107

Table 4.4: The effective masses obtained by linear χ^2 fits to the generalized eigenvalues for the N^*, G_{2g} channel.

	M	δM	time	χ^2/N
4×4 g.s.	0.419178	0.0119531	$9-15$	0.421173
4×4 1st e.s.	0.444625	0.0100141	$9-14$	0.362973
4×4 2nd e.s.	0.548404	0.017724	$9-13$	0.436659
3×3 g.s.	0.421969	0.00983865	$9-16$	1.465589
3×3 1st e.s.	0.452819	0.0127426	$10-14$	0.349284
3×3 2nd e.s.	0.549361	0.0178778	$9-14$	0.259710
2×2 g.s.	0.421935	0.00981714	$9-16$	1.445589
2×2 1st e.s.	0.453224	0.0126099	$10-14$	0.381026
2×2 2nd e.s.	$-$	$-$	$-$	$-$

Not all operators strongly couple to the ground state. From Fig. 4.15 it is clear that the operator $\left| N^* : G_{2u}, \mathrm{MA_{iso}} \otimes \mathrm{MA_{Drc}}, \hat{T}_1 \overline{\Psi}^{H_g} \right\rangle$ (part (b) in the figure) couples to an excited state whose mass lies around 0.5 whereas the operator $\left| N^* : G_{2u}, \mathrm{MS_{iso}} \otimes \mathrm{S_{Drc}}, \hat{T}_1 \overline{\Psi}^{H_g,1} \right\rangle$ (part (d) in the figure) couples to the low-lying state whose mass lies around 0.4 or less.

Reference [37] shows spectra of G_2 for both parities. However, they used only one type of operator, namely, $\left| N^* : G_{2u}, \mathrm{MA_{iso}} \otimes \mathrm{MA_{Drc}}, \hat{T}_1 \overline{\Psi}^{H_g} \right\rangle$, for G_2 correlation functions. The effective masses corresponding to this operator are included in Fig. 4.15 part (a) and (b). Their analysis shows that the mass of the gerade state is 16% smaller than that of the ungerade state. This conclusion may not hold when a larger set of operators is used. In fact, we find in this simulation that the ungerade state is lighter than the gerade state, as we will see shortly. This is one of the reasons why using only one type of operator may be misleading. Construction of large set of operators is important for baryon spectroscopy.

The largest matrix we could diagonalize is 4×4 for G_{2g}. The lowest three effective masses are
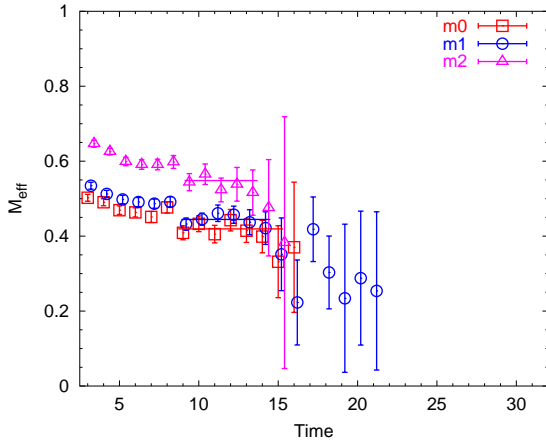
(a) Ground state
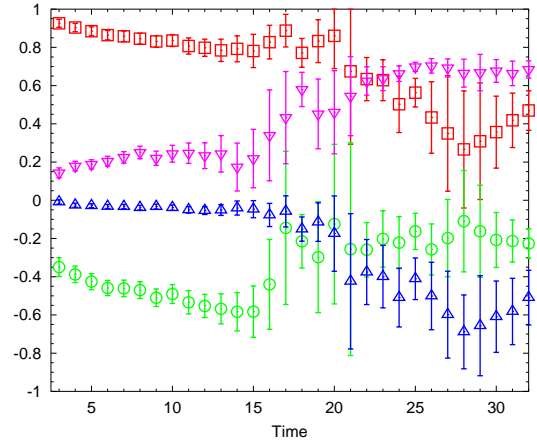
(b) Ground state eigenvector
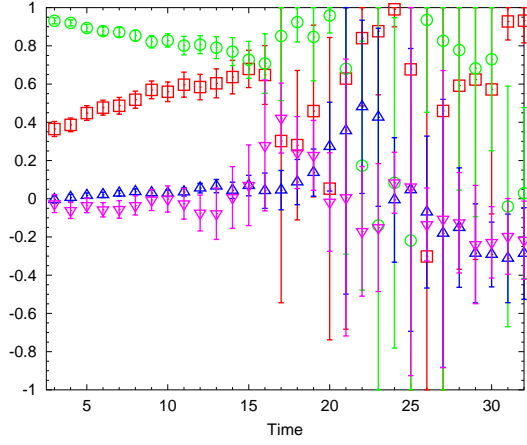
(c) first-excited state eigenvector
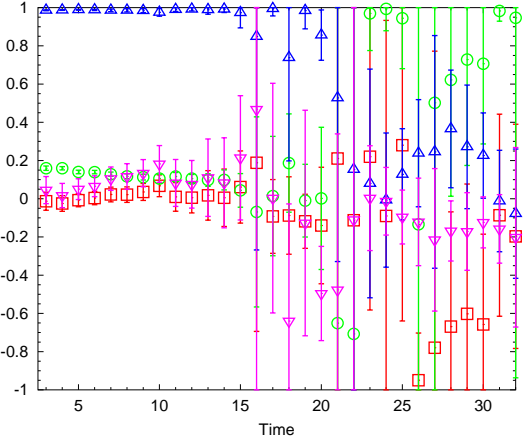
(d) second-excited state eigenvector
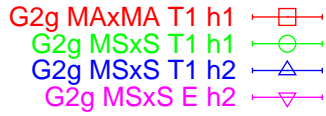
Figure 4.16: The effective masses of G_{2g} obtained by the diagonalization method based on a 4×4 correlation matrix. The lowest three masses are shown in (a) and corresponding eigenvectors are shown in (b)-(d).

(a) 3×3

(b) 2×2
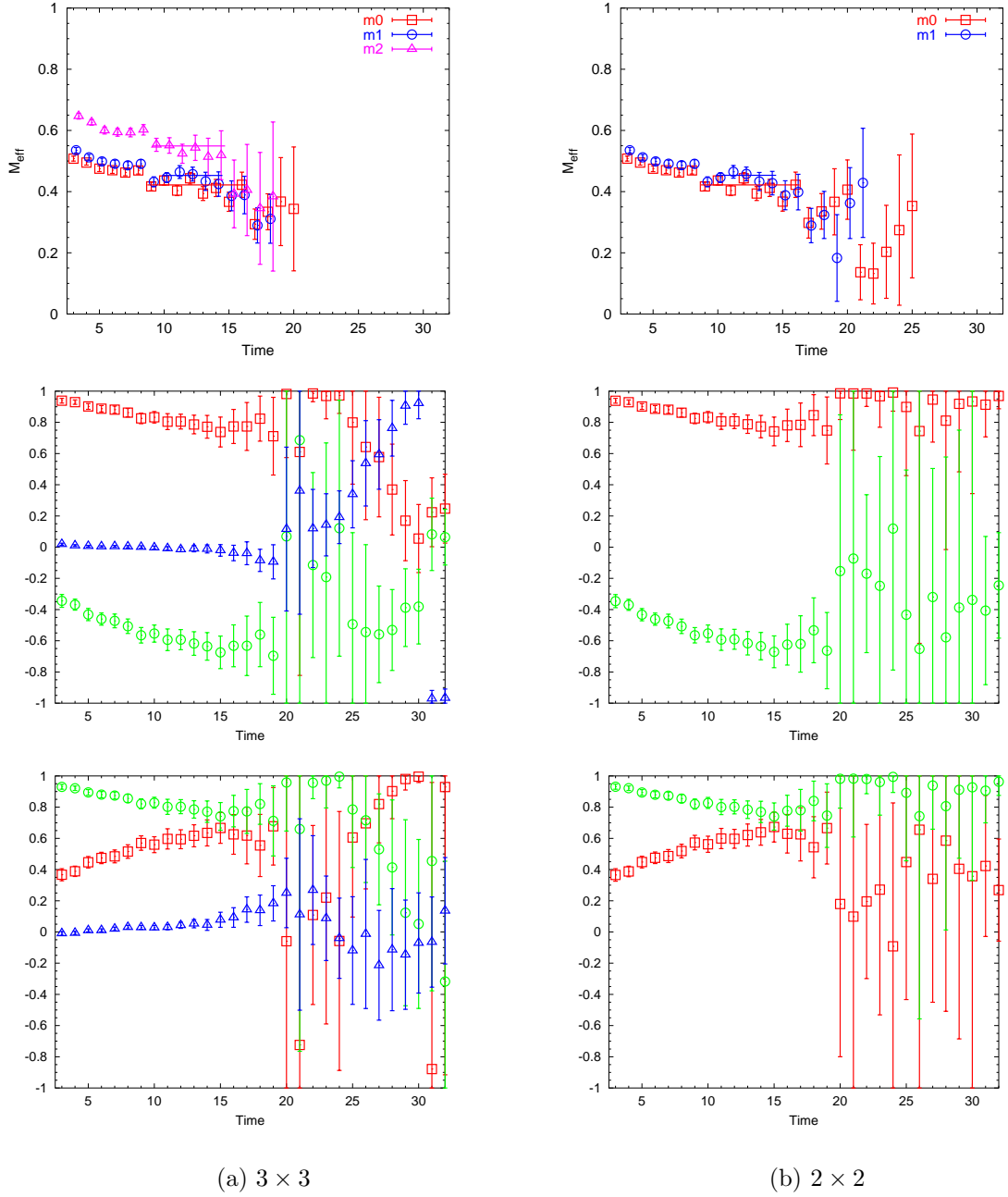
Figure 4.17: The effective masses of G_{2g} using 3×3 and 2×2 correlation matrices. The first row shows the effective masses, the second row shows eigenvectors for the ground state and the third row shows eigenvectors for the first-excited state. The description of the operators is given in Fig. 4.16.
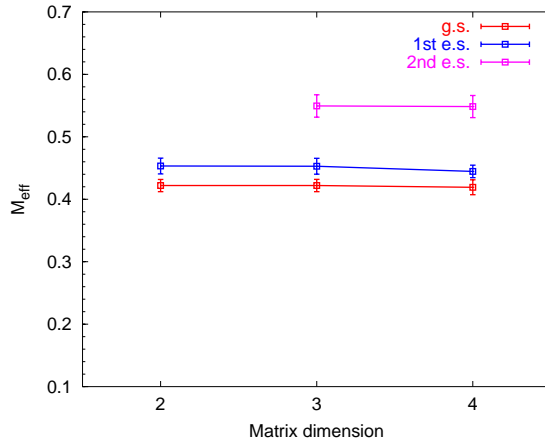
Figure 4.18: Plot of the fitted effective masses for G_{2g}. The lowest two effective masses are shown based on correlation matrices of dimension 4×4, 3×3, and 2×2. The error bars are the statistical errors of the fit.

shown in Fig. 4.16, together with eigenvectors. Even the ground state does not stay on a plateau very long in time, unlike the G_1 states. In order to extract more reliable signals, one needs lattices that are longer at least in temporal direction. Nevertheless, we could pick up seven time-slices where the ground state stays on a plateau, and also six time-slices where the first-excited state stays on a plateau. For the second-excited state of G_{2g}, the signal-to-noise ratio becomes worse, so the effective mass is not reliable. Despite the poor quality of data, the eigenvectors corresponding to these masses are fairly stable. No obvious crossover is observed for time range $t < 15$.

Operator $\left| N^* : G_{2g}, \mathrm{MA_{iso}} \otimes \mathrm{MA_{Drc}}, \hat{T}_1 \overline{\Psi}^{H_g} \right\rangle$ and operator $\left| N^* : G_{2g}, \mathrm{MS_{iso}} \otimes \mathrm{S_{Drc}}, \hat{T}_1 \overline{\Psi}^{H_g} \right\rangle$ contribute significantly to the lowest two mass eigenstates. We keep these operators and eliminate other operators to reduce the dimension of the correlation matrix. Therefore we diagonalized a 3×3 matrix and a 2×2 matrix for G_{2g}. The results are given in Fig. 4.17. The mixing ratio of the two operators mentioned above are almost the same for the lowest two mass eigenstates (open squares and open circles in the figure). This ensures the stability of the lowest two effective masses. The fitted values of effective masses for G_{2g} are plotted for different sizes of matrices in Fig. 4.18 and the detailed values of the fitting is given in Table 4.4.

111

Table 4.5: The effective masses obtained by linear χ^2 fits to the generalized eigenvalues for the N^*, G_{2u} channel.

	M	δM	time	χ^2/N
3×3 set 1 g.s.	0.32618	0.019694	$17 - 22$	0.478684
3×3 set 1 1st e.s.	0.41819	0.0273802	$13 - 17$	0.114857
3×3 set 2 g.s.	0.340569	0.0206161	$15 - 20$	0.755677
3×3 set 2 1st e.s.	0.515365	0.0175717	$10 - 16$	0.261401

For G_{2u} states, the cleanest signals are obtained by diagonalization of a 3×3 matrix of correlation functions. The effective masses and corresponding eigenvectors are given in Fig. 4.19. The ground state is fairly stable, but excited states are not. A single operator dominates the ground state eigenvector. This operator, $\left| N^* : G_{2g}, \mathrm{MS}_{\mathrm{iso}} \otimes \mathrm{S}_{\mathrm{Drc}}, \hat{T}_1 \overline{\Psi}^{H_g,1} \right\rangle$, also contributes significantly for the gerade ground state. The other two operators dominate the first-excited state. Since three operators have significant contributions to the lowest two mass eigenstates and the ground state is dominated by one operator, diagonalization of a 2×2 correlation matrix simply gives two mass eigenstates whose eigenvector component is dominated by one operator. This is trivial. So instead, we diagonalized a 3×3 matrix by replacing one operator $\left| N^* : G_{2u}, \mathrm{MS}_{\mathrm{iso}} \otimes \mathrm{S}_{\mathrm{Drc}}, \hat{T}_1 \overline{\Psi}^{H_g,2} \right\rangle$ with another operator $\left| N^* : G_{2u}, \mathrm{MS}_{\mathrm{iso}} \otimes \mathrm{S}_{\mathrm{Drc}}, \hat{E} \overline{\Psi}^{H_u,1} \right\rangle$ to see if the first-excited state still carries the same mass. Results obtained by diagonalizing this second set of 3×3 correlation matrix are given in Fig. 4.20 in a similar fashion. We could diagonalize another set of 3×3 matrix, but it results in a noisier ground state effective mass, so we do not show the results here.

The linear χ^2 fits to the two sets of 3×3 matrices of G_{2u} are performed and summarized in Table 4.5. The fitted mass values for the ground state have a difference of about 4.2% between the set 1 and set 2 matrices, but the statistical error bars overlap. The excited states have very different fitted values. This means that the stability of the first-excited state is poor. We need more operators to obtain a reliable first-excited state mass for G_{2u}.
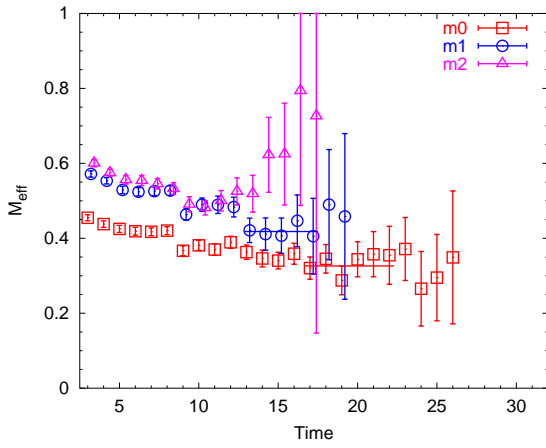
(a) Ground state
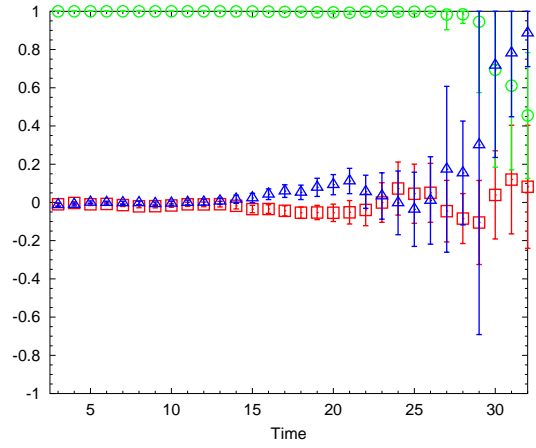
(b) Ground state eigenvector
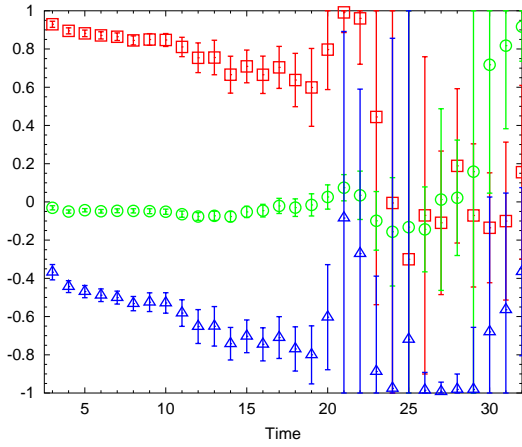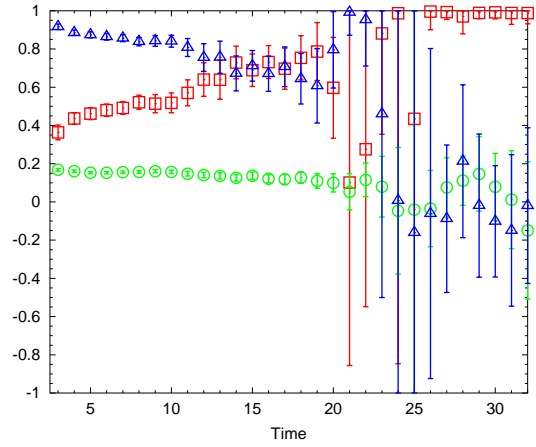
(c) first-excited state eigenvector

(d) second-excited state eigenvector

Figure 4.19: The effective masses of G_{2u} obtained by the diagonalization method based on the first set of 3×3 correlation matrix. The lowest three masses are shown in (a) and corresponding eigenvectors are shown in (b)-(d).

113
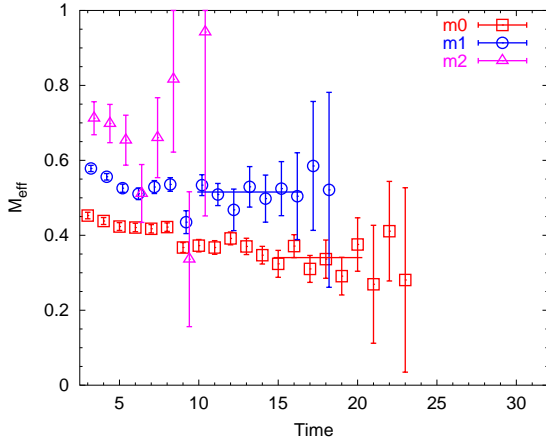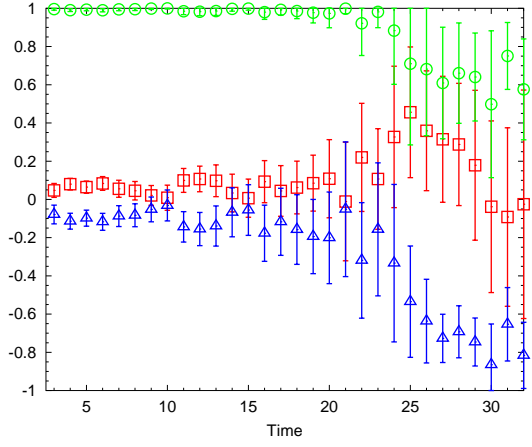
(a) Ground state
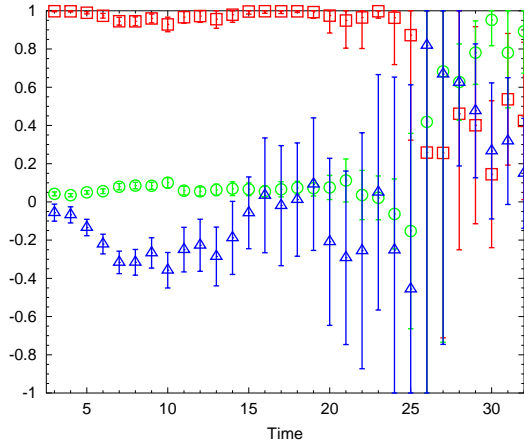
(b) Ground state eigenvector
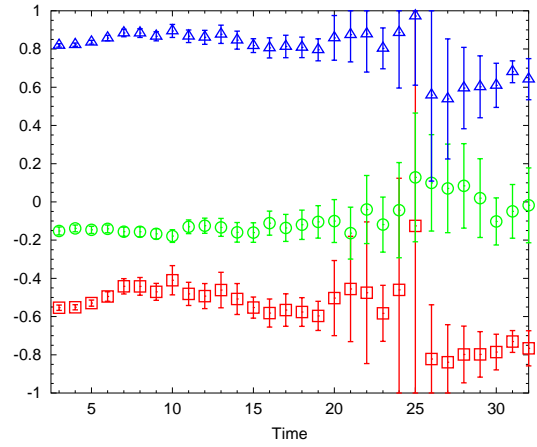
(c) first-excited state eigenvector

(d) second-excited state eigenvector

Figure 4.20: The effective masses of G_{2u} obtained by the diagonalization method based on the second 3×3 correlation matrix. The lowest three masses are shown in (a) and corresponding eigenvectors are shown in (b)-(d).

4.4.3 The H spectrum

The H irreps correspond to spin $3/2, 5/2, 7/2$, *etc.* It is expected that the spectrum of H that reflects spin $5/2$ resembles that of G_2, because G_2 also couples to spin $5/2$. The spectrum of H that reflects spin $3/2$ should be distinct from spin $5/2$, though their masses may be close.

The number of available operators for H using quasi-local and one-link construction is 28, which is the largest set among G_1, G_2, and H. All available operators are given in Eqs. (4.36)-(4.53).

$$\left| N^* : H_g, \ \mathrm{MA_{iso}} \otimes \mathrm{MA_{Drc}}, \ \overline{\Psi}^{H_g} \right\rangle ; \tag{4.36}$$

$$\left| N^* : H_g, \ \mathrm{MA_{iso}} \otimes \mathrm{MA_{Drc}}, \ \hat{T}_1 \overline{\Psi}^{G_{1u},k} \right\rangle , \quad k = 1, 2, 3; \tag{4.37}$$

$$\left| N^* : H_g, \ \mathrm{MA_{iso}} \otimes \mathrm{MA_{Drc}}, \ \hat{T}_1 \overline{\Psi}^{H_u} \right\rangle ; \tag{4.38}$$

$$\left| N^* : H_g, \ \mathrm{MA_{iso}} \otimes \mathrm{MA_{Drc}}, \ \hat{T}_1 \overline{\Psi}^{H'_u} \right\rangle ; \tag{4.39}$$

$$\left| N^* : H_g, \ \mathrm{MA_{iso}} \otimes \mathrm{MA_{Drc}}, \ \hat{E} \overline{\Psi}^{G_{1g},k} \right\rangle , \quad k = 1, 2, 3; \tag{4.40}$$

$$\left| N^* : H_g, \ \mathrm{MA_{iso}} \otimes \mathrm{MA_{Drc}}, \ \hat{E} \overline{\Psi}^{H_g} \right\rangle ; \tag{4.41}$$

$$\left| N^* : H_g, \ \mathrm{MA_{iso}} \otimes \mathrm{MA_{Drc}}, \ \hat{A}_1 \overline{\Psi}^{H_g} \right\rangle ; \tag{4.42}$$

$$\left| N^* : H_g, \ \mathrm{MA_{iso}} \otimes \mathrm{A_{Drc}}, \ \hat{T}_1 \overline{\Psi}^{G_{1u}} \right\rangle ; \tag{4.43}$$

$$\left| N^* : H_g, \ \mathrm{MA_{iso}} \otimes \mathrm{A_{Drc}}, \ \hat{E} \overline{\Psi}^{G_{1g}} \right\rangle ; \tag{4.44}$$

$$\left| N^* : H_g, \ \mathrm{MS_{iso}} \otimes \mathrm{MS_{Drc}}, \ \hat{E} \overline{\Psi}^{G_{1g},k} \right\rangle , \quad k = 1, 2, 3; \tag{4.45}$$

$$\left| N^* : H_g, \ \mathrm{MS_{iso}} \otimes \mathrm{MS_{Drc}}, \ \hat{E} \overline{\Psi}^{H_g} \right\rangle ; \tag{4.46}$$

$$\left| N^* : H_g, \ \mathrm{MS_{iso}} \otimes \mathrm{MS_{Drc}}, \ \hat{A}_1 \overline{\Psi}^{H_g} \right\rangle ; \tag{4.47}$$

$$\left| N^* : H_g, \ \mathrm{MS_{iso}} \otimes \mathrm{S_{Drc}}, \ \hat{T}_1 \overline{\Psi}^{G_{1u}} \right\rangle ; \tag{4.48}$$

$$\left| N^* : H_g, \ \mathrm{MS_{iso}} \otimes \mathrm{S_{Drc}}, \ \hat{T}_1 \overline{\Psi}^{H_u,k} \right\rangle , \quad k = 1, 2; \tag{4.49}$$

$$\left| N^* : H_g, \ \mathrm{MS_{iso}} \otimes \mathrm{S_{Drc}}, \ \hat{T}_1 \overline{\Psi}^{H'_u,k} \right\rangle , \quad k = 1, 2; \tag{4.50}$$

$$\left| N^* : H_g, \ \mathrm{MS_{iso}} \otimes \mathrm{S_{Drc}}, \ \hat{E} \overline{\Psi}^{G_{1g}} \right\rangle ; \tag{4.51}$$

$$\left| N^* : H_g, \ \mathrm{MS_{iso}} \otimes \mathrm{S_{Drc}}, \ \hat{E} \overline{\Psi}^{H_g,k} \right\rangle , \quad k = 1, 2; \tag{4.52}$$

$$\left| N^* : H_g, \ \mathrm{MS_{iso}} \otimes \mathrm{S_{Drc}}, \ \hat{A}_1 \overline{\Psi}^{H_g,k} \right\rangle , \quad k = 1, 2. \tag{4.53}$$

In Eqs. (4.39) and (4.50) the operators have a prime $\hat{T}_1 \overline{\Psi}^{H'_u}$, specifying that continuum Clebsch-Gordan coefficients of SU(2) do not apply. Continuum Clebsch-Gordan coefficients apply for every unprimed operator.

Representative effective masses for H_g and H_u for quasi-local, T_1, and E one-link operators are shown in Fig. 4.21. Correlation functions of same source and sink are used. Like the case of G_1 the same tendency of the masses is observed, i.e., the quasi-local operators couple to the lightest mass and give the cleanest signals, the T_1-link operators are the next, and the E-link operators couple to heavy masses and are most contaminated. Operators of Eqs. (4.41), (4.42), (4.45), and (4.46) are too noisy, so they are excluded from the analysis.

The largest matrix we analyze is the 12×12 for H_g and is also the 12×12 for H_u. Matrices of dimension larger than 12 are either not diagonalizable or result in too noisy a spectrum. Especially, it is true that inclusion of E-link operators likely introduces noise, so we did not include E-link operators in the matrices. Let us show the lowest six effective masses obtained by the diagonalization in Fig. 4.22. Both gerade and ungerade masses are given in the figure. It is evident from the figure that for H_g masses, the mass splittings are very small among the lowest five or six eigenstates. This is one of the features of H_g spectrum. Mass separations are much larger, say, in the G_{1g} spectrum. The eigenvectors corresponding to the lowest four mass eigenstates based on 12×12 H_g correlation matrix are shown in Fig. 4.23. Similarly, The eigenvectors corresponding to the lowest four mass eigenstates based on 12×12 H_u correlator matrix are shown in Fig. 4.24.

The stability of the eigenvectors (and eigenvalues) is examined by reducing the dimension of correlator matrices. The lowest dimension we analyze is 4×4 for H_g, and is also 4×4 for H_u. Plots for the obtained effective masses and eigenvectors are a little too lengthy, so we do not provide them here. Instead, we simply summarize the linear χ^2 fitted values in Table 4.6 and Table 4.7 for H_g and H_u, respectively. These fitted values are plotted with respect to the matrix dimension in Fig. 4.25. The mean values of fitted effective masses do not depend much on the dimensions of matrices. However, in H_g eigenstates, the masses of the excited states tend to decrease as the matrix dimension increases. As the dimension of a correlation matrix increases, more operators are
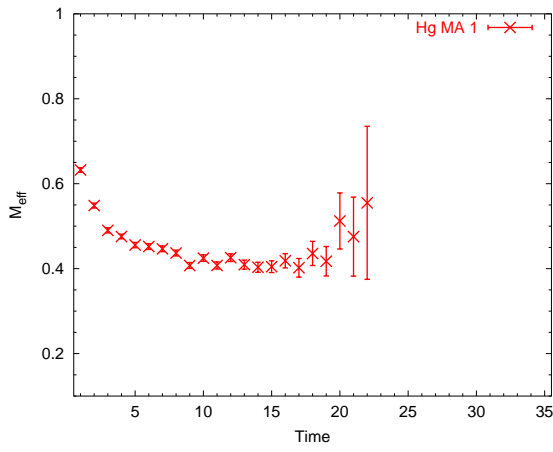
(a) H_g, quasi-local op
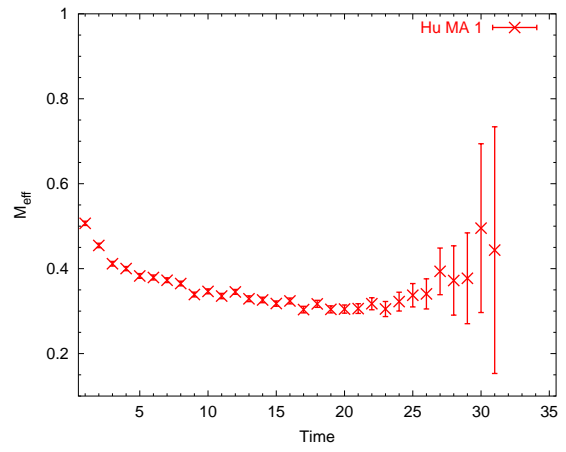
(b) H_u, quasi-local op
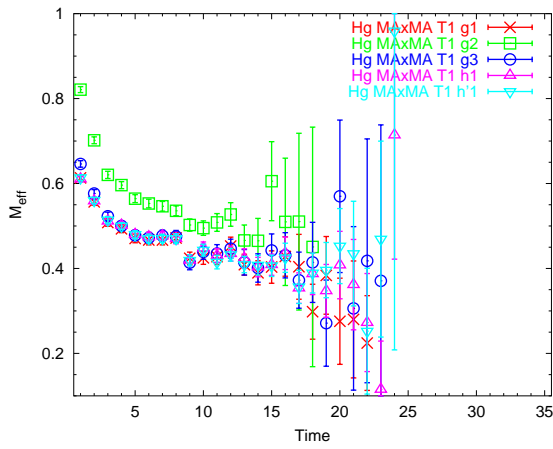
(c) H_g, $\mathrm{MA_{iso}} \otimes \mathrm{MA_{Drc}}, T_1$ ops
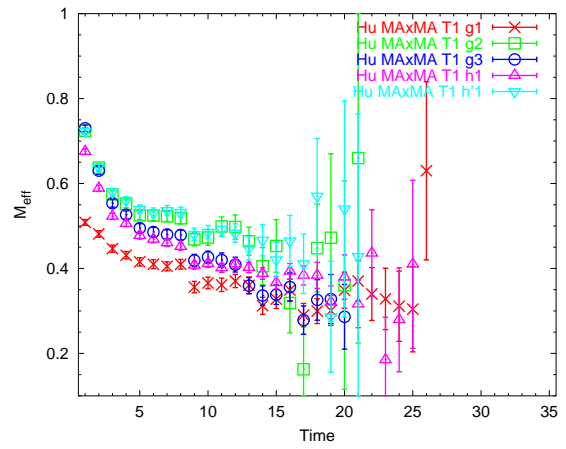
(d) H_u, $\mathrm{MA_{iso}} \otimes \mathrm{MA_{Drc}}, T_1$ ops
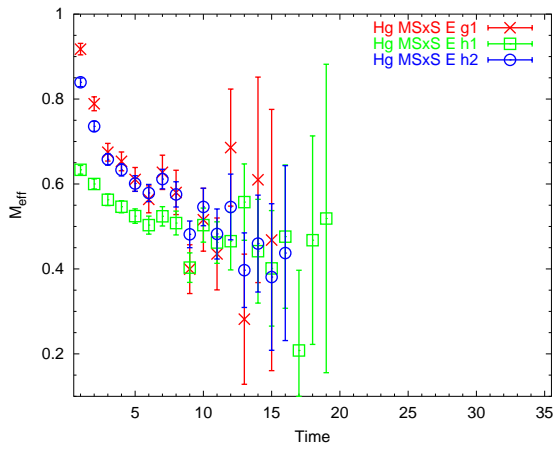
(e) H_g, $\mathrm{MS_{iso}} \otimes \mathrm{S_{Drc}}, E$ ops
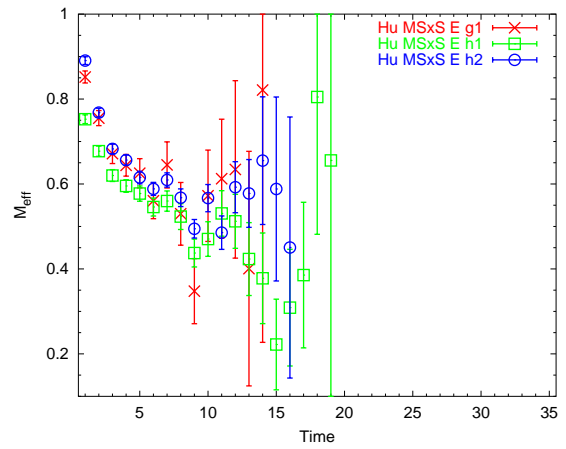
(f) H_u, $\mathrm{MS_{iso}} \otimes \mathrm{S_{Drc}}, E$ ops

Figure 4.21: The effective masses of the diagonal elements of the H correlation matrix. The vertical axis is in lattice units.
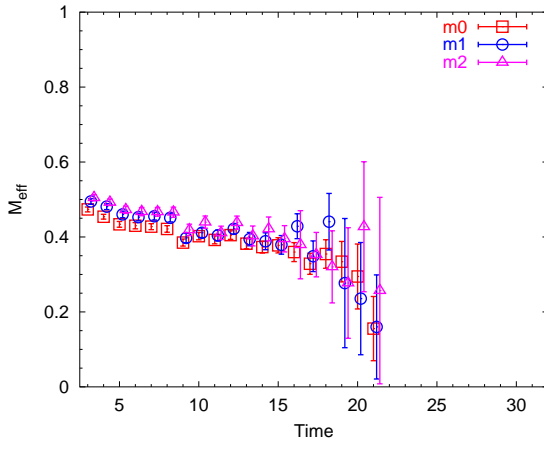
(a) H_g lowest three
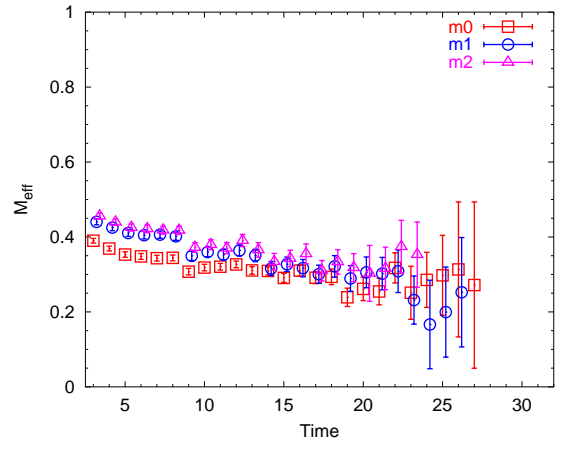
(b) H_u lowest three
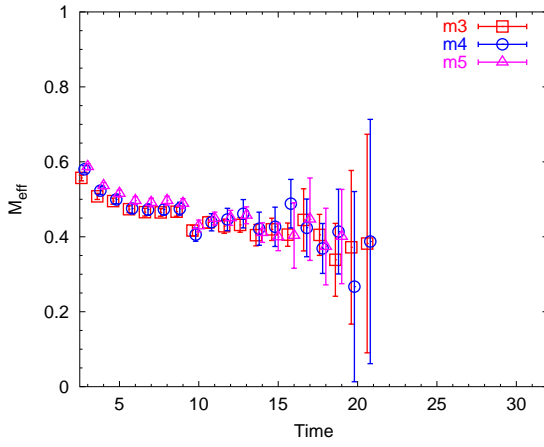
(c) H_g 3rd-5th excited states
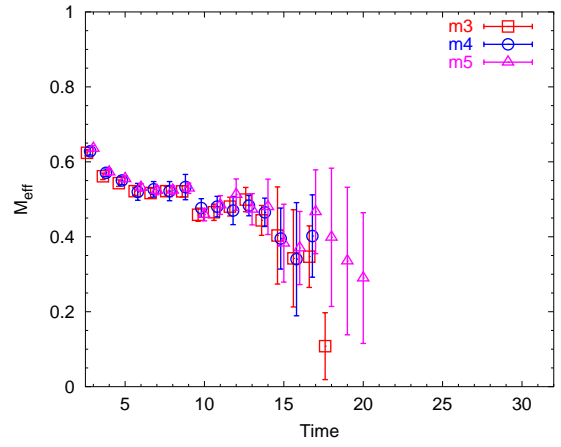
(d) H_u 3rd-5th excited states
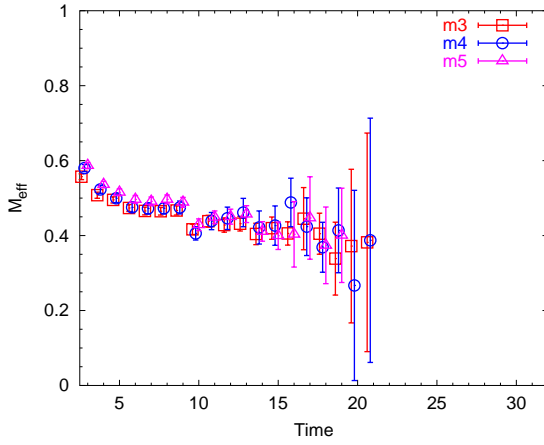
(c) H_g 6th-8th excited states
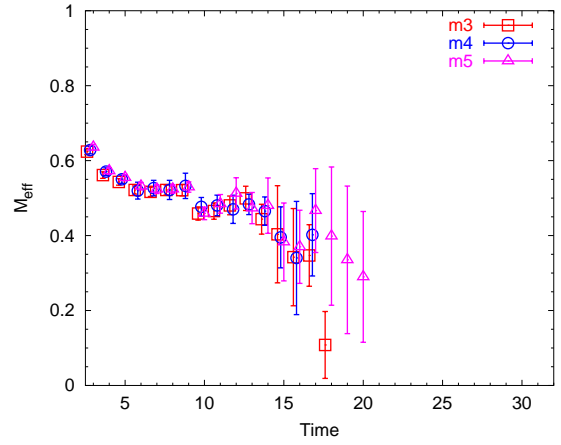
(d) $H_u u$ 6th-8th excited states

Figure 4.22: The effective masses of low-lying mass eigenstates based on a 12×12 correlation matrices for H_g and H_u.

(a)

(b)

(c)

(d)

Hg MA 1
Hg MAxA T1 g1
Hg MAxMA T1 g3
Hg MAxMA T1 h1
Hg MAxMA T1 g1
Hg MSxS T1 h2
Hg MAxMA T1 g2
Hg MSxS T1 h'1
Hg MSxS T1 h'2
Hg MAxMA T1 h'1
Hg MSxS T1 g1
Hg MSxS T1 h1
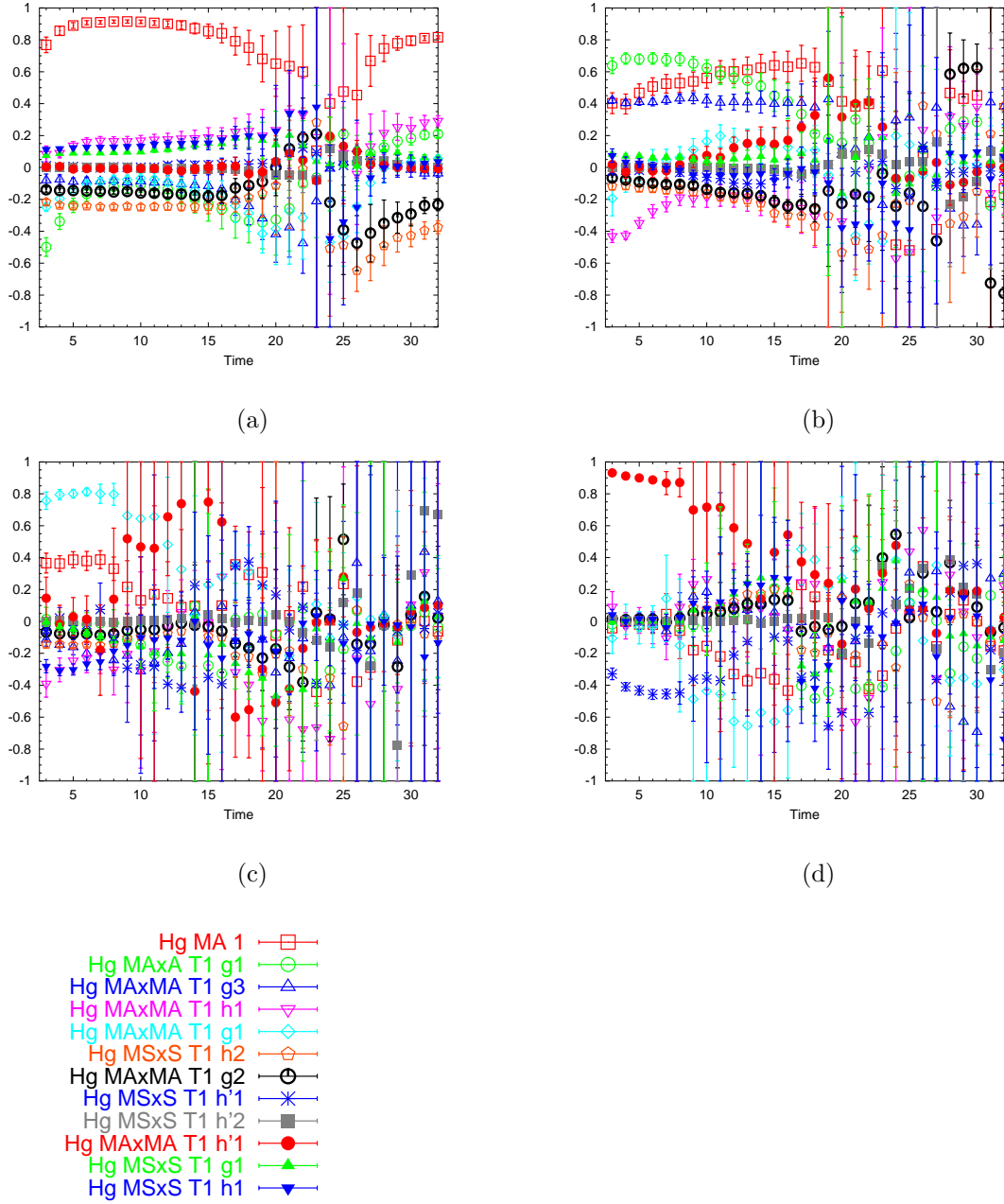
Figure 4.23: The eigenvectors corresponding to the lowest four effective masses based on a 12×12 correlation matrix for H_g. Part (a) shows the eigenvector of the lowest mass, part (b) shows the eigenvector of the first-excited state. part (c) shows the eigenvector of the second-excited state, and part (d) shows the eigenvector of the third-excited state.
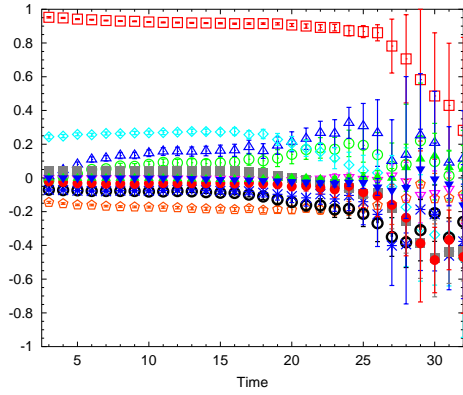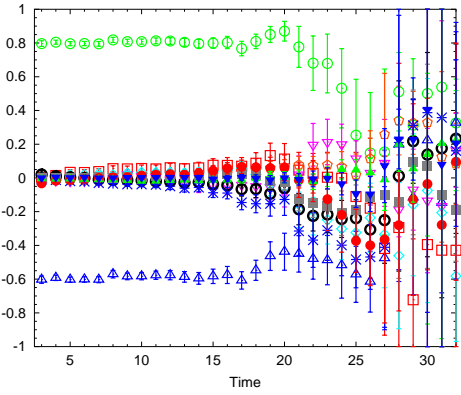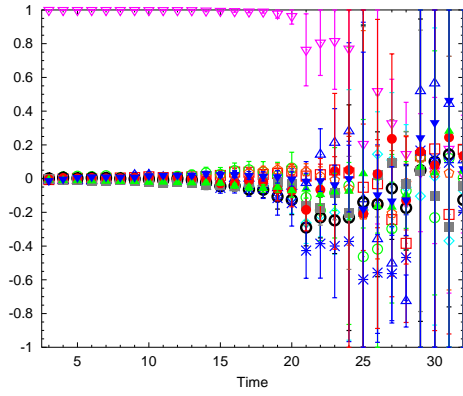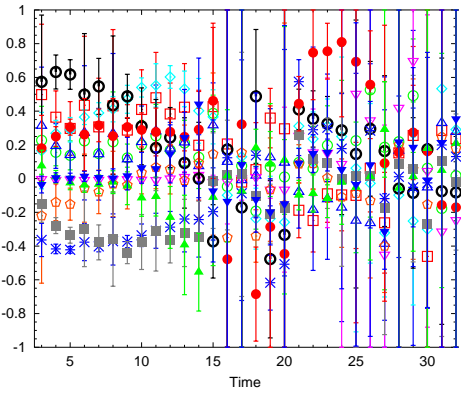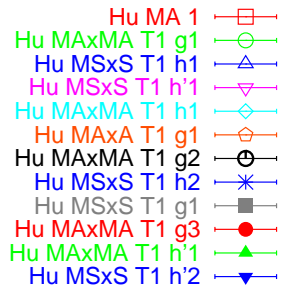
Figure 4.24: The eigenvectors corresponding to the lowest four effective masses based on a 12×12 correlation matrix for H_u. Part (a) shows the eigenvector of the lowest mass, part (b) shows the eigenvector of the first-excited state, part (c) shows the eigenvector of the second-excited state, and part (d) shows the eigenvector of the third-excited state.

Table 4.6: The effective masses obtained by linear χ^2 fits to the generalized eigenvalues for the N^*, H_g channel.

	M	δM	time	χ^2/N
12×12 g.s.	0.397209	0.00782107	$10-15$	1.208325
12×12 1st e.s.	0.406735	0.00695646	$9-15$	0.648227
12×12 2nd e.s.	0.424591	0.00908677	$9-15$	0.434407
12×12 3rd e.s.	0.424962	0.00847421	$9-15$	0.561533
11×11 g.s.	0.400324	0.00798338	$10-15$	1.438357
11×11 1st e.s.	0.406798	0.00695887	$9-15$	0.591598
11×11 2nd e.s.	0.424875	0.00854806	$9-15$	0.628917
11×11 3rd e.s.	0.427823	0.0110111	$9-15$	0.411966
10×10 g.s.	0.402362	0.00788071	$10-15$	1.601315
10×10 1st e.s.	0.407032	0.00695363	$9-15$	0.637982
10×10 2nd e.s.	0.423677	0.00863921	$9-16$	0.668653
10×10 3rd e.s.	0.436486	0.0112902	$9-15$	0.688714
9×9 g.s.	0.398862	0.00684633	$9-14$	1.456906
9×9 1st e.s.	0.408268	0.00720867	$9-15$	0.648469
9×9 2nd e.s.	0.431488	0.00951856	$9-15$	0.143450
9×9 3rd e.s.	0.436888	0.0111245	$9-15$	0.701409
8×8 g.s.	0.398896	0.00684647	$9-14$	1.445429
8×8 1st e.s.	0.408282	0.00720788	$9-15$	0.647726
8×8 2nd e.s.	0.431558	0.00923279	$9-16$	0.123090
8×8 3rd e.s.	0.442231	0.0119143	$10-17$	0.382061

	M	δM	time	χ^2/N
7×7 g.s.	0.399015	0.0068542	$9 - 14$	1.476761
7×7 1st e.s.	0.408598	0.00725482	$9 - 15$	0.671899
7×7 2nd e.s.	0.432929	0.0125404	$9 - 14$	0.542164
7×7 3rd e.s.	0.447449	0.0146957	$10 - 15$	0.374078
6×6 g.s.	0.400496	0.00631915	$9 - 15$	1.478361
6×6 1st e.s.	0.412834	0.00672509	$9 - 15$	0.641335
6×6 2nd e.s.	0.433497	0.0124985	$9 - 14$	0.538730
6×6 3rd e.s.	0.447602	0.0148047	$10 - 15$	0.363067
5×5 g.s.	0.400894	0.00609504	$9 - 15$	1.412278
5×5 1st e.s.	0.41705	0.00611911	$9 - 15$	0.708278
5×5 2nd e.s.	0.433455	0.0124723	$9 - 14$	0.520266
5×5 3rd e.s.	0.447428	0.0145539	$10 - 15$	0.374199
4×4 g.s.	0.406357	0.00616342	$9 - 15$	1.400649
4×4 1st e.s.	0.417024	0.00615963	$9 - 15$	0.702313
4×4 2nd e.s.	0.447446	0.0169468	$10 - 17$	0.289255
4×4 3rd e.s.	$-$	$-$	$-$	$-$

	g.s.	1st e.s.	2nd e.s.
Average effective mass for different size of matrices	0.400491	0.410291	0.431502
Standard deviation	0.00265162	0.00424185	0.00721937
Largest statistical error (largest δM)	0.00798338	0.00725482	0.0169468
Smallest statistical error (smallest δM)	0.00609504	0.00611911	0.00854806

Table 4.7: The effective masses obtained by linear χ^2 fits to the generalized eigenvalues for the N^*, H_u channel.

	M	δM	time	χ^2/N
12×12 g.s.	0.302357	0.00924202	$14-18$	1.083966
12×12 1st e.s.	0.317845	0.0112956	$14-21$	0.255208
12×12 2nd e.s.	0.335562	0.0137541	$14-21$	0.363828
12×12 3rd e.s.	0.470108	0.0117967	$9-13$	0.439419
11×11 g.s.	0.302569	0.00920345	$14-18$	1.076838
11×11 1st e.s.	0.317852	0.0113052	$14-21$	0.255895
11×11 2nd e.s.	0.335614	0.0138078	$14-21$	0.365788
11×11 3rd e.s.	0.471825	0.0116727	$9-13$	0.620016
10×10 g.s.	0.302612	0.00920978	$14-18$	1.095235
10×10 1st e.s.	0.317822	0.0113082	$14-21$	0.257335
10×10 2nd e.s.	0.335973	0.0137785	$14-21$	0.369091
10×10 3rd e.s.	$-$	$-$	$-$	$-$
9×9 g.s.	0.302547	0.00918724	$14-18$	0.986169
9×9 1st e.s.	0.318442	0.0112113	$14-21$	0.277202
9×9 2nd e.s.	0.335417	0.0135823	$14-22$	0.345609
9×9 3rd e.s.	$-$	$-$	$-$	$-$
8×8 g.s.	0.302259	0.00927233	$14-18$	0.850446
8×8 1st e.s.	0.318577	0.0108257	$14-22$	0.226296
8×8 2nd e.s.	0.338642	0.0141648	$14-18$	0.607318
8×8 3rd e.s.	$-$	$-$	$-$	$-$

	M	δM	time	χ^2/N
7×7 g.s.	0.303128	0.00894899	14−18	0.852205
7×7 1st e.s.	0.321727	0.0105883	14−22	0.291965
7×7 2nd e.s.	0.338775	0.0137574	14−19	0.469439
7×7 3rd e.s.	−	−	−	−
6×6 g.s.	0.305927	0.00853894	14−18	0.880801
6×6 1st e.s.	0.322143	0.0105563	14−22	0.307807
6×6 2nd e.s.	0.33921	0.0142164	14−18	0.635638
6×6 3rd e.s.	−	−	−	−
5×5 g.s.	0.311723	0.00797625	14−18	0.469662
5×5 1st e.s.	0.322192	0.0105992	14−22	0.301117
5×5 2nd e.s.	0.339462	0.0139342	14−19	0.471212
5×5 3rd e.s.	−	−	−	−
4×4 g.s.	0.31552	0.00808784	14−18	0.368656
4×4 1st e.s.	0.322728	0.0106756	14−22	0.344622
4×4 2nd e.s.	0.339447	0.0139307	14−19	0.470106
4×4 3rd e.s.	−	−	−	−

	g.s.	1st e.s.	2nd e.s.
Average effective mass for different size of matrices	0.305405	0.319925	0.337567
Standard deviation	0.00488476	0.00218591	0.00185194
Largest statistical error (largest δM)	0.00927233	0.0113082	0.0142164
Smallest statistical error (smallest δM)	0.00797625	0.0105563	0.0135823
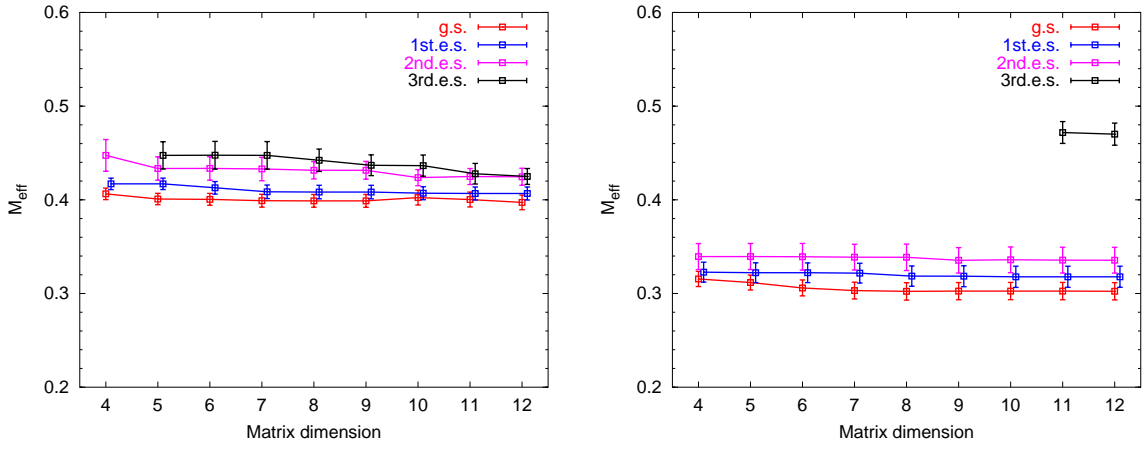
Figure 4.25: Plot of the fitted effective masses for H_g (left) and H_u (right). The lowest four effective masses are shown based on correlation matrices of dimension 4×4 up to 12×12. The error bars are the statistical errors of the fit.

involved to form a linear combination to give a mass eigenstate, and eventually optimized linear combinations would be obtained. The variational principle states that mass eigenstates can be finely separated with a large set of operators.

4.4.4 The $\hat{A}_1$ link operators

Operators with A_1 links are constructed by taking a quasi-local operators $\overline{\Psi}_\lambda^{\Lambda,k}$ of irrep Λ and row λ, and then applying the A_1 one-link displacement (sum over all six displacements) on the third quark, i.e., $\hat{A}_1^{(3)}\overline{\psi}_\lambda^{\Lambda,k}$. Such A_1 link operators can accompany both MA Dirac indices or MS Dirac indices[3]. Because the A_1 link on the third quark makes the quark nonlocal, it is distinct from the other quarks. This fact makes A_1 link operators with $\mathrm{MA_{Drc}}$, A_1 link operators with $\mathrm{MS_{Drc}}$, and quasi-local operators (with $\mathrm{MA_{Drc}}$) all linearly independent operators. Note that A_1 link operators with $\mathrm{MA_{Drc}}$ and A_1 link operators with $\mathrm{MS_{Drc}}$ become exactly the same without A_1 links.

We have observed effective masses of A_1 link operators. It turns out that existence of the A_1 link affects the spectrum very little. The effective masses of quasi-local operators, those of A_1 link operators with $\mathrm{MA_{Drc}}$ and those of A_1 link operators with $\mathrm{MS_{Drc}}$ are almost the same. The evidence for this is given in Fig. 4.26. In part (a) of the figure it is observed that the first embedding of quasi-local operator, $\overline{\Psi}^{G_{1g},1}$, and the first embedding of the A_1 link operator, $\hat{A}_1\overline{\Psi}^{G_{1g},1}$, with $\mathrm{MA_{Drc}}$ coincide. The same is true for the second and third embeddings. The same is also true for part (b) of the figure, where the effective masses of the i-th embedding of quasi-local operator and the i-th embedding of the A_1 link operators with $\mathrm{MS_{Drc}}$ coincide. Though Fig. 4.26 shows only G_{1g} effective masses, the same behaviors are observed as well in other channels: $G_{1u}, G_{2g}, G_{2u}, H_g$, and H_u.

Because of these nearly identical behaviors of A_1 link operators and quasi-local operators, the basis operators are too parallel and diagonalizations of correlation matrices involving these operators fail. We have eliminated all embeddings of the A_1 link operators with $\mathrm{MA_{Drc}}$ and the A_1 link operators with $\mathrm{MS_{Drc}}$ from correlator matrices throughout our analysis for this reason. Quasi-local operators use smeared quark fields by use of the covariant Gaussian smearing. The Gaussian smearing can be written in terms of the identity and A_1 links in an iterative manner as in Eq. (2.53). The A_1 link operator is obtained by applying the A_1 link to an already Gaussian-

---

[3]The A_1 link operators with $\mathrm{A_{Drc}}$ or $\mathrm{S_{Drc}}$ are obtained by forming $R^A\left[(u_\alpha d_\beta - d_\alpha u_\beta)\hat{A}_1 u_\gamma\right]$ or $R^S\left[(u_\alpha d_\beta - d_\alpha u_\beta)\hat{A}_1 u_\gamma\right]$. The index ordering operators, R^A and R^S, are defined in Appendix C.
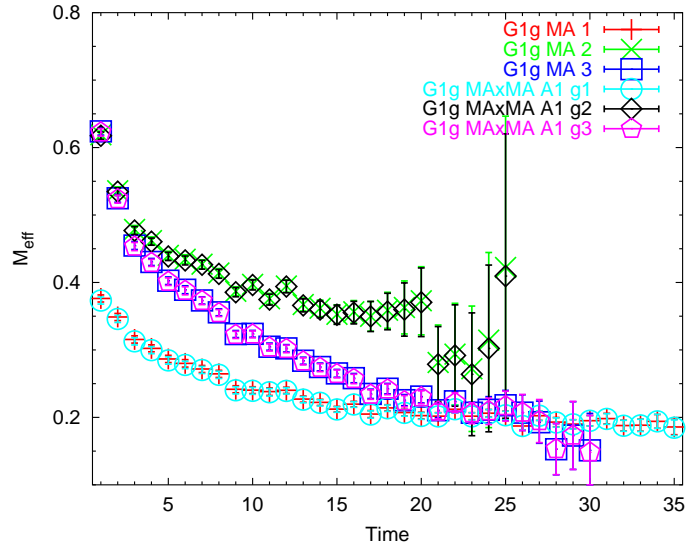
(a)
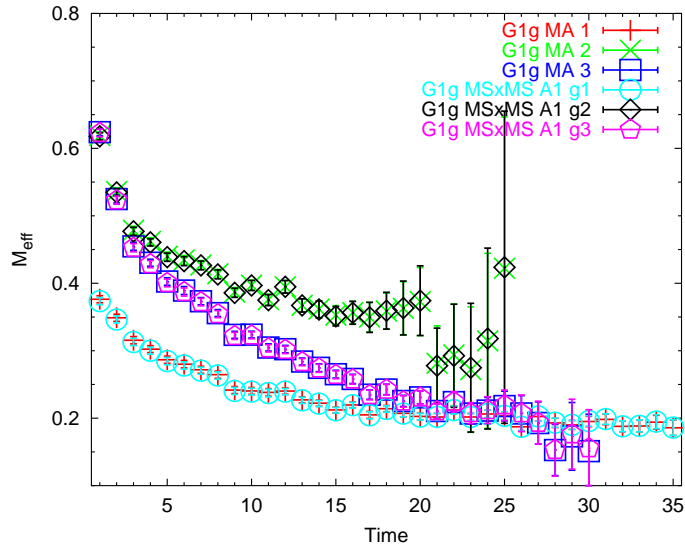
(b)

Figure 4.26: The effective masses of (a) the A_1 link operators with MA_{Drc} and quasi-local operators, and (b) the A_1 link operators with MS_{Drc} and quasi-local operators. Every operator is selected from G_{1g}. There are three embeddings for each of the A_1 operators and the quasi-local operators.

smeared quark field. Since a smeared quark field is a spatially extended object, one additional A_1 link applied to the smeared field seems not to make the quark field significantly different. This would explain why the A_1 link operators behave the same way as quasi-local operators do.

4.5 Delta baryon spectrum

We have assumed that up-quark and down-quark masses are degenerate. So, there is no distinction between up-quark propagators and down-quark propagators. This means that simulations of delta baryon spectrum and that of nucleon spectrum can share the same quark propagators. We analyzed mass spectra of delta baryons by using delta baryon operators from the quasi-local and one-link constructions as discussed in Chapter 3. For a given parity and row, there are maximally 12 G_1, 4 G_2, and 17 H operators for a delta baryon. The way of forming these operators is summarized in Table 4.8. Recall that T_1 one-link operators with $\mathrm{S_{Drc}}$ are *not* permitted for isospin 3/2 operators.

Table 4.8: The delta baryon operators with quasi-local and with one-link displacement used in our simulation. The numbers of operators for G_{1g} row 1, G_{2g} row 1, and H_g row 1 are listed. Numbers of ungerade operators are exactly the same.

Type	Eq.	Table	G_{1g}	G_{2g}	H_g
quasi-local	2.28	2.9	1	0	2
one-link A_1	2.49	2.11	4	0	3
one-link E	2.49	2.13, 2.11	3	3	7
one-link T_1	2.49	2.12, 2.11	4	1	5
total			12	4	17

The easiest example to see this would be Δ^{++} baryon with each quark carrying Dirac index of 1, i.e., $u_1 u_1 D_i u_1 = (1/3) D_i [u_1 u_1 u_1]$, and summation over all space gives zero because of the total derivative. Thus, T_1 one-link operators with $\mathrm{S_{Drc}}$ are excluded from Table 4.8.

We first observed an individual effective mass of each operator in order to determine which operators are appropriate to form correlation matrices. One-link delta baryon operators use two kinds of Dirac index symmetries: $\mathrm{MS_{Drc}}$ and $\mathrm{S_{Drc}}$. The quasi-local construction uses only $\mathrm{S_{Drc}}$. As discussed in the last subsection, A_1 link operators are not significantly different from quasi-local operators, so they must be excluded from correlator matrices also. Counting the operators without

these excluded ones, there are 9 G_1, 2 G_2, and 12 H operators available.

We have numerically solved the generalized eigenvalue equation of Eq. (3.14) for the irreps G_{1g}, G_{1u}, H_g, and H_u. The dimensions of the correlator matrices are varied to see if the low-lying spectra are stable. For the irreps of G_{2g} and G_{2u}, the analysis is done in a unique way because there are too few good operators to have well-separated mass eigenstates. We will show the results of G_2 later in this section.

4.5.1 The G_1 and H spectra

The dimension of the G_{1g} correlation matrices is varied from 3 to 5, that of the G_{1u} is varied from 3 to 6, that of H_g is varied from 3 to 6, and that of H_u is varied from 3 to 7. We do not provide all graphs of effective masses and eigenvectors for delta baryons in this thesis, because it is a little too lengthy. We only show the effective mass plots based on the largest dimensions for $G_{1g/u}$ and $H_{g/u}$ in Fig. 4.27.

Tables 4.9-4.12 summarize fitted values for G_{1g}, G_{1u}, H_g, and H_u, respectively. The tables also provide the forms of operators used in the correlator matrices. These fitted values are plotted as a function of matrix dimensions in Fig. 4.28.

The effective masses are the cleanest in the H_g channel for the delta baryon. Relatively large time ranges can be used to extract masses. Other irreps, G_{1g}, G_{1u}, and H_u are not very clean compared to H_g. Only $5-6$ time-slices can be used to extract masses even for the ground states. Despite this, the spectra are fairly consistent with respect to changes in the dimension of correlator matrix. A possible exception is seen in the first-excited state for G_{1u} using a 3×3 correlator matrix. It may mean that a 3×3 matrix has too few degrees of freedom to separate the mass eigenvalues.
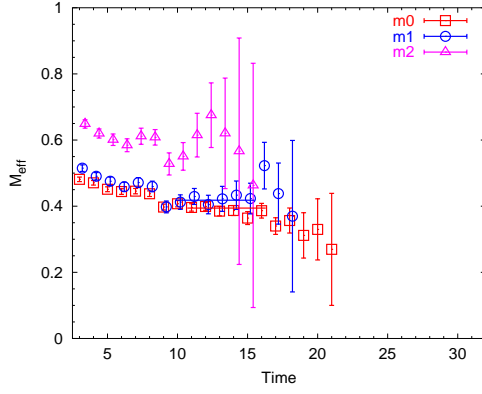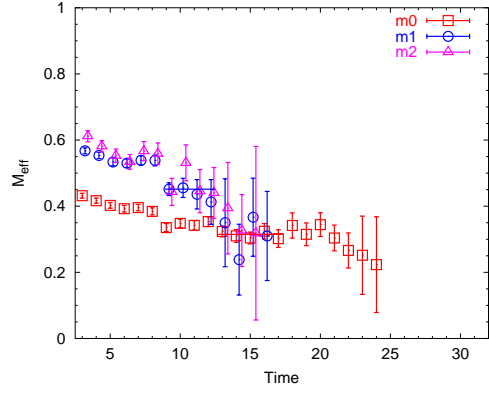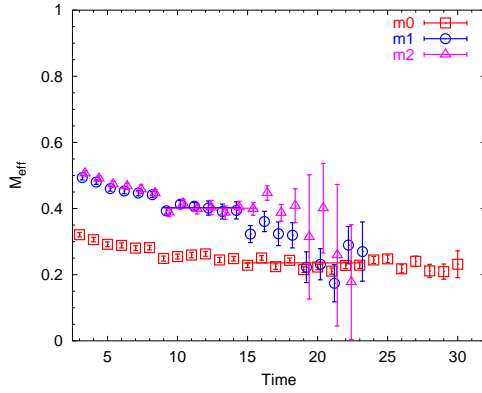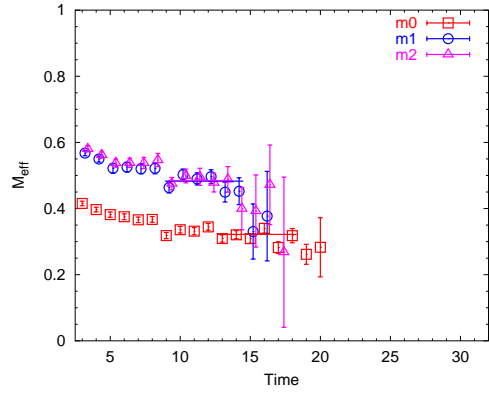
Figure 4.27: The low-lying effective masses obtained by the diagonalization method for delta baryons. Part (a) shows the G_{1g} masses, part (b) shows the G_{1u} masses, part (c) shows the H_g masses, and part (d) shows the H_u masses. The dimensions of matrices are 5, 6, 6, and 7 for G_{1g}, G_{1u}, H_g, and H_u, respectively.

Table 4.9: The effective masses obtained by linear χ^2 fits to the generalized eigenvalues for the delta baryon, G_{1g} channel.

	M	δM	time	χ^2/N	operators
5×5 g.s.	0.394393	0.00940513	$11-16$	0.820122	$(1)-(5)$
5×5 1st e.s.	0.41812	0.0143942	$10-15$	0.184723	
4×4 g.s.	0.401329	0.00599376	$9-16$	0.919465	$(1)-(4)$
4×4 1st e.s.	0.418291	0.0142908	$10-15$	0.199621	
3×3 g.s.	0.399852	0.00594971	$9-16$	0.697776	$(1)-(3)$
3×3 1st e.s.	$-$	$-$	$-$	$-$	

Operators:

(1) $\left| \Delta : G_{1g}, \mathrm{S_{iso}} \otimes \mathrm{S_{Drc}}, \overline{\Psi}^{G_{1g}} \right\rangle$

(2) $\left| \Delta : G_{1g}, \mathrm{S_{iso}} \otimes \mathrm{MS_{Drc}}, \hat{T}_1 \overline{\Psi}^{G_{1u},1} \right\rangle$

(3) $\left| \Delta : G_{1g}, \mathrm{S_{iso}} \otimes \mathrm{MS_{Drc}}, \hat{T}_1 \overline{\Psi}^{G_{1u},3} \right\rangle$

(4) $\left| \Delta : G_{1g}, \mathrm{S_{iso}} \otimes \mathrm{MS_{Drc}}, \hat{T}_1 \overline{\Psi}^{H_u} \right\rangle$

(5) $\left| \Delta : G_{1g}, \mathrm{S_{iso}} \otimes \mathrm{MS_{Drc}}, \hat{T}_1 \overline{\Psi}^{G_{1u},2} \right\rangle$

Table 4.10: The effective masses obtained by linear χ^2 fits to the generalized eigenvalues for the delta baryon, G_{1u} channel.

	M	δM	time	χ^2/N	operators
6×6 g.s.	0.314647	0.0121577	$13-17$	0.364080	$(1)-(6)$
6×6 1st e.s.	0.451343	0.017911	$9-12$	0.097409	
5×5 g.s.	0.31493	0.0114679	$13-19$	0.581231	$(1)-(5)$
5×5 1st e.s.	0.450288	0.0176298	$9-13$	0.100772	
4×4 g.s.	0.314871	0.0114467	$13-19$	0.620995	$(1)-(4)$
4×4 1st e.s.	0.461986	0.0179538	$9-12$	0.380244	
3×3 g.s.	0.321895	0.00850909	$13-21$	1.209761	$(1)-(3)$
3×3 1st e.s.	0.500097	0.0164972	$10-14$	0.330371	

Operators:

(1) $\left| \Delta : G_{1u}, \mathrm{S}_{\mathrm{iso}} \otimes \mathrm{S}_{\mathrm{Drc}}, \overline{\Psi}^{G_{1u}} \right\rangle$

(2) $\left| \Delta : G_{1u}, \mathrm{S}_{\mathrm{iso}} \otimes \mathrm{MS}_{\mathrm{Drc}}, \hat{T}_1 \overline{\Psi}^{G_{1g},1} \right\rangle$

(3) $\left| \Delta : G_{1u}, \mathrm{S}_{\mathrm{iso}} \otimes \mathrm{MS}_{\mathrm{Drc}}, \hat{T}_1 \overline{\Psi}^{G_{1g},2} \right\rangle$

(4) $\left| \Delta : G_{1u}, \mathrm{S}_{\mathrm{iso}} \otimes \mathrm{MS}_{\mathrm{Drc}}, \hat{T}_1 \overline{\Psi}^{G_{1g},3} \right\rangle$

(5) $\left| \Delta : G_{1u}, \mathrm{S}_{\mathrm{iso}} \otimes \mathrm{MS}_{\mathrm{Drc}}, \hat{T}_1 \overline{\Psi}^{H_g} \right\rangle$

(6) $\left| \Delta : G_{1u}, \mathrm{S}_{\mathrm{iso}} \otimes \mathrm{MS}_{\mathrm{Drc}}, \hat{E} \overline{\Psi}^{H_u} \right\rangle$

Table 4.11: The effective masses obtained by linear χ^2 fits to the generalized eigenvalues for the delta baryon, H_g channel.

	M	δM	time	χ^2/N	operators
6×6 g.s.	0.23579	0.00522589	$15-23$	3.832300	$(1)-(6)$
6×6 1st e.s.	0.40087	0.0072398	$9-14$	0.728026	
6×6 2nd e.s.	0.402896	0.00637045	$9-14$	0.670212	
6×6 3rd e.s.	0.422823	0.00670332	$9-15$	0.635465	
5×5 g.s.	0.236632	0.00518272	$15-23$	3.666206	$(1)-(5)$
5×5 1st e.s.	0.399142	0.00735197	$9-14$	0.756241	
5×5 2nd e.s.	0.414215	0.00673186	$9-15$	1.146886	
5×5 3rd e.s.	0.423266	0.00674365	$9-15$	0.681428	
4×4 g.s.	0.240378	0.00430277	$15-23$	3.523842	$(1)-(4)$
4×4 1st e.s.	0.40847	0.00570735	$9-14$	0.560303	
4×4 2nd e.s.	0.416189	0.0072191	$9-15$	0.491973	
4×4 3rd e.s.	0.421266	0.0089179	$10-19$	0.388352	
3×3 g.s.	0.240401	0.00430421	$15-23$	3.530316	$(1)-(3)$
3×3 1st e.s.	0.408549	0.00572832	$9-14$	0.568267	
3×3 2nd e.s.	0.419171	0.0107455	$10-15$	0.280695	
3×3 3rd e.s.	$-$	$-$	$-$	$-$	

Operators:

(1) $\left| \Delta : H_g, \mathrm{S_{iso}} \otimes \mathrm{S_{Drc}}, \overline{\Psi}^{H_g,1} \right\rangle$

(2) $\left| \Delta : H_g, \mathrm{S_{iso}} \otimes \mathrm{S_{Drc}}, \overline{\Psi}^{H_g,2} \right\rangle$

(3) $\left| \Delta : H_g, \mathrm{S_{iso}} \otimes \mathrm{MS_{Drc}}, \hat{T}_1 \overline{\Psi}^{H_u} \right\rangle$

(4) $\left| \Delta : H_g, \mathrm{S_{iso}} \otimes \mathrm{MS_{Drc}}, \hat{T}_1 \overline{\Psi}^{H'_u} \right\rangle$

(5) $\left| \Delta : H_g, \mathrm{S_{iso}} \otimes \mathrm{MS_{Drc}}, \hat{T}_1 \overline{\Psi}^{G_{1u},1} \right\rangle$

(6) $\left| \Delta : H_g, \mathrm{S_{iso}} \otimes \mathrm{MS_{Drc}}, \hat{T}_1 \overline{\Psi}^{G_{1u},2} \right\rangle$

A prime on a local operator means the continuum Clebsch-Gordan coefficients are not applicable.

Table 4.12: The effective masses obtained by linear χ^2 fits to the generalized eigenvalues for the delta baryon, H_u channel.

	M	δM	time	χ^2/N	operators
7×7 g.s.	0.321978	0.00856541	$13-18$	2.366126	$(1)-(7)$
7×7 1st e.s.	0.482849	0.0108755	$9-14$	1.380500	
7×7 2nd e.s.	0.484879	0.0124884	$9-13$	0.451216	
6×6 g.s.	0.322001	0.00856711	$13-18$	2.358374	$(1)-(6)$
6×6 1st e.s.	0.482892	0.0108205	$9-14$	1.447331	
6×6 2nd e.s.	0.48602	0.0132303	$9-13$	0.699815	
5×5 g.s.	0.323054	0.00889734	$13-18$	1.978800	$(1)-(5)$
5×5 1st e.s.	0.480186	0.010134	$9-14$	1.575607	
5×5 2nd e.s.	0.483803	0.0128564	$9-14$	0.794721	
4×4 g.s.	0.325201	0.00791653	$13-18$	1.888675	$(1)-(4)$
4×4 1st e.s.	0.488164	0.00987458	$9-16$	1.528421	
4×4 2nd e.s.	$-$	$-$	$-$	$-$	
3×3 g.s.	0.327148	0.00682781	$13-18$	1.697340	$(1)-(3)$
3×3 1st e.s.	0.490878	0.0105619	$9-16$	1.115643	
3×3 2nd e.s.	$-$	$-$	$-$	$-$	

Operators:

$$(1) \quad \left| \Delta : H_g, \mathrm{S}_{\mathrm{iso}} \otimes \mathrm{S}_{\mathrm{Drc}}, \overline{\Psi}^{H_u,1} \right\rangle$$

$$(2) \quad \left| \Delta : H_g, \mathrm{S}_{\mathrm{iso}} \otimes \mathrm{S}_{\mathrm{Drc}}, \overline{\Psi}^{H_u,2} \right\rangle$$

$$(3) \quad \left| \Delta : H_g, \mathrm{S}_{\mathrm{iso}} \otimes \mathrm{MS}_{\mathrm{Drc}}, \hat{T}_1 \overline{\Psi}^{H_g} \right\rangle$$

$$(4) \quad \left| \Delta : H_g, \mathrm{S}_{\mathrm{iso}} \otimes \mathrm{MS}_{\mathrm{Drc}}, \hat{T}_1 \overline{\Psi}^{G_{1g},2} \right\rangle$$

$$(5) \quad \left| \Delta : H_g, \mathrm{S}_{\mathrm{iso}} \otimes \mathrm{MS}_{\mathrm{Drc}}, \hat{T}_1 \overline{\Psi}^{G_{1g},3} \right\rangle$$

$$(6) \quad \left| \Delta : H_g, \mathrm{S}_{\mathrm{iso}} \otimes \mathrm{MS}_{\mathrm{Drc}}, \hat{T}_1 \overline{\Psi}^{G_{1g},1} \right\rangle$$

$$(7) \quad \left| \Delta : H_g, \mathrm{S}_{\mathrm{iso}} \otimes \mathrm{MS}_{\mathrm{Drc}}, \hat{T}_1 \overline{\Psi}^{H'_u} \right\rangle$$
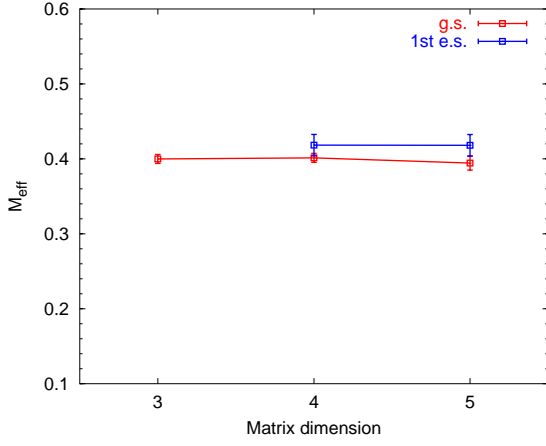
(a) G_{1g}
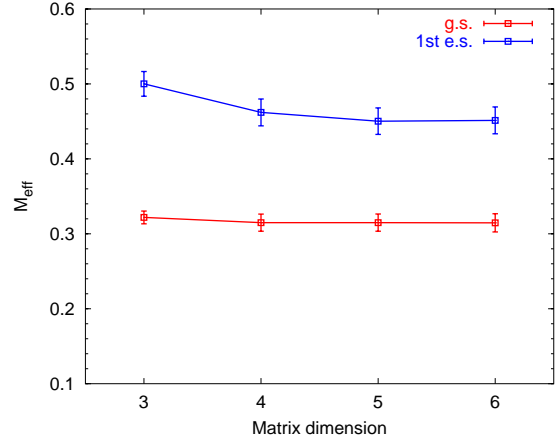
(b) G_{1u}
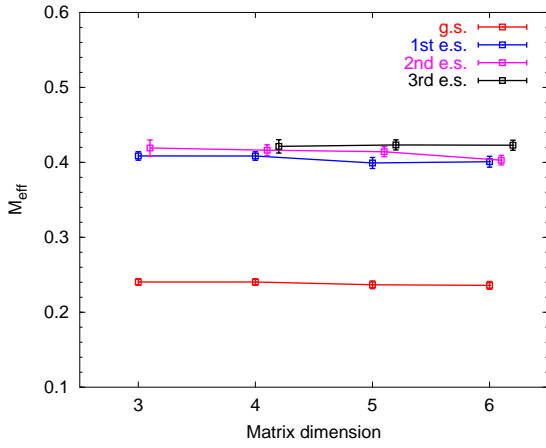
(c) H_g
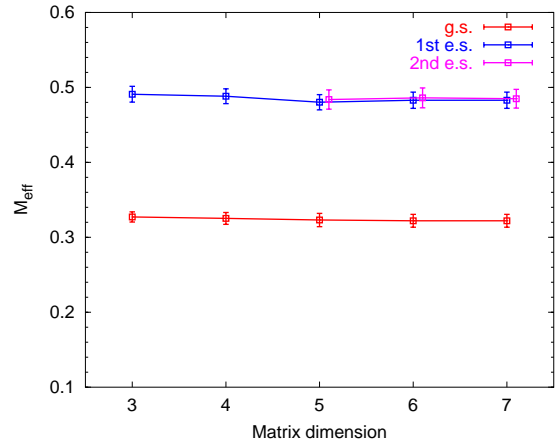
(d) H_u

Figure 4.28: Plots of the fitted effective masses for $G_{1g/u}$ and $H_{g/u}$ channels of delta baryons. The dimension of the matrix is on the horizontal axis and the effective masses are on the vertical axis in lattice units. The error bars are the statistical errors of the fit.

4.5.2 The G_2 spectrum

There are only two operators for G_2. The (gerade) operators are,

$$\left| \Delta : G_{2g}, \mathrm{S}_{\mathrm{iso}} \otimes \mathrm{MS}_{\mathrm{Drc}}, \hat{T}_1 \overline{\Psi}^{H_u} \right\rangle,$$

$$\left| \Delta : G_{2g}, \mathrm{S}_{\mathrm{iso}} \otimes \mathrm{MS}_{\mathrm{Drc}}, \hat{E} \overline{\Psi}^{H_g} \right\rangle. \tag{4.54}$$

The diagonalization of 2×2 matrices using these operators failed for both parities. So we simply analyze correlation functions without diagonalization for each parity using the plateau method. The effective mass plots using operators in Eq. (4.54) are given in Fig. 4.29, where all time-slices are displayed. The noise is strong in the intermediate time ranges, therefore not so many time-slices can be used to extract masses. Since effective masses do not stay on plateaus for many time-slices, we fit the correlation functions to a lower bound and an upper bound of the low-lying masses for selected time ranges. For both parities of G_2 we use the operator $\left| \Delta : G_{2g}, \mathrm{S}_{\mathrm{iso}} \otimes \mathrm{MS}_{\mathrm{Drc}}, \hat{T}_1 \overline{\Psi}^{H_{u/g}} \right\rangle$ to find lower and upper bounds of the gerade ground state. For G_{2g} this T_1 one-link operator couples to the ground state more strongly than the other operator with E one-link displacement. For G_{2u} it is less obvious that this operator provides better coupling to the low-lying state, but it has a smaller upper bound than the other operator (given in Eq. (4.54)).

(a) G_{2g} (b) G_{2u}
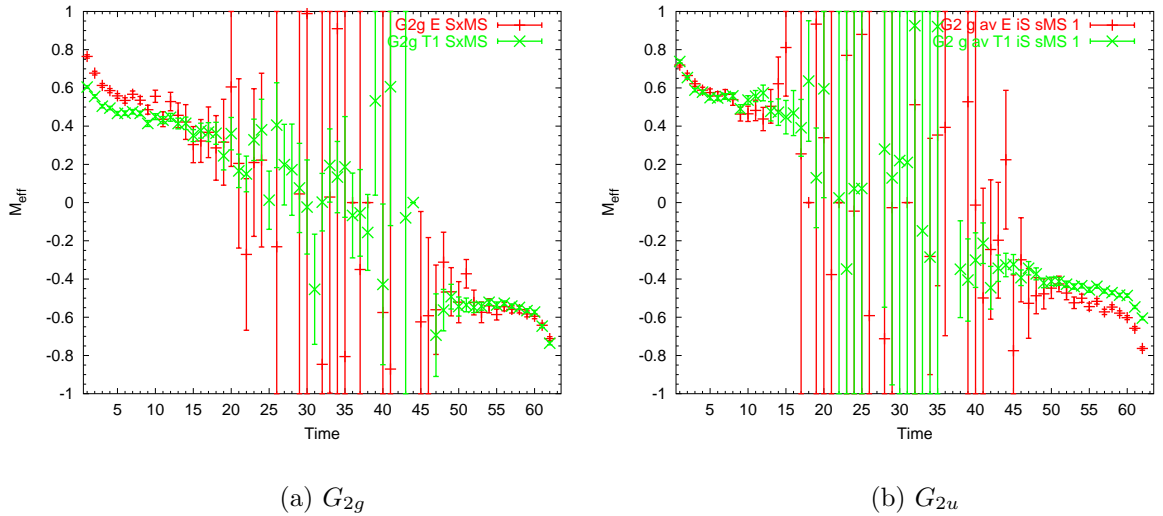
Figure 4.29: Plots for the effective masses for both parities of G_2, delta baryon.

Upper bound = 0.468   Upper bound = 0.551

Lower bound = 0.351   Lower bound = 0.465

(a) G_{2g} (b) G_{2u}
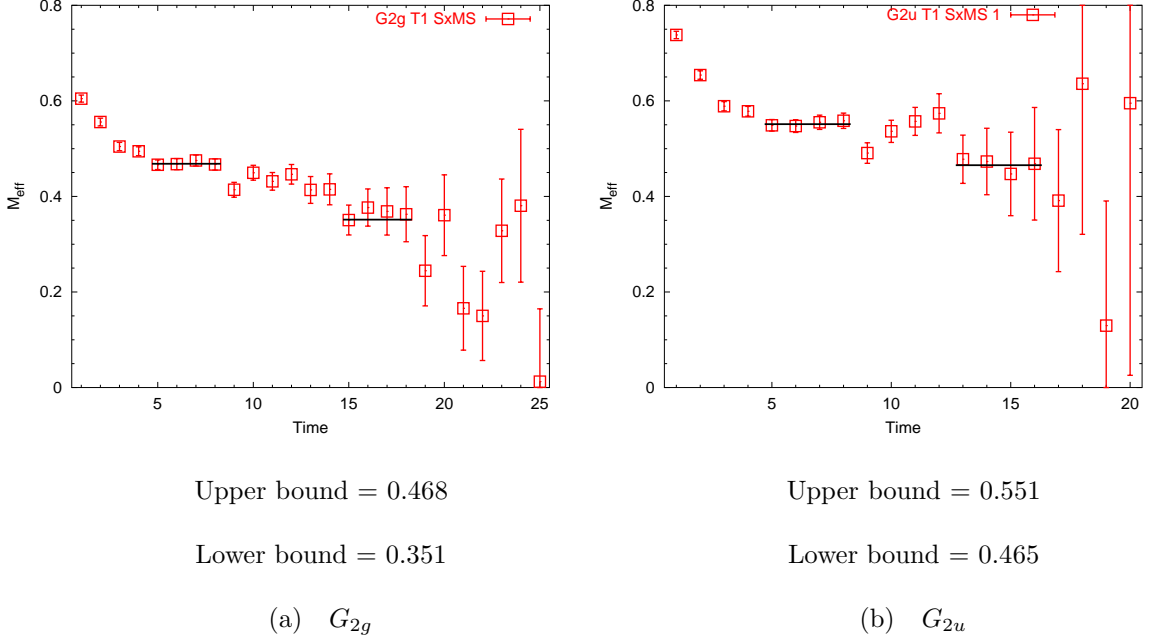
Figure 4.30: Plots for the effective masses for both parities of G_2, delta baryon with fitted

upper bound and lower bound masses.

The effective mass plots of G_{2g} and G_{2u} using the T_1 one-link operator are shown with the

fitted lower bound mass and upper bound mass in Fig. 4.30. The lower bound mass of the gerade

state is 0.351 fitted in time range $15-18$, and the upper bound mass is 0.468 fitted in time range

$5-8$. The lower bound mass for the ungerade state is 0.465 fitted in time range $13-16$, and the

upper bound mass is 0.551 in time range $5-8$. Since there are only four time-slices used in each

fit, the reliability of the fitted values is poor. For more precise determination of G_2 masses for the

delta baryon, we need a larger set of operators.

4.6 Comparison with physical baryon spectra

We have obtained mass spectra of N^* and delta baryons for six channels: $G_{1g/u}, G_{2g/u}$, and $H_{g/u}$, by quenched lattice QCD calculations. We now compare these computed spectra with empirical data for baryon spectra. Our simulation conditions are far from the real world. The pion mass is about $500\,\mathrm{MeV}$, the spatial volume of the lattices is only $(1.6\,\mathrm{fm})^3$, and quark loops are neglected. Nevertheless, it is important to analyze the results using such restricted conditions first, then move on to better conditions and redo the analysis, and so forth. Finally one will obtain results for various conditions, where one can see the trends of the physical observables, including chiral extrapolation, volume dependence, and unquenching effects, *etc.* This procedure eventually leads us to the solution of QCD.

Sasaki *et al.* recently reported lattice QCD results for N^* and delta baryon spectra with $J^P = 1/2^{\pm}, 3/2^{\pm}$ in Ref. [32], where hyperfine mass splittings motivated by SU(6) quark model are studied. They used spin $3/2$ operators obtained by the Rarita-Schwinger spin-projection method. We will show our analysis of the spectra along a similar line in this section, but we have much larger sets of operators, including $J^P = 5/2^{\pm}$.

We have obtained mass spectra using correlation matrices of various dimensions, which confirms the stability of mass eigenstates. We regard the fitted masses obtained by diagonalizing a correlation matrix of the largest dimension as the final results for a given symmetry channel, although we could use data obtained from correlation matrices of any dimension. With a larger set of operators there are more degrees of freedom to separate mass eigenstates, therefore results are more reliable. For isospin $1/2$, G_{1g} and G_{1u} channels, the results based on $10{\times}10$ correlation matrices are used. For G_{2g} and G_{2u} channels, those based on $4{\times}4$ and $3{\times}3$ (set 1) matrices are used, respectively. For H_g and H_u channels, those based on $12{\times}12$ matrices are used. For isospin $3/2$ G_{1g} and G_{1u} channels, the results based on $5{\times}5$ and $4{\times}4$ matrices are used, respectively. For H_g and H_u channels, those based on $6{\times}6$ and $7{\times}7$ matrices are used, respectively. For isospin $3/2$ G_{2g} and G_{2u} channels, results are not discussed here because these masses are not well-established in this simulation. One needs a larger set of operators to have better estimates of isospin $3/2$ G_{2g}

and G_{2u} spectra.

Low-lying states of N^* obtained by our lattice simulations are schematically presented in Fig. 4.31, where six channels, $G_{1g/u}, G_{2g/u}$, and $H_{g/u}$, are shown separately. Experimental values also appear in the figure on physical scale. The mean effective mass of the lowest-lying state of G_{1g} and the physical state $N(939)$ are placed at the same level. The order of experimentally observed N^* masses is [4]

$$N(939)\,1/2^+ < N(1520)\,3/2^- \lesssim N(1535)\,1/2^- < \cdots. \tag{4.55}$$

Note that the mass difference between $N(1520)$ and $N(1535)$ is less than 1% compared to their average, whereas the mass difference between $N(939)$ and $N(1520)$ is relatively large. Results obtained by our simulations have the following order of masses,

$$N(G_{1g}, \text{g.s.}) < N(G_{1u}, \text{g.s.}) \lesssim N(H_u, \text{g.s.}) < \cdots, \tag{4.56}$$

where "g.s." stands for a ground state *for each channel*. Recall that G_1 includes total angular momenta $J = 1/2, 7/2, \cdots$, H includes $J = 3/2, 5/2, 7/2, \cdots$, G_2 includes $J = 5/2, 7/2, \cdots$. Though our results show that the mean value of the lowest $1/2^-$ mass is less than that of $3/2^-$ mass, which is opposite to what is observed in nature, the error bars for these states overlap. The mass ratios of the lowest $1/2^-$ and $3/2^-$ states to the $1/2^+$ state for $N*$ are given below[5],

$$
\begin{aligned}
\frac{N(1535)1/2^-}{N(939)1/2^+} &= 1.635, \quad \text{(experimental)} \\
\frac{N(G_{1u}, \text{g.s.})}{N(G_{1g}, \text{g.s.})} &= 1.521(77);
\end{aligned}
\tag{4.57}
$$

$$
\begin{aligned}
\frac{N(1520)3/2^-}{N(939)1/2^+} &= 1.619, \quad \text{(experimental)} \\
\frac{N(H_u, \text{g.s.})}{N(G_{1g}, \text{g.s.})} &= 1.533(67).
\end{aligned}
\tag{4.58}
$$

The mass ratios found in our analysis are somewhat below those found in nature. This probably is due to too heavy quark masses used in our simulations. All baryon masses become close as the

---

[4]The $N(1440)1/2^+$ is not compared here.

[5]Error analysis is taken into account. Let an ensemble A have a mean a and a standard deviation (stdv) Δa, and B have a mean b and a stdv Δb. If A and B are uncorrelated, then $X = A/B$ has a mean $x = a/b$ and a stdv $x\sqrt{\left(\frac{\Delta a}{a}\right)^2 + \left(\frac{\Delta b}{b}\right)^2}$.
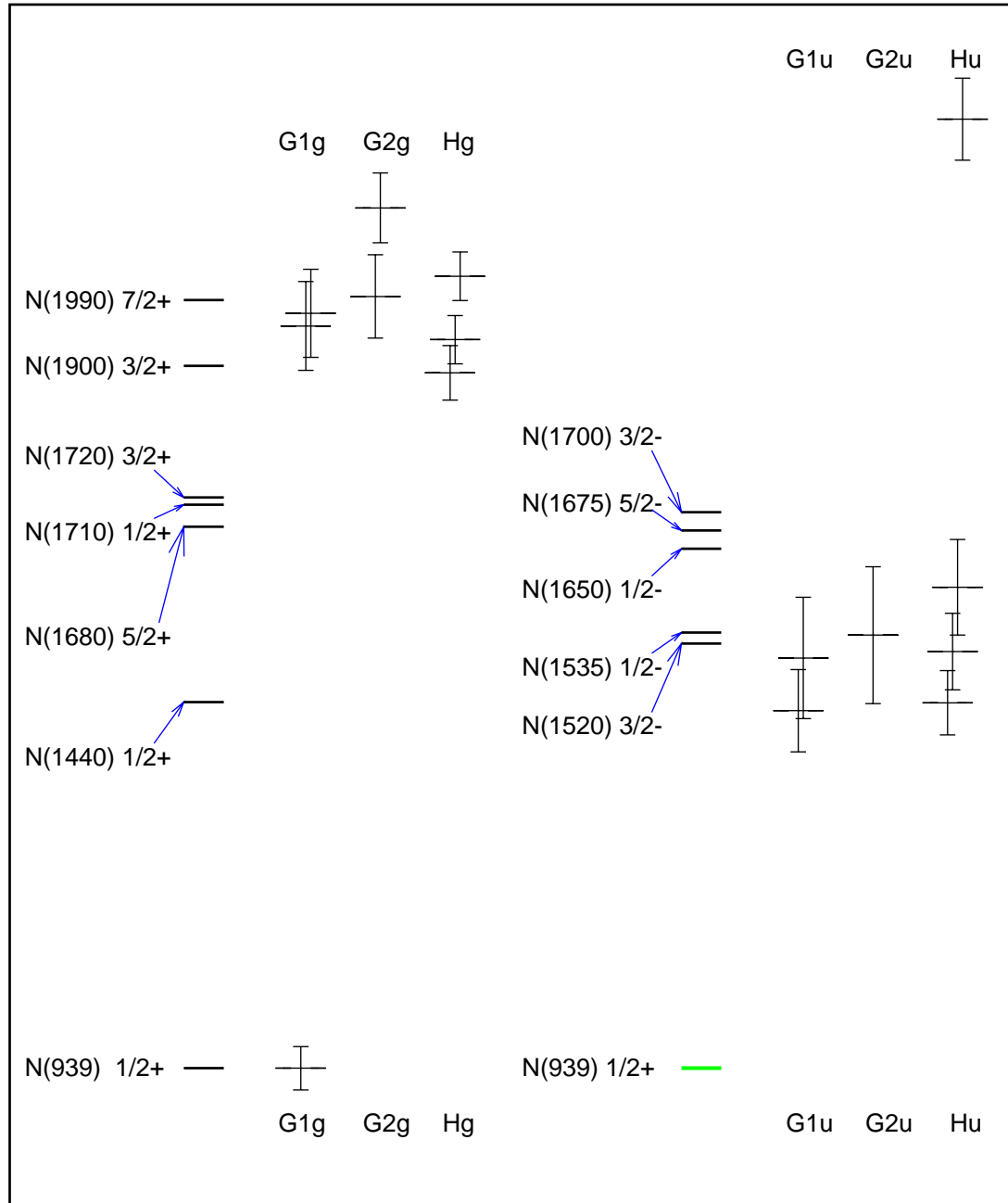
Figure 4.31: The N^* physical masses vs. effective masses obtained from the $16^3 \times 64$ lattice.

Gerade states are on the left side and ungerade states are on the right side.

quark mass becomes heavy. In the heavy quark mass limit, where a baryon mass is given by a sum of constituent quark masses, SU(6) symmetry is approached and mass splittings tend to zero. The G_{2u} mass of N^* we observe is relatively too small, compared with the physical $N(1675)\,5/2^-$ state. However, the statistical error of G_{2u} is too large, so we need further investigation with a larger set of G_2 operators and more gauge configurations.

Positive-parity excitations have very large masses in our results for N^* as compared with the experimentally observed masses. The mass ratio of $N(1680)\,5/2^+$ to $N(939)\,1/2^+$ in nature is about 1.789, whereas the mass ratio of $N(H_g,\text{g.s.})$ to $N(G_{1g},\text{g.s.})$ that we compute is 2.013(75). Similarly, the mass ratio of the first-excited state of G_{1g} to the ground state of G_{1g} is too high compared with the mass ratio of $N(1710)\,1/2^+$ to $N(939)\,1/2^+$. Though these positive-parity excitations have too large masses (roughly twice as large as the $1/2^+$ ground state) their relative magnitudes are rather consistent with experimental values, i.e.,

$$\frac{N(1710)\,1/2^+}{N(1680)\,5/2^+} = 1.018, \quad \text{(experimental)}$$
$$\frac{N(G_{1g},\text{1st e.s.})}{N(H_g,\text{g.s.})} = 1.034(38). \tag{4.59}$$

The ratios match within errors. The lowest H_g and G_{2g} states should correspond to the $N(1680)\,5/2^+$ state, because the $5/2$ state is included in both H and G_2 channels, but not in G_1. The $N(G_{2g},\text{g.s.})$ is a little too high compared to $N(H_g,\text{g.s.})$, which we do not understand. Since there is a limited number of operators of G_2 in our simulations, a larger set of G_2 operators might resolve this discrepancy.

It is intriguing to observe how overly large masses of positive-parity excitations change when lattices with a larger volume are used. The spatial lattice spacing in these simulations is about $0.1\,\text{fm}$. The lattice size is $16^3 \times 64$, where 64 is the size of temporal direction. Therefore, the box size is approximately $1.6\,\text{fm}$ in one spatial dimension. Since the mean charge radius of a proton is about $0.870\,\text{fm}$ [5], its diameter barely fits in the lattice. Excited states are expected to have more extended distributions. The finite volume of the lattice squeezes the wavefunctions of excited states, therefore pushing their internal momenta up [89]. This motivates a study of the volume dependence of baryon masses, and we will report the analysis completed recently using lattices

with spatial volume $(2.4\,\text{fm})^3$ in the next section.

The lightest excited state of isospin $1/2$, $N(1440)\,1/2^+$ or the so-called Roper resonance, is not evident in our data. Many speculations for this state have appeared in the literature, but its theoretical understanding is still controversial. The fact that the $N(1440)\,1/2^+$ signals are absent in our data may indicate that this state has small overlap with a three-quark state for the pion mass used in this simulation ($\simeq 500\,\text{MeV}$). A level crossing of positive-parity excited state and negative-parity state may occur for lower pion mass [62].

Low-lying states of the delta baryon obtained in our lattice simulations are schematically shown in Fig. 4.32. Four channels $G_{1g/u}, H_{g/u}$ are given in the figure, and $G_{2g/u}$ channels are not shown because their masses are not well-established in our simulations. The mean mass value of the lowest-lying state $\Delta(H_g, \text{g.s.})$ and the physical mass of the $\Delta(1232)\,3/2^+$ are placed on the same level. The ratios of the three lowest-lying delta baryon measured in our simulations well-reproduce the ratios of experimentally observed masses as follows.

$$
\begin{aligned}
\frac{\Delta(1620)\,1/2^-}{\Delta(1232)\,3/2^+} &= 1.315, \quad \text{(experimental)} \\
\frac{\Delta(G_{1u}, \text{g.s.})}{\Delta(H_g, \text{g.s.})} &= 1.334(59);
\end{aligned}
$$

$$
\tag{4.60}
$$

$$
\begin{aligned}
\frac{\Delta(1700)\,3/2^-}{\Delta(1232)\,3/2^+} &= 1.380, \quad \text{(experimental)} \\
\frac{\Delta(H_u, \text{g.s.})}{\Delta(H_g, \text{g.s.})} &= 1.365(47).
\end{aligned}
$$

These mass ratios that we compute clearly agree with the experimental values within the statistical error bars. Positive-parity excitations of the delta baryon are overly heavy with respect to the $3/2^+$ ground state in our results, much like the case for N^* positive parity excitations. The first-excited states for G_{1u} and H_u channels are very heavy also with respect to their corresponding ground states. These mass ratios do not reproduce the mass ratio of $\Delta(1900)1/2^-$ to $\Delta(1620)1/2^-$ or the mass ratio of $\Delta(1930)5/2^-$ to $\Delta(1700)3/2^-$. The pattern is different from N^* spectra where the N^* first-excited states of G_{1u} and H_u are rather close to their ground states. We do not understand what causes these high masses for first-excited states of delta G_{1u} and H_u channels.
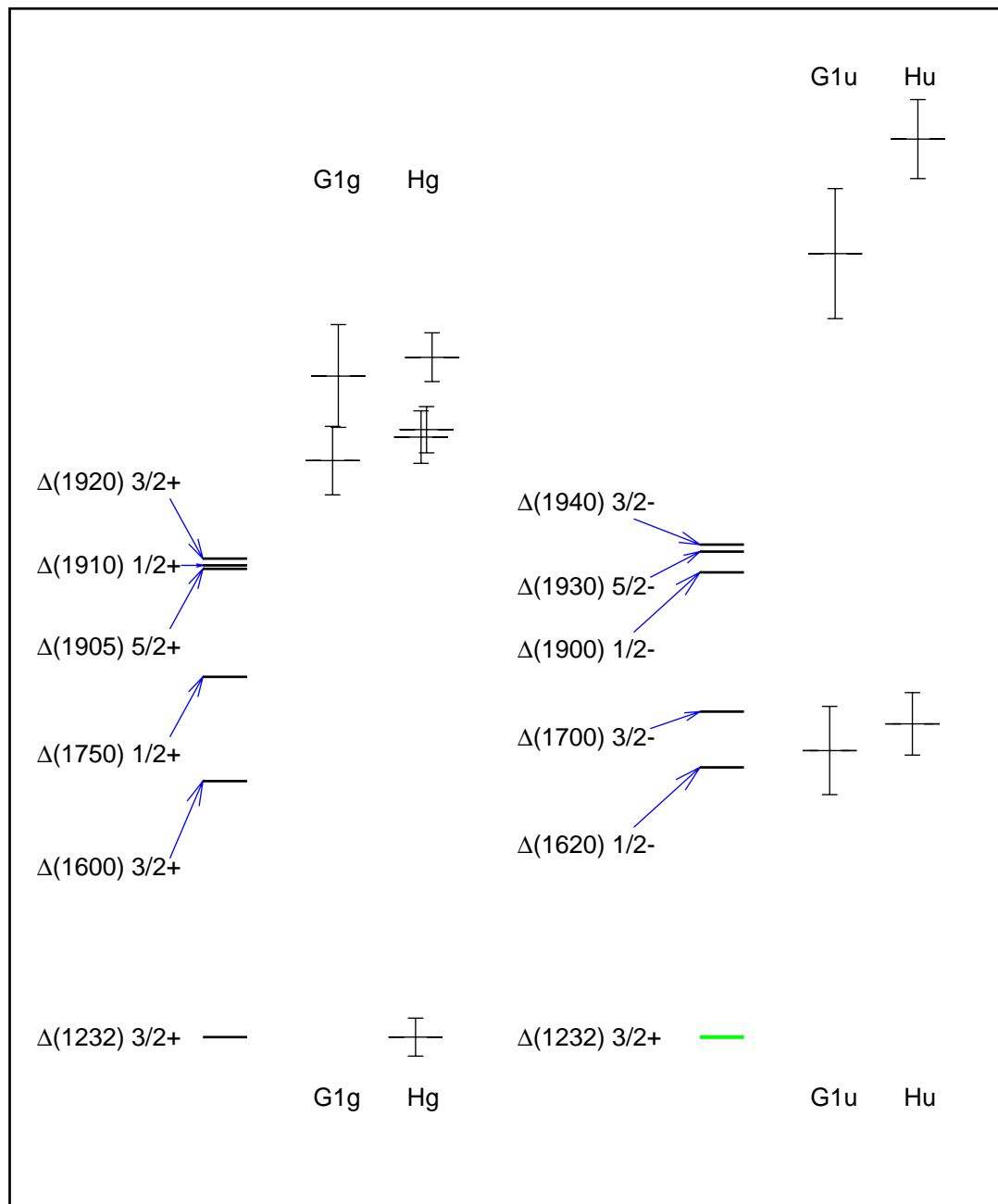
Figure 4.32: The Δ baryon physical masses vs. effective masses obtained from the $16^3 \times 64$ lattice. Gerade states are on the left side and ungerade states are on the right side. The masses for $G_{2g/u}$ are not well-determined in our simulation, therefore they are not shown.

Table 4.13: The masses of a few low-lying states from N^* and Δ. Mass M is in the units of $a^{-1} = 6.0\text{GeV}$.

$[I, J^P]$	M	physical (MeV)
$[1/2, 1/2^+]$	0.197(6)	939
$[1/2, 1/2^-]$	0.300(9)	1535
$[1/2, 3/2^-]$	0.302(20)	1520
$[3/2, 1/2^+]$	0.394(18)	1750
$[3/2, 1/2^-]$	0.315(12)	1620
$[3/2, 3/2^+]$	0.236(5)	1232
$[3/2, 3/2^-]$	0.322(8)	1700

Studying these states at lower pion mass is of particular interest.

Table 4.13 gives masses of the lowest three or four states for both N^* and delta baryons. We now study hyperfine mass splittings of $I = 1/2$ and $3/2$ baryons. In the non-relativistic quark model with an assumption that the hamiltonian is independent of the flavor and spin, baryons obey SU(6) symmetry. Under SU(6) symmetry, the S-wave baryons form a **56**-plet, where $N(939)\,1/2^+$ and $\Delta(1232)\,3/2^+$ would be degenerate, and P-wave baryons form a **70**-plet, where $N(1535)\,1/2^-$ and $\Delta(1700)\,3/2^-$ would be degenerate. Note that the **56**-plet has totally symmetric Young Tableau in flavor-spin space (the S-wave has symmetric spatial distributions and color label takes care of the total antisymmetry) and that the **70**-plet has mixed-symmetric Young Tableau in flavor-spin space as shown in Fig. 4.33. Introducing a spin dependent interaction into the lagrangian breaks SU(6) symmetry. Isgur and Karl calculated the mass splitting of $N(939)\,1/2^+$ and $\Delta(1232)\,3/2^+$ by taking a spin-spin interaction caused by the one-gluon exchange as a perturbation and with reasonable choices of input parameters they found the mass splitting to be about $300\,\text{MeV}$ [90–93].

56 **70**
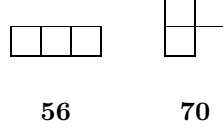
Figure 4.33: The Young tableaux of the SU(6) irreducible representations for three quarks. The standard rule of counting the dimensions gives 56 states for the totally symmetric tableau and 70 states for the mixed-symmetric tableau.

The ratios of this hyperfine mass splitting between these states to the sum are given below.

$$
\frac{\Delta(1232)\,3/2^+ - N(939)\,1/2^+}{\Delta(1232)\,3/2^+ + N(939)\,1/2^+} = 0.135, \quad \text{(experimental)}
$$
$$
\frac{\Delta(H_g, \text{g.s.}) - N(G_{1g}, \text{g.s.})}{\Delta(H_g, \text{g.s.}) + N(G_{1g}, \text{g.s.})} = 0.0889(20). \tag{4.61}
$$

The hyperfine mass splitting with respect to the sum of nucleon and delta ground state masses observed in our simulations is $65.9 \pm 1.5\,\%$ of the physical value. Sasaki *et al.* observed that $M_\Delta - M_N$ is *roughly* inversely proportional to $M_\Delta + M_N$ by changing the bare quark masses, where M_Δ and M_N are masses of ground states of the delta baryon and nucleon [32]. The hyperfine mass splitting has a strong dependence on quark masses such that as the quark mass decreases, the hyperfine mass splitting increases. Sasaki *et al.* give a plot of hyperfine mass splittings as a function of $M_\Delta + M_N$, where they have include several data points for different quark masses along with chiral extrapolated value. The inverse proportionality to mass mentioned above can be recognized in their plot. Their results are re-plotted in physical units in Fig. 4.34. Our data point also appears in the plot. Our data point clearly supports Sasaki *et al.*'s results fairly well.

Next we consider the hyperfine mass splitting for the P-wave **70**-plet. The splitting of $\Delta(1700)\,3/2^- - N(1535)\,1/2^-$ with respect to their sum is given below,

$$
\frac{\Delta(1700)3/2^- - N(1535)1/2^-}{\Delta(1700)3/2^- + N(1535)1/2^-} = 0.0510, \quad \text{(experimental)}
$$
$$
\frac{\Delta(H_u, \text{g.s.}) - N(G_{1u}, \text{g.s.})}{\Delta(H_u, \text{g.s.}) + N(G_{1u}, \text{g.s.})} = 0.0352(17). \tag{4.62}
$$

The value that we found in our data is $69.0 \pm 3.3\,\%$ of the physical value. This percentage is close to the value of S-wave given in Eq. (4.61). It is interesting to see the tendencies of these values

146
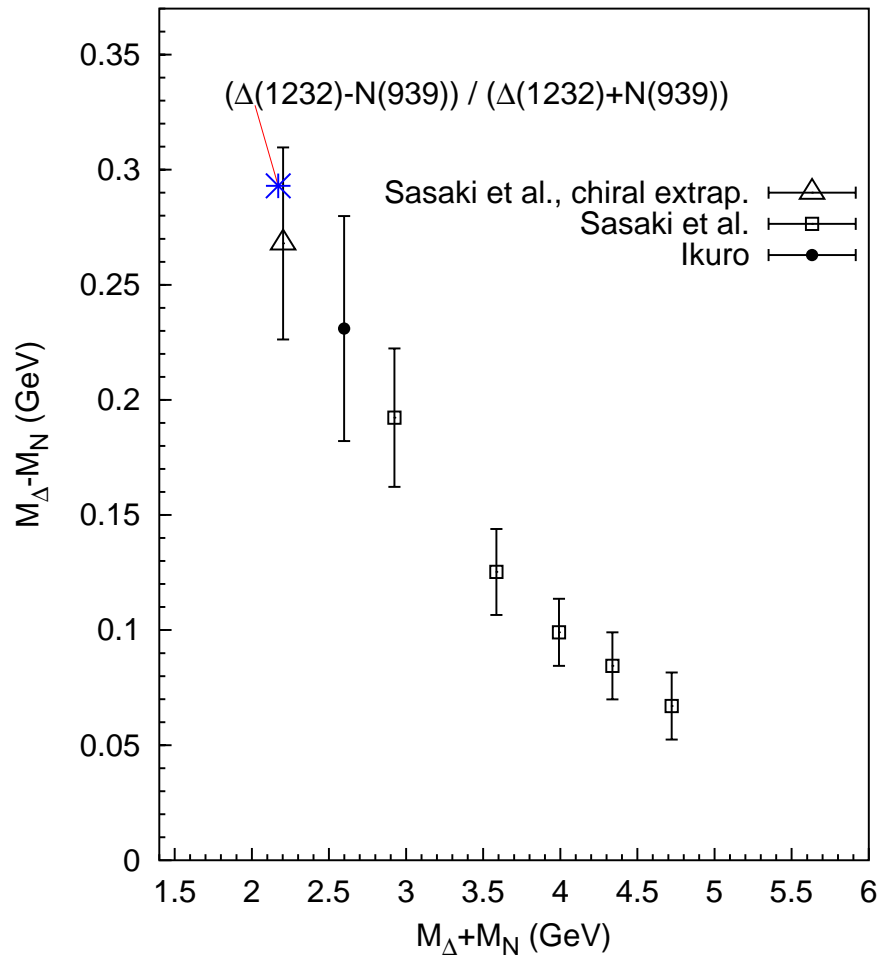
Figure 4.34: The hyperfine splitting between the $\Delta(1232)\,3/2^+$ and $N(939)\,1/2^+$ states as a function of M_Δ and M_N. Data points shown by open squares are obtained by Sasaki *et al.* for different values of quark masses. The open triangle is the chiral extrapolated value. A star is the experimental value. A bullet is a data point obtained in our simulations.

for different values of quark mass. Mass splittings should be suppressed at larger quark masses for both S- and P-waves.

4.7 Volume dependence of baryon masses

Very recently, we repeated the analysis of excited baryon spectra using lattices that have larger spatial volume. The new volume is $24^3 \times 64$ with the same lattice spacings and the same pion mass 500 MeV is used. The number of gauge configurations used is 167. We examined the volume dependence of N^* and delta baryon spectra based on these two lattice volumes. In this section, we briefly report the results in order to asses the volume dependence of our results.

In the previous section, we found that the ordering of the masses that we computed using $16^3 \times 64$ lattices is consistent with the empirical data for low-lying states, and that the mass ratio of the positive-parity excited state to the lightest state is too large in our results compared with the physical value, whereas the mass ratio of the lowest negative-parity state to the lightest state is close to the physical value in both N^* and delta baryons.

The low-lying masses obtained from $16^3 \times 64$ lattices and from $24^3 \times 64$ lattices are shown in Fig. 4.35. The pattern of the masses obtained from $24^3 \times 64$ lattices is very similar to the one with $16^3 \times 64$ lattices, which is a bit of a surprise. This means that the volume dependence of the baryon masses at this pion mass is not strong. The mean mass values of the excited states are reduced in $24^3 \times 64$ data by about 1%; however, these shifts are well within the statistical error bars. The mass splittings among low-lying negative-parity states are small in our results, which agrees with the pattern observed in the experimental data. For the positive-parity excited states, the experimental data shows that mass splitting between $\Delta(1232)3/2^+$ and $\Delta(1750)1/2^+$ is relatively large, which also agrees with the pattern seen in our results. Overly large masses for positive-parity excitations are not affected a lot by changing the lattice volume from 16^3 to 24^3.

Since the pion mass used in this simulation is about 3.57 times larger than the physical pion mass, the quark mass used in this simulation would be much larger than the physical quark mass. A heavy quark mass tends to suppress the kinetic energy, allowing quarks to reside in a smaller volume. The fact that the volume dependence of baryon masses is weak implies that the lattice volume of 16^3 is sufficient for excited baryons at this pion mass. The volume dependence of baryon masses is expected to become more significant at smaller pion masses.
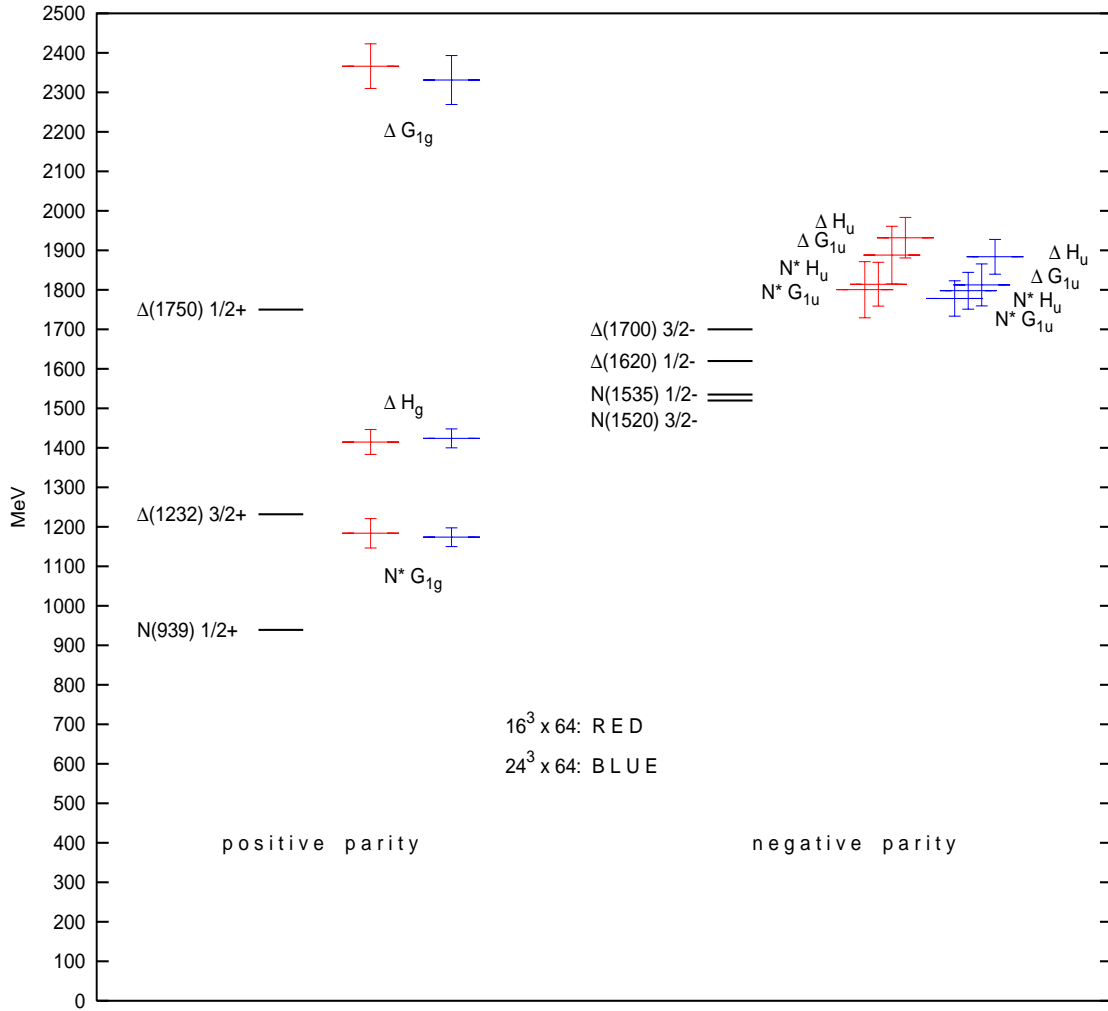
Figure 4.35: The masses of the lowest $G_{1g/u}$ and $H_{g/u}$ states for N^* and delta baryons computed using $16^3 \times 64$ lattices (expressed by red color in the figure) and $24^3 \times 64$ lattices (expressed by blue color in the figure) are shown using a physical scale. The corresponding experimental baryon masses are also shown. The $N^* H_g$ mass is excluded from the figure because the identification of the spin is yet unclear.

4.8 Summary

Numerical data that we obtained for excited baryon spectroscopy in quenched lattice QCD is provided in detail in this chapter. Orthogonality relations that are proved in Chapter 3 are numerically demonstrated. We examined correlation functions consisting of operators of different irreps, different rows within the same irrep, and different parities. It is shown that these correlation functions vanish within the statistical errors.

Similarly, it is shown that a correlation function is not a function of rows in our operator constructions. Therefore, correlation functions of different rows can be averaged so as to improve statistics. We took advantage of this symmetry in our simulations.

Results of lattice QCD calculations of N^* spectra are detailed in each channel of irreps. It is found that in general quasi-local operators are likely to couple to the ground states and their noises are comparatively small. One-link operators with T_1 type displacements also play important roles in low-lying states. From the effective mass plots, the signals of one-link operators are dominated by excited states in early time-slices and gradually decrease toward the middle of the time extension. One-link operators with E type displacements play smaller roles in low-lying states. It turns out that E one-link operators couple to highly excited states and signal-to-noise ratio becomes poor quickly. Effective mass plots obtained by diagonalizing correlation matrices show reasonable plateaus where masses can be determined for the lowest few eigenstates. Diagonalizations are performed on matrices of correlation functions of different dimensions for a given channel of isospin and irrep. The purpose of changing the dimensions is to see the stability and consistency of effective masses and generalized eigenvectors. No anomalous behaviors are observed, so we conclude that the stability is confirmed for N^* spectra calculated in these simulations.

Spectra of delta baryon are provided in a similar fashion to N^* spectra. Stability of $G_{1g/u}$ and $H_{g/u}$ is confirmed. However, we do not obtain robust results for $G_{2g/u}$ spectra. Too few operators are available for $G_{2g/u}$ delta baryon to confirm stability of the masses. We need a larger set of operators to have better estimates of masses of $G_{2g/u}$ delta baryon.

Obtained masses of N^* and delta baryons are compared with spectra of physically observed

baryonic states. Our simulations are performed using an unrealistic pion mass; the pion mass calculated in our lattices is about $500\,\mathrm{MeV}$. However, comparisons of mass ratios computed in our sumilation with the experimentally observed results are still interesting. Mass ratios of low-lying N^* states are somewhat smaller than those observed in nature. However, positive-parity excited states that we calculate are too heavy with respect to the ground state of the nucleon. To study the cause of this, we need to have lighter quark masses as well as larger lattice volume because the excited states are expected to be spatially-extended objects. It has been shown that use of larger volume is very important for hadron spectroscopy in full QCD simulations [94].

Mass ratios of a few low-lying states of delta barons are consistent with the experimentally observed mass ratios. The positive-parity excited states are again too massive with respect to the ground state mass for the delta baryon.

Hyperfine mass splitting motivated by the SU(6) quark model is measured. The obtained values for the S-wave are compared with the work done by Sasaki *et al*. Our calculation of hyperfine mass splitting is quite consistent with their results, as is displayed in Fig 4.34. Similarly, hyperfine mass splitting of P-wave is calculated. The ratio of the hyperfine splitting to the sum of individual masses is smaller than the physical value for P-wave by a factor that is close to the factor for S-wave within the error.

Lastly, the volume dependence of excited baryon masses is examined using the very recent data we obtained using $24^3 \times 64$ lattices. At $500\,\mathrm{MeV}$ pion mass used in these calculations, the volume dependence of baryon masses is very small. The masses of excited states are slightly decreased in the larger volume, but the shifts are well within the statistical errors. We expect that the volume dependence will be stronger, when a smaller quark mass is used.

Chapter 5

Summary and Future

Lattice QCD, a numerical method to solve QCD, is a rapidly growing subject in particle physics. Computational resources are being improved year by year, and sophisticated algorithms for simulations are being developed by various groups. Nonperturbative study of hadron spectroscopy is essential in order to give validity to QCD as the theory of strong interaction. In this thesis, baryon spectroscopy is studied focusing on improving baryonic interpolating field operators on lattices. Numerical simulations are performed using these operators and mass spectra of light baryons are calculated.

Baryon operators suitable for lattice QCD simulations are designed by making use of the spatial symmetries of the lattice. Nonlocal constituent quark fields are considered so as to impose nonzero orbital angular momentum to the baryon operators. Irreducible representations of the octahedral group are used to classify baryonic operators in order to study patterns corresponding to total angular momentum in the continuum limit. The orthogonality relations of sink and source operators from different rotational irreps, rows, and parities are formulated. Irreps of spatially displaced operators are determined by using the Clebsch-Gordan coefficients of the double octahedral group to form linear combinations of the direct products of spatial (vectorial) irreps and spinorial irreps.

Obtained operators are programmed to compute correlation matrices in each channel of irreps for N^* and delta baryons. Correlation matrices are then evaluated using the variational method, i.e., generalized eigenvalues of correlation matrices are numerically determined. The eigenvalues are then fitted by the linear χ^2 fitting method based on jackknife ensembles to give effective masses. A few low-lying masses in each channel are obtained. The stability of the obtained masses is examined by diagonalizing matrices consisting of different sets of operators. All effective

masses show stability, except for the delta baryon operators of the G_2 irrep. A larger set of operators is needed to have better estimates for this state.

The N^* and delta baryon spectra calculated in our simulations are compared with physically observed states. The comparison is based on the mass ratio of two states. The pattern of the low-lying masses that we compute is consistent with the pattern found in nature, although the mass splittings are considerably larger for positive-parity excited states. Hyperfine mass splittings motivated by the SU(6) quark model are studied in S-wave and P-wave. Hyperfine mass splitting of S-wave computed in our simulations agrees with published results. Both S-wave and P-wave hyperfine mass splittings that we calculate are smaller than the physical values by factors, which match with each other within the errors.

One way to improve the statistics without increasing the number of gauge configurations is to utilize the backward-propagating charge-conjugate states. Identification of charge-conjugate operators is simple in our operator construction and there are one-to-one correspondences in the operator tables provided in this thesis, thus use of the backward propagating signals should be straightforward.

Quark propagators that we used in this study correspond to a pion mass of about $500\,\mathrm{MeV}$, which is substantially larger than the physically observed pion mass, $140\,\mathrm{MeV}$. In the future we should redo the simulations using lower pion masses. Study of baryon mass ratios at different pion masses is very interesting. Chiral extrapolation to the physical pion mass also should be performed.

The lattice volume that we used in the analysis is $16^3 \times 64$, which corresponds to $\simeq (1.6\,\mathrm{fm})^3 \times 2.1\,\mathrm{fm}$. Very recently, we repeated the same analysis using $24^3 \times 64$ lattices with the same lattice spacings and same quark mass. Using these two lattice volumes, we studied the volume dependence of baryon masses. It turned out that the baryon spectra computed from these two lattices are almost the same for low-lying states. The mean values of the excited state masses are decreased slightly; however, the mass shifts are well within the statistical error bars. So we conclude that the volume dependence of baryon masses is not strong at this pion mass, where the role of internal

quark momenta to the spectrum is partially suppressed because of the large quark mass. The volume dependence will likely be more significant for smaller pion masses.

The operator construction method outlined in this work can be applied to different kinds of particles such as hybrids, glueballs, and pentaquarks. Since a pentaquark consists of five quarks, there will be a much larger set of pentaquark operators than baryon operators. All published results so far used only a few types of pentaquark operators [95–98]. The existence of the pentaquark state Θ^+ is still controversial in the lattice community as well as the experimental community. With a larger set of operators one could access more reliably the existence of the pentaquark state.

Because the irreps of the octahedral group correspond to superpositions of different angular momentum states, we are not able to precisely determine the spin. The spins would be better identified by calculating three-point Green's functions of the form

$$\langle 0|\, v_{k'}^{(n)}(t_f, t_0) B_\lambda^{\Lambda, k'} \mathbf{J}^2 v_k^{(n)}(t_i, t_0) \overline{B}_\lambda^{\Lambda, k} \,|0\rangle\,, \tag{5.1}$$

where $\mathbf{J}$ is suitably defined total angular momentum operator in lattice gauge theory and $v_k^{(n)}(t, t_0)$ represents generalized eigenvectors obtained in this study. Evaluations of spins are interesting issues as an additional topic in baryon spectroscopy.

Chiral extrapolations of baryon masses calculated in large enough, unquenched lattices will give the final results for baryon spectroscopy. Use of improved baryon interpolating operators as discussed in this work is crucial for baryon spectroscopy, especially for higher spin states, in lattice QCD simulations.

Appendix A

Group Theoretical Projection Operator

Suppose that $\vec{\mathbf{b}}$ is an arbitrary vector in a certain vector space L, and that this vector space L is invariant under transformations $T(G_a)$ induced by the elements G_a of a group $\mathcal{G}$. In general L will be reducible. A projection operator $P^{(\Lambda)}$ is an operator that projects $\vec{\mathbf{b}}$ onto a vector in the irreducible subspace Λ. Let $\mathbf{e}_i{}^{(\Lambda)}$ be the i-th element in a set of basis vectors spanning the irreducible subspace Λ. Then,

$$P^{(\Lambda)}\mathbf{e}_i{}^{(\Lambda')} = \mathbf{e}_i{}^{(\Lambda)}\delta_{\Lambda\Lambda'}, \tag{A.1}$$

$$P^{(\Lambda)}\vec{\mathbf{b}} = \sum_i c_i{}^{(\Lambda)}\mathbf{e}_i{}^{(\Lambda)}, \tag{A.2}$$

where c_i's are appropriate coefficients. The equation for the projection operator is given by

$$P^{(\Lambda)} = \frac{d_\Lambda}{g} \sum_{G_a \in \mathcal{G}} \chi^{(\Lambda)*}(G_a)\,T(G_a), \tag{A.3}$$

where g is the total number of elements in group $\mathcal{G}$, d_Λ is the dimension of irrep Λ, and $\chi^{(\Lambda)}(G_a)$ is the character (trance) of the irreducible representation of the group element G_a. The proof of Eq. (A.1) is straightforward by using the following relation:

$$\sum_{G_a \in \mathcal{G}} T_{ip}{}^{(\Lambda)}(G_a)T_{jq}{}^{(\Lambda')*}(G_a) = \frac{g}{d_\Lambda}\delta_{\Lambda\Lambda'}\delta_{ij}\delta_{pq}. \tag{A.4}$$

Thus, one can find a set of basis vectors for irreducible subspace Λ by finding all the linearly independent eigenvectors of $P^{(\Lambda)}$.

A group element G_a is said to be conjugate to another element G_b, if there exist an element G_m such that $G_a = G_m G_b G_m^{-1}$. In such case, elements G_a and G_b belong to the same conjugacy class p. Each group element in the group belongs to one and only one conjugacy class. The group elements in the same conjugacy class have the same character.

The reduction of the representation is written as

$$T(G_a) = T^{(\Lambda_1)}(G_a) \dotplus T^{(\Lambda_2)}(G_a) \dotplus \cdots. \tag{A.5}$$

The dot over the plus sign tells that $T^{(\Lambda)}(G_a)$ operates in a different subspace of L. Or in short,

$$T = \sum_\Lambda^{\cdot} m_\Lambda T^{(\Lambda)}, \tag{A.6}$$

where m_Λ is a multiplicity that tells how many times the irreducible representation $T^{(\Lambda)}$ occurs in the reduction, and m_Λ is given by the following formula:

$$m_\Lambda = \frac{1}{g} \sum_p N_p \, \chi_p^{(\Lambda)*} \chi_p \tag{A.7}$$

where N_p is the number of group elements in class p, $\chi_p^{(\Lambda)} = \chi^{(\Lambda)}(G_a \in p)$, and χ_p is the character of full-size (reducible) matrix in class p.

Appendix B

Dirac Matrices

Various conventions for the Dirac matrices are useful. Each is related by a unitary transformation to the Dirac-Pauli representation as follows,

$$\gamma_\mu = U \gamma_\mu^{(\mathrm{DP})} U^\dagger, \tag{B.1}$$

where

$$\gamma_j^{(\mathrm{DP})} = \begin{pmatrix} 0 & -i\sigma_j \\ i\sigma_j & 0 \end{pmatrix}, \quad \gamma_4^{(\mathrm{DP})} = \begin{pmatrix} 1 & 0 \\ 0 & -1 \end{pmatrix}. \tag{B.2}$$

The unitary matrix that generates the Weyl convention is

$$U^{(W)} = \frac{1 + \gamma_5^{(\mathrm{DP})} \gamma_4^{(\mathrm{DP})}}{\sqrt{2}}, \tag{B.3}$$

and the unitary transformation that generates the DeGrand-Rossi convention is

$$U^{(\mathrm{DR})} = \frac{-i\gamma_2^{(\mathrm{DP})} + \gamma_1^{(\mathrm{DP})} \gamma_3^{(\mathrm{DP})}}{\sqrt{2}}. \tag{B.4}$$

A quark field expressed in terms of the Dirac-Pauli representation may be re-expressed in the DeGrand-Rossi convention, for example, by

$$q_\Lambda^{(\text{DP})} = \left(U^{(\text{DR})\dagger}\right)_{\Lambda\beta} q_\beta^{(\text{DR})}. \tag{B.5}$$

In order to display the spin and parity of fields in a transparent way, we employ spin subscripts and ρ-spin superscripts in place of the four Dirac components $\mu = 1, 2, 3$ and 4 of each quark field in the Dirac-Pauli representation as shown in Table 2.7.

This encoding of the Dirac indices is based on the SU(2)⊗SU(2) representation of the Dirac matrices, where the first SU(2) is generated by 2×2 Pauli matrices for ρ-spin,

$$\rho_1 = \begin{pmatrix} 0 & 1 \\ 1 & 0 \end{pmatrix}, \quad \rho_2 = \begin{pmatrix} 0 & -i \\ i & 0 \end{pmatrix}, \quad \rho_3 = \begin{pmatrix} 1 & 0 \\ 0 & -1 \end{pmatrix}, \quad \rho_4 = \begin{pmatrix} 1 & 0 \\ 0 & 1 \end{pmatrix}, \tag{B.6}$$

and the second SU(2) is generated by the Pauli matrices for ordinary spin,

$$\sigma_1 = \begin{pmatrix} 0 & 1 \\ 1 & 0 \end{pmatrix}, \quad \sigma_2 = \begin{pmatrix} 0 & -i \\ i & 0 \end{pmatrix}, \quad \sigma_3 = \begin{pmatrix} 1 & 0 \\ 0 & -1 \end{pmatrix}, \quad \sigma_4 = \begin{pmatrix} 1 & 0 \\ 0 & 1 \end{pmatrix}. \tag{B.7}$$

In terms of these sets of 2×2 matrices, the 4×4 Dirac matrices are expressed as direct products of ρ-spin matrices and spin matrices as follows,

$$
\begin{aligned}
I &= \rho_4 \otimes \sigma_4, \\
\gamma_4 &= \rho_3 \otimes \sigma_4, \\
\gamma_5 &= \rho_1 \otimes \sigma_4, \\
\gamma_5\gamma_4 &= -i\rho_2 \otimes \sigma_4, \\
\gamma_5\gamma_k &= i\rho_3 \otimes \sigma_k, \\
\gamma_k &= \rho_2 \otimes \sigma_k, \\
\sigma_{4k} &= \rho_1 \otimes \sigma_k, \\
\sigma_{kl} &= -\epsilon_{klm}\rho_4 \otimes \sigma_m, \tag{B.8}
\end{aligned}
$$

where k, l and m take the values 1, 2 and 3.

Lattice rotations of spinors are generated by the 4×4 σ_{kl} matrices. A rotation by angle θ about an axis specified by unit vector $\hat{\mathbf{n}}$ has the form

$$R(\theta, \hat{\mathbf{n}}) = \rho_4 \otimes e^{i(\theta/2)\sigma \cdot \hat{\mathbf{n}}}, \tag{B.9}$$

where $\sigma \cdot \hat{\mathbf{n}} = \sigma_1 n_1 + \sigma_2 n_2 + \sigma_3 n_3$ is a linear combination of Pauli spin matrices. The rotation matrices are diagonal in ρ-spin.

Appendix C

Symmetry of Three Dirac Fields

The Dirac indices categorized in each Young tableau in Fig. 2.2 should be further reduced into G_1 or H irreps[1] for the purpose of operator construction. Decomposition of the Dirac index into ρ-spin and ordinary two-component spin (s-spin) helps to identify irreps and parities as discussed in Section 2.2.3.

The S (totally-symmetric), MS (mixed-symmetric), and MA (mixed-antisymmetic) combinations of three s-spins are defined as follows.

$$\text{S} \quad : \quad |{+}{+}{+}\rangle \,; \, \frac{|{+}{+}{-}\rangle + |{+}{-}{+}\rangle + |{-}{+}{+}\rangle}{\sqrt{3}} \,; \, \frac{|{+}{-}{-}\rangle + |{-}{+}{-}\rangle + |{-}{-}{+}\rangle}{\sqrt{3}} \,; \, |{-}{-}{-}\rangle. \tag{C.1}$$

$$\text{MS} \quad : \quad \frac{1}{\sqrt{6}}\left(2\,|{+}{+}{-}\rangle - |{+}{-}{+}\rangle - |{-}{+}{+}\rangle\right); -\frac{1}{\sqrt{6}}\left(2\,|{-}{-}{-}\rangle - |{-}{+}{-}\rangle - |{+}{-}{-}\rangle\right). \tag{C.2}$$

$$\text{MA} \quad : \quad \frac{1}{\sqrt{2}}\left(|{+}{-}{+}\rangle - |{+}{-}{+}\rangle\right); \frac{1}{\sqrt{2}}\left(|{+}{-}{-}\rangle - |{-}{+}{-}\rangle\right). \tag{C.3}$$

The four states of total spin in Eq. (C.1) are $|j, m\rangle = \left|\frac{3}{2}\frac{3}{2}\right\rangle, \left|\frac{3}{2}\frac{1}{2}\right\rangle, \left|\frac{3}{2} - \frac{1}{2}\right\rangle$, and $\left|\frac{3}{2} - \frac{3}{2}\right\rangle$ respectively. The two states of total spin in Eq. (C.2) are $\left|\frac{1}{2}\frac{1}{2}\right\rangle$ and $\left|\frac{1}{2} - \frac{1}{2}\right\rangle$ while the two states in Eq. (C.3) are $\left|\frac{1}{2}\frac{1}{2}\right\rangle$ and $\left|\frac{1}{2} - \frac{1}{2}\right\rangle$. All these states are orthogonal to one other. Because S states in Eq. (C.1) span total spin 3/2, they are the bases of an H irrep (no matter which ρ-spins are involved in making up the Dirac indices). The MS and MA states in Eq. (C.2, C.3) span total spin 1/2, so they are the bases of G_1 irreps.

---

[1] There is no G_2 irrep with three Dirac spinors.

Table C.1: Relation among Dirac spin symmetry, irrep, and the direct product of ρ-spins and s-spins.

Dirac sym	irrep	emb	$\rho \otimes s$
$\mathrm{S_{Dirac}}$	G_1	1	$\mathrm{MA}_\rho \otimes \mathrm{MA}_s \oplus \mathrm{MS}_\rho \otimes \mathrm{MS}_s$
	H	1,2	$\mathrm{S}_\rho \otimes \mathrm{S}_s$
$\mathrm{MS_{Dirac}}$	G_1	1,2	$\mathrm{S}_\rho \otimes \mathrm{MS}_s$
		3	$\mathrm{MA}_\rho \otimes \mathrm{MA}_s \ominus \mathrm{MS}_\rho \otimes \mathrm{MS}_s$
	H	1	$\mathrm{MS}_\rho \otimes \mathrm{S}_s$
$\mathrm{MA_{Dirac}}$	G_1	1,2	$\mathrm{S}_\rho \otimes \mathrm{MA}_s$
		3	$\mathrm{MA}_\rho \otimes \mathrm{MS}_s \oplus \mathrm{MS}_\rho \otimes \mathrm{MA}_s$
	H	1	$\mathrm{MA}_\rho \otimes \mathrm{S}_s$
$\mathrm{A_{Dirac}}$	G_1	1,2	$\mathrm{MA}_\rho \otimes \mathrm{MS}_s \ominus \mathrm{MS}_\rho \otimes \mathrm{MA}_s$

Products of three ρ-spins are categorized in exactly the same way. Direct products of states of three ρ-spins and states of three s-spins are simple when they are expressed in the bases of S, MS, and MA. For instance, $\mathrm{MA}_\rho \otimes \mathrm{S}_s$ with subscripts denoting ρ-spin and s-spin describes eight states; four of which are ρ-spin up states (negative ρ-parity), and four of which are ρ-spin down states (positive ρ-parity). The four states of each parity span H irreps because irreps of O^D are determined only by the s-spins. The direct product of $\mathrm{MA}_\rho \otimes \mathrm{S}_s$, with $\left|\frac{1}{2}, -\frac{1}{2}\right\rangle_\rho$ and $\left|\frac{3}{2}, \frac{1}{2}\right\rangle_s$ is written as follows.

$$\frac{|+--\rangle_\rho - |-+-\rangle_\rho}{\sqrt{2}} \otimes \frac{|++-\rangle_s + |+-+\rangle_s + |-++\rangle_s}{\sqrt{3}}$$
$$= \frac{1}{\sqrt{6}} \left(\left|{}^{+--}_{++-}\right\rangle + \left|{}^{+--}_{+-+}\right\rangle + \left|{}^{+--}_{-++}\right\rangle - \left|{}^{-+-}_{++-}\right\rangle - \left|{}^{-+-}_{+-+}\right\rangle - \left|{}^{-+-}_{-++}\right\rangle \right)$$
$$= \frac{1}{\sqrt{6}} \left(|134\rangle + |143\rangle + |233\rangle - |313\rangle - |323\rangle - |413\rangle \right) \tag{C.4}$$

The second line of Eq. (C.4) employs the notation of $\left|{}^{\rho_1\rho_2\rho_3}_{s_1 s_2 s_3}\right\rangle$, and the third line is $|\mu_1\mu_2\mu_3\rangle$ with $\mu_i = 1, 2, 3, 4$ in Dirac-Pauli representation. The translation of μ to (ρ, s) is given in Table 2.7. It is clear that the obtained Dirac indices are antisymmetric under exchange of first two labels but

not totally antisymmetric. Thus, we denote $MA_\rho \otimes S_s = MA_{Dirac}$. The nucleon operator that follows from this example is labeled as H_g, row 2 in Table 2.8.

From such considerations one obtains Table C.1, which provides the relations of Dirac index symmetries (abbreviated as "Dirac sym" in the table) to irreps of Dirac indices, and direct products of ρ-spins and s-spins. Note that $MA_\rho \otimes MA_s$ and $MS_\rho \otimes MS_s$ both have a mixture of S_{Dirac} and MS_{Dirac}. One can easily see that addition of a state from $MA_\rho \otimes MA_s$, say G_{1g}, row 1, and a state from $MS_\rho \otimes MS_s$ of the same G_{1g}, row 1 yields a pure S_{Dirac} state. The subtraction of the states yields a pure MS_{Dirac} state. Similarly, $MA_\rho \otimes MS_s$ and $MS_\rho \otimes MA_s$ have a mixture of MA_{Dirac} and A_{Dirac}. A pure MA_{Dirac} is obtained by adding states from $MA_\rho \otimes MS_s$ and $MS_\rho \otimes MA_s$ and a pure A_{Dirac} is obtained by the subtraction.

Explicit combinations of Dirac indices $\mu_1\mu_2\mu_3$ are given in Table C.2 and Table C.3. Table C.2 contains S and MS combinations of three Dirac indices, assigning each to an irrep ($G_{1g/u}$ or $H_{g/u}$), embedding, and row. Table C.3 contains all MA and A combinations of three Dirac indices in a similar way. The third column of Table C.1 shows an embedding that has a connection to Table C.2 in a self-explanatory way.

All 64 states given in the tables are *orthogonal* to one another. This means that MS combinations of Dirac indices do not contain S combinations, or their inner products are zero. Similarly, MA's do not contain A's. Each category of indices, S, MS, MA, or A, has a definite *index ordering*. Let us define the following index ordering operators,

$$R^S |\mu_1\mu_2\mu_3\rangle = |\mu_1\mu_2\mu_3\rangle + |\mu_2\mu_1\mu_3\rangle + |\mu_2\mu_3\mu_1\rangle + |\mu_3\mu_2\mu_1\rangle + |\mu_3\mu_1\mu_2\rangle + |\mu_1\mu_3\mu_2\rangle, \quad (C.5)$$

$$R^{MS} |\mu_1\mu_2\mu_3\rangle = |\mu_1\mu_2\mu_3\rangle + |\mu_2\mu_1\mu_3\rangle - \frac{1}{2}(|\mu_2\mu_3\mu_1\rangle + |\mu_3\mu_2\mu_1\rangle + |\mu_3\mu_1\mu_2\rangle + |\mu_1\mu_3\mu_2\rangle)), (C.6)$$

$$R^{MA} |\mu_1\mu_2\mu_3\rangle = |\mu_1\mu_2\mu_3\rangle - |\mu_2\mu_1\mu_3\rangle - |\mu_2\mu_3\mu_1\rangle + |\mu_3\mu_2\mu_1\rangle, \quad (C.7)$$

$$R^A |\mu_1\mu_2\mu_3\rangle = |\mu_1\mu_2\mu_3\rangle - |\mu_2\mu_1\mu_3\rangle + |\mu_2\mu_3\mu_1\rangle - |\mu_3\mu_2\mu_1\rangle + |\mu_3\mu_1\mu_2\rangle - |\mu_1\mu_3\mu_2\rangle. \quad (C.8)$$

With these definitions, the index ordering operators R^S, R^{MS}, R^{MA}, and R^A make the Dirac indices to be $S_{Drc}, MS_{Drc}, MA_{Drc}$, and A_{Drc}, respectively, and make states mutually orthogonal.

Table C.2: Irreps of S, MS combinations of Dirac indices for tri-quark states in Dirac-Pauli representation. The first entry of MS table reads $2\overline{q}_1^{f_1}\overline{q}_1^{f_2}\overline{q}_2^{f_3} - \overline{q}_1^{f_1}\overline{q}_2^{f_2}\overline{q}_1^{f_3} - \overline{q}_2^{f_1}\overline{q}_1^{f_2}\overline{q}_1^{f_3}$ for G_{1g}, embedding 1, row 1 local operator.

sym.	irrep	emb.	row	$q_{\mu_1}q_{\mu_2}q_{\mu_3}$
S	G_{1g}	1	1	$-2(332 + 323 + 233) + 341 + 431 + 314 + 413 + 134 + 143$
			2	$2(144 + 414 + 441) - 234 - 342 - 423 - 243 - 324 - 432$
	G_{1u}	1	1	$2(114 + 141 + 411) - 123 - 213 - 132 - 231 - 321 - 312$
			2	$-2(223 + 232 + 322) + 214 + 124 + 241 + 142 + 421 + 412$
	H_g	1	1	111
			2	$112 + 121 + 211$
			3	$122 + 212 + 221$
			4	222
		2	1	$133 + 313 + 331$
			2	$233 + 323 + 332 + 134 + 341 + 413 + 143 + 431 + 314$
			3	$144 + 414 + 441 + 234 + 342 + 423 + 243 + 432 + 324$
			4	$244 + 424 + 442$
	H_u	1	1	$113 + 131 + 311$
			2	$411 + 141 + 114 + 312 + 123 + 231 + 321 + 213 + 132$
			3	$322 + 232 + 223 + 412 + 124 + 241 + 421 + 214 + 142$
			4	$224 + 242 + 422$
		2	1	333
			2	$334 + 343 + 433$
			3	$344 + 434 + 443$
			4	444
MS	G_{1g}	1	1	$2(112) - 121 - 211$
			2	$-2(221) + 212 + 122$
		2	1	$2(332 + 314 + 134) - 341 - 323 - 143 - 431 - 413 - 233$
			2	$-2(441 + 423 + 243) + 432 + 414 + 234 + 342 + 324 + 144$
		3	1	$-2(332 + 413 + 143) + 323 + 233 + 134 + 314 + 341 + 431$
			2	$2(441 + 324 + 234) - 414 - 144 - 243 - 423 - 432 - 342$
	G_{1u}	1	1	$2(114 + 132 + 312) - 123 - 141 - 321 - 213 - 231 - 411$
			2	$-2(223 + 241 + 421) + 214 + 232 + 412 + 124 + 142 + 322$
		2	1	$2(334) - 343 - 433$
			2	$-2(443) + 434 + 344$
		3	1	$2(114 + 231 + 321) - 141 - 411 - 312 - 132 - 123 - 213$
			2	$-2(223 + 142 + 412) + 232 + 322 + 421 + 241 + 214 + 124$
	H_g	1	1	$-2(331) + 313 + 133$
			2	$-2(332 + 341 + 431) + 314 + 134 + 323 + 143 + 413 + 233$
			3	$-2(342 + 432 + 441) + 324 + 144 + 414 + 234 + 423 + 243$
			4	$-2(442) + 424 + 244$
	H_u	1	1	$2(113) - 131 - 311$
			2	$2(114 + 123 + 213) - 132 - 312 - 141 - 321 - 231 - 411$
			3	$2(124 + 214 + 223) - 142 - 322 - 232 - 412 - 241 - 421$
			4	$2(224) - 242 - 422$

Table C.3: Irreps of MA, A combinations of Dirac indices for tri-quark states in Dirac-Pauli representation. The caption in Table C.2 describes how to read this table.

sym.	irrep	emb.	row	$q_{\mu_1} q_{\mu_2} q_{\mu_3}$
MA	G_{1g}	1	1	$121 - 211$
			2	$122 - 212$
		2	1	$143 - 233 + 323 - 413 + 341 - 431$
			2	$144 - 234 + 324 - 414 + 342 - 432$
		3	1	$-233 + 323 + 134 - 314 - 341 + 431$
			2	$-414 + 144 - 243 + 423 + 432 - 342$
	G_{1u}	1	1	$123 - 213 + 141 - 231 + 321 - 411$
			2	$124 - 214 + 142 - 232 + 322 - 412$
		2	1	$343 - 433$
			2	$344 - 434$
		3	1	$-141 + 411 - 312 + 132 + 123 - 213$
			2	$232 - 322 + 421 - 241 - 214 + 124$
	H_g	1	1	$133 - 313$
			2	$134 - 314 + 143 - 323 + 233 - 413$
			3	$144 - 324 + 234 - 414 + 243 - 423$
			4	$244 - 424$
	H_u	1	1	$131 - 311$
			2	$132 - 312 + 141 - 321 + 231 - 411$
			3	$142 - 322 + 232 - 412 + 241 - 421$
			4	$242 - 422$
A	G_{1g}	1	1	$134 - 314 + 341 - 431 + 413 - 143$
			2	$234 - 324 + 342 - 432 + 423 - 243$
	G_{1u}	1	1	$-123 + 213 - 231 + 321 - 312 + 132$
			2	$-124 + 214 - 241 + 421 - 412 + 142$

Appendix D

Relations of $N_{\mu_1\mu_2\mu_3}$ to Most Commonly Used Nucleon

Operators

Various groups have performed lattice simulations using the following two interpolating fields for a nucleon:

$$\chi_1^{1/2} = \left(u^T C \gamma_5 d\right) u, \tag{D.1}$$

$$\chi_2^{1/2} = \left(u^T C d\right) \gamma_5 u, \tag{D.2}$$

where space-time arguments are omitted. Matrix C is a charge conjugation operator, defined by $C = \gamma_4\gamma_2$. Each of these four-component operators corresponds to a G_1 irrep and may be written in terms of $\Psi_{S,S_z}^{\Lambda,k}$. Positive and negative ρ-parity parts of $\chi_1^{1/2}$ are projected in Dirac-Pauli representation as follows,

$$\frac{1+\gamma_4}{2}\chi_1^{1/2} = \begin{pmatrix} -N_{121} - N_{341} \\ -N_{122} - N_{342} \end{pmatrix} = \begin{pmatrix} -\Psi_{1/2,+1/2}^{G_{1g},1} - \frac{1}{\sqrt{3}}(\Psi_{1/2,+1/2}^{G_{1g},2} - \Psi_{1/2,+1/2}^{G_{1g},3}) \\ -\Psi_{1/2,-1/2}^{G_{1g},1} - \frac{1}{\sqrt{3}}(\Psi_{1/2,-1/2}^{G_{1g},2} - \Psi_{1/2,-1/2}^{G_{1g},3}) \end{pmatrix} \tag{D.3}$$

$$\frac{1-\gamma_4}{2}\chi_1^{1/2} = \begin{pmatrix} -N_{123} - N_{343} \\ -N_{124} - N_{344} \end{pmatrix} = \begin{pmatrix} \frac{1}{\sqrt{3}}(\Psi_{1/2,+1/2}^{G_{1u},1} + \Psi_{1/2,+1/2}^{G_{1u},3}) - \Psi_{1/2,+1/2}^{G_{1u},2} \\ \frac{1}{\sqrt{3}}(\Psi_{1/2,-1/2}^{G_{1u},1} + \Psi_{1/2,-1/2}^{G_{1u},3}) - \Psi_{1/2,-1/2}^{G_{1u},2} \end{pmatrix}. \tag{D.4}$$

The upper component corresponds to $S_z = +1/2$. Similarly $\chi_2^{1/2}$ can be projected to operators of definite ρ-parity,

$$\frac{1+\gamma_4}{2}\chi_2^{1/2} = \begin{pmatrix} N_{143} - N_{233} \\ N_{144} - N_{234} \end{pmatrix} = \frac{1}{\sqrt{3}}\begin{pmatrix} 2\Psi_{1/2,+1/2}^{G_{1g},2} + \Psi_{1/2,+1/2}^{G_{1g},3} \\ 2\Psi_{1/2,-1/2}^{G_{1g},2} + \Psi_{1/2,-1/2}^{G_{1g},3} \end{pmatrix}, \tag{D.5}$$

$$\frac{1-\gamma_4}{2}\chi_2^{1/2} = \begin{pmatrix} N_{141} - N_{231} \\ N_{142} - N_{232} \end{pmatrix} = \frac{1}{\sqrt{3}}\begin{pmatrix} 2\Psi_{1/2,+1/2}^{G_{1u},1} - \Psi_{1/2,+1/2}^{G_{1u},3} \\ 2\Psi_{1/2,-1/2}^{G_{1u},1} - \Psi_{1/2,-1/2}^{G_{1u},3} \end{pmatrix}. \tag{D.6}$$

These results show how the the components of $\chi_1^{1/2}$ and $\chi_2^{1/2}$ nucleon operators are related to operators in Table 2.8.

Appendix E

Clebsch-Gordan Coefficients of Cubic Group

The continuum rotation group has an infinite number of irreps, and its basis is denoted by $|j, m\rangle$ with total angular momentum, j and its projection onto z-axis, m. A direct product of two states from irreps can be projected onto a single irrep using the Clebsch-Gordan formula,

$$|J, M\rangle = \sum_{m_1, m_2} C \begin{pmatrix} J & j_1 & j_2 \\ M & m_1 & m_2 \end{pmatrix} |j_1, m_1\rangle |j_2, m_2\rangle, \tag{E.1}$$

or

$$C \begin{pmatrix} J & j_1 & j_2 \\ M & m_1 & m_2 \end{pmatrix} = \langle j_1, m_1| \langle j_2, m_2 | J, M \rangle. \tag{E.2}$$

In the octahedral group, the number of irreps is finite and a similar Clebsch-Gordan formula shows how irreps may be built from direct products of irreps,

$$\overline{\mathcal{O}}_\lambda^\Lambda = \sum_{\lambda_1, \lambda_2} C \begin{pmatrix} \Lambda & \Lambda_1 & \Lambda_2 \\ \lambda & \lambda_1 & \lambda_2 \end{pmatrix} \overline{\mathcal{O}}_{\lambda_1}^{\Lambda_1} \overline{\mathcal{O}}_{\lambda_2}^{\Lambda_2}, \tag{E.3}$$

where $\Lambda(\Lambda_i)$ and $\lambda(\lambda_i)$ represents irrep and row, respectively. The notation $\overline{\mathcal{O}}_\lambda^\Lambda$ is used to express $\hat{A}_1, \hat{A}_2^\lambda, \hat{E}^\lambda, \hat{T}_1^\lambda, \hat{T}_2^\lambda, \overline{\Psi}_\lambda^{G_{1g}}, \overline{\Psi}_\lambda^{G_{1u}}, \overline{\Psi}_\lambda^{H_g}$, or $\overline{\Psi}_\lambda^{H_u}$. Altmann and Herzig have tabulated all Clebsch-Gordan coefficients of the octahedral group. Clebsch-Gordan coefficients depend upon the basis of irrep operators; different choices of the bases are related to one another by unitary transformations. Because our basis operators differ from those published by Altmann and Herzig, we have performed the required unitary transformation and obtained suitable Clebsch-Gordan coefficients for all possible direct products of two irreps of the octahedral group. An overall phase factor may be omitted from operators in the same irrep in lattice calculations, so we have omitted phase factors such that all of our Clebsch-Gordan coefficients are real.

In each Clebsch-Gordan coefficient table, the resultant irrep appearing on the left side of Eq. (E.3) is listed in the first row and second column, and the two irreps appearing on the right side of Eq. (E.3) are listed in the second row and the first column. The following table explains how to read Clebsch-Gordan tables provided in the rest of this appendix.

Table E.1: Description for tables of Clebsch-Gordan coefficients.

$\overline{O}^{\Lambda_1} \otimes \overline{O}^{\Lambda_2}$	$\overline{\mathcal{O}}^{\Lambda}_{\lambda}$
$\overline{\mathcal{O}}^{\Lambda_1}_{\lambda_1}\quad \overline{\mathcal{O}}^{\Lambda_2}_{\lambda_2}$	$sgn\left[C\begin{pmatrix}\Lambda & \Lambda_1 & \Lambda_2 \\ \lambda & \lambda_1 & \lambda_2\end{pmatrix}\right]\left|C\begin{pmatrix}\Lambda & \Lambda_1 & \Lambda_2 \\ \lambda & \lambda_1 & \lambda_2\end{pmatrix}\right|^2$

$A_2 \otimes E$	E^1	E^2
$A_2 E^1$	0	-1
$A_2 E^2$	1	0

$A_2 \otimes T_1$	T_2^1	T_2^2	T_2^3
$A_2 T_1^1$	0	0	-1
$A_2 T_1^2$	0	-1	0
$A_2 T_1^3$	1	0	0

$A_2 \otimes T_2$	T_1^1	T_1^2	T_1^3
$A_2 T_2^1$	0	0	-1
$A_2 T_2^2$	0	1	0
$A_2 T_2^3$	1	0	0

$A_2 \otimes G_1$	G_2^1	G_2^2
$A_2 G_1^1$	1	0
$A_2 G_1^2$	0	1

$A_2 \otimes G_2$	G_1^1	G_1^2
$A_2 G_2^1$	1	0
$A_2 G_2^2$	0	1

$A_2 \otimes H$	H^1	H^2	H^3	H^4
$A_2 H^1$	0	0	-1	0
$A_2 H^2$	0	0	0	1
$A_2 H^3$	1	0	0	0
$A_2 H^4$	0	-1	0	0

$E \otimes E$	A_1	A_2	E^1	E^2
$E^1 E^1$	1/2	0	1/2	0
$E^1 E^2$	0	1/2	0	-1/2
$E^2 E^1$	0	-1/2	0	-1/2
$E^2 E^2$	1/2	0	-1/2	0

$E \otimes T_1$	T_1^1	T_1^2	T_1^3	T_2^1	T_2^2	T_2^3
$E^1 T_1^1$	1/4	0	0	3/4	0	0
$E^1 T_1^2$	0	-1	0	0	0	0
$E^1 T_1^3$	0	0	1/4	0	0	-3/4
$E^2 T_1^1$	0	0	3/4	0	0	1/4
$E^2 T_1^2$	0	0	0	0	-1	0
$E^2 T_1^3$	3/4	0	0	-1/4	0	0

$E \otimes T_2$	T_1^1	T_1^2	T_1^3	T_2^1	T_2^2	T_2^3
$E^1 T_2^1$	3/4	0	0	1/4	0	0
$E^1 T_2^2$	0	0	0	0	-1	0
$E^1 T_2^3$	0	0	-3/4	0	0	1/4
$E^2 T_2^1$	0	0	-1/4	0	0	-3/4
$E^2 T_2^1$	0	-1	0	0	0	0
$E^2 T_2^1$	1/4	0	0	-3/4	0	0

$E \otimes G_1$	H^1	H^2	H^3	H^4
$E^1 G_1^1$	0	-1	0	0
$E^1 G_1^2$	0	0	1	0
$E^2 G_1^1$	0	0	0	-1
$E^2 G_1^2$	1	0	0	0

$E \otimes G_2$	H^1	H^2	H^3	H^4
$E^1 G_2^1$	0	0	0	-1
$E^1 G_2^2$	1	0	0	0
$E^2 G_2^1$	0	1	0	0
$E^2 G_2^2$	0	0	-1	0

$E \otimes H$	G_1^1	G_1^2	G_2^1	G_2^2	H^1	H^2	H^3	H^4
$E^1 H^1$	0	0	0	-1/2	1/2	0	0	0
$E^1 H^2$	1/2	0	0	0	0	-1/2	0	0
$E^1 H^3$	0	-1/2	0	0	0	0	-1/2	0
$E^1 H^4$	0	0	1/2	0	0	0	0	1/2
$E^2 H^1$	0	-1/2	0	0	0	0	1/2	0
$E^2 H^2$	0	0	-1/2	0	0	0	0	1/2
$E^2 H^3$	0	0	0	1/2	1/2	0	0	0
$E^2 H^4$	1/2	0	0	0	0	1/2	0	0

$T_1 \otimes T_1$	A_1	E^1	E^2	T_1^1	T_1^2	T_1^3	T_2^1	T_2^2	T_2^3
$T_1^1 T_1^1$	0	0	1/2	0	0	0	0	1/2	0
$T_1^1 T_1^2$	0	0	0	1/2	0	0	1/2	0	0
$T_1^1 T_1^3$	1/3	1/6	0	0	1/2	0	0	0	0
$T_1^2 T_1^1$	0	0	0	-1/2	0	0	1/2	0	0
$T_1^2 T_1^2$	-1/3	2/3	0	0	0	0	0	0	0
$T_1^2 T_1^3$	0	0	0	0	0	1/2	0	0	1/2
$T_1^3 T_1^1$	1/3	1/6	0	0	-1/2	0	0	0	0
$T_1^3 T_1^2$	0	0	0	0	0	-1/2	0	0	1/2
$T_1^3 T_1^3$	0	0	1/2	0	0	0	0	-1/2	0

$T_1 \otimes T_2$	A_2	E^1	E^2	T_1^1	T_1^2	T_1^3	T_2^1	T_2^2	T_2^3
$T_1^1T_2^1$	1/3	0	1/6	0	0	0	0	-1/2	0
$T_1^1T_2^2$	0	0	0	0	0	1/2	0	0	1/2
$T_1^1T_2^3$	0	1/2	0	0	-1/2	0	0	0	0
$T_1^2T_2^1$	0	0	0	1/2	0	0	1/2	0	0
$T_1^2T_2^2$	1/3	0	-2/3	0	0	0	0	0	0
$T_1^2T_2^3$	0	0	0	0	0	1/2	0	0	-1/2
$T_1^3T_2^1$	0	-1/2	0	0	-1/2	0	0	0	0
$T_1^3T_2^2$	0	0	0	-1/2	0	0	1/2	0	0
$T_1^3T_2^3$	-1/3	0	-1/6	0	0	0	0	-1/2	0

$T_1 \otimes G_1$	G_1^1	G_1^2	H^1	H^2	H^3	H^4
$T_1^1G_1^1$	0	0	1	0	0	0
$T_1^1G_1^2$	2/3	0	0	1/3	0	0
$T_1^2G_1^1$	-1/3	0	0	2/3	0	0
$T_1^2G_1^2$	0	1/3	0	0	2/3	0
$T_1^3G_1^1$	0	-2/3	0	0	1/3	0
$T_1^3G_1^2$	0	0	0	0	0	1

$T_1 \otimes G_2$	G_2^1	G_2^2	H^1	H^2	H^3	H^4
$T_1^1G_2^1$	0	0	0	0	-1	0
$T_1^1G_2^2$	2/3	0	0	0	0	1/3
$T_1^2G_2^1$	-1/3	0	0	0	0	2/3
$T_1^2G_2^2$	0	1/3	2/3	0	0	0
$T_1^3G_2^1$	0	-2/3	1/3	0	0	0
$T_1^3G_2^2$	0	0	0	-1	0	0

$T_2 \otimes T_2$	A_1	E^1	E^2	T_1^1	T_1^2	T_1^3	T_2^1	T_2^2	T_2^3
$T_2^1T_2^1$	0	0	-1/2	0	0	0	0	-1/2	0
$T_2^1T_2^2$	0	0	0	0	0	-1/2	0	0	-1/2
$T_2^1T_2^3$	1/3	1/6	0	0	-1/2	0	0	0	0
$T_2^2T_2^1$	0	0	0	0	0	1/2	0	0	-1/2
$T_2^2T_2^2$	1/3	-2/3	0	0	0	0	0	0	0
$T_2^2T_2^3$	0	0	0	1/2	0	0	1/2	0	0
$T_2^3T_2^1$	1/3	1/6	0	0	1/2	0	0	0	0
$T_2^3T_2^2$	0	0	0	-1/2	0	0	1/2	0	0
$T_2^3T_2^3$	0	0	-1/2	0	0	0	0	1/2	0

$T_1 \otimes H$	G_1^1	G_1^2	G_2^1	G_2^2	H^1	H^2	H^3	H^4	H^1	H^2	H^3	H^4
$T_1^1H^1$	0	0	1/6	0	0	0	0	0	0	0	0	-5/6
$T_1^1H^2$	0	0	0	-1/2	-2/5	0	0	0	1/10	0	0	0
$T_1^1H^3$	1/6	0	0	0	0	-8/15	0	0	0	-3/10	0	0
$T_1^1H^4$	0	1/2	0	0	0	0	-2/5	0	0	0	1/10	0
$T_1^2H^1$	0	0	0	-1/3	3/5	0	0	0	1/15	0	0	0
$T_1^2H^2$	-1/3	0	0	0	0	1/15	0	0	0	-3/5	0	0
$T_1^2H^3$	0	-1/3	0	0	0	0	-1/15	0	0	0	3/5	0
$T_1^2H^4$	0	0	-1/3	0	0	0	0	-3/5	0	0	0	-1/15
$T_1^3H^1$	1/2	0	0	0	0	2/5	0	0	0	-1/10	0	0
$T_1^3H^2$	0	1/6	0	0	0	0	8/15	0	0	0	3/10	0
$T_1^3H^3$	0	0	-1/2	0	0	0	0	2/5	0	0	0	-1/10
$T_1^3H^4$	0	0	0	1/6	0	0	0	0	5/6	0	0	0

$T_2 \otimes G_1$	G_2^1	G_2^2	H^1	H^2	H^3	H^4
$T_2^1G_1^1$	0	-2/3	1/3	0	0	0
$T_2^1G_1^2$	0	0	0	-1	0	0
$T_2^2G_1^1$	1/3	0	0	0	0	-2/3
$T_2^2G_1^2$	0	-1/3	-2/3	0	0	0
$T_2^3G_1^1$	0	0	0	0	1	0
$T_2^3G_1^2$	-2/3	0	0	0	0	-1/3

$T_2 \otimes G_2$	G_1^1	G_1^2	H^1	H^2	H^3	H^4
$T_2^1G_2^1$	0	-2/3	0	0	-1/3	0
$T_2^1G_2^2$	0	0	0	0	0	-1
$T_2^2G_2^1$	1/3	0	0	2/3	0	0
$T_2^2G_2^2$	0	-1/3	0	0	2/3	0
$T_2^3G_2^1$	0	0	1	0	0	0
$T_2^3G_2^2$	-2/3	0	0	1/3	0	0

$T_2 \otimes H$	G_1^1	G_1^2	G_2^1	G_2^2	H^1	H^2	H^3	H^4	H^1	H^2	H^3	H^4
$T_2^1H^1$	0	0	1/2	0	0	0	0	0	0	0	0	1/2
$T_2^1H^2$	0	0	0	1/6	2/3	0	0	0	1/6	0	0	0
$T_2^1H^3$	1/2	0	0	0	0	0	0	0	-1/2	0	0	0
$T_2^1H^4$	0	-1/6	0	0	0	0	-2/3	0	0	0	1/6	0
$T_2^2H^1$	0	-1/3	0	0	0	0	1/3	0	0	0	1/3	0
$T_2^2H^2$	0	0	1/3	0	0	0	0	1/3	0	0	0	-1/3
$T_2^2H^3$	0	0	0	1/3	-1/3	0	0	0	1/3	0	0	0
$T_2^2H^4$	-1/3	0	0	0	0	-1/3	0	0	0	-1/3	0	0
$T_2^3H^1$	1/6	0	0	0	0	-2/3	0	0	0	1/6	0	0
$T_2^3H^2$	0	-1/2	0	0	0	0	0	0	0	-1/2	0	0
$T_2^3H^3$	0	0	-1/6	0	0	0	0	2/3	0	0	0	1/6
$T_2^3H^4$	0	0	0	-1/2	0	0	0	0	1/2	0	0	0

$G_1 \otimes G_1$	A_1	T_1^1	T_1^2	T_1^3
$G_1^1G_1^1$	0	1	0	0
$G_1^1G_1^2$	1/2	0	1/2	0
$G_1^2G_1^1$	-1/2	0	1/2	0
$G_1^2G_1^2$	0	0	0	1

$G_1 \otimes H$	E^1	E^2	T_1^1	T_1^2	T_1^3	T_2^1	T_2^2	T_2^3
$G_1^1 H^1$	0	1/2	0	0	0	0	1/2	0
$G_1^1 H^2$	0	0	1/4	0	0	3/4	0	0
$G_1^1 H^3$	1/2	0	0	1/2	0	0	0	0
$G_1^1 H^4$	0	0	0	0	3/4	0	0	1/4
$G_1^2 H^1$	0	0	-3/4	0	0	1/4	0	0
$G_1^2 H^2$	1/2	0	0	-1/2	0	0	0	0
$G_1^2 H^3$	0	0	0	0	-1/4	0	0	3/4
$G_1^2 H^4$	0	1/2	0	0	0	0	-1/2	0

$G_1 \otimes G_2$	A_2	T_2^1	T_2^2	T_2^3
$G_1^1 G_2^1$	0	0	0	-1
$G_1^1 G_2^2$	1/2	0	-1/2	0
$G_1^2 G_2^1$	-1/2	0	-1/2	0
$G_1^2 G_2^2$	0	1	0	0

$G_2 \otimes H$	E^1	E^2	T_1^1	T_1^2	T_1^3	T_2^1	T_2^2	T_2^3
$G_2^1 H^1$	1/2	0	0	1/2	0	0	0	0
$G_2^1 H^2$	0	0	0	0	-3/4	0	0	-1/4
$G_2^1 H^3$	0	-1/2	0	0	0	0	-1/2	0
$G_2^1 H^4$	0	0	1/4	0	0	3/4	0	0
$G_2^2 H^1$	0	0	0	0	-1/4	0	0	3/4
$G_2^2 H^2$	0	-1/2	0	0	0	0	1/2	0
$G_2^2 H^3$	0	0	3/4	0	0	-1/4	0	0
$G_2^2 H^4$	1/2	0	0	-1/2	0	0	0	0

$G_2 \otimes G_2$	A_1	T_1^1	T_1^2	T_1^3
$G_2^1 G_2^1$	0	1	0	0
$G_2^1 G_2^2$	1/2	0	1/2	0
$G_2^2 G_2^1$	-1/2	0	1/2	0
$G_2^2 G_2^2$	0	0	0	1

$H \otimes H$	A_1	A_2	E^1	E^2	T_1^1	T_1^2	T_1^3	T_1^1	T_1^2	T_1^3	T_2^1	T_2^2	T_2^3	T_2^1	T_2^2	T_2^3
$H^1 H^1$	0	0	0	0	0	0	0	0	0	25	0	0	3	0	0	0
$H^1 H^2$	0	1	0	1	0	0	0	0	0	0	0	-1	0	0	1	0
$H^1 H^3$	0	0	0	0	3	0	0	3	0	0	1	0	0	1	0	0
$H^1 H^4$	1	0	1	0	0	9	0	0	-1	0	0	0	0	0	0	0
$H^2 H^1$	0	1	0	-1	0	0	0	0	0	0	0	-1	0	0	-1	0
$H^2 H^2$	0	0	0	0	-4	0	0	9	0	0	3	0	0	0	0	0
$H^2 H^3$	-1	0	1	0	0	-1	0	0	-9	0	0	0	0	0	0	0
$H^2 H^4$	0	0	0	0	0	0	3	0	0	3	0	0	-1	0	0	1
$H^3 H^1$	0	0	0	0	3	0	0	3	0	0	1	0	0	-1	0	0
$H^3 H^2$	1	0	-1	0	0	-1	0	0	-9	0	0	0	0	0	0	0
$H^3 H^3$	0	0	0	0	0	0	-4	0	0	9	0	0	-3	0	0	0
$H^3 H^4$	0	-1	0	1	0	0	0	0	0	0	0	-1	0	0	-1	0
$H^4 H^1$	-1	0	-1	0	0	9	0	0	-1	0	0	0	0	0	0	0
$H^4 H^2$	0	0	0	0	0	0	3	0	0	3	0	0	-1	0	0	-1
$H^4 H^3$	0	-1	0	-1	0	0	0	0	0	0	0	-1	0	0	1	0
$H^4 H^4$	0	0	0	0	0	0	0	25	0	0	-3	0	0	0	0	0
$denom.$	4	4	4	4	10	20	10	40	20	40	8	4	8	2	4	2

The numbers shown in the table should be divided
by the number given at the bottom row before
a square root is taken.

Appendix F

Jackknife Method

It is important to use appropriate statistical tools for an estimation of statistical uncertainties. Standard methods for calculating the uncertainties are sometimes inconvenient for a certain system. The Jackknife method is a way to give an estimate of statistical uncertainty. This method reduces the bias of the estimator to determine the variance of the system reliably. It is known that with an infinitely large number of random samples the jackknife method and the standard calculation of the error give the same variance.

Jackknife method is first invented by Quenouille in 1956 and developed further by Turkey in 1958. So the method is sometimes referred as Quenouille-Turkey jackknife method. We outline the method below.

Let X_i, $i = 1, \cdots, N$ be random samples and $F(X_i)$ be the function of X_i. The average of the ensemble $\{F(X_i)\}$ is

$$\overline{F}(X) = \frac{1}{N} \sum_{i=1}^{N} F(X_i). \tag{F.1}$$

The standard deviation $\sigma(F(X))$ of the ensemble is given by

$$\sigma^2(F(X)) = \frac{1}{N-1} \sum_{i=1}^{N} \left[\overline{F}(X) - F(X_i) \right]^2. \tag{F.2}$$

In some situations $F(X_i)$ may be ill-defined due to a large fluctuation in the original samples X_i. An example of such function would be a logarithm, in which case $F(X_i)$ with negative X_i is not defined. The jackknife method yields the following trick.

Let $Y^{(i)}$ be the average of the ensemble X_i with $N - 1$ samples such that

$$Y^{(i)} = \frac{1}{N-1} \sum_{k=1, k\neq i}^{N} X_k. \tag{F.3}$$

Then the mean value of the function based on the jackknife ensemble is given by

$$\overline{F}(Y) = \frac{1}{N} \sum_{i=1}^{N} Y^{(i)}. \tag{F.4}$$

169

The jackknife error σ_J is defined as

$$\sigma_J^2 = \frac{N-1}{N} \sum_{i=1}^{N} \left[\overline{F}(Y) - F\left(Y^{(i)}\right) \right]^2. \tag{F.5}$$

Note that the quantity $F\left(Y^{(i)}\right)$ is more reliably determined than the quantity $F\left(X_i\right)$, because the statistical fluctuation is reduced in the set $\{Y^{(i)}\}$ by order of $\sim 1/\sqrt{N}$.

BIBLIOGRAPHY

[1] M. Gell-Mann, Phys. Rev. **125**, 1067 (1962).

[2] M. Gell-Mann, Phys. Rev. Lett. **8**, 214 (1964).

[3] Y. Ne'eman, Nucl. Phys. **26**, 222 (1961).

[4] C. Zweig, CERN Rep. 8121/TH 401 and 8419/TH 412 (1964).

[5] S. Eidelman *et al.*, Phys. Lett. B**592**, 1 (2004).

[6] F. Halzen and A. D. Martin, *Quarks & Leptons: An Introductory Course in Mordern Particle Physics* (John Wiley & Sons, Inc., New York, 1984)

[7] F. E. Close, *An introduction to quarks and partons* (Academic Press, 1979).

[8] O. W. Greenberg, Phys. Rev. Lett., **13**, 598 (1964).

[9] M. E. Peskin and D. V. Schroeder, *An Introduction to Quantum Field Theory* (Perseus Books Publishing, Cambridge, 1995).

[10] T. Cheng and L. Li, *Gauge Theory of Elementary Particle Physics* (Clarendon Press, Oxford, 84).

[11] P. Ramond, *Field Theory: A Modern Primer* (Addison-Wesley Publishing Company, Inc., 1989).

[12] C. Morningstar, unpublished notes circulated among Lattice Hadron Physics Collaboration, 2005.

[13] H. J. Rothe, *Lattice Gauge Theories* (World Scientific, Singapore, 1994).

[14] I. Montvay and G. Münster, *Quantum Fields on a Lattice* (Cambridge Univ. Press, United Kingdom, 1994).

[15] M. Creutz, *Quarks, gluons and lattices* (Cambridge University Press, Cambridge, 1985).

[16] M. D. Pierro, `hep-lat/0009001`.

[17] R. Gupta, `hep-lat/9807028`.

[18] D. G. Richards, Phys. Rept. **378**, 207 (2003).

[19] D. J. Gross and F. Wilczek, Phys. Rev. Lett. **30**, 1343 (1973).

[20] H. D. Politzer, Phys. Rev. Lett. **30**, 1346 (1973).

[21] K. G. Wilson, Phys. Rev. D**10**, 2445 (1974).

[22] S. Aoki, G. Boyd, R. Burkhalter, S. Ejiri, M. Fukugita, S. Hashimoto, N. Ishizuka, K. Kanaya, T. Kaneko, Y. Kuramashi, K. Nagai, M. Okawa, H. P. Shanahan, A. Ukawa and T. Yoshië, Phys. Rev. D **67**, 034503 (2003).

[23] See the latest conference proceedings. Nucl. Phys. B Proc. Suppl. **140** (2004).

[24] B. DeWitt, Phys. Rev. **103**, 1565 (1956).

[25] U. Wiese, Nucl. Phys. B Proc. Suppl. **9**, 609 (1989).

[26] M. Lüscher, Nucl. Phys. B **364**, 237 (1991).

[27] F. Zimmerman, *et al.*, Nucl. Phys. B Proc. Suppl. **30**, 879 (1993).

[28] K. Rummukainen and S. Gottlieb, Nucl. Phys. B **450**, 397 (1995).

[29] Y. Nemoto, N. Nakajima, H. Matsufuru and H. Suganuma, Phys. Rev. D **68**, 094505 (2003).

[30] M. Göckeler, R. Horsley, D. Pleiter, P. E. L. Rakow, G. Schierholz, C. M. Maynard and D. G. Richards, Phys. Lett. B**532**, 63 (2002).

[31] LHPC Collaboration, QCDSF Collaboration, UKQCD Collaboration: M. Gockeler, R. Horsley, C. M. Maynard, D. Pleiter, P. E. L. Rakow, D. G. Richards, G. Schierholz, Phys. Lett. B**532**, 63 (2002).

[32] K. Sasaki and S. Sasaki, `hep-lat/0503026`.

[33] S. Sasaki, T. Blum and S. Ohta, Phys. Rev. D **65**, 074503 (2003).

[34] W. Melnitchouk, S. Bilson-Thompson, F. D. R. Bonnet, J. N. Hedditch, F. X. Lee, D. B. Lein-weber, A. G. Williams, J. M. Zanotti and J. B. Zhang, Phys. Rev. D **67**, 114506 (2003)

[35] D. Brömmel, P. Crompton, C. Gattringer, L. Y. Glozman, C. B. Lang, S. Schaefer and A. Schäfer, Phys. Rev. D **69**, 094513 (2004).

[36] J. M. Zanotti, D. B. Leinweber, A. G. Williams and J. B. Zhang, W. Melnitchouk and S. Choe, Phys. Rev. D **68**, 054506 (2003).

[37] S. Basak, R. Edwards, R. Fiebig, G. T. Fleming, U. M. Heller, C. Morningstar, D. Richards, I. Sato, S. Wallace, Nucl. Phys. Proc. Suppl. **140**, 278 (2005).

[38] S. Basak, R. Edwards, R. Fiebig, G. T. Fleming, U. M. Heller, C. Morningstar, D. Richards, I. Sato, S. Wallace, Nucl. Phys. Proc. Suppl. **140**, 281 (2005).

[39] S. Basak, R. Edwards, R. Fiebig, G. T. Fleming, U. M. Heller, C. Morningstar, D. Richards, I. Sato, S. Wallace, Nucl. Phys. Proc. Suppl. **140**, 287 (2005).

[40] S. Basak, R. Edwards, R. Fiebig, G. T. Fleming, U. M. Heller, C. Morningstar, D. Richards, I. Sato, S. Wallace, `hep-lat/0506029`.

[41] C. Morningstar, M. Peardon, Phys. Rev. D **60**, 034509 (1999).

[42] C. Michael, Nucl. Phys. B**259**, 58 (1985).

[43] M. Lüscher and U. Wolf, Nucl. Phys. B**339**, 222 (1990).

[44] R. C. Johnson, Phys. Lett. B**114**, 147 (1982).

[45] J. P. Elliott and P. G. Dawber, *Symmetry in Physics* (Oxford University Press, New York, 1979).

[46] S. L. Altmann and P. Herzig, *Point-Group Theory Tables* (Oxford University Press, New York, 1994).

[47] J. Mandula, G. Zweig, and J. Govaerts, Nucl. Phys. B**228**, 91 (1983).

[48] J. Mandula and E. Shpiz, Nucl. Phys. B**232**, 180 (1982).

[49] P. H. Butler, *Point Group Symmetry Applications* (Prenum Press, New York, 1981).

[50] S. L. Altmann and A. P. Cracknell, Reviews of Mordern Physics **37**, 1 (1965).

[51] R. Dirl, R. W. Haase, P. Herzig, P. Weinberger and S. L. Altmann, Phys. Rev. B **32**, 2 (1985).

[52] M. Wingate, T. DeGrand, S. Collins and U. Heller, Phys. Rev. D **52**, 307 (1995).

[53] P. Lacock, C. Michael, P. Boyle and P. Rowland, Phys. Rev. D **54**, 6997 (1996).

[54] J. L. Gammel, M. T. Menzel, and W. R. Wortman, Phys. Rev. D **3**, 2175 (1971).

[55] J. J. Kubis, Phys. Rev. D **6**, 547 (1972).

[56] C.R. Allton, *et al.* (UKQCD Collaboration), Phys. Rev. D **47**, 5128 (1993).

[57] S. Guesken, Nucl. Phys. Proc. Suppl. **17**, 361 (1990).

[58] M. Alford, T. Klassen, and P. Lepage, Nucl. Phys. Proc. Suppl. **47**, 370 (1996).

[59] M. Albanese *et al.* (APE Collaboration), Phys. Lett. B**192**, 163 (1987).

[60] A. Hasenfratz and F. Knechtli, Phys. Rev. D **64**, 034504 (2001).

[61] C. Morningstar and M. Peardon, Phys. Rev. D **69**, 054501 (2004).

[62] N. Mathur, Y. Chen, S. J. Dong, T. Draper, I. Horváth, F. X. Lee, K. F. Liu and J. B. Zhang, Phys. Lett. B**605**, 137 (2005).

[63] D. Guadagnoli, M. Papinutto and S. Simula, Phys. Lett. B**604**, 74 (2004).

[64] T. Burch, C. Gattringer, L. Y. Glozman, R. Kleindl, C. B. Lang, A. Schaefer Phys. Rev. D **70**, 054502 (2004)

[65] C. M. Maynard and D. G. Richard, Nucl. Phys. Proc. Suppl. **119**, 287 (2002).

[66] G. P. Lepage *et al.*, Nucl. Phys. B Proc. Suppl. **106**, 12 (2002).

[67] R. Fiebig, Phys. Rev. D **65**, 094512 (2002).

[68] F. X. Lee, S. J. Dong, T. Draper, I. Horváth, K. F. Liu, N. Mathur, and J. B. Zhang, Nucl. Phys. Proc. Suppl. **119**, 296 (2003).

[69] S. Sasaki, K. Sasaki, T. Hatsuda, and M. Asakawa, Nucl. Phys. Proc. Suppl. **129**, 212 (2004).

[70] Y. Chen *et al.*, `hep-lat/0405001`.

[71] R. Fiebig, unpublished notes circulated among Lattice Hadron Physics Collaboration, 2005.

[72] D. B. Carpenter and C. F. Baillie, Nucl. Phys. B**260**, 103 (1985).

[73] P. Chen, Phys. Rev. D **64**, 023409 (2001).

[74] M. Alford, T. R. Klassen, G. P. Lepage, Nucl. Phys. B**496**, 377 (1997).

[75] H. W. Hamber and C. M. Wu, Phys. Lett. B **133** (1983).

[76] H. R. Fiebig and R. M. Woloshyn, Phys. Lett. B**385**, 273 (1996).

[77] R. Lewis and R. M. Woloshyn, Phys. Rev. D**56**, 1571 (1997).

[78] F. X. Lee and D. Leinweber, `hep-lat/9606005`.

[79] J. Foley, A. Ó Cais, M. Peardon, and S. M. Ryan, `hep-lat/0405030`.

[80] T. R. Klassen, Nucl. Phys. B**533**, 557 (1998).

[81] J. Engels, F. Karsch, and T. Scheideler, Nucl. Phys. Proc. Suppl. **63**, 427 (1998).

[82] M. Fujisaki *et al.* (QCDTARO Collaboration), Nucl. Phys. Proc. Suppl. **53**, 426 (1997).

[83] Y. Iwasaki and T. Yoshie, Phys. Lett. B **216**, 387 (1989).

[84] T. Blum *et al.*, Phys. Rev. D **55**, 1133 (1997).

[85] G. Lepage, Phys. Rev. D **59**, 074502 (1999).

[86] K. Orginos and D. Toussaint, Phys. Rev. D **59**, 014501 (1999).

[87] K. Orginos, D. Toussaint, R. Sugar, Phys. Rev. D **60**, 054503 (1999).

[88] J. Zanotti *et al.*, Phys. Rev. D **65**, 074507 (2002).

[89] M. Fukugita, H. Mino, M. Okawa, G. Parisi, and A. Ukawa, Phys. Lett. B **294**, 380 (1992).

[90] S. Capstick and W. Roberts, Prog. Part. Nucl. Phys. **45**, S241 (2000).

[91] N. Isgur and G. Karl, Phys. Rev. D **18**, 4187 (1978).

[92] N. Isgur and G. Karl, Phys. Rev. D **19**, 2653 (1979).

[93] N. Isgur and G. Karl, Phys. Rev. Lett. **41**, 1269 (1978).

[94] S. Aoki, T. Umemura, M. Fukugita, N. Ishizuka, H. Mino, M. Okawa, and A. Ukawa, Phys. Rev. D **50**, 1 (1994).

[95] F. Csikor, Z. Fodor, S. D. Katz, and T. G. Kovacs, JHEP **0311**, 070 (2003).

[96] S. Sasaki, Phys. Rev. Lett. **93**, 152001 (2004).

[97] T. W. Chiu and T. H. Hsieh, `hep-lat/0404007`.

[98] N. Mathur *et al.*, Phys. Rev. D **70**, 074508 (2004).